ABSTRACT

Title of Dissertation: QUANTUM CONTROL AND MEASUREMENT ON FLUXONIUMS

Haonan Xiong, Doctor of Philosophy, 2022

Dissertation Directed by: Professor Vladimir E. Manucharyan
Department of Physics

Superconducting circuit is a promising platform for quantum computing and quantum simulation. A number of efforts have been made to explore the physics in transmon systems and optimize the qubit performance. Compared to transmon, fluxonium is a relatively new type of qubit and attracts more attention recently due to its high coherence time and large anharmonicity. In this thesis, we summarize recent progress toward high fidelity two-qubit gate and readout for fluxonium qubits. We report improved fluxonium coherence either in cavity or cavityless environment. In the former case, we demonstrate single-shot joint readout for two fluxonium qubits and explore various two-qubit gate schemes such as controlled-Z(CZ) gate, controlled-phase(CP) gate, bSWAP gate and cross-resonance(CR) gate. The CZ gate realized by near-resonantly driving the high transitions exhibits 99.2% fidelity from randomized benchmarking. A continuous CP gate set can be implemented by off-resonantly driving the high transitions and shows an average 99.2% fidelity from the cross-entropy benchmarking technique. Other gates involving only computational states are also explored to further improve the gate fidelity, which can take advantage of the high

coherence of the fluxonium lower levels. In the cavityless environment, we demonstrate fluorescence shelving readout with 1.7 MHz radiative decay rate for the readout transition while maintaining 52 μs coherence time for the qubit transition. Our research explores the basic elements for fluxonium-based quantum processors. The results suggest that fluxonium can be an excellent candidate for not only universal quantum computation but also quantum network and quantum optics studies.

QUANTUM CONTROL AND MEASUREMENT ON FLUXONIUM

by

Haonan Xiong

Dissertation submitted to the Faculty of the Graduate School of the
University of Maryland, College Park in partial fulfillment
of the requirements for the degree of
Doctor of Philosophy
2022

Dissertation Committee:
Professor Vladimir E. Manucharyan, Chair
Professor Sankar Das Sarma
Professor Jay Deep Sau
Professor Benjamin S. Palmer
Professor Ichiro Takeuchi, Dean's Representative

Acknowledgement

Pursuing a PhD for five years in a foreign land is never an easy journey. Fortunately, I was surrounded by a group of people who care about me and supported me through the hard times. Words are not enough to repay the kindness from them, which I know is priceless. But right now at the final stage of my graduate study, I still thank all of you for making this day come true.

I first thank my mom and dad, Dongmei and Qinglin, for their unconditional love and support all the time. Even though they had a different opinion on my future career when I chose to study physics in college nine years ago, they were always with me in no time whenever I needed their help. They make me feel there is a place in this world called home which is waiting for me wherever I go, with hot food and a comfy bed.

I would like to thank my advisor, Vladimir Manucharyan, without whom my accomplishments of all these years will be never possible. I still remember when I sent him my derivation of a JPA circuit in my first year, he sent me back his derivation immediately on a small piece of paper he managed to find nearby. I can also recall the time we spent together soldering the skinny cables and testing the copper powders, not to mention the numerous meetings on my projects. When a visitor came, he introduced me as ”the next generation” and indeed, I learned a lot from him, not only the scientific knowledge and experimental experiences, but also the ability to present the work. He tirelessly gave me feedbacks on the slides of my talk and the figures in the paper. Thanks to the training of all these years, I am much more professional on visualize the data and convey the ideas efficiently on a

presentation. Vlad also gave me lots of suggestions when I was having trouble finding the committee members. Besides, I express my gratitude to other members of the committee: Professors Das Sarma, Sau, Palmer, and Takeuchi, for fitting my defense into their busy schedule.

When I first came to the lab, Prof. Yen-Hsiang Lin, who was a postdoc at that time, became my closest friend. Nothing can be more comforting than working with someone speaking the native language during my first year in a foreign country. Yen-Hsiang is warm-hearted, patient, and encouraging. I felt no pressure when discussing projects with him and I could ask any stupid questions. He always explained to me nicely and leaded me onto the right track. He was very experienced and taught me all most everything in the lab, including the basics of fluxoniums, the measurement setup, designing cavities and waveguides .... I am afraid I will run out of spaces if I list every details here. Yen-Hsiang was also cared about my well-being and willing to offer any help and suggestions in my life. Together, we improved the fluorescence experiment and got it published. This project was launched by Dr. Nathanaël Cottet. Nat left the lab before I came in. It is a pity that I do not have the chance to work with him in person in the lab. But his experiment summary was so well-organized that I could easily understand the basic principles. Nat and I had several meetings when finalizing the work. Even though it is a short period of time, I was still impressed by his patience and creativeness.

Dr. Long Nguyen was a senior graduate student when I joined the lab. He loves to communicate with others and soon we became friends. He had many good ideas and showed me many good references for the decoherence and the gate. He was always ready to help and gave us lots of suggestions in the fluorescence project. Later, he taught me how to characterize the gate and handed over the two-qubit experiment to me. In addition, he was also a humorous person and made the lab a fun place to stay.

I am grateful to Dr. Quentin Ficheux who worked closely with me in all the two-qubit projects. Quentin is very knowledgeable both in theory and experiments. He had an agile

mind. Whenever I was confused about a concept he brought, he said, ”OK, let me show it to you”. Then he just started to derive on the while board without any hesitation and preparation. He was an excellent example of a professional researcher and at the same time, he was a good teacher with great pedagogical skill. He taught me many good experiment habits. ”Whenever you see anything you don’t understand, you should try your best to figure it out. Otherwise, it will eventually affect your experiment, in a way that you may not expect or notice.” This is one of the most important lessons that I learned from him.

Dr. Ivan Pechenezhskiy was the one who guided me into the world of python. Before I entered the lab, I rarely coded with python. With Ivan’s help, I quickly mastered it. We spent many days writing and debugging the drivers for the instruments. We had many fruitful discussions and I got familiar with professional coding and how the instruments work and communicate. Thanks to Ivan, the whole lab has well-written python scripts to use in daily experiments.

Unfortunately I am running out of spaces for my thanks to the group members. I also would like to thank Dr. Roman Kuzmin for the help in fridge maintenance. I am thankful to Dr. Aaron Somoroff for patiently teaching me all kinds of fab techniques, from silicon to sapphire. I thank Raymond Mencia for always sharing with me the news in latest research. I appreciate the help of Dr. Nitish Mehta and sharing the instruments with me. I express my gratitude to Dr. Nicholas Grabon, Dr. Natalia Pankratova, and Dr. Hanho Lee for their help in my fabrication and various little stuff in the lab. Wei-Ju Lin, Shukai Liu, and Dr. Arunav Bordoloi are new members in the lab. I want to thank Wei-Ju in particular, for his timely help on the experiments with no complaints while I was busy for graduation.

I appreciate the support from our collaborators. Dr. Konstantin Nesterov shared with me his code and notes in two-qubit simulation. Prof. Maxim Vavilov gave me many good suggestions in the gate projects. Prof. Chen Wang and his students Ebru Dogan and Dario Rosenstock contributed in the gate project and shared with me their experimental skills which are quite helpful. I thank you all for the discussions we had.

I want to thank other faculty members at UMD who offered help during my time here. I thank Prof. Christopher Lobb for introducing me to Vlad and this wonderful team. I thank Prof. Frederick Wellstood who gave me lots of advice on my scholarly paper. I thank Prof. Benjamin Palmer for sharing their device with us. I also thank Prof. Johnpierre Paglione for sharing their magnet data with us to debug our experiments.

I express my thank you to other labs who hosted my visits. I thank Prof. Michel Devoret for his generous invitation and insightful discussions. I thank Prof. Andreas Wallraff for showing me all the wonderful projects and acknowledging my ability. I thank Prof. Xiaobo Zhu for introducing their experiments. I thank Dr. Haifeng Yu for inviting me to the new labs. I also thank Dr. Fei Yan for hosting me at SIQSE.

When I first went to college, I had no idea about research. Prof. Chuangang Ning showed me the way to entering the field of scientific research. After that, I joined Prof. Luming Duan's team. During the two years in the lab, Dr. Yipu Song, Dr. Hongyi Zhang, and Prof. Luyan Sun introduced me to superconducting circuit community. During this time, I had a short visit to Prof. Hong Tang's group at Yale and spent a meaningful summer with Wance, Mohan, Hanyu, Changling and Dr. Chang-Ling. I give my thanks to all of you for your help and advice.

I would also like to thank all my old friends. I thank Wentao, Wei, Zhixin, Xueyue, Xinghan, ... I was always looking forward to the gathering at the March meeting. I thank Yu for being a close friend accompanying me starting from a small town in China all the way to America. I thank Min for the suggestion and help in college and in my graduate study. I thank Hsiang-Sheng and Junling for sharing their experience and opinion on the industry.

It will be boring if I spent the five years without my friends at College Park. I thank Zhiyu, Mingshu, Yihang, Yixu, Yalun, and Xiangyu for the fantastic parties and the supports in my life. I also thank my roommates Shuyang, Kaixin, Haining, Fei,and Yizhou for facing the problems together that we encountered in the house. I am grateful to Zhuo, Zeyu, and

Peng for the entertainments in my holidays. I thank Mr. Jinlong Han, Riots, and Bilibili for their wonderful products as my moral support.

Most importantly, I want to say thank you to my partner Tong. I appreciate your patience over the five years and I am sincerely grateful to your support and understanding to help me get through the difficult times. You also gave me lots of great advice and led to my reflection on myself. You are the love of my life, forever and ever.

Table of Contents

List of Figures

List of Tables

Nomenclatures

Abbreviations

AlOx Aluminum Oxide

AWG Arbitrary waveform generator

BOE Buffered Oxide Etch

CNC Computer numerical control

CNOT Controlled-NOT gate

CP, CPhase Controlled-Phase

CQED Cavity quantum electrodynamics

cQED Circuit quantum electrodynamics

CR Cross-resonance

CZ Controlled-Z

DRAG Derivative removal by adiabatic gate

EOM Equation of motion

IPA Isopropanol

IQ In-phase, Quadrature

IRB Interleaved randomized benchmarking

JBA Josephson bifurcation amplifier

JC Jaynes-Cummings

JJ Josephson junction

JPA Josephson parametric amplifier

JPC Josephson parametric converter

JTWPA Josephson traveling wave parametric amplifier

LO Local oscillator

MLE Maximum likelihood estimation

NISQ Noisy intermediate-scale quantum

PB Purity benchmarking

QEC Quantum error correction

QND Quantum non-demolition

QPT Quantum process tomography

QST Quantum state tomography

RB Randomized benchmarking

RF Radio frequency

RWA Rotating wave approximation

SEM Scanning electron microscope

SMA SubMiniature version A

SNR Signal to noise ratio

SPAM State preparation and measurement

SQUID Superconducting quantum interference device

SSB Single sideband

TLS Two-level system

VNA Vector network analyzer

XEB Cross-entropy benchmarking

Greek Letters

α Anharmonicity

χ Dispersive shift

Δ_{Al} Superconducting energy gap of aluminum (Al), $1.8 \times 10^{-4}\,\mathrm{eV}$

η Quantum efficiency

Γ Relaxation rate

κ Coupling/relaxation rate of cavity

Ω Rabi frequency

ω_p Josephson junction plasma frequency

$\omega_{\alpha\beta}$ Qubit transition frequency between states α and β

Φ Magnetic flux threading a loop

ϕ Phase operator

ρ Density matrix

σ_I, σ_0 Pauli identity matrix

σ_X, σ_1 Pauli X matrix

σ_Y, σ_2 Pauli Y matrix

σ_Z, σ_3 Pauli Z matrix

Latin Letters

$a^\dagger, a$ Creation and annihilation operators

C Capacitance

D Oscillator displacement operator

E_C Electric charging energy

E_J Josephson energy

E_L Magnetic inductive energy

G Gain

g Coupling constant

H Hamiltonian

I Pauli identity matrix

I_c Junction critical current

J_C	Capacitive coupling constant
L	Inductance
L_i	Lindblad operators
L_J	Josephson inductance
M_e	Error matrix of the readout
n	Charge number operator
n_{th}	Thermal photon number
P	Population
Q	Quality factor
Q^{ext}	External quality factor
Q^{in}	Internal quality factor
r	Reflection coefficient
R_N	Normal resistance of a Josephson junction
$S(\omega)$	Noise spectral density
S_{ij}	S parameter of a microwave network
T_1	Relaxation time of qubit
T_2	Coherence time of qubit
T_2^{echo}	Coherence time of qubit obtained from echo measurement
T_2^{Ramsey}	Coherence time of qubit obtained from Ramsey measurement

T_ϕ Pure dephasing time

T_c Critical temperature

X Pauli X matrix

x_{qp} Quasiparticle density

Y Pauli Y matrix

$Y(\omega)$ Admittance

Z Pauli Z matrix

Physical Constants

$\hbar$ Reduced Planck constant, $1.054 \times 10^{-34}\,\mathrm{J \cdot s}$

Φ_0 Magnetic flux quantum, $2.067 \times 10^{-15}\,\mathrm{T \cdot m^2}$

ϕ_0 Reduced magnetic flux quantum, $0.3291 \times 10^{-15}\,\mathrm{T \cdot m^2}$

e Electronic charge, $1.602 \times 10^{-19}\,\mathrm{C}$

h Planck constant, $6.626 \times 10^{-34}\,\mathrm{J \cdot s}$

k_B Boltzmann constant, $1.38 \times 10^{-23}\,\mathrm{J/K}$

Citations to Published Work

Parts of Chapters 3, 4, and 5 have appeared in the following papers:

N. Cottet, H. Xiong, L. B. Nguyen, Y.-H. Lin, and V. E. Manucharyan, "Electron shelving of a superconducting artificial atom," *Nature Communications*, vol. 12, p. 6383, 12 2021.

Q. Ficheux, L. B. Nguyen, A. Somoroff, H. Xiong, K. N. Nesterov, M. G. Vavilov, and V. E. Manucharyan, "Fast Logic with Slow Qubits: Microwave-Activated Controlled-Z Gate on Low-Frequency Fluxoniums," *Physical Review X*, vol. 11, p. 021026, 5 2021

H. Xiong, Q. Ficheux, A. Somoroff, L. B. Nguyen, E. Dogan, D. Rosenstock, C. Wang, K. N. Nesterov, M. G. Vavilov, and V. E. Manucharyan, "Arbitrary controlled-phase gate on fluxonium qubits using differential ac Stark shifts," *Physical Review Research*, vol. 4, p. 023040, 4 2022.

Chapter 1

Introduction

1.1 Quantum Computation and Simulation

Richard Feynman proposed the concept of a quantum computer at a conference on "Simulating physics with computers" in 1981 [1]. He believes that a quantum system is too hard to simulate for a classical computer, but it is affordable with quantum computer elements. Before this conference, Paul Benioff already studied a quantum model of the Turing machine [2]. But Feynman described the quantum computer as

> *It's not a Turing machine, but a machine of a different kind.*

One of the main reason is that he thinks there are too many variables that define the status of a large quantum system. This idea was shared by Yuri Manin

> *The quantum phase space is much bigger than classical.*

So actually the original proposal of quantum computer is for quantum simulation tasks. It is more like a quantum simulator, rather than a computer. The idea is to study (simulate) large scale complex quantum systems with much fewer quantum elements (atoms, for example) or at least in a controllable way such that the predominant interaction is maintained and easy to debug.

Years after, David Deutsch, Umesh Vazirani, and Ethan Bernstein developed Feynman's idea of quantum computation. It was proposed that a quantum computer can solve problems that have nothing to do with quantum systems and it can have a speedup on some tasks over a classical computer. Then Peter Shor came up with the famous algorithm for factoring large numbers with a exponential speedup. Due to its close relation to cryptography, the concept of quantum computation began its public fame.

At the same time, what a quantum computer should be like becomes clear and specific. It should base on fundamentally quantum mechanical objects (qubits) and be able to perform any algorithm written in the gate and circuit language. This machine is called a universal quantum computer, which is the ultimate goal for this thesis. As Feynman already pointed out, this is not an easy problem. The biggest obstacle in this field has been, and will still be, decoherence in a quantum system. Two outstanding atomic physicists Serge Haroche and Jean-Michel Raimond said in 1996

> *The large-scale quantum machine, though it may be the computer scientist's dream, is the experimenter's nightmare.*

Decoherence brings errors on the qubit. Its time scale determines the lifetime of quantum information stored in the system. On the other hand, decoherence originates from the interaction between the qubit and the environment, which is an interesting topic itself. Figuring out where the interactions come from and how to engineer them is crucial to understand the microscopic world, which can also inspire new research directions in material science or even cosmology.

One solution to fight against decoherence is quantum error correction. It requires a large number of qubits, and more importantly, operation fidelity above a certain threshold. The idea is to use multiple physical qubits to construct a logical qubit that has a much lower error rate. Google published their 54-qubit quantum processor Sycamore in 2019 on which they demonstrated quantum supremacy [3]. Unfortunately, it only showed advantage over a specific task and its practical benefit is obscure. It can not efficiently run any advantageous quantum algorithms due to the error rate on the gates. Following experiments [4] showed the possibility to build logical qubits on the same device. Even though the total physical qubit error rate is still above the threshold required by the surface code, there is still hope that we can cross the line in the near future. This work pointed out two main limiting factors on the current superconducting qubit device – readout and two-qubit gate. These two aspects will be the main topic of this thesis.

Nevertheless, Google's experiment of quantum supremacy is a successful demonstration that the current noisy quantum hardware is able to outperform classical computer in certain situations, which sets a milestone of the Noisy Intermediate-Scale Quantum (NISQ) era. It is not clear yet how a quantum processor without error correction can benefit us. At least, it provides a new tool to study quantum systems. For example, NISQ devices can already accomplish simulation tasks such as simulating energy spectrum of various systems [5]–[7]. These type of quantum simulators are closer to what Feynman imagines. The NISQ devices do not look so powerful at this stage. However, as many competing efforts are devoted to

investigating the possibilities across different physical systems, any breakthroughs or new ideas may be able to trigger an revolution that has a profound impact upon the society.

In principle, any quantum system with well-defined distinct two levels can be the potential building block of a quantum computer, i.e. qubit. The two levels can be the microscopic degree of freedom, such as the spin or orbital states of the electron. They can also be the collective modes, such as the electron wavefunction of a superconductor. If we use universe to describe all the possible qubits in nature, there are some stars that are brighter than the others after years of research. Superconducting qubits are defined by the states of the superconducting wavefunction and are the focus of this thesis. Ion trap systems confine ions in vacuum through electromagnetic field. Progress has been reported in achieving high-fidelity gates and scaling up the system [8]. The coherent photonic state of a microwave resonator is another type of macroscopic qubit and has been successfully used to exhibit unique quantum error correction techniques [9]–[11]. On the other hand, travelling photon in free space can also be harnessed for quantum computing, but it belongs to another architecture called the measurement-based quantum computing [12]. Recently, high-fidelity two-qubit gates were reported on the silicon spin qubit system, pushing it further towards the logical qubit era, which attracts more attention in this field.

1.2 Outline

The rest of this dissertation is organized as follows. In chapter 2, we introduce the circuit models in circuit quantum electrodynamics, especially for the fluxonium. We derive the key properties of fluxonium in different environments and briefly review the energy relaxation and dephasing mechanisms in superconducting systems. We then present the first part of the experimental results on the qubit readout and initialization in chapter 3. We will discuss two different readout schemes. One is dispersive readout with a 3D cavity. The other is fluorescence readout in a 3D waveguide, which we call a cavityless environment. We will explain the concept of non-QNDness and show the corresponding data for both cases. In chapter 4, we will present the experiments on microwave gates with fluxonium. We begin with introducing the gate characterization techniques, including quantum process tomography and randomized benchmarking based techniques (IRB, PB, XEB). Then we will explain the principles of the single-qubit and two-qubit gates and show the experimental data. In the end, we will conclude all the experiments in chapter 5. We will emphasize the significance and provide insights for future research.

In this thesis, we will use the following symbols for Pauli matrices $\{\sigma_0, \sigma_1, \sigma_2, \sigma_3\}$

$= \{\sigma_I, \sigma_x, \sigma_y, \sigma_z\} = \{I, X, Y, Z\}$ and

$$\sigma_0 = \begin{pmatrix} 1 & 0 \\ 0 & 1 \end{pmatrix},\ \sigma_1 = \begin{pmatrix} 1 & 0 \\ 0 & -1 \end{pmatrix},\ \sigma_2 = \begin{pmatrix} 0 & 1 \\ 1 & 0 \end{pmatrix},\ \sigma_3 = \begin{pmatrix} 0 & -i \\ i & 0 \end{pmatrix}. \tag{1.1}$$

Chapter 2

Superconducting Circuit Models

In this chapter, we will introduce the basic concepts and models in circuit quantum electrodynamics (cQED)[13]–[15]. Starting from the observation of coherent quantum superposition and oscillation in superconducting circuits [16], [17], it has been realized that the coherent electron wavefunction of the superconductor can be used to create a macroscopic quantum object, thanks to the Bose-Einstein condensation of the Cooper pairs. One key ingredient to make superconducting circuits nontrivial compared to the conventional circuits is the nonlinearity given by the Josephson junction, which will be introduced in Sec. 2.1. Without nonlinearity there is no way to create a quantum superposition and the system can always be described classically [9]–[11]. Josephson junction is the core for all the superconducting qubits such that they can be an artificial atom. The invention of circuit quantization technique [18]–[20] provides a useful tool to study cQED systems. It becomes straightforward to design new qubit structures and understand how it behaves. There used to be three types of superconducting qubits [20], the charge qubit [17], the flux qubit [21] and the phase qubit [22]. After years of improvement and exploration, the superconducting qubits are experiencing an evolution and modern types of qubits are realized experimentally during the process including transmon [23], fluxonium [24], C-shunt flux qubit [25], $0-\pi$ qubit [26], Blochnium [27], etc. These new qubits come with the abilities to suppress the noise from the environment and the environment itself is engineered in a more sophisticated way than ever. We will introduce fluxonium as the main topic in the cQED context and discuss the interaction with the environment and in the presence of another fluxonium.

2.1 Josephson Junction

Josephson junction (JJ), first introduced in [28], is the essential building block of any type of superconducting qubits. It is a trilayer structure created by two superconducting layer sandwiching an insulating layer. For most superconducting qubits, the junction is made of Al/AlOx/Al. This is the simplest way to make Josephson junctions and it turns out to be quite robust. Aluminum is not necessarily the best material for making Josephson junctions. One criteria is the critical temperature T_c. Even though superconductor has zero dc resistance at $T \ll T_c$, it exhibits non-zero ac losses and surface resistance at finite temperature [15], [29]. This is because electrons can be thermally excited from the Cooper pair state with a binding energy $2\Delta = 3.52 k_B T_c$ and become 'quasiparticles'. These quasiparticles add a loss channel in the superconducting system, which will also be discussed in Sec. 2.5.1. Therefore, a higher T_c means lower resistive loss and will be beneficial for the qubit lifetime. For example, tantalum ($T_c = 4.48$ K) and niobium ($T_c = 9.5$ K) have higher T_c than aluminum ($T_c = 1.14$ K). However, aluminum still has the advantage in terms of the fabrication feasibility such as the stability of the oxide layer and the uniformity of the edges. On the other hand, the property of the interface between the metal and the substrate (the air or the oxide layer) is also important, as the defects in these interfaces can be detrimental to the qubit lifetime. So one need to consider multiple aspects and it is not straightforward to judge whether a material is better than the other without any tests. There are ongoing efforts to introduce new materials in the superconducting circuit system, which has always been a hot topic [30]–[38].

The most useful property of a Josephson junction as a circuit element is relations between the phase difference across the junction ϕ, the junction current I and the junction voltage V. They can be described by the Josephson equations

$$I = I_c \sin\phi, \tag{2.1}$$

$$V = \phi_0 \frac{d\phi}{dt}, \tag{2.2}$$

where $\phi_0 = \Phi_0/2\pi = \hbar/2e$ is the reduce flux quantum. (Φ_0 is the flux quantum.) Combining the two equations, we can have

$$V = \frac{\phi_0}{I_c \cos\phi} \frac{dI}{dt}. \tag{2.3}$$

This is similar to the property of a classical inductor $V = L_J(dI/dt)$, where

$$L_J = \frac{\phi_0}{I_c \cos\phi}. \tag{2.4}$$

Therefore, the Josephson junction can be treated as a non-linear inductor classically. This feature will be utilized when we derive the gain of a Josephson parametric amplifier (JPA) in Sec. 3.3.

For a classical linear inductor, the voltage equals the changing rate of the flux Φ threading the loop

$$V = \frac{d\Phi}{dt}. \tag{2.5}$$

So the phase difference in the context of Josephson junction is equivalent to the reduced flux in the context of the loop inductance $\phi = 2\pi\Phi/\Phi_0$. This is not surprising because the flux and phase difference are linked with the Aharonov-Bohm effect [39]. This is why ϕ is still called the reduced flux in some cases where the Josephson junction is not connected to a loop and there is actually no well-defined physical 'flux' in the system.

The inductance of a classical linear inductor comes from the fact that the energy in the circuit can be converted to the magnetic field, which is determined by the wire geometry. This type of inductance is called the geometric inductance. However, the inductance of a Josephson junction L_J can be much larger considering its small geometry. This is because the source of L_J is the inertia of the electrons at the junction and it is called kinetic inductance which has a different origin from the inductance of a coil. The existence of kinetic inductance makes it possible that a large inductance can be created without fabricating a huge coil on the chip.

The energy of a linear inductor is $H_L = E_L\phi^2/2$, where $E_L = \phi_0^2/L$ is called the inductive energy. The energy of a Josephson junction is $H_J = -E_J\cos\phi$ (droping a constant), where $E_J = \phi_0^2/L_J$ is the Josephson energy. E_J is also related to the normal resistance R_N of the junction at room temperature $E_J = \Delta_{\mathrm{Al}}R_Q/(2R_N)$, where $R_Q = h/(2e)^2$ is the resistance quantum. R_N and L_J is inversely proportional to the junction area A. Therefore we have $E_J \propto A$. There also exists a small capacitance C_J between the two superconducting layer of the junction and the energy associated with it is $H_C = 4E_Cn^2$, where n is the charge number and $E_C = e^2/(2C_J)$ is the charging energy of the junction. For a Al/AlOx/Al junction, the empirical value for C_J per area is about 45 $\mathrm{fF}/\mu\mathrm{m}^2$. Another important property of a Josephson junction is the plasma frequency

$$\omega_p = \frac{1}{\hbar}\sqrt{8E_JE_C} = \frac{1}{\sqrt{L_JC_J}}. \tag{2.6}$$

From the definition, we can find that ω_p does not depend on the junction and only depends on the transparency of the insulating layer. For Al/AlOx/Al junctions, the oxidation process is the most important factor. Typically its plasma frequency can be $10-40$ GHz [40]. In our

experiment, ω_p is usually around 20 GHz.

2.2 Resonator, Transmon and Fluxonium

There are three major elements in cQED: capacitor, inductor, and Josephson junction, which can be characterized with the charging energy E_C, the inductive energy and the Josephson energy. Different combinations of these three elements can create the common circuit models: a resonator, a transmon, or a fluxonium.

A resonator is a capacitor shunted by an inductor as show in Fig. 2.1. In the experiment, it can be the resonant mode of a metal structure. For example, the lowest mode of a on-chip metal strip (2D coplanar waveguide cavity), the lowest mode of a copper box (3D cavity), or a piece of metal pad (capacitor) connected with a Josephson junction chain (inductor) [27], [41] can all be treated as a resonator. Its Hamiltonian can be written as

$$H_{\text{resonator}} = 4E_C n^2 + \frac{1}{2}E_L\phi^2. \tag{2.7}$$

Now n and ϕ are canonically conjugate quantum operators that satisfy the canonical commutation relation $[\phi, n] = i$. n and ϕ are just like the momentum p and the position x operator of a mass on the spring. $4E_C n^2$ is the kinetic energy and $\frac{1}{2}E_L\phi^2$ is the potential energy. A resonator is essentially a harmonic oscillator. We can introduce the annihilation and creation operators a and $a^\dagger$ in the second quantization formalism.

$$\phi = \frac{1}{\sqrt{2}}\left(\frac{8E_C}{E_L}\right)^{\frac{1}{4}}(a^\dagger + a), \tag{2.8}$$

$$n = \frac{i}{\sqrt{2}}\left(\frac{E_L}{8E_C}\right)^{\frac{1}{4}}(a^\dagger - a). \tag{2.9}$$

Eq. 2.8 and Eq. 2.9 are important when numerically simulating a arbitrary circuit Hamiltonian in the harmonic oscillator basis (using the Qutip python package for example). With these equations, the Hamiltonian can be written as

$$H_{\text{resonator}} = \hbar\omega(a^\dagger a + \frac{1}{2}), \tag{2.10}$$

where $\omega = \sqrt{8E_L E_C}/\hbar = 1/\sqrt{LC}$ is the resonant frequency. The energy of the eigenstates is $E_n = \hbar\omega(n+1/2)$, n=0, 1, 2, ... The vacuum state energy $E_0 = \hbar\omega/2$ will conventionally be offset to 0 for simplicity in the following text. As shown in Fig. 2.1d, because of the quadratic potential given by the inductor, the resonator spectrum is equally spaced. We can

define the anharmonicity of the system using the first three levels $\alpha = (E_2 - E_1) - (E_1 - E_0)$, which is obviously zero for a resonator. For this reason, a resonator itself can not be used as a qubit. There is no way one can prevent the population leaking to higher two levels without introducing a non-linear element in the circuit. If a drive with frequency ω is applied to the resonator, it can be imagined that the population will keep climbing the equally-spaced level ladder. Strictly speaking, for any linear classical drive, the evolution of the resonator is described by the displacement operator $D(\alpha) = \exp(-|\alpha|^2)\exp(\alpha a^\dagger)\exp(-\alpha a)$. α is a complex number determined by the drive parameters. Applying the displacement operator to the vacuum state, we can get a coherent state [42]

$$|\alpha\rangle = D(\alpha)\,|0\rangle \tag{2.11}$$

$$= \exp(-|\alpha|^2)\sum_n \frac{\alpha^n}{\sqrt{n!}}\,|n\rangle\,. \tag{2.12}$$

The coherent state is the eigenstate of the annihilation operator $a\,|\alpha\rangle = \alpha\,|\alpha\rangle$ and the mean photon number is $\bar{n} = \langle\alpha|\,a^\dagger a\,|\alpha\rangle = |\alpha|^2$. The parameters of the drive can only determines the mean photon number and the phase of the coherent state, but can not change the fact that the final state is a classical-like superposition of a series of Fock states and can not be a qubit. This problem can only be solved after introducing a non-linearity by coupling the resonator to a qubit. A cat state, a superposition of coherent states, can be created and used as a qubit. Several error correction schemes have been explore in this type of system.

Now if we connect a Josephson junction in parallel with a large capacitor (which is usually a large piece of metal pad), we can create a transmon. It is worth noticing that in this case the extra capacitance is much larger than the capacitance of the junction itself, that is, $C \gg C_J$. The charging energy is dominated by the extra capacitance $E_C = e^2/(2C)$. In order to be in the transmon regime, E_J should be much larger than E_C. This is necessary to suppress the charge noise. In general, the transmon Hamiltonian can be written as

$$H_{\text{transmon}} = 4E_C(n - n_g)^2 - E_J\cos\phi, \tag{2.13}$$

where n_g is the offset charge on the Cooper pair island (which is the metal pad connecting to the junction). n_g can fluctuate due to the quasiparticle tunneling. In the case of large E_C (small capacitance), the energy spectrum has a strong dispersion on the offset charge. Tunneling events can significantly change the energy levels and cause decoherence. With a small E_C, n_g barely affect the energy and can be set at 0 in the spectrum analysis. But the suppression of charge noise comes with a price. The system anharmonicity also becomes smaller. This can be more clear in the second quantization language. First, we need to

expand $\cos\phi$ in Taylor series and substitute Eq. 2.8 and Eq. 2.9 into the Hamiltonian. After dropping the fast rotating terms and the constants, the transmon Hamiltonian can be written as

$$H_{\text{transmon}} = \hbar(\omega + \frac{\alpha}{2})a^\dagger a + \frac{\hbar\alpha}{2}(a^\dagger a)^2. \tag{2.14}$$

where $\omega = \sqrt{8E_J E_C}/\hbar$, $\alpha = -E_C$ is the anharmonicity. For a typical transmon, $\alpha/2\pi$ is on the order of 100 or 200 MHz [43] (the $0-1$ frequency is on the order of 5 GHz).

The existence of the anharmonicity α makes it possible to use the transmon $0-1$ transition as a qubit and α sets a limit on how fast we can perform a gate on this qubit. For example, the Fourier spectrum of a Gaussian π pulse can not have a line width exceeding $|\alpha|$. Otherwise the population can be excited to the higher levels. Therefore in the time domain, the width of the π pulse should be longer than $1/|\alpha|$. 100 MHz anharmonicity corresponds to a time scale of 10 ns and this is the typical single-qubit gate time for transmon qubits on state-of-the-art superconducting quantum processors. One way to suppress the leakage at large drive strength is the Derivative Removal by Adiabatic Gate (DRAG) technique. By adding an additional derivative component on the orthogonal quadrature of the control pulse, the Fourier spectrum of the pulse can be engineered to avoid the leakage transition. The pulse can be more adiabatic and there will be less leakage at the end of the pulse.

Now let's combine all the three circuit elements and connect them in parallel. In this way, a fluxonium can be created and it is the main topic of this thesis. Fig. 2.2 shows the design of a fluxonium. The fluxonium has a pair of antenna to couple to the external environment, which also provides the charging energy. The inductance is provided by the long Josephson junction array. Typically the number of junctions in the chain N is on the order of 100. The junction size is much larger than the small junction on top of the loop. The area ratio is on the order of 50, meaning that each junction has a very large Josephson energy E_J^{chain}. Because the phase across each junction in the chain is $\phi/N \ll 1$, the energy contribution from the chain is

$$\sum_i^N -E_J^{\text{chain}} \cos\frac{\phi}{N} \approx \sum_i^N -E_J^{\text{chain}} \left(1 - \frac{1}{2}\left(\frac{\phi}{N}\right)^2\right) \tag{2.15}$$

$$= -NE_J^{\text{chain}} + \frac{1}{2}\frac{E_J^{\text{chain}}}{N}\phi^2. \tag{2.16}$$

Eq. 2.16 demonstrates that in the limit of small phase difference across each junction, the Josephson junction chain behaves like a linear inductor with inductive energy $E_L = E_J^{\text{chain}}/N$. One reason for large chain junctions is to suppress the phase slip which can

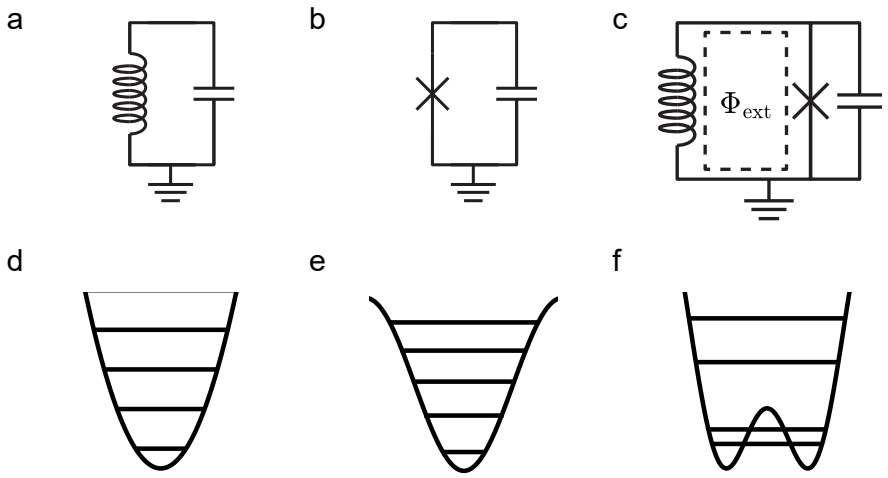

Figure 2.1: Circuit diagrams and energy spectrum for a resonator, transmon and fluxonium. (a) A resonator. It can be modeled as an inductor and a capacitor connected in parallel. (b) A transmon. The Josephson junction behaves like a non-linear inductor and makes the system anharmonic. (c) A fluxonium. The Josephson junction is shunted by a large linear inductor. This forms a loop where an external flux can be applied to tune the circuit Hamiltonian. (d, e, f) The potential energy and energy spectra for a typical resonator, transmon, and a fluxonium at half flux quanta. The resonator has equally spaced spectrum. The transmon spectrum has smaller spacing between higher levels due to the weak anharmonicity. On the contrary, fluxonium system can have much larger anharmonicity that comes from the non-trivial potential.

cause decoherence. This requires $\exp(-\sqrt{8E_J^{\text{chain}}/E_C^{\text{chain}}}) \ll 1$ [40].

A long chain with hundreds of junctions may look difficult to fabricate. However, it turns out the yield is quite high and the recipe is as easy as making a single junction. The junction chain is deposited together with the small Josephson junction in the same double-angle deposition process and no extra steps are needed. Yet, one need to avoid a chain that is too long, because the chain modes can be lower down to the GHz range and have a strong interaction with the typical fluxonium spectrum [44], [45]. Using the Josephson junction chain as the linear inductor is not the only choice. In fact, there have been some studies exploring the fluxonium fabricated by replacing the junction chain with granular aluminum [46] or geometric inductor [47].

The junction chain forms a closed loop with the small Josephson junction. The external magnetic flux Φ_{ext} threading the loop corresponds to an extra phase difference $\phi_{\text{ext}} = 2\pi\Phi_{\text{ext}}/\Phi_0$. The fluxonium Hamiltonian can hence be expressed as

$$H_{\text{fluxonium}} = 4E_C n^2 - E_J \cos(\phi - \phi_{\text{ext}}) + \frac{1}{2}E_L\phi^2. \tag{2.17}$$

Compared to the transmon Hamiltonian, the potential in a fluxonium Hamiltonian is more complicated and can be tuned with the external flux. The potential has a quadratic envelope coming from the inductor and multiple small wells coming from the $\cos$ term of the small Josephson junction that sit inside the parabola. At integer flux quanta ($\phi_{\text{ext}} = ..., -2\pi, 0, 2\pi, ...$), the wavefunctions of $|0\rangle$ and $|1\rangle$ are localized in the same well. The transition of these type of states is called the plasmon transition. On the other hand, the inter-well transition is called the fluxon transition. At half flux quanta ($\phi_{\text{ext}} = ..., -\pi, \pi, 3\pi...$), the potential has a double-well shape as shown in Fig. 2.1f. The local wavefunctions of the two wells get hybridized and form the lowest two levels which are close in frequency. The $|0\rangle$ state wavefunction has even parity and the $|1\rangle$ wavefunction has odd parity. The rules are similar for higher levels: the parity of state number indicates the parity of the wavefunction. The transition between the states with the same parity is called an even transition and the transition between the states with opposite parity is an odd transition. The parity rule is quite useful when judging whether a matrix element is zero or not. For example, ϕ is an odd function. Hence the integrand in the calculation of $\langle 0|\,\phi\,|2\rangle$ is also an odd function, which gives $\langle 0|\,\phi\,|2\rangle = 0$. The matrix element of n is proportional to the matrix element of ϕ

$$\langle \alpha|\,n\,|\beta\rangle = \frac{i\hbar\omega_{\alpha\beta}}{8E_C}\,\langle \alpha|\,\phi\,|\beta\rangle\,, \tag{2.18}$$

where $\omega_{\alpha\beta} = \omega_\alpha - \omega_\beta$ is the transition frequency between state $|\alpha\rangle$ and $|\beta\rangle$. This relation

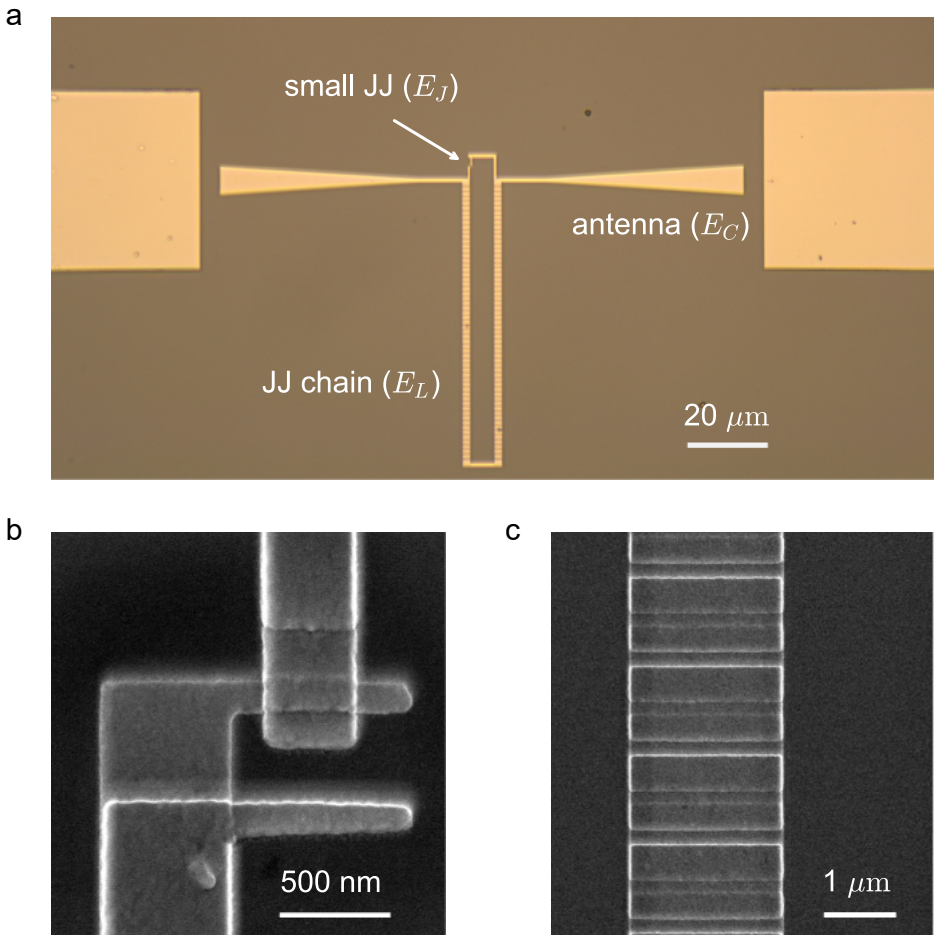

Figure 2.2: Optical and SEM images for a single fluxonium (a) The optical image of a single fluxonium. The metal strip connecting to the loop is the antenna that provides the charging energy E_C and also couples the fluxonium to the external environment. A small Josephson junction (JJ) sits On the upper side of the loop and provides the Josephson energy E_J. The lower part of the loop is a chain of Josephson junctions. Because of the large area of the junction here, the chain behaves like a linear inductor and provides the inductive energy E_L in the circuit model. (b) The SEM image of the small Josephson junction. The Al-AlOx-Al junction is fabricated with the standard Dolan bridge technique. (c) The SEM image of the junction chain. The chain usually contains hundreds of large Josephson junctions that are fabricated together with the small junction in the same batch.

holds for any circuits that can be described with the Hamiltonian $4E_C n^2 + V(\phi)$. To prove this, one needs to use the commutation relation

$$[H, \phi] = [4E_C n^2 + V(\phi), \phi] = [4E_C n^2, \phi] = -8iE_C n. \tag{2.19}$$

We can calculate the matrix element for both sides. The left hand side gives

$$\langle\alpha| [H, \phi] |\beta\rangle = \langle\alpha| (H\phi - \phi H) |\beta\rangle = (E_\alpha - E_\beta) \langle\alpha| \phi |\beta\rangle , \tag{2.20}$$

and the right hand side gives $-8iE_C \langle\alpha| n |\beta\rangle$. It is easy to arrive at Eq. 2.18 by equalling the two sides. The matrix elements for a typical fluxonium at different flux are shown in Fig. 2.3. For the $0-1$ transition at half flux quanta, the frequency can be 10 times smaller than that at integer flux. The charge matrix element reaches minimum and the phase matrix element reaches maximum at half flux quanta. From the state parity, we can know that the even transitions have zero matrix elements for n and ϕ at half and integer flux quanta. This is called the selection rule and will be frequently used when working at these flux points.

Unlike transmon, fluxonium is naturally insensitive to the offset charge noise because the two sides of the small Josephson junction are galvanically connected by the inductor. This ability is achieved without the price of sacrificing the anharmonicity. On the contrary, the anharmonicity is much large than that of a transmon. For typical fluxonium parameter regime, $E_J/E_C \sim 1-10$ and $E_J > E_L$ [48]. The anharmonicity $\alpha = (E_2 - E_1) - (E_1 - E_0)$ can easily achieve few GHz at half flux quanta, which is one order of magnitude larger than the transmon. The non-trivial potential can push $0-1$ transition down to sub GHz level while keep $1-2$ transition still at several GHz. Therefore the $0-1$ transition is well-isolated with other higher transitions and can be treated like a real spin. This feature is quite convenient for quantum simulation tasks on spin-based models. On the other hand, for using fluxonium as a qubit, the high anharmonicity also relieves the constraint on the single qubit gate speed. Basically there is no need to worry about the population going to the higher levels while driving the $0-1$ transition even with few nanosecond long π pulse. In this case, other factors need to be taken into account when ramping up the single-qubit gate rate. For example, a strong drive on a low-frequency qubit can break the rotating wave approximation. One need to consider this effect when calibrating the pulses. On the other hand, low-frequency fluxonium qubits have small charge matrix element (they are also called heavy fluxoniums) and the charge matrix element determines how strong it couples to the external microwave drive. This means it is harder to drive these low-frequency qubits. In order to do fast gates, one need to crank up the RF power, which increases the heat load

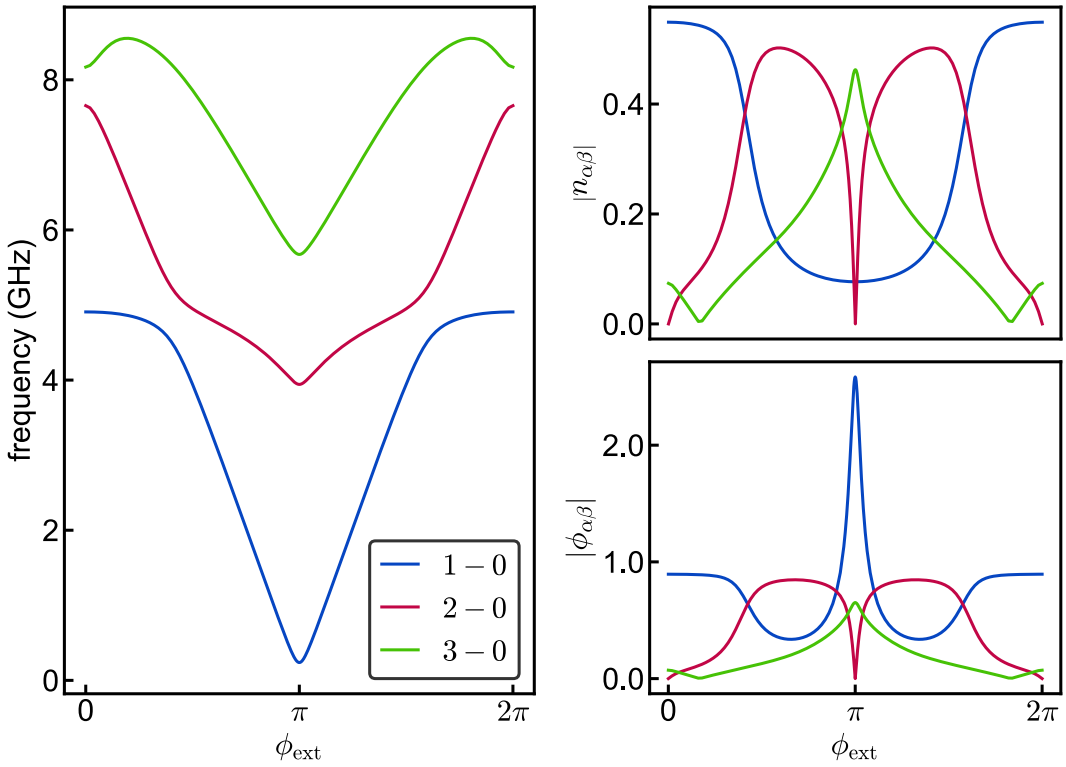

Figure 2.3: Spectrum and matrix elements for a fluxonium. The left panel shows the $1-0$ (blue), $2-0$ (red), and $3-0$ (green) transitions of a typical fluxonium with $E_C = 1$ GHz, $E_J = 4$ GHz, $E_L = 0.5$ GHz. The right panels show the charge matrix element $n_{\alpha\beta}$ and the phase matrix element $\phi_{\alpha\beta}$ accordingly. At 0 flux, fluxonium's $1-0$ transition frequency and matrix elements can be similar to that of a transmon. At half flux quanta $\phi_{\text{ext}} = \pi$, the $1-0$ transition can be much lower and the charge matrix element also becomes much smaller. The $2-0$ transition has vanishing matrix elements at half flux quanta because of the even parity.

of the dilution refrigerator. Another solution is to use flux pulse to activate single-qubit rotations [49].

The most important advantage of fluxonium is its high coherence. It has been reported that the coherence time can achieve hundreds of microseconds and one device achieved 1 ms [50], [51]. This is mainly because the small charge matrix element suppresses the dielectric loss, which will be introduced in Sec. 2.5.1.

2.3 Dispersive Coupling

In order to readout a qubit state while protecting the qubit from radiative decay, one common strategy is to let the qubit interact with the environment through a resonator. This well-studied in cavity quantum electrodynamics (CQED). In our experiment, the qubit is located at the center of a 3D copper cavity as shown in Fig 2.4b. In the GHz regime, the copper box can filter out the noise and prevent the qubit from directly emitting photons into the transmission line. It only lets in the photons that are on resonant with the modes in the cavity through the SMA connectors. These photons can be used to readout qubit states. For clarification, the Jaynes-Cummings Hamiltonian can be a simple example: a two-level system with frequency ω_q coupled to a resonator with frequency ω_r. The coupling strength is g.

$$H_{JC} = \hbar\omega_r a^\dagger a + \frac{\hbar\omega_q}{2}\sigma_z + \hbar g(a\sigma_+ + a^\dagger\sigma_-) \tag{2.21}$$

In the dispersive regime, the qubit-resonator detuning $\Delta_{qr} = \omega_q - \omega_r$ is much larger than the coupling strength $|\Delta_{qr}| \gg g$. Eq. 2.21 can be simplified with perturbation theory [15], [52]

$$H_{JC} = \hbar\omega_r a^\dagger a + \frac{\hbar\omega_q}{2}\sigma_z + \hbar\frac{g^2}{\Delta_{qr}}\left[a^\dagger a + \frac{1}{2}\right]\sigma_z. \tag{2.22}$$

On one hand, the Hamiltonian can be rewritten as

$$H_{JC} = \hbar\left(\omega_r + \frac{g^2}{\Delta_{qr}}\sigma_z\right)a^\dagger a + \frac{\hbar}{2}\left(\omega_q + \frac{g^2}{\Delta_{qr}}\right)\sigma_z, \tag{2.23}$$

indicating the resonator frequency is dependent on the qubit state. The frequency shift is called the dispersive shift

$$\chi = 2g^2/\Delta_{qr}. \tag{2.24}$$

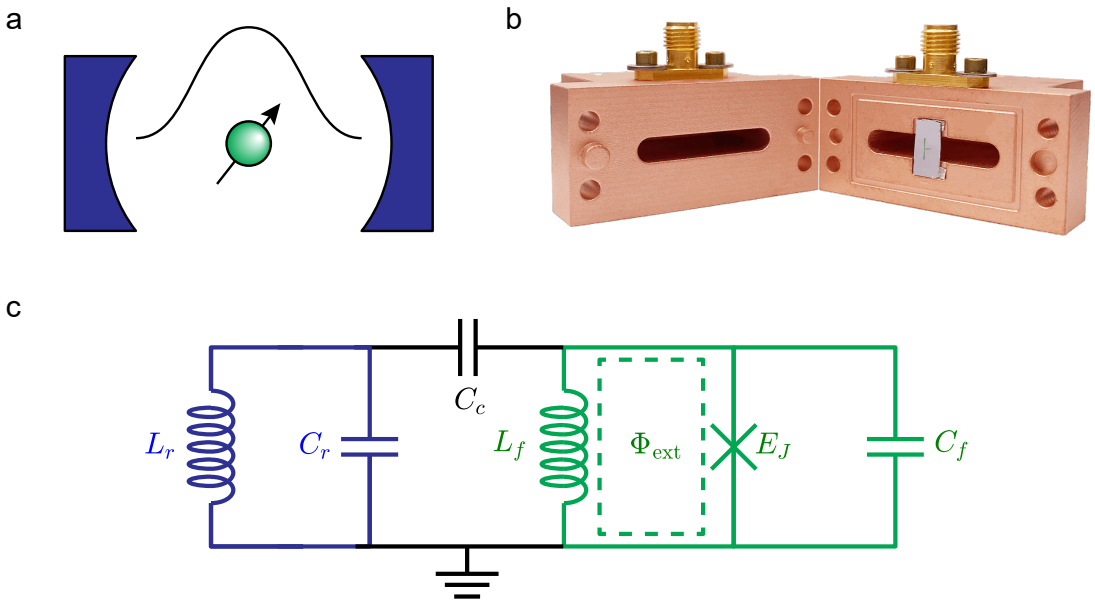

Figure 2.4: A fluxonium capacitively coupled to a resonator (a) A spin inside a cavity. The qubit interacts with the harmonic oscillator through a dipole coupling, which is commonly described by the Jaynes-Cummings Hamiltonian. (b) A fluxonium device inside a copper 3D cavity. The two halves of the cavity are sealed with indium [not shown]. The size of the fluxonium in this picture is exaggerated for better visibility. (c) The circuit diagram for a fluxonium capacitively coupled to a resonator. The blue part is the resonator and the green part is the fluxonium. The two parts are coupled with a capacitance C_c.

This mechanism can be utilized to readout a qubit. The experimental implementation is further discussed in Sec. 3.1.1. On the other hand, we can also rewrite the Hamiltonian in the form of

$$H_{JC} = \hbar\omega_r a^\dagger a + \frac{\hbar}{2}(\omega_q + \frac{g^2}{\Delta_{qr}} + \frac{2g^2}{\Delta_{qr}} a^\dagger a)\sigma_z. \tag{2.25}$$

The qubit frequency now depends on the photon number through the Stark shift term $2\bar{n}g^2/\Delta_{qr}$. There have been experiments carried out to use a Cooper pair box to detect the photon number in a cavity [53].

To simulate a full spectrum of a fluxonium coupled to a resonator, one can consider a circuit model shown in Fig. 2.4 with a capacitive coupling. For small coupling capacitance $C_c \ll C_r, C_f$, the Hamiltonian can be approximated as [52], [54]

$$H_{rf} = H_r + H_f + V_{rf}, \tag{2.26}$$

$$H_r = 4E_{C_r} n_r^2 + \frac{1}{2} E_{L_r} \phi_r^2, \tag{2.27}$$

$$H_f = 4E_{C_f} n_f^2 - E_J \cos(\phi - \phi_{\text{ext}}) + \frac{1}{2} E_{L_f} \phi_f^2, \tag{2.28}$$

$$V_{rf} = J_C n_r n_f \tag{2.29}$$

where $J_C = 4e^2 C_c/(C_r C_f)$. For a 3D cavity, it is usually unnecessary to use three independent parameters L_r, C_r, C_c to model the resonator and the coupling. We can introduce the annihilation and creation operators of the resonator from Eq. 2.8 and Eq. 2.9 first to simplify the notations.

$$H_r = \hbar\omega_r a^\dagger a, \tag{2.30}$$

$$V_{rf} = i g_n (a^\dagger - a) n_f, \tag{2.31}$$

$$g_n = \frac{J_C}{\sqrt{2}} \left(\frac{E_{L_r}}{8E_{C_r}}\right)^{\frac{1}{4}}. \tag{2.32}$$

Now we can just use two parameters ω_r and g_n to describe the resonator and the coupling. Together with the fluxonium parameters E_{C_f}, E_{L_f}, and E_J, one can simulate the full spectrum with 5 independent parameters.

Without an accurate numerical simulation, we can still use perturbation theory to get an idea about what determine the dispersive shift of the resonator photon on the fluxonium

[40], [55].

$$\chi_\alpha = g_n^2 \sum_{\beta\neq\alpha} |n_{\alpha\beta}|^2 \frac{2\omega_{\alpha\beta}}{\omega_{\alpha\beta}^2 - \omega_r^2}. \tag{2.33}$$

χ_α is the dispersive shift felt by the fluxonium state α when there is an extra photon in the resonator. Because $g_n > 0$, the frequency shift can be thought of as the repulsion between all the related fluxonium transitions and the resonator transition. $\omega_{\alpha\beta} > \omega_r$ means the resonator pushes the upper level α up and the lower level β down, and vice versa for $\omega_{\alpha\beta} < \omega_r$. In experiment, we are more concerned about differential dispersive shift $\chi_{\alpha\beta} = \chi_\alpha - \chi_\beta$. For example, the dispersive shift of the $0-1$ transition is

$$\chi_{10} = g_n^2 \left(\sum_{\alpha\neq 1} |n_{1\alpha}|^2 \frac{2\omega_{1\alpha}}{\omega_{1\alpha}^2 - \omega_r^2} - \sum_{\alpha\neq 0} |n_{0\alpha}|^2 \frac{2\omega_{0\alpha}}{\omega_{0\alpha}^2 - \omega_r^2} \right). \tag{2.34}$$

Therefore for a fluxonium qubit, even though the qubit frequency can be very far away from the resonator frequency with a detuning on the order of GHz, the dispersive shift on the qubit can be large thanks to the contributions from the higher levels. One can compare Eq. 2.34 with Eq. 2.24 to treat the $0-1$ transition as a spin and write down the effective coupling g_{JC} in the Jaynes-Cummings model

$$g_{JC} = g_n \sqrt{(\omega_{10} - \omega_r) \left(\sum_{\alpha\neq 1} |n_{1\alpha}|^2 \frac{\omega_{1\alpha}}{\omega_{1\alpha}^2 - \omega_r^2} - \sum_{\alpha\neq 0} |n_{0\alpha}|^2 \frac{\omega_{0\alpha}}{\omega_{0\alpha}^2 - \omega_r^2} \right)}. \tag{2.35}$$

For inductive coupling, the coupling term V_{rf} takes the form of $V_{rf} = g_\phi(a^\dagger + a)\phi$. This corresponds to the case where the resonator and the fluxonium have shared junctions. One can arrive at a similar result but replacing the charge matrix element $n_{\alpha\beta}$ with the phase matrix element $\phi_{\alpha\beta}$.

Apart from the frequency shift, the hybridization between the resonator mode and the fluxonium mode makes it possible to drive the side-band transitions. For clarification, we can denote the fluxonium-resonator state as $|\alpha, n\rangle$. α is the state index of the fluxonium and n is the photon number in the resonator. There are two types of side-band transitions. Assuming $\alpha > \beta$, the red side-band transition $|\beta, n\rangle - |\alpha, n-1\rangle$ locates at the frequency $|\omega_r - \omega_{\alpha\beta}|$. The blue side-band transition $|\alpha, n\rangle - |\beta, n-1\rangle$ locates at the frequency $|\omega_r + \omega_{\alpha\beta}|$. In a fluxonium-resonator spectrum, the fluxonium transitions are offset by the resonator frequency to form the side-band transitions. That makes the resonator transition look like a

mirror, as the blue side-band and the red side-band transitions are distributed symmetrically with respect to the resonator. Another way to identify the side-band transition is that their spectral lines disappear at half flux quanta due to vanishing matrix elements. The side-band transitions can be used to initialize the qubit, which will be discussed in Sec. 3.4.

2.4 Coupled Fluxoniums

Now let's move on to study a fluxonium that is coupled to another fluxonium, which is a requirement to realize a two-qubit gate. We can start from the simplest case of two coupled spins (set $\hbar = 1$ for simplicity)

$$H = -\frac{\omega_A}{2}\sigma_z^A - \frac{\omega_B}{2}\sigma_z^B + J\sigma_x^A\sigma_x^B. \tag{2.36}$$

Without loss of generality, we can assume the bare frequencies $\omega_B > \omega_A > 0$. The Hamiltonian can be diagnosed

$$\tilde{H} = -\frac{\tilde{\omega}_A}{2}\tilde{\sigma}_z^A - \frac{\tilde{\omega}_B}{2}\tilde{\sigma}_z^B. \tag{2.37}$$

The coupled system can still be described with two independent spins in the new dressed state basis (the Pauli matrices are labeled as $\tilde{\sigma}_i$) and the energies are shifted to $\tilde{\omega}_\alpha, \alpha = A, B$. Let's define $\omega_\pm = \omega_B \pm \omega_A, \tilde{\omega}_\pm = \tilde{\omega}_B \pm \tilde{\omega}_A$. The relation between the bare energies and the dressed energies is

$$\left(\frac{\tilde{\omega}_\pm}{2}\right)^2 = \left(\frac{\omega_\pm}{2}\right)^2 + J^2. \tag{2.38}$$

The coupling makes the total energy of the two spins higher and also pushes the two spin frequencies away from each other. In the bare basis, the driving term can be expressed as $V = F\cos\omega_d t$ and

$$F = \Omega_A\sigma_x^A + \Omega_B\sigma_x^B \tag{2.39}$$

$\Omega_{A(B)}$ is the driving strength on spin A(B). The tensor product with the identity matrix of the other qubit is omitted in the each term above. Without the coupling, the external drive can only manipulate each spin individually. Now with the coupling, the actual qubits are the dressed eigenstates and the external drive can create an entanglement in the new basis.

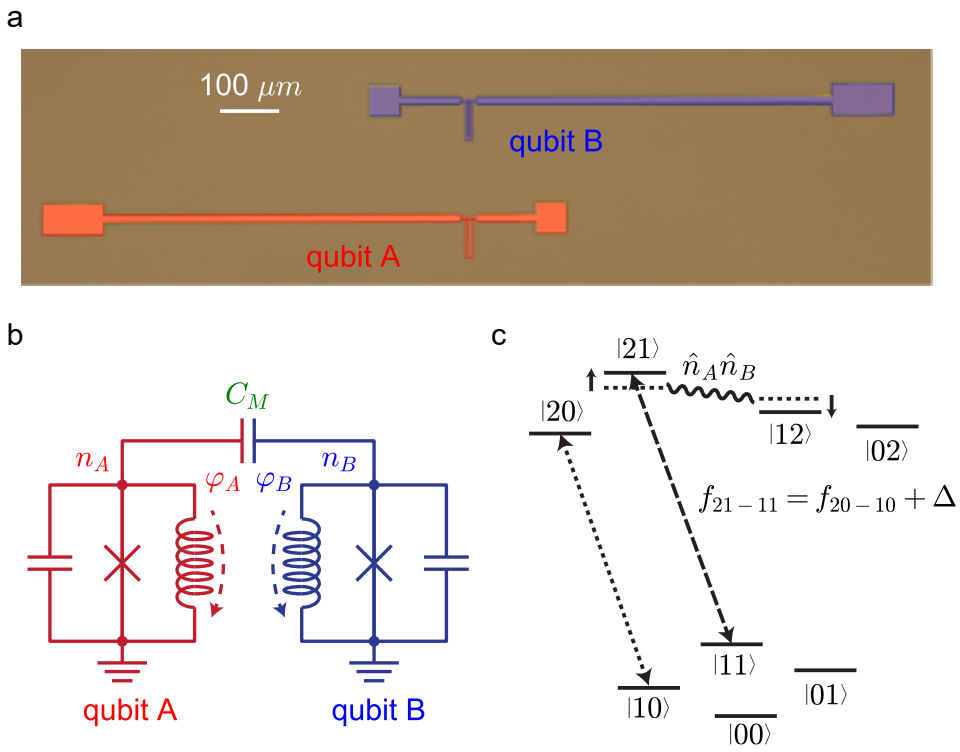

Figure 2.5: Two fluxoniums coupled with a capacitor. (a) The optical image of two capacitively coupled fluxoniums. The capacitance mainly comes from the antenna of the two fluxoniums. (b) The circuit diagram of the system. C_M is the capacitance between the two fluxoniums. (c) The energy diagram considering the coupling term. The two fluxoniums are coupled by the charge operators. This coupling term pushes state $|21\rangle$ against $|12\rangle$ and lifts the degeneracy between transition $|20\rangle - |10\rangle$ and $|21\rangle - |11\rangle$. The energy splitting is Δ.

In the dressed basis, $V \to \tilde{V} = \tilde{F}\cos\omega_d t$ and

$$\begin{aligned}\tilde{F} = &\Omega_A \cos(\theta_- - \theta_+)\tilde{\sigma}_x^A + \Omega_A \sin(\theta_- - \theta_+)\tilde{\sigma}_z^A\tilde{\sigma}_x^B \\ &+ \Omega_B \cos(\theta_- + \theta_+)\tilde{\sigma}_x^B - \Omega_B \sin(\theta_- + \theta_+)\tilde{\sigma}_x^A\tilde{\sigma}_z^B,\end{aligned} \tag{2.40}$$

where $\cos\theta_\pm = \sqrt{(1+\omega_\pm/\tilde{\omega}_\pm)/2}$ and $\sin\theta_\pm = \sqrt{(1-\omega_\pm/\tilde{\omega}_\pm)/2}$. The extra $ZX(XZ)$ term indicates that the drive applied at spin A(B) can also flip qubit B(A) with a rate that is dependent on the state of qubit A(B). This mechanism can be exploited to construct multiple types of two-qubit gates that will be introduced in Sec. 4.3.

Now let's consider a more complicated case where two fluxoniums are coupled together. This can be done either through the capacitance between the antenna or sharing junctions

in the junction. The former case corresponds to capacitive coupling shown in Fig. 2.5, which will be discussed here. The details of the latter case corresponding to inductive coupling can be found in Ref. [54], [56]. The system Hamiltonian is

$$H_{AB} = H_A + H_B + V_{AB}. \tag{2.41}$$

The individual fluxonium Hamiltonian is

$$H_\alpha = 4E_{C,\alpha}n_\alpha^2 - E_{J,\alpha}\cos(\phi_\alpha - \phi_{\text{ext},\alpha}) + \frac{1}{2}E_{L,\alpha}\phi_\alpha^2, \tag{2.42}$$

where $\alpha = A, B$. The coupling term is

$$V_{AB} = J_C n_A n_B, \tag{2.43}$$

$$J_C = 4e^2\frac{C_M}{C_A C_B}. \tag{2.44}$$

Due to fluxonium's multi-level nature, the interaction from the higher levels changes the energies of the computational states. If we only consider the lowest two levels of both fluxoniums, the Hamiltonian is

$$H = -\frac{\omega_A}{2}\sigma_z^A - \frac{\omega_B}{2}\sigma_z^B + \frac{\xi_{zz}}{4}\sigma_z^A\sigma_z^B. \tag{2.45}$$

The last term is the static ZZ interaction coming from the level pushing of the higher transitions, which is absent in the previous spin models. The effect of the ZZ interaction can be thought of as conditional Z rotations. This means that the qubits can get entangled automatically even if no external drive is applied. One solution is to inducing a ZZ interaction with opposite sign to cancel it out as discussed in Sec. 4.3.1. Another way is to design the qubit with lower frequencies. It has been observed that the low-frequency qubits have smaller static ZZ interaction in general with the same coupling strength J_C.

We can also extend the concept of static ZZ interaction to non-computational states such as the $1-2$ manifolds. Due to the level repulsion between $|21\rangle$ and $|12\rangle$, the degeneracy between $|10\rangle - |20\rangle$ and $|11\rangle - |21\rangle$ is lifted and the energy splitting is denoted by Δ as demonstrated in Fig. 2.5c. This type of ZZ interaction is order of magnitude larger than that of the computational states. Therefore it is possible to use these high energy transitions for fast two-qubit gates shown in Sec. 4.3.

Similar to the spin model, the external drive can entangle the two qubits. Again, the

driving term is $V = F\cos\omega_d t$ and

$$F = \Omega_A n_A + \Omega_B n_B. \tag{2.46}$$

In order to see its behavior in the computational space, we can calculate the matrix elements of n_A and n_B in the coupled fluxonium basis. This can be done perturbatively and by keeping the terms with major contributions [57]. We can define $V_{kl,k'l'} = \langle kl| V_{AB} |k'l'\rangle = J_C \langle k_A| n_A |l_A\rangle \langle k'_B| n_B |l'_B\rangle$ and express the dressed states in the bare fluxonium basis,

$$|00\rangle \approx |0_A\rangle|0_B\rangle - \frac{V_{11,00}}{\omega_{10}^A+\omega_{10}^B}|1_A\rangle|1_B\rangle - \frac{V_{31,00}}{\omega_{30}^A+\omega_{10}^B}|3_A\rangle|1_B\rangle - \frac{V_{13,00}}{\omega_{10}^A+\omega_{30}^B}|1_A\rangle|3_B\rangle + \cdots, \tag{2.47}$$

$$|11\rangle \approx |1_A\rangle|1_B\rangle + \frac{V_{00,11}}{\omega_{10}^A+\omega_{10}^B}|0_A\rangle|0_B\rangle - \frac{V_{20,11}}{\omega_{21}^A-\omega_{10}^B}|2_A\rangle|0_B\rangle + \frac{V_{02,11}}{\omega_{10}^A-\omega_{21}^B}|0_A\rangle|2_B\rangle + \cdots, \tag{2.48}$$

$$|01\rangle \approx |0_A\rangle|1_B\rangle - \frac{V_{10,01}}{\omega_{10}^A-\omega_{10}^B}|1_A\rangle|0_B\rangle - \frac{V_{12,01}}{\omega_{10}^A+\omega_{21}^B}|1_A\rangle|2_B\rangle - \frac{V_{30,01}}{\omega_{30}^A-\omega_{10}^B}|3_A\rangle|0_B\rangle + \cdots, \tag{2.49}$$

$$|10\rangle \approx |1_A\rangle|0_B\rangle + \frac{V_{01,10}}{\omega_{10}^A-\omega_{10}^B}|0_A\rangle|1_B\rangle - \frac{V_{21,10}}{\omega_{21}^A+\omega_{10}^B}|2_A\rangle|1_B\rangle + \frac{V_{03,10}}{\omega_{10}^A-\omega_{30}^B}|0_A\rangle|3_B\rangle + \cdots. \tag{2.50}$$

We keep the first order terms with non-zero matrix elements and truncate the Hilbert space up to the $|3\rangle$ states. From the expansion, we can find the parity is conserved in the dressed states, which indicates that matrix elements between the same parity states are zeros. For example, $\langle 00| n_A |00\rangle = \langle 10| n_A |01\rangle = \langle 00| n_A |11\rangle = 0$.

Because $\langle k| n_\alpha |l\rangle$ is pure imaginary in our convention, we can define $n_{kl}^\alpha = -i\langle k_\alpha| n_\alpha |l_\alpha\rangle$ to simplify the expression and calculate other matrix elements of n_A and n_B. For example,

the cross matrix elements for transitions of the other qubit are

$$\langle 00|\, n_A \,|01\rangle \approx -2iJ_C n_{01}^B \left[\frac{\left(n_{01}^A\right)^2 \omega_{10}^A}{\left(\omega_{10}^A\right)^2 - \left(\omega_{10}^B\right)^2} + \frac{\left(n_{03}^A\right)^2 \omega_{30}^A}{\left(\omega_{30}^A\right)^2 - \left(\omega_{10}^B\right)^2} \right], \tag{2.51}$$

$$\langle 10|\, n_A \,|11\rangle \approx 2iJ_C n_{01}^B \left[\frac{\left(n_{01}^A\right)^2 \omega_{10}^A}{\left(\omega_{10}^A\right)^2 - \left(\omega_{10}^B\right)^2} - \frac{\left(n_{12}^A\right)^2 \omega_{21}^A}{\left(\omega_{21}^A\right)^2 - \left(\omega_{10}^B\right)^2} \right], \tag{2.52}$$

$$\langle 00|\, n_B \,|10\rangle \approx 2iJ_C n_{01}^A \left[\frac{\left(n_{01}^B\right)^2 \omega_{10}^B}{\left(\omega_{10}^A\right)^2 - \left(\omega_{10}^B\right)^2} + \frac{\left(n_{03}^B\right)^2 \omega_{30}^B}{\left(\omega_{10}^A\right)^2 - \left(\omega_{30}^B\right)^2} \right], \tag{2.53}$$

$$\langle 01|\, n_B \,|11\rangle \approx -2iJ_C n_{01}^A \left[\frac{\left(n_{01}^B\right)^2 \omega_{10}^B}{\left(\omega_{10}^A\right)^2 - \left(\omega_{10}^B\right)^2} - \frac{\left(n_{12}^B\right)^2 \omega_{21}^B}{\left(\omega_{10}^A\right)^2 - \left(\omega_{21}^B\right)^2} \right]. \tag{2.54}$$

One can use the matrix elements to express n_α in terms of Pauli operators when only considering computational states. For example,

$$n_A^{\text{comp}} = \frac{\xi_{XI}}{2}\sigma_x^A\sigma_0^B + \frac{\xi_{XZ}}{2}\sigma_x^A\sigma_z^B + \frac{\xi_{IX}}{2}\sigma_0^A\sigma_x^B + \frac{\xi_{ZX}}{2}\sigma_z^A\sigma_x^B. \tag{2.55}$$

The absence of other terms such as IZ, ZZ, XX etc. is because of the zero matrix element.

$$\xi_{XI} = \langle 00|\, n_A \,|10\rangle + \langle 01|\, n_A \,|11\rangle, \tag{2.56}$$

$$\xi_{XZ} = \langle 00|\, n_A \,|10\rangle - \langle 01|\, n_A \,|11\rangle, \tag{2.57}$$

$$\xi_{IX} = \langle 00|\, n_A \,|01\rangle + \langle 10|\, n_A \,|11\rangle, \tag{2.58}$$

$$\xi_{ZX} = \langle 00|\, n_A \,|01\rangle - \langle 10|\, n_A \,|11\rangle. \tag{2.59}$$

ξ_{XI} is the zeroth order term. This is trivial term corresponding to direct drive on qubit A. ξ_{IX} and ξ_{ZX} are linear in J_C, meaning that the electric field on qubit A can excite qubit B. ξ_{XZ} is quadratic in J_C. This term indicates that the drive directly applied on qubit A can also slightly depend on the state of qubit B. We can compare the result to Eq. 2.40 and find that the higher level of fluxonium give rise to the extra IX and XZ terms that are absent in the simple spin model. In Sec. 4.3, we are going to explain how we can use these terms for two-qubit gates with only computational states.

2.5 Energy Relaxation and Dephasing

Before introducing the last circuit model of a fluxonium in a waveguide, it is necessary to first discuss the concepts in noise and decoherence. The noise from the environment

is always inevitable and can cause energy relaxation and dephasing in superconducting circuits. These effects can be treated with the master equation in Lindblad form [52], [58], [59] in order to simulate the evolution of a quantum system.

$$\frac{d\rho_t}{dt} = -\frac{i}{\hbar}[H, \rho_t] + \sum_i \mathcal{D}[L_i](\rho_t) \tag{2.60}$$

$\mathcal{D}[L](\rho_t)$ is called dissipator and is defined as

$$\mathcal{D}[L_i](\rho_t) = L_i \rho_t L_i^\dagger - \frac{1}{2} L_i^\dagger L_i \rho_t - \frac{1}{2} \rho_t L_i^\dagger L_i. \tag{2.61}$$

L_i are the Lindblad operators. $L_1 = \sqrt{\Gamma_\downarrow}\sigma_-$ is for the downward transition. $L_2 = \sqrt{\Gamma_\uparrow}\sigma_+$ is for the upward transition. $L_3 = \sqrt{\Gamma_\phi/2}\sigma_z$ is for pure dephasing. We can consider a simplest example by assuming $H = 0$ and only keeping the dissipators. The differential equation can be written in Pauli coordinates

$$dx_t = -\left(\frac{\Gamma_1}{2} + \Gamma_\phi\right) x_t dt \tag{2.62}$$

$$dy_t = -\left(\frac{\Gamma_1}{2} + \Gamma_\phi\right) y_t dt \tag{2.63}$$

$$dz_t = -\Gamma_1 \left(z_t - z_{\text{th}}\right) dt. \tag{2.64}$$

Even though the upward and downward transitions are in opposite directions, the two transition rates contribute to the energy relaxation rate with the same sign $\Gamma_1 = \Gamma_\uparrow + \Gamma_\downarrow$. The transition direction makes a difference when it comes to the expectation value of σ_z at thermal equilibrium $z_{\text{th}} = (\Gamma_\uparrow - \Gamma_\downarrow)/\Gamma_1$. Γ_1 determines how fast the Z component of the qubit Bloch vector decays to the equilibrium value and the decoherence rate $\Gamma_2 = \Gamma_1/2 + \Gamma_\phi$ determines how fast the transverse components decay to zero.

The energy relaxation time $T_1 = 1/\Gamma_1$ and the coherence time $T_2 = 1/\Gamma_2$ can be measured experimentally with the pulse sequence shown in Fig. 2.6. To measure T_1, one needs to flip the qubit, wait for a variable amount of time and measure the qubit population. Assuming the qubit is always at the ground state $|0\rangle$ at the beginning of the sequence and the qubit pulse length can be neglected, the excited state population measured at the end of the sequence is $P_{|1\rangle} = e^{-t/T_1}$. It is worth mentioning that sometimes the T_1 curve can take double-exponential form, which can come from T_1 fluctuations caused by quasiparticles [60].

To measure T_2, there are two common pulse protocols and they can give different T_2 values. One is the Ramsey sequence, where the qubit is first flipped to the equator on the

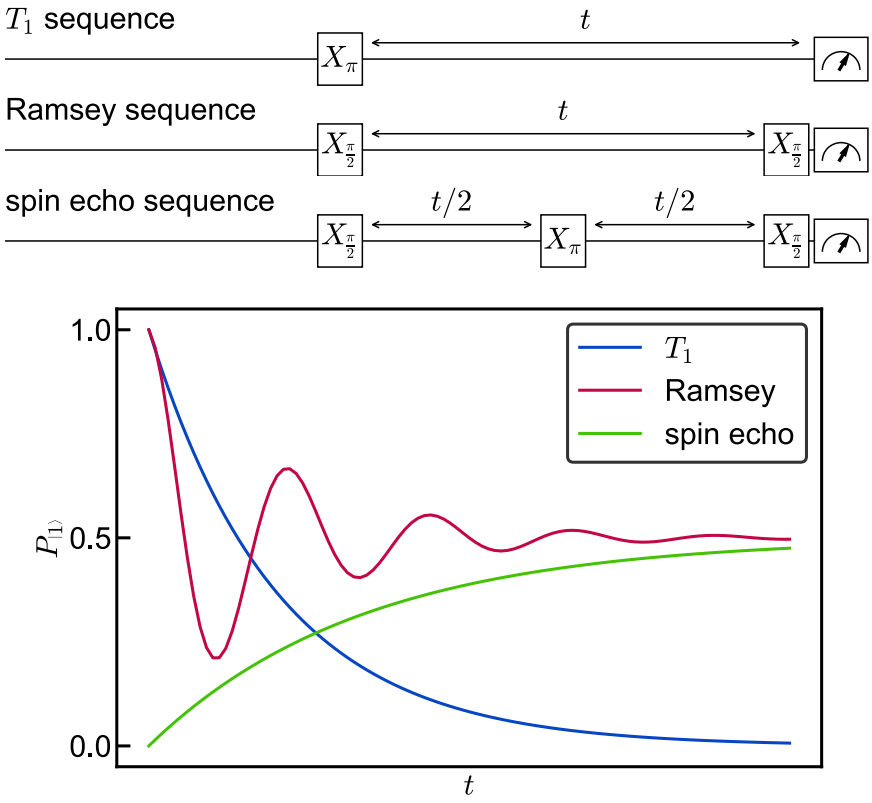

Figure 2.6: T_1, Ramsey and spin echo measurements. X_π and $X_{\frac{\pi}{2}}$ are π and $\pi/2$ pulses around X axis. Assuming the qubit starts from the ground state and the qubit pulses are much faster than the decay time, the T_1 and Ramsey curves starts from $P_{|1\rangle} = 1$ and the spin echo curve starts from $P_{|1\rangle} = 0$. The Ramsey curve oscillation rate equals the detuning of the drive.

Bloch sphere with a $\pi/2$ pulse, evolve for time t and applied a second $\pi/2$ pulse. The final population is $P_{|1\rangle} = e^{-t/T_2^{\text{Ramsey}}} \cos(\delta\omega t) + 1/2$, where T_2^{Ramsey} is the measured T_2 with this Ramsey sequence and $\delta\omega$ is the detuning of the qubit drive. The other pulse protocol is the spin echo sequence. It is similar to the Ramsey sequence, but there is an extra π pulse in the middle of the sequence to refocus the qubit phase on the XY plane. The σ_z rotations coming from the drive detuning before and after the π pulse are cancelled out. There will be no oscillations on the spin echo trace and the population is $P_{|1\rangle} = -e^{-t/T_2^{\text{echo}}} + 1/2$. Typically $T_2^{\text{echo}} > T_2^{\text{Ramsey}}$ because the spin echo sequence can filter out low frequency noise on the qubit phase. Imagine the case where the qubit frequency is drifting randomly over a long time scale. In experiment one need to average the Ramsey traces from multiple repetitive measurements to get a good contrast. Because these traces oscillates at different frequency, the average curve decays faster than each of the single trace. But averaging echo traces will not introduce this problem because each single trace does not oscillate and decays with the same rate. T_2 can typically be longer using the dynamical decoupling technique with more π pulses in the sequence. One can have more rigorous comparison on the filtering effect by calculating the filter function for different pulse sequence [61]. It is worth noticing that T_2 curves can also have non-exponential behavior depending on the noise type [62].

2.5.1 Energy relaxation mechanisms

Generally speaking, the energy relaxation rate can be calculated with Fermi's golden rule [63], [64]. The relaxation rate from state α to state β is

$$\Gamma_{\alpha\beta} = \frac{1}{\hbar^2} |\langle\beta| \hat{O} |\alpha\rangle|^2 S(\omega_{\alpha\beta}) \tag{2.65}$$

$\hat{O}$ is the operator that couples the quantum system to the noise source. $S(\omega_{\alpha\beta})$ is the noise spectral density at frequency $\omega_{\alpha\beta}$. In most cases, the spectral density satisfy the relation $S(-\omega)/S(\omega) = e^{-\hbar\omega/k_B T}$ in thermal equilibrium, where $S(\omega)$ corresponds to the downward transition and $S(-\omega)$ corresponds to the upward transition. This leads to the detailed balance relation in thermal equilibrium

$$\Gamma_\uparrow/\Gamma_\downarrow = e^{-\hbar\omega/k_B T}. \tag{2.66}$$

The upward transition is more significant for low frequency qubits such as fluxoniums at half flux quanta. Assuming the temperature of a dilution refrigerator at base plate is 20 mK. This corresponds to a frequency at 417 MHz, which is the typical frequency of the fluxonium $0-1$ transition.

Superconducting qubit T_1 are susceptible to several noise source, such as dielectric loss, Purcell effect, quasiparticle loss and 1/f flux noise. These are the typical relaxation mechanism considered for superconducting circuits.

Dielectric loss

Dielectric loss comes from the defects in the environment. These defects behave like lossy two-level systems (TLSs) exchanging energy with the superconducting circuit and they exist on different interfaces such as the metal-substrate interface, substrate-air interface, etc [65]. This can be modeled by assuming the capacitor in the circuit is filled with lossy dielectric materials such that $C_{\text{eff}} = C(1 + \tan\delta_C)$. $\tan\delta_C$ is called the loss tangent. In this way, the dielectric loss rate can be written as

$$\Gamma^{\text{diel}}_{\alpha\beta} = \frac{1}{(2e)^2} |\langle\beta|\phi|\alpha\rangle|^2 S_{\text{diel}}(\omega_{\alpha\beta}), \tag{2.67}$$

$$S_{\text{diel}}(\omega) = 2\hbar\omega \text{Re}[Y_{\text{diel}}(\omega)] \left|\coth\left(\frac{\hbar\omega_{\alpha\beta}}{2k_BT} + 1\right)\right|, \tag{2.68}$$

$$\text{Re}[Y_{\text{diel}}(\omega)] = \omega C \tan\delta_C. \tag{2.69}$$

The temperature dependence comes from the stimulated emission by thermal photons in the lossy environment [18], [50]. Combine the equations above, the relaxation rate is

$$\Gamma^{\text{diel}}_{\alpha\beta} = \frac{\hbar\omega^2_{\alpha\beta}}{8E_C} |\langle\beta|\phi|\alpha\rangle|^2 \tan\delta_C \left|\coth\left(\frac{\hbar\omega}{2k_BT}\right) + 1\right| \tag{2.70}$$

This formula demonstrates that $1/(T_1^{\text{diel}}|\langle\beta|\phi|\alpha\rangle|^2)$ can have a quadratic dependence on qubit frequency at zero temperature assuming the loss tangent is constant. It also has been observed experimentally that the loss tangent can have a weak dependence on frequency [50]. Using Eq. 2.18, the relaxation rate can also be expressed in term of the charge matrix element

$$\Gamma^{\text{diel}}_{\alpha\beta} = \frac{8E_C}{\hbar} |\langle\beta|n|\alpha\rangle|^2 \tan\delta_C \left|\coth\left(\frac{\hbar\omega_{\alpha\beta}}{2k_BT}\right) + 1\right|, \tag{2.71}$$

where the $\omega^2_{\alpha\beta}$ dependence is absorbed in the charge matrix element. Therefore fluxoniums can have suppressed dielectric loss with low qubit frequency and small matrix elements. At the same time, there are on-going efforts to experiment with different materials [30]–[38]. Because the total loss tangent comes from different parts of the material, it is also possible to make it smaller by optimizing the qubit design and engineering the participation ratios [65]. The dieletric loss introduced above is considered to be an averaged effect from

many defects in the material. Recent work also shows that there are some two-level systems that can be coupled strongly with the qubit. Qubit T_1 can drop significantly When the qubit frequency is near these two-level systems [66]. These defects are distributed randomly over the spectrum, can drift over time and can be quite different between different cool-downs.

Purcell effect

Another energy relaxation channel is Purcell effect [67] when the qubit is coupled to a lossy resonator. The qubit can lose energy to the environment when exchanging excitation with the resonator. Assuming the resonator line width is κ, the coupling strength is g and the detuning is Δ_{qr}. The Purcell decay rate can be derived with the Jaynes-Cummings model [52]

$$\Gamma_{\text{Purcell}} = |g|^2 \frac{\kappa}{\Delta_{qr}^2 + (\kappa/2)^2}. \tag{2.72}$$

On the other hand, one can also derive the relaxation rate from a circuit model for a qubit coupled to a coplanar waveguide resonator [40], [68]. Because fluxonium qubit frequency is much lower than the resonator frequency, the Purcell effect can be neglected in this case. However, the high energy transitions such as the $0-3$ transition can be close to the resonator and limited by the Purcell effect. In the more extreme case where the cavity has a strong coupling to the external environment and becomes a waveguide, the high transition can have a large spontaneous emission rate and emit fluorescence signal that depends on the ground state population (See Sec. 2.6 and Sec. 3.1.2).

1/f flux noise

1/f flux noise is one of the main noise source for dissipation in flux qubits. There has been research demonstrating that the absorbed molecular O_2 at the surface is the main contributor of the magnetic noise [69]. The flux noise is coupled to the qubit through the term $H_{\delta\Phi_{\text{ext}}} = I_L \delta\Phi_{\text{ext}}$. $I_L = \Phi/L$ is the current flow around the loop [25], [70]

$$\Gamma_{\alpha\beta}^{\Phi} = \frac{1}{2e^2L^2} |\langle\beta|\phi|\alpha\rangle|^2 S_\Phi(\omega_{\alpha\beta}), \tag{2.73}$$

$$S_\Phi(\omega) = \frac{A_\Phi^2}{\omega}. \tag{2.74}$$

Flux qubits have faster relaxation rate at low frequency due to the $1/\omega$ dependence. However, this effect is not observed in fluxonium system, which can be explained by the large inductance provided by the junction chain. For typical fluxonium parameters, the corresponding relaxation rate can be smaller by a factor of $10^2 - 10^4$ compared to flux qubits.

Quasiparticle loss

Quasiparticle loss is also an important relaxation channel for superconducting circuits. Quasiparticles are unpaired electrons and can affect qubit lifetime when they tunnel through the junctions. In fluxonium system, the tunneling can happen at the small junction and the junction chain. The corresponding relaxation rates are [71]

$$\Gamma_{\alpha\beta}^{\mathrm{qp,SJJ}} = \frac{8E_J}{\pi\hbar}\sqrt{\frac{2\Delta_{\mathrm{g}}}{\hbar\omega_{\alpha\beta}}}|\left\langle\beta\right|\sin(\frac{\phi-\phi_{\mathrm{ext}}}{2})\left|\alpha\right\rangle|^2 x_{\mathrm{qp}}, \tag{2.75}$$

$$\Gamma_{\alpha\beta}^{\mathrm{qp,chain}} = \frac{8E_L}{\pi\hbar}\sqrt{\frac{2\Delta_{\mathrm{g}}}{\hbar\omega_{\alpha\beta}}}|\left\langle\beta\right|\frac{\phi}{2}\left|\alpha\right\rangle|^2 x_{\mathrm{qp}}, \tag{2.76}$$

$$x_{\mathrm{qp}} = \left(\sqrt{2\pi T/\Delta_g}\right)e^{-\Delta_g/T}. \tag{2.77}$$

Δ_{g} is the superconductor energy gap. x_{qp} is the normalized quasiparticle density. These equations are based on two assumptions. First, the quasiparticle is in thermal equilibrium. In reality, the observed quasiparticle density is higher than that corresponding to the environment temperature, which means the non-equilibrium quasiparticles is quite common. Still, the above relations hold with some effective x_{qp} and T_{eff} [72], [73]. The second assumption is that the qubit is in the high-frequency regime $\omega_{\alpha\beta} \gg \delta E$, where δE is the characteristic energy of a quasiparticle. In thermal equilibrium, $\delta E \sim T$. For a low frequency qubit, if we still use Eq. 2.75 and 2.76, the accurate expression of x_{qp} can have a dependence on frequency [71]. But the good new is that, when $\omega_{\alpha\beta} \sim T$ which is the typical case for fluxonium qubit, the deviation of Eq. 2.77 is still acceptable. In order to measure the quasiparticle density x_{qp}, one can fit the T_1 curve with double exponential formula [74], measure T_1 variations [75], [76], monitor the quantum jumps [77] or measure the frequency jump of the charge-sensitive Cooper pair box [76], [78].

At half flux quanta $\phi_{\mathrm{ext}} = \pi$, the parity of the operator in Eq. 2.75 leads to $\Gamma_{10}^{\mathrm{qp,SJJ}} = 0$. The quasiparticle loss is dominated by the tunneling event happened in the junction chain. It has been reported that cosmic rays [76], high energy photons [79]–[81] and strong microwave pulses [75], [77] can generate quasiparticles on the sample. The general strategy of suppressing quasiparticle loss is to have good shielding and filtering. Infrared filters such as Eccosorb filters are widely used to filter out the high energy photons in the measurement line. It is believed that these photons (over 100 GHz) are a common source in superconducting experiments and these filters need to be few centimeters long. One has to make sure that the sample holder is well sealed and there are no apertures or slits on the last few stage of shielding where the infrared filters are located. Otherwise the high

energy photons can leak into the measurement line after the infrared filter through the slits at the connectors. There are also some other techniques to mitigate quasiparticle loss such as trapping quasiparticles with vortices[75], quasiparticle pumping[74], engineering the superconducting gap and using normal metal to absorb quasiparticles [82]–[84].

2.5.2 Dephasing mechanism

The coherence time T_2 is limited by T_1 and the dephasing time $T_\phi = \Gamma_\phi$. By definition,

$$\frac{1}{T_2} = \frac{1}{2T_1} + \frac{1}{T_\phi}. \tag{2.78}$$

This indicates T_2 should be always shorter than $2T_1$. Because T_2 determines how long the quantum information can survive in qubits, it is worth the efforts to suppress the dephasing rate in order to push T_2 to the $2T_1$ limit. Dephasing process is often modeled as the noise on the qubit phase (or qubit frequency) [54], [62]. In terms of the noise spectral density, the noise can be classified as white noise, 1/f noise, long-time correlated noise and telegraph noise. The mathematical form of the noise spectral density determines the shape of the decay curves measured in Ramsey or spin echo experiments. Most of the time, the decaying envelope takes the form of e^{-t/T_ϕ}, which corresponds to a white noise. For other types of noise, the decaying envelope can be more complicated and can be usually approximated as $e^{-(t/T_\phi)^2}$. It worth noticing that the Gaussian type of decay does not necessarily indicate non-white noise. Non-accurate π pulse in the spin echo sequence shown in Fig. 2.6 can also lead to Gaussian decay envelope.

One common dephasing mechanism for flux-tunable qubits is flux noise. It is especially important when the qubit is not at flux sweet spot. A fluctuation on the external flux can be translated to qubit frequency fluctuation through the derivative with respect to the external flux $\partial\omega/\partial\Phi_{\text{ext}}$ of the spectrum. It is also possible that the flux noise can affect the qubit through the second order effect where the frequency fluctuation depends on the $\partial^2\omega/\partial\Phi_{\text{ext}}^2$. But it is not the dominate dephasing mechanism for recent qubit experiments [50].

The white flux noise induced dephasing time has a quadratic dependence on $\partial\omega/\partial\Phi$

$$\Gamma_\phi = \left(\frac{\partial\omega}{\partial\Phi_{\text{ext}}}\right)^2 \frac{S_{\text{white}}}{2}. \tag{2.79}$$

S_{white} is a constant. For white noise, Ramsey and spin echo measurements will give the same dephasing rate. It is reported that the flux noise spectral density has 1/f behavior

[25], [70]. In this case, the spin echo decay envelope is Gaussian $e^{-(\Gamma_\phi t)^2}$ and the dephasing rate is

$$\Gamma_\phi^{\text{echo}} = \frac{\partial\omega}{\partial\Phi_{\text{ext}}} S_{1/f} \sqrt{\ln 2}. \tag{2.80}$$

$S_{1/f}$ is the 1/f noise spectral density strength. The decay envelope for Ramsey measurement is more complicated in theory but Gaussian is still a good approximation [62]

$$\Gamma_\phi^{\text{Ramsey}} \propto \frac{\partial\omega}{\partial\Phi_{\text{ext}}} S_{1/f}. \tag{2.81}$$

Because Ramsey measurement is sensitive to the noise at low frequency, or equivalently speaking, the long-time scale frequency fluctuations. Γ^{Ramsey} under 1/f noise can be dependent on the total measurement duration and it is faster than Γ^{echo}.

At flux sweet spot, $\partial\omega/\partial\Phi_{\text{ext}} = 0$, which means fluxonium can be protected against flux noise at this point. Therefore fluxoniums are usually biased at the sweet spot for gate operation and readout. But in order to do flux-activated gates, the external flux will be tuned away and the flux noise need to be considered during this flux pulse [49], [85].

Similar to flux noise, offset charge noise has been the dominate dephasing channel for charge qubits, because the qubit frequency is sensitive to offset charge n_g [23]. The invention of transmon solved this problem though a large capacitance. On the other hand, fluxonium avoid the charge noise by shunting the circuit with a junction chain, such that the offset charge can flow through the chain and will not accumulate on the metal pads [24].

At flux sweet spot, thermal photon shot noise becomes an important dephasing mechanism. When the qubit is dispersively coupled to a resonator, the qubit frequency can be shifted according to the resonator photon number as shown in Sec. 2.3. In thermal equilibrium, the photon number can fluctuate randomly and lead to qubit frequency fluctuation. The dephasing rate of the $0-1$ transition due to these thermal photons is

$$\Gamma_\phi = \frac{n_{\text{th}} \kappa \chi_{01}^2}{\kappa^2 + \chi_{01}^2}. \tag{2.82}$$

n_{th} is the thermal photon number. κ is the resonator line width. χ_{01} is the dispersive shift of the $0-1$ transition. If we fix κ, the larger χ_{01} is, the larger Γ_ϕ will be. If we fix χ_{01}, the dephasing rate reaches maximum at $\kappa = \chi_{01}$. Because the parameters κ and χ_{01} are also related to the readout fidelity. One need to be careful when optimizing these parameters in order to keep a balance between a good readout fidelity and the thermal photon dephasing rate.

Another way to address this dephasing channel is to make the resonator colder. This does not just mean that the resonator itself should be thermalized well. For example, the 3D copper cavity is directly mounted on the cold fingers. The copper body should be as cold as the base plate. However, the measured thermal photon temperature is typically higher than the base temperature. This is because the thermal photons mainly come from the measurement line as explained in Appendix B.4. The thermal photon number can be related with the effective temperature using the Bose-Einstein distribution

$$n_{\text{th}} = \frac{1}{e^{\hbar\omega_r/k_B T_{\text{eff}}} - 1}. \tag{2.83}$$

Similar dephasing mechanism can appear in a cavityless environment described in Sec. 2.6. There is no cavity mode and dispersive coupling in this case. Instead, the thermal photons can directly excite the high energy transitions that are strongly coupled to the transmission line and have large downward transition rates. The qubit absorbs a photon at a rate $\Gamma_\uparrow = \Gamma_\downarrow e^{-\hbar\omega/k_B T_{\text{eff}}}$ and decays back to the $0-1$ manifold immediately due to the large fluorescence rate. The emitted photon carries the qubit phase information and flies away. Therefore the qubit loses its coherence during this process. Because the qubit can be excited by the thermal photon at 0 state or at 1 state depending on the environment, the corresponding dephasing rate can be written as [86]

$$\Gamma_{\phi,10} \sim \sum_{i>1} (\Gamma_{i0} e^{-\hbar\omega_{i0}/k_B T_{\text{eff}}} + \Gamma_{i1} e^{-\hbar\omega_{i1}/k_B T_{\text{eff}}}). \tag{2.84}$$

2.6 Fluxonium in a Cavityless Environment

One fundamental challenge in quantum technology is to interface qubits with travelling photons. This is essential in constructing quantum network where qubits can get entangled remotely by exchanging photons. In this architecture, waveguide is the key component to propagate microwave photons from one qubit to another with low loss [87]. One simple case to study the interaction between the qubit and the photons in the waveguide is the reflection setup where the qubit sits inside a waveguide with a closed end. In experiment, we can replace the small pin of the cavity to a gigantic launcher to ensure free access of the microwave from the transmission line to the space inside the box as shown in Fig. 2.7. The port can be viewed as a broadband coaxial-to-waveguide adapter [41]. Therefore the box does not behave like a single mode cavity and a continuous spectrum of modes can exist in the box. The photons go into the box and bounce back into transmission line. Standing waves are formed inside the box and the qubit can interact with the microwaves which do

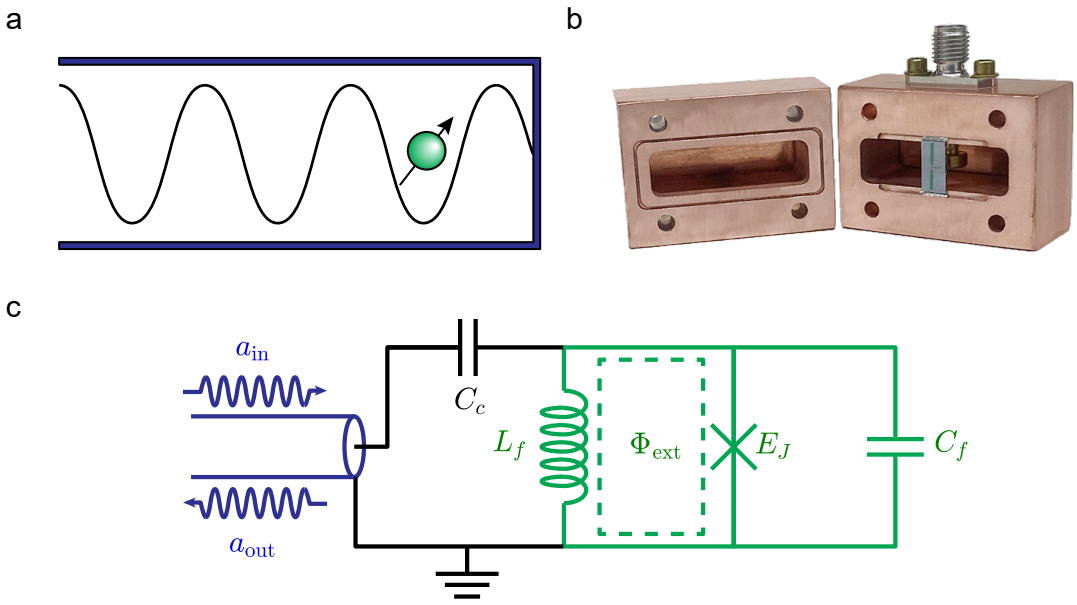

Figure 2.7: A fluxonium in a waveguide. (a) A spin inside a waveguide with a closed end. Within certain frequency range, the photons can travel inside a waveguide and interacts with the qubit. (b) A fluxonium device inside a copper waveguide. The two halves of the waveguide are sealed with indium [not shown]. The size of the fluxonium in this picture is exaggerated for better visibility. (c) The circuit diagram for a fluxonium capacitively coupled to a transmission line. The blue part is the transmission line and the green part is the fluxonium. The two parts are coupled with a capacitance C_c.

not have a node at the qubit position.

The circuit diagram is depicted in Fig. 2.7. The fluxonium circuit is directly coupled to the transmission line where the incoming photon mode is a_{in} and the outgoing photon mode is a_{out}. For clarification, we are going to consider a semi-classical model and treat the fluxonium transition as a spin, instead of solving the full fluxonium spectrum [88].

The spin evolution in the presence of the input field can be described by the Hamiltonian

$$H = \frac{\hbar\omega_q}{2}\sigma_z + i\hbar\sqrt{\Gamma_r}(a_{\text{in}} + a_{\text{in}}^\dagger)(\sigma_+ - \sigma_-). \tag{2.85}$$

Γ_r is the radiative Purcell rate that quantifies how strong the spin is coupled to the transmission line. Here we treat the photon field classically $a_{\text{in}} = \alpha_{\text{in}} e^{-i\omega_d t}$, where α_{in} is a real number without loss of generality. In the rotating frame at ω_d and with the Rotating Wave

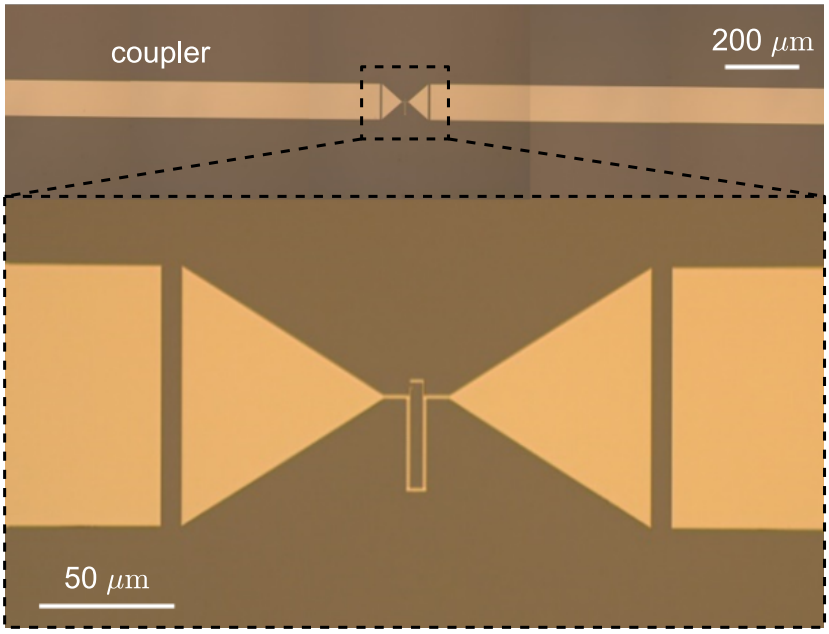

Figure 2.8: Optical image of a fluxonium inside a waveguide. In order to increase the coupling between the fluxonium and the itinerant photons, a pair of couplers is designed next to the fluxonium. The couplers are 3 mm long Al strips that are deposited with the qubit within the same batch.

Approximation (RWA), we arrive at the textbook spin Hamiltonian in the presence of drive

$$H_R = \hbar\frac{\delta}{2}\sigma_z - \hbar\frac{\Omega}{2}\sigma_y, \tag{2.86}$$

where $\delta = \omega_q - \omega_d$ is the drive detuning and $\Omega = 2\sqrt{\Gamma_r}\alpha_{\text{in}}$ is the drive strength. It can be noticed that the same Hamiltonian is used for driving a qubit inside a cavity. In both cases, the driving term comes from the direct coupling between the qubit and the input port. What is different in the waveguide setup is that the bulky launcher together with the coupler design shown in Fig. 2.8 significantly increases the Purcell rate Γ_r.

At the same time, the spin is coupled to the outgoing field through the same Purcell rate. This can be treated as an incoherent channel in the spin evolution. In general, the qubit energy relaxation rate $\Gamma_1 = \Gamma_r + \Gamma_{nr}$, where Γ_{nr} includes all the non-radiative channels such as the dielectric loss, quasiparticle loss, etc. We can use master equation to model this system.

$$\frac{d\rho_t}{dt} = -\frac{i}{\hbar}[H, \rho_t] + \mathcal{D}[\sqrt{\Gamma_1}\sigma_-](\rho_t) + \mathcal{D}[\sqrt{\frac{\Gamma_\phi}{2}}\sigma_z](\rho_t). \tag{2.87}$$

In the steady state where $t \to \infty$, the components of the Bloch vector are

$$x_\infty = \Gamma_1\Gamma_2\Omega/(\Gamma_1(\Gamma_2^2+\delta^2)+\Gamma_2\Omega^2), \tag{2.88}$$

$$y_\infty = \Gamma_1\delta\Omega/(\Gamma_1(\Gamma_2^2+\delta^2)+\Gamma_2\Omega^2), \tag{2.89}$$

$$z_\infty = -1+\Gamma_2\Omega^2/(\Gamma_1(\Gamma_2^2+\delta^2)+\Gamma_2\Omega^2). \tag{2.90}$$

This can be calculated using $x_\infty = \langle\sigma_x\rangle = \mathrm{tr}(\rho_t\sigma_x)$, $y_\infty = \langle\sigma_y\rangle = \mathrm{tr}(\rho_t\sigma_y)$, and $z_\infty = \langle\sigma_z\rangle = \mathrm{tr}(\rho_t\sigma_z)$.

The outgoing field a_{out} can be calculated in terms of the incoming field and the qubit operator from the input-output formalism [20] $a_{\mathrm{out}} = a_{\mathrm{in}} - \sqrt{\Gamma_r}\sigma_-$. In circuit language, this is equivalent to the boundary condition of the incoming wave and the outgoing wave at the end of a transmission line with a lumped circuit $V_{\mathrm{out}} + V_{\mathrm{in}} = V$. The outgoing field can also be considered as the result of the interference between the directly reflected field that does not interact with the qubit and the field radiated by the qubit. In experiment, one can measure the reflection coefficient $r = \langle a_{\mathrm{out}}\rangle/\langle a_{\mathrm{in}}\rangle$. The expectation values for the field operators are the oscillation amplitude that we introduced earlier $\langle a_{\mathrm{in(out)}}\rangle = \alpha_{\mathrm{in(out)}}$. Even though α_{in} is a real number in our convention, α_{out} can be complex. Substituting Eq. 2.88–Eq. 2.90 into $\langle\sigma_-\rangle = (\langle\sigma_x\rangle - i\langle\sigma_y\rangle)/2$ and assuming $\Gamma_r \gg \Gamma_{nr}, \Gamma_\phi$, the reflection coefficient is

$$r = 1 - 2\frac{1+2i\delta/\Gamma_r}{1+4(\delta/\Gamma_r)^2+2(\Omega/\Gamma_r)^2}. \tag{2.91}$$

This model can be applied to the high energy transitions (e.g. $0-3$) of a fluxonium that are strongly coupled to the continuum of photon states. In this case, the spin refers to the two levels of that transition instead of the computational states in the usual context. The total population p_0 on these two levels adds a contrast factor in Eq. 2.91

$$r = 1 - 2p_0\frac{1+2i\delta/\Gamma_r}{1+4(\delta/\Gamma_r)^2+2(\Omega/\Gamma_r)^2}. \tag{2.92}$$

This can serve as a novel readout scheme to measure fluxonium qubit population. The experiment implementations are presented in Sec. 3.1.2.

Chapter 3

Experiments on Readout and Initialization

The quantum error correction (QEC) codes on superconducting qubits require the qubit readout need to be single-shot, high-fidelity, and fast [4], [89]–[91]. For whatever readout scheme, the qubit signal is typically rather weak and needs multi-stage amplifications in order to fight against the thermal noise picked up during the trip from the base plate to the room temperature digitizer. Without a quantum amplifier [92]–[94] at the base temperature, a single experiment needs to be repeated thousands of times and the measured signal needs to be averaged over all the realizations to get a better signal-to-noise ratio (SNR). Therefore this type of measurement gives the expectation value (e.g. $\mathrm{tr}(\rho\sigma_z)$) over a ensemble and it is impossible to identify whether there is an error among one of the realizations. According to Copenhagen interpretation of quantum mechanics, the wavefunction collapses instantaneously after a projective measurement and the measurement outcome should be the eigenvalues of the measurement operator. In QEC codes like surface code, the eigenvalues should be obtained in a single run instead of averaging over all the realizations. This is called single-shot measurement. The readout fidelity depends on the SNR the single-shot histogram and whether extra transitions are induced during the readout process. This puts a constraint on the readout pulse strength and duration. When one qubit is being measured, other qubits are still suffering from decoherence. Hence the readout pulse should be as short as possible. On the state-of-art quantum processors, the readout pulse is much longer than the gate time. High-fidelity readout with short pulses have been reported in a few demonstrations, indicating the current quantum processors can have better readout performance potentially [59].

In this chapter, the main topic will be on qubit readout and introduce relevant concepts.

The last section is focused on initialization schemes for fluxonium qubits. On one hand, QEC requires qubit reset during the algorithm and fluxonium qubits have long T_1. On the other hand, fluxonium qubits have low frequency, resulting in significant thermal populations. The characteristic frequency of 20 mK is 417 MHz, corresponding to a thermal population of $P_{|1\rangle} = 0.27$. Therefore high-fidelity fast initialization techniques are quite beneficial in fluxonium experiments and several initialization schemes are discussed in this section.

3.1 Readout schemes

Fluxonium qubits can be measured with or without cavity. When the qubit coupled to the cavity, we can perform dispersive readout by measuring the cavity transmission. The cavity mode frequency depends on the qubit state and the transmitted signal can change in phase and amplitude accordingly. When the fluxonium is strongly coupled to the transmission line using a waveguide, we can perform fluorescence readout taking advantage of the higher transitions. We used $0 - 3$ transition as the fluorescence transition and $0 - 1$ transition as the qubit. The change of qubit population is manifested in the reflection coefficient.

In both cases, the outgoing signal is down-converted and recorded by the digitizer. We performed heterodyne detection in which both quadratures, named I and Q, of the oscillating signal are simultaneously measured. The two quadratures correspond to the real and the imaginary part of the complex amplitude. It is a common technology in microwave measurements. The heterodyne setups are depicted in Sec. B.4.

3.1.1 Dispersive Readout

As introduced in Sec. 2.3, dispersive readout is the most common way to readout a qubit. The qubit can be detuned away from the cavity frequency for protection against the Purcell effect while dispersively coupled to the cavity mode for readout. It has been demonstrated that the cavity frequency is dependent on the qubit state in the JC model. How does give us the state-dependent IQ signal in the experiment? We need to first understand how a single cavity respond to external drives.

In general, the cavity's response is measured in the form of transmission or reflection. Depending on how the cavity is connected to the external circuits, the response can be different. For a 3D cavity, the setup can either be one-port (reflection) or two-port (transmission). In 2D architecture, the widely adopted hanger geometry is another type of reflection setup. Here in this thesis, we focus on the 3D architecture.

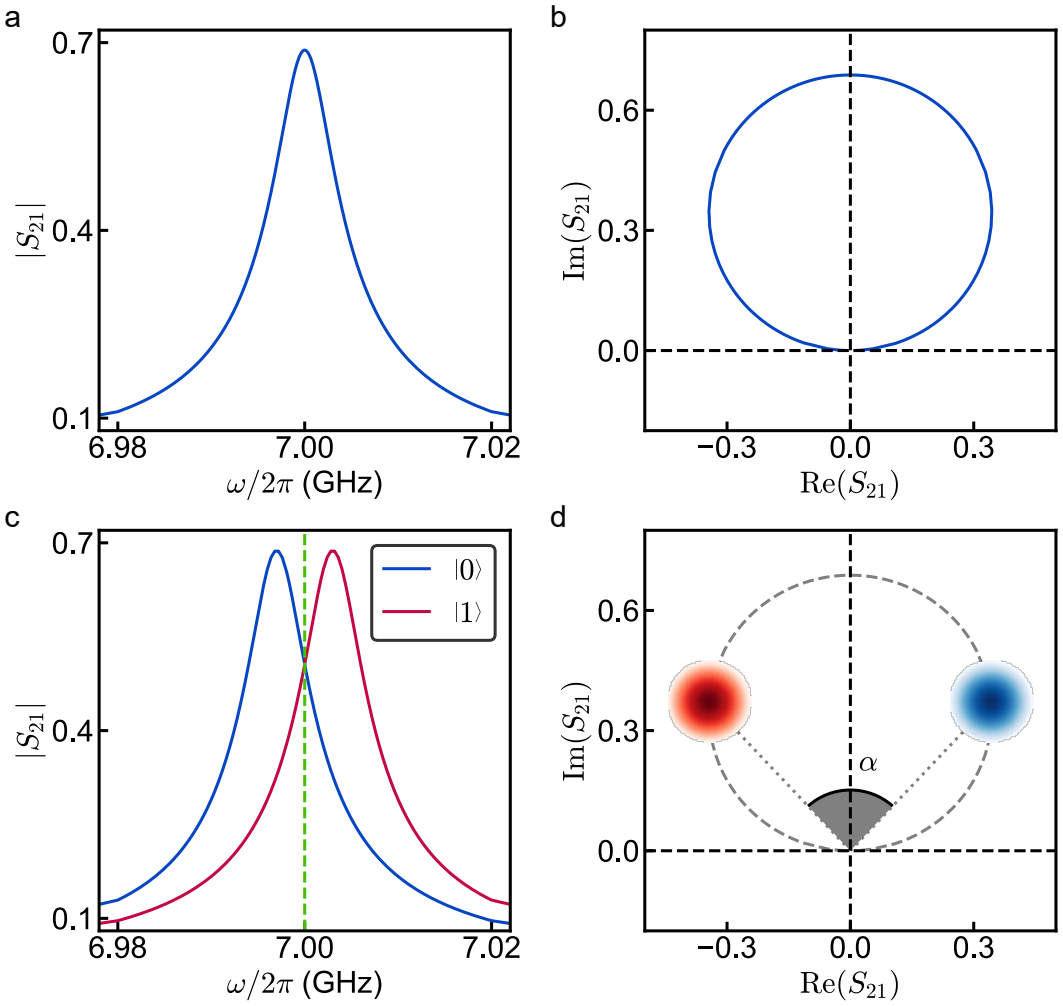

Figure 3.1: Two-port cavity transmission. (a) Transmission coefficient amplitude $|S_{21}|$ of a cavity at 7 GHz calculated from Eq. 3.2. $\kappa_1 = 1$ MHz, $\kappa_2 = 5$ MHz, $\kappa_L = 0.5$ MHz. The parameters are close to the case for a copper cavity in the experiment. (b) Transmission coefficient on the complex plane (IQ plane) at different drive frequency. The trace forms a circle. The points with large detuning are close to the origin. (c) Cavity transmission when dispersively coupled to a qubit. $\chi = 6$ MHz. The blue peak corresponds to the qubit at $|0\rangle$ state. The red peak corresponds to the qubit at $|1\rangle$ state. (d) The readout signal on the IQ plane when reading at the frequency indicated by the light green dashed line in (c). The blue and the red blobs correspond to the qubit at $|0\rangle$ and $|1\rangle$ state. The angle spanned by the two blobs $\alpha \approx \arctan \chi/\kappa_{\mathrm{tot}}$ when the readout frequency is at the middle of the two peaks and α is small.

The S parameters are defined as the transmission and reflection coefficients for a multi-port system. For a 3D cavity, the reflection S_{11} and the transmission S_{21} are

$$S_{11}(\omega) = \frac{\kappa_1 - \kappa_2 - \kappa_L + 2i(\omega - \omega_r)}{\kappa_1 + \kappa_2 + \kappa_L - 2i(\omega - \omega_r)} \tag{3.1}$$

$$S_{21}(\omega) = \frac{2\sqrt{\kappa_1 \kappa_2}}{\kappa_1 + \kappa_2 + \kappa_L - 2i(\omega - \omega_r)} \tag{3.2}$$

ω_r is the cavity frequency. κ_1 (κ_2) is the coupling rate to port 1 (2), corresponding to the external quality factor $Q_i^{\text{ext}} = \omega_r/\kappa_i$. κ_L is the cavity internal loss rate, corresponding to the internal quality factor $Q^{\text{in}} = \omega_r/\kappa_L$. One may notice that the phase definitions can be different in the literature. For example, the definition can be $S_{ij} \to -S_{ij}^*$ in some other references. $\kappa_{\text{tot}} = \kappa_1 + \kappa_2 + \kappa_L$ is the total damping rate. $Q = \omega_r/\kappa_{\text{tot}}$ is the cavity quality factor. We use Eq. 3.1 to measure the external quality factors for the multi-port cavity and use Eq. 3.2 to fit the total damping rate.

As shown in Fig. 3.1, the transmission amplitude reaches maximum at the resonance frequency. The amplitude square has a Lorentzian shape. On the IQ plane, the transmission data at different drive frequency fall on a circle. When it is far detuned, the transmission is at the origin. When it is on resonance, the transmission is at the other end of the circle on the imaginary axis. If the cavity is coupled to a qubit, there will be a frequency shift depending on the state of the qubit. For example in Fig. 3.1c, if the qubit is at ground state, the transmission is the blue curve. If the qubit is at the excited state, the transmission is the red curve. If the population is equally distributed on the two states, the transmission would be the summation of two complex transmission numbers weighted on the population on each state. This could be a way to measure qubit population in principle. In practice, the measurement line itself can have non-trivial frequency-dependent transmission due to attenuation, reflection or amplification. The height of the Lorentzian can not be directly converted to population. A better way to measure population would be the single-shot readout (Sec. 3.1.1).

If the readout frequency is set the position indicated by the green dashed line Fig. 3.1c, the S_{21} in the two cases correspond to the position of the two blobs on the IQ plane in Fig. 3.1d. When $\chi \ll \kappa_{\text{tot}}$, the angle spanned by the two blobs $\alpha \approx \arctan \chi/\kappa_{\text{tot}}$. In the experiment, we usually directly work with the transmitted signal instead of S_{21} which is the ratio between the input and the output. We can assume that the positions of the two blobs on the IQ plane of the signal are $b_k = x_k + iy_k$ and $k = 0, 1$ and the populations are p_0, p_1. The averaged signal would be $m = p_0 b_0 + p_1 b_1$ and $p_0 + p_1 = 1$. When the qubit population changes, the point m moves on the line connected by the two blobs. Therefore

its quadratures are linearly dependent on the qubit population. We can rewrite the the population with the expectation value of the Pauli matrix $p_0 = (\langle\sigma_I\rangle + \langle\sigma_z\rangle)/2$ and $p_1 = (\langle\sigma_I\rangle - \langle\sigma_z\rangle)/2$. Then we have $m = \beta_I\langle\sigma_I\rangle + \beta_Z\langle\sigma_z\rangle$, where $\beta_I = 1/2$ and $\beta_Z = (p_0 - p_1)/2$. From this formula, we can see that the averaged signal m is actually the expectation value of the measurement operator

$$M = \beta_I\sigma_I + \beta_Z\sigma_z, \tag{3.3}$$

and $m = \langle M\rangle = \mathrm{tr}(\rho M)$ [59].

Joint Readout

When a cavity is coupled to two qubits simultaneously, we perform joint readout to the two-qubit system. Assuming the dispersive shifts are χ_A and χ_B for the two qubits, the shifted cavity frequencies are

$$\omega_r^{00} = \omega_r - \frac{\chi_A}{2} - \frac{\chi_B}{2}, \tag{3.4}$$

$$\omega_r^{01} = \omega_r - \frac{\chi_A}{2} + \frac{\chi_B}{2}, \tag{3.5}$$

$$\omega_r^{10} = \omega_r + \frac{\chi_A}{2} - \frac{\chi_B}{2}, \tag{3.6}$$

$$\omega_r^{11} = \omega_r + \frac{\chi_A}{2} + \frac{\chi_B}{2}. \tag{3.7}$$

There are four blobs on the IQ plane, corresponding to the four computational states $|00\rangle$, $|01\rangle$, $|10\rangle$, and $|11\rangle$ as demonstrated in Fig. 3.2. One need to avoid the case where $\chi_A \pm \chi_B \sim 0$, as this will result in overlap of two blobs and making the two states indistinguishable. The optimal situation would be $\chi_A \sim \pm 2\chi_B$ (assuming κ is large) and the four blobs get maximum separation.

The measurement operator is

$$M = \beta_{II}\sigma_I \otimes \sigma_I + \beta_{IZ}\sigma_I \otimes \sigma_z + \beta_{ZI}\sigma_z \otimes \sigma_I + \beta_{ZZ}\sigma_z \otimes \sigma_z. \tag{3.8}$$

Because the averaged signal now depends on the population of the four blobs, its trace can be more complicated. It is not limited on a straight line but can be any where in the region spanned by the four blobs. For example, when one measures the T_1 of qubit A by looking at one quadrature of the signal, the fitted decay rate can be inaccurate if qubit B is also decaying at the same time. To solve this problem, one can apply a $\pi/2$ pulse on qubit B to equalize the population at the $|0\rangle$ state and $|1\rangle$ state. This only works when qubit B is not

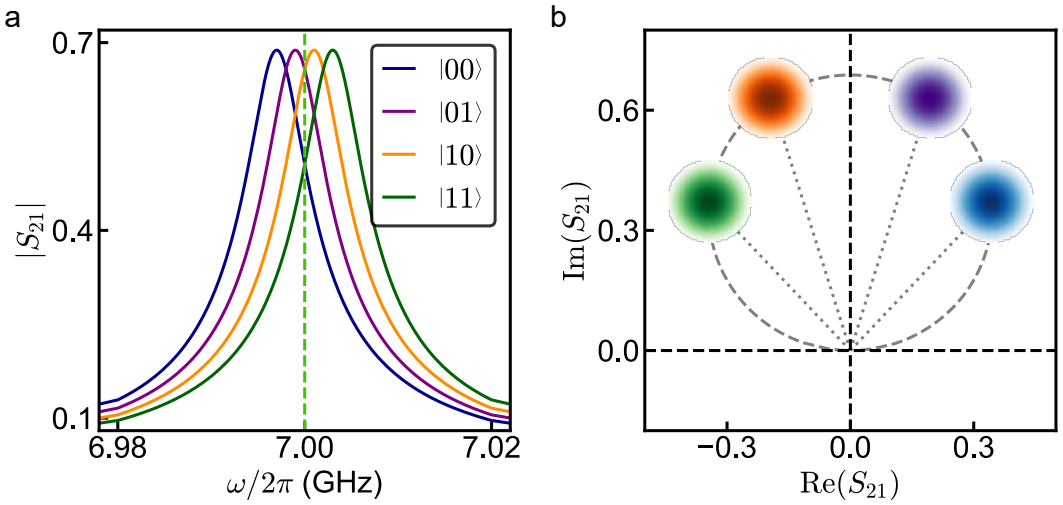

Figure 3.2: Joint readout for two qubits in the same cavity. (a) $|S_{21}|$ of a cavity in the case for four computational states. The simulation parameters are the same as those in Fig. 3.1. $\chi_A = 4$ MHz, $\chi_B = 2$ MHz. (b) The readout signal when reading at the frequency indicated by the light green dashed line in (a). There are four different blobs corresponding to the four computational states. The population of both qubits can affect the averaged signal.

at a coherent superposition of $|0\rangle$ and $|1\rangle$. That is, its density matrix can be described by $\rho_B = (\sigma_I + (2p_0^B - 1)\sigma_z)/2$. Otherwise, or if the $\pi/2$ pulse is not accurate, the populations may not equal.

Single-shot Readout

When the readout SNR is good enough, one can distinguish qubit state in a single acquisition without averaging over many traces. In this case, we are able to perform single-shot readout which is essential for quantum error correction codes. Single-shot readout has been demonstrated and well-studied for dispersive readout. As shown in Fig. 3.1, depending on the qubit state, the cavity transmission can be at either of the two blobs on the IQ plane. At low power, the probability of the data point falling on the positions around the blob follows a Gaussian distribution. The width of the Gaussian is determined by the quantum-limited noise from the uncertainty principle after amplification and the added noise from the components on the readout line. Therefore the criteria to distinguish the two blobs is the distance between the blobs d should be larger than the width of the blobs. The smaller overlap the blobs have, the higher readout fidelity one can achieve.

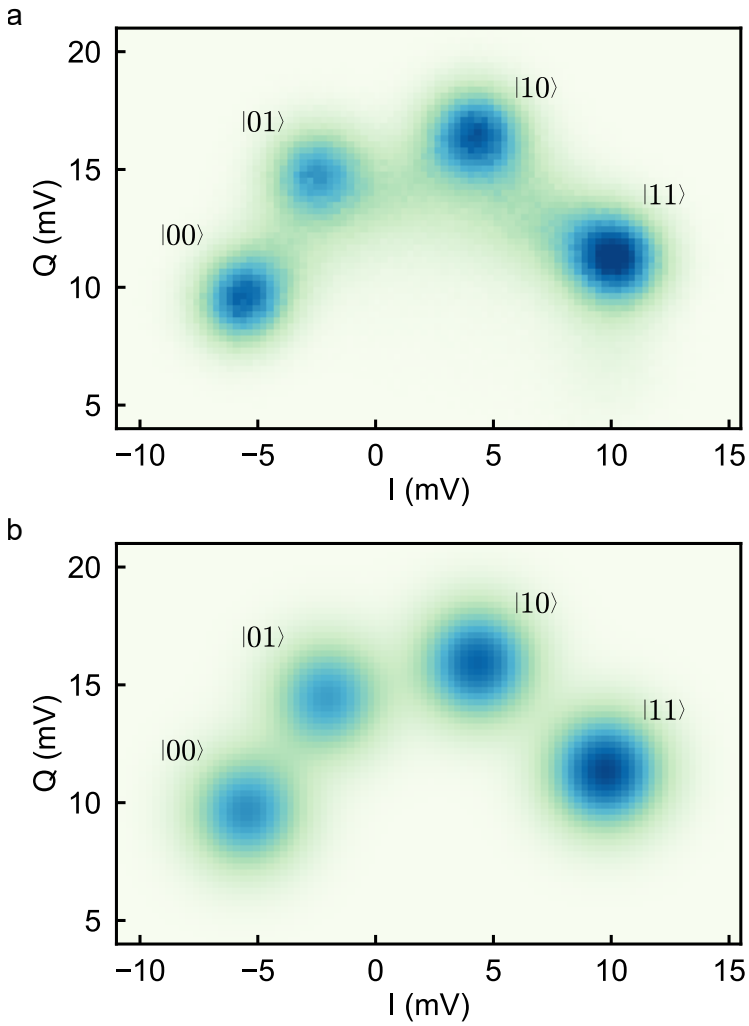

Figure 3.3: Single-shot histograms. (a) Single-shot data taken from the experiment. The four blobs correspond to the four computational states and have the same width. There are some data points fallen between the blobs, which are caused by non-QNDness during readout. (b) Fitted histograms. The slight difference between the fit and the data comes from the readout non-QNDness.

Single-shot readout provides a simple way to measure the qubit population in CQED. One can make a histogram of the single-shot data and fit it to multiple Gaussian functions as shown in Fig. 3.3. The blobs have the same width and the heights are proportional to the population at corresponding state. Another way is to separate the IQ into different regions and determine the qubit state by the region where data point falls into. For example, one can use a linear support vector machine which divides the plane with perpendicular bisectors of the two blobs. Or one can draw a circle around each blob and discard the points outside the circle as demonstrated in Fig. 3.13. After setting up the regions, one can simply count the number of points in each region and the ratio give the population.

In practice, the non-QND effect can be observed in fluxonium single-shot experiments. This can result in blob distortion as the population can change during the readout process. Some of the data points can migrate to other blobs due to the cavity photons and some other points get 'captured' midway and fall on the lines connecting two blobs. This effect will be discussed in Sec. 3.2.

3.1.2 Fluorescence readout

Another way to readout the qubit is through the high energy transition fluorescence, which is also called shelving readout. As introduced in Sec. 2.6, we mount the device chip inside a rectangular waveguide with a specially designed single input/output port. Above the waveguide cut-off frequency, given by its dimensions, the photons can enter or leave the box freely and interact with the fluxonium strongly. As shown in Fig. 3.4d, the port coupling is near unity in a few-GHz band. Below the cut-off, the port coupling drops rapidly with frequency. It is designed that the $0-3$ transition is within the passband to emit fluorescence and other transitions are protected by the cut-off frequency. Therefore, the radiative lifetime of state $|1\rangle$ can be orders of magnitude longer than that of state $|3\rangle$, even though transitions $|0\rangle$-$|1\rangle$ and $|0\rangle$-$|3\rangle$ have comparable dipoles – matrix elements of the Cooper pair number operator $-i\partial_\phi$. Moreover, radiative decays $|3\rangle \to |1\rangle$ and $|3\rangle \to |2\rangle \to |1\rangle$ are inhibited by the parity selection rule and the weak port coupling, respectively. As a result, resonant driving of $|0\rangle$-$|3\rangle$ transition would continuously generate fluorescence if and only if the atom (and hence the qubit) is initially in state $|0\rangle$. Despite a periodic transit of population through the non-computational state $|3\rangle$, the atom rapidly relaxes back to state $|0\rangle$ on switching off the drive. Likewise, the atom starting in state $|1\rangle$ remains unperturbed by the far off-resonant readout drive (fluorescence is absent or "shelved").

We begin our experiment by probing the readout transition (Fig. 3.5a,b). The measured reflection amplitude r as a function of drive frequency ω and amplitude Ω fits well to the

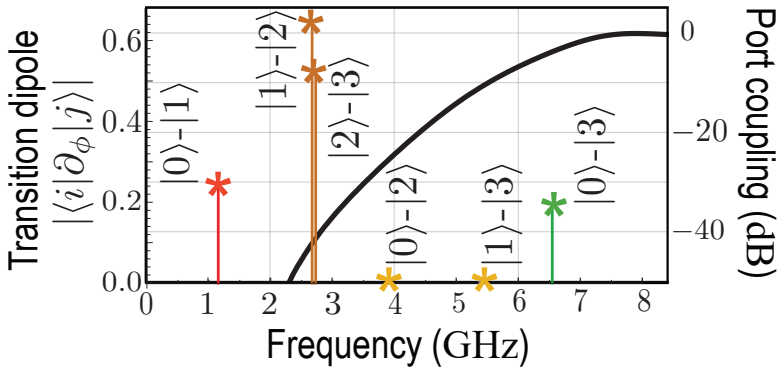

Figure 3.4: Measured port coupling (solid black) vs. frequency and the calculated transition dipoles (colored stars). Note the absence of resonant modes in the adapter in the entire $0-8$ GHz frequency range. The $|0\rangle - |3\rangle$ transition is within the passband of the waveguide. Other transitions such as $|0\rangle - |1\rangle\,, |1\rangle - |2\rangle\,, |2\rangle - |3\rangle$ are protected against the Purcell effect by the high waveguide cutoff frequency.

Eq. 2.92 model. Only four adjustable parameters are used in the global fit: $\omega_{03} = 2\pi \times 6.544$ GHz, $\Gamma = 2\pi \times 1.74$ MHz, the thermal equilibrium ground state population $p_0^{\rm th} = 0.78$, and the scaling factor converting the value of Ω to the RF-source amplitude. We integrate the reflection signal during a time $\tau_m = 0.5$ μs after a delay $\tau_w = 0.5$ μs. The wait time is chosen so that it is much longer than the characteristic emission time $1/\Gamma = 91$ ns but much shorter than the time scale of non-radiative processes in the system. As a result the atom is in the driven steady state while fluorescence is being integrated. At low power, $\Omega \ll \Gamma$, the reflection amplitude r as a function of frequency becomes a circle in the parametric IQ-plot, bounded by the values $\mathrm{Re}[r] = 1$ for $|\omega - \omega_{03}| \gg \Gamma$ and $\mathrm{Re}[r] = 1 - 2p_0^{\rm th}$ at $\omega = \omega_{03}$. As stronger driving saturates the $|0\rangle$-$|3\rangle$ transition, the circle deforms into an ellipse and progressively shrinks into a point at $r = 1$ for $\Omega \gg \Gamma$. This good agreement between spectroscopy data and the Eq. 2.92 model indicates that transition $|0\rangle$-$|3\rangle$ is coupled to itinerant radiation with a nearly unit efficiency, similarly to previous works on artificial two-level atoms.

The characterization presented in Fig. 3.5a,b provides absolute calibration of the measurement records in terms of the ground state population p_0. This is in regard with standard superconducting qubit readout based on the dispersive interaction with a far-detuned cavity, where the measurement records are only known up to a scaling factor to the qubit population and have to be independently calibrated. In order to account for small thermal fluctuations over the course of the experiment, we repeated the previous calibration over 5 days.

We find an average thermal equilibrium value of $p_0^{\text{th}} = 0.76 \pm 0.026$, which corresponds to the atom being at thermal equilibrium with the effective temperature $T = 45 \pm 5$ mK, which is indeed commonly encountered in superconducting qubits. In what follows, we operate the readout at the optimal power/frequency settings (Fig. 3.5a – black star) where the reflection amplitude becomes a real positive number between zero and unity, with $p_0 = 1 - r$.

The protocol for time-domain qubit manipulations matches that of traditional circuit quantum electrodynamics. For example, applying a drive at the qubit frequency $\omega_{01} = 2\pi \times 1.15$ GHz prior to the readout pulse results in Rabi oscillations of p_0 as a function of drive duration (Fig. 3.5c - left panel). Operating the circuit slightly off the sweet-spot at $\phi_{\text{ext}}/2\pi = 0.507$, i.e. weakly breaking the parity selection rule, we could produce Rabi oscillations between states $|0\rangle$ and $|2\rangle$ by compensating the vanishing transition dipole with a strong drive at frequency $\omega_{02} = 2\pi \times 3.88$ GHz. Importantly, the non-zero decay rates of even transitions resulting from breaking the parity selection rule remain several orders of magnitude smaller than other decoherence processes. The reflection coefficient measured during Rabi oscillations between $|0\rangle$ and $|1\rangle$ or $|2\rangle$ yields equilibrium ratios $p_1^{\text{th}}/p_0^{\text{th}} = 0.329$ and $p_2^{\text{th}}/p_0^{\text{th}} = 0.007$ independently of the absolute calibration of p_0^{th}. Assuming $p_0^{\text{th}} + p_1^{\text{th}} + p_2^{\text{th}} = 1$, we obtain the equilibrium value of $p_0^{\text{th}} = 0.75$, in close agreement with the spectroscopic calibration.

The energy relaxation signal following the $0-1$ swap is exponential with a characteristic decay time $T_1 = 52$ μs, which is nearly three orders of magnitude longer than the radiative decay time of the $|3\rangle$-state (Fig. 3.5c - right panel). Yet, given the highly suppressed port coupling at the qubit frequency, such value of T_1 is still too short to be accounted for by radiative decay. In fact, the qubit decay is likely due to the dielectric loss in the circuit's antenna capacitance with an effective quality factor $Q_{\text{diel}} = 5 \times 10^5$. The spin-echo signal decay is also exponential with a characteristic coherence time $T_2 = 52$ μs. The additional dephasing $\Gamma_\varphi = 1/T_2 - 1/2T_1$ is likely due to measurement induced dephasing caused by thermal photons at readout frequency. In fact, the rate of thermal jumps $|0\rangle \rightarrow |3\rangle$ can be linked to the effective photon temperature T at the microwave port via the detailed balance equation $\Gamma_\varphi = \Gamma \exp(-\hbar\omega_{03}/k_B T)$. Plugging in the same value $T = 45 \pm 5$ mK corresponding to the equilibrium ground state population leads to a close agreement with the measured dephasing rate. Such an error process could be exponentially suppressed in the future by a moderate improvement of circuit thermalization and increasing the readout transition frequency.

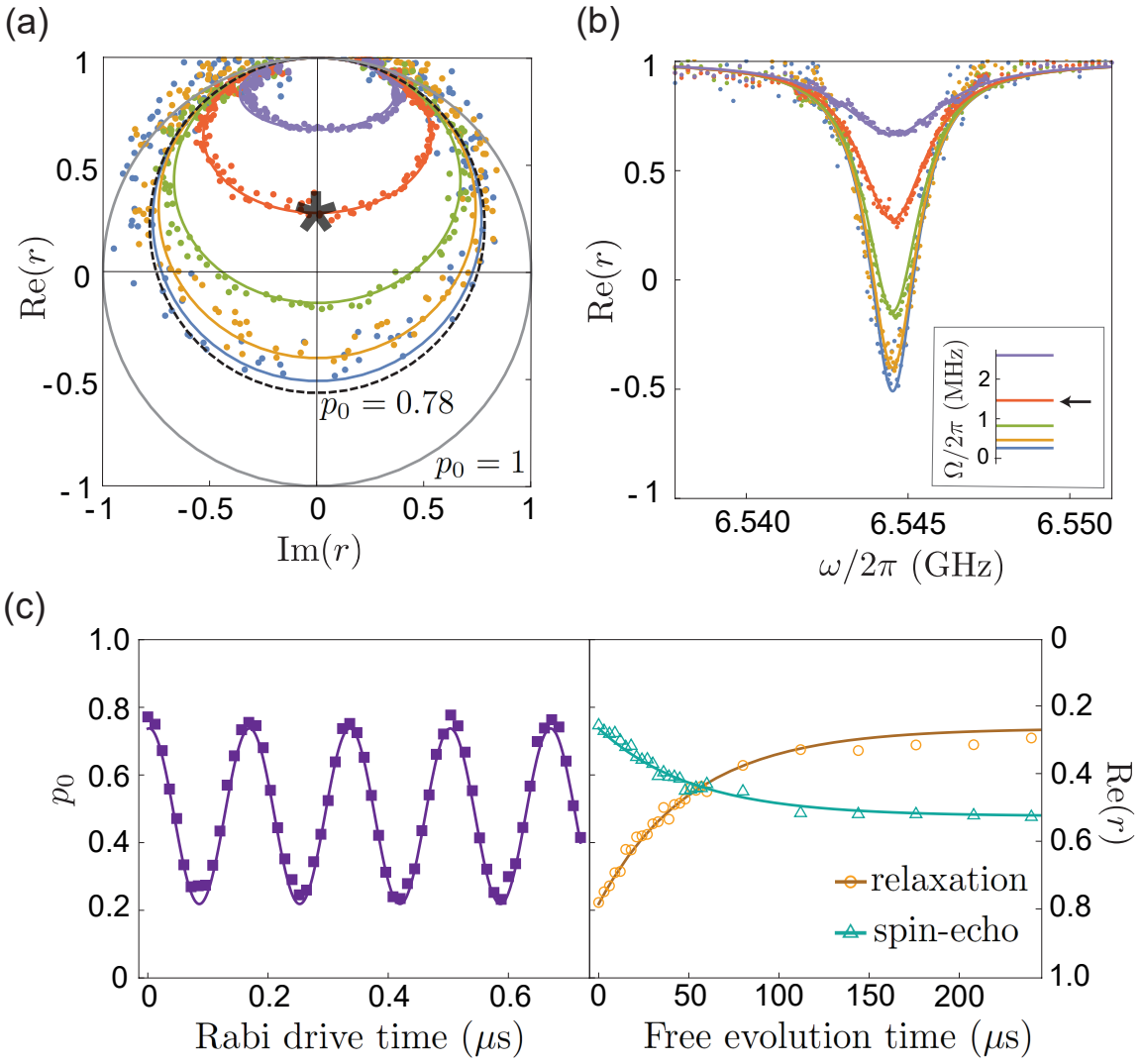

Figure 3.5: Conditional fluorescence readout. (a) Complex plane representation and (b) real part of the reflection coefficient r as a function of readout drive frequency ω at various powers represented by the $|0\rangle$-$|3\rangle$ transition Rabi frequency Ω (inset). The experimental data (colored dots) are fitted by the theory of Eq. 2.92 (lines) with $\Gamma = 2\pi \times 1.74$ MHz and $p_0 = 0.78$ due to thermal occupation of excited states. In the limit $\Omega \to 0$, the data in Fig. 2a becomes a circle with a radius p_0 (gray circle, $p_0 = 1$ and dashed circle, $p_0 = 0.78$). The optimal readout settings are highlighted by the black star and arrow (see text). (c) Rabi oscillations (left panel), energy relaxation (right panel, yellow circles), and spin-echo coherence decay (green triangles) measured using conditional fluorescence readout at optimal settings. Fitting to exponential decay yields (coincidentally) $T_1 = T_2 = 52$ μs.

3.2 non-QNDness

Quantum non-demolition (QND) measurement means that the quantum state is read out without being 'destroyed' in contrast with the destructive measurement. A classical example for destructive measurement is when detecting a flying photon with a photon-counter. The photon is absorbed and destroyed at the detector. On the contrary, a strong QND measurement projects the qubit state to the eigenstates of the measurement operator and another immediate QND measurement after that will generate the same measurement result. Ideally, the readout should be single-shot and QND to reach high fidelity. The readout fidelity is

$$F = 1 - P(e|g) - P(g|e), \tag{3.9}$$

where $P(e|g)$ is the probability of measuring the qubit to be at the excited state when preparing the qubit at the ground state assuming perfect preparation and vice versa for $P(g|e)$. Ideally, it is related to the overlap of the blobs in the single-shot histogram. Intuitively, a larger readout power can lead to a greater separation of the blobs and thus smaller overlap. However, a large photon number in the resonator can induce extra transition rates between qubit levels through measurement-induced qubit state mixing [95], [96] and non-RWA coupling [97]. This unwanted dynamics adds an additional error rate to the probabilities of $P(x|y)$. There is an trade-off between the overlap error and the non-QND error when choosing the readout power. On the other hand, another important property of a readout pulse is the integration time. The trade-off should also considered when determine the integration time. On a multi-qubit quantum processor, a longer integration time means the other qubits that are not been measured are more susceptible to the decoherence error while the measured qubit is suffering from the non-QND error. A shorter integration time, however, will cause wider spread of the blob (the integration process can be considered as another type of averaging but in a single-shot manner). This can be compensate with larger power. Therefore one need to optimize the power and integration time simultaneously to minimize the summation of the effects from overlap error, non-QND error, and decoherence error during the readout, because they can all contribute to the logical error in a QEC code.

3.2.1 non-QNDness for dispersive readout

The non-QND process is observed by measuring the qubit population after a readout pulse as demonstrated in Fig. 3.6 for a two-qubit device. The populations of four computational states are changed by the first readout pulse. The measurement-induced transitions move

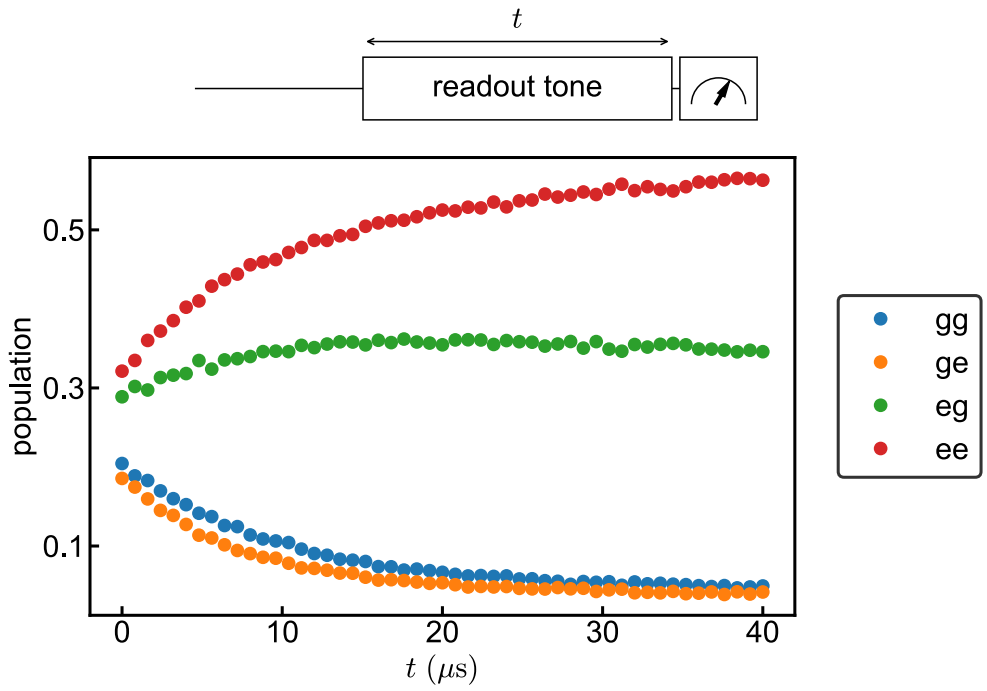

Figure 3.6: Non-QND process of the cavity readout pulse. Non-QNDness is usually observed in two-fluxonium joint readout experiment at large power. A pulse at the readout frequency and with the same amplitude and varying duration is applied to the qubits followed by a joint single-shot readout. The qubit populations tends to be moved to the excited states after applying a long cavity pulse. The readout pulse duration is $6\ \mu$s in this experiment.

the population to the $|eg\rangle$ state. The system is prepared with $\pi/2$ pulses on both qubits. Because the second readout pulse integration time is 6 μs, it can be seen that already a significant non-QND effect at the beginning of the traces ($t = 0$).

In our two-qubit experiment, the qubit population is measured by fitting the single-shot histogram acquired with many repetitions. In this case, one can compensate the non-QND error on the population measurement empirically. We assume the measured populations p'_{ij} are linked to populations p_{ij} at the beginning of the readout by a linear transformation M_e,

$$\begin{pmatrix} p'_{gg} \\ p'_{ge} \\ p'_{eg} \\ p'_{ee} \end{pmatrix} = M_e \begin{pmatrix} p_{gg} \\ p_{ge} \\ p_{eg} \\ p_{ee} \end{pmatrix}. \tag{3.10}$$

The error matrix M_e has 6 parameters that account for the incorrect mapping $|0\rangle \rightarrow |1\rangle$ and $|1\rangle \rightarrow |0\rangle$ for both qubits and entangling transitions between the two qubits during the readout. The error matrix reads

$$M_e = \begin{pmatrix} 1-a_1-b_1 & b_2 & a_2 & 0 \\ b_1 & 1-a_1-b_2-c_1 & c_2 & a_2 \\ a_1 & c_1 & 1-a_2-b_1-c_2 & b_2 \\ 0 & a_1 & b_1 & 1-a_2-b_2 \end{pmatrix}. \tag{3.11}$$

Among the 6 parameters, a_1 and a_2 represent incorrect mappings $|0\rangle_A \rightarrow |1\rangle_A$ and $|1\rangle_A \rightarrow |0\rangle_A$. b_1 and b_2 represent incorrect mappings $|0\rangle_A \rightarrow |1\rangle_B$ and $|1\rangle_B \rightarrow |0\rangle_A$. c_1 and c_2 describe the readout cross-talk where the two qubits swap excitations. In addition to these six parameters, the initial populations for the two qubits p^0_{gA}, p^0_{gB} are also two unknown variables that need to be determined. To calibrate the eight parameters, we perform Rabi measurements on each qubits while the other qubit is left in the $|+\rangle$ state, as shown in Fig. 3.7. Assuming that the system starts with the populations

$$\begin{pmatrix} p_{gg} \\ p_{ge} \\ p_{eg} \\ p_{ee} \end{pmatrix} = \begin{pmatrix} p^0_{gA}p^0_{gB} \\ p^0_{gA}(1-p^0_{gB}) \\ (1-p^0_{gA})p^0_{gB} \\ (1-p^0_{gA})(1-p^0_{gB}) \end{pmatrix}, \tag{3.12}$$

one can predict the Rabi oscillation amplitudes and offsets in the two Rabi measurements of Fig. 3.7 as a function of the 6 parameters of the error matrix plus 2 parameters for the qubit initial population. In each Rabi measurement, there are 4 equations for the amplitude and 4 equations for the oscillation offset. Even though there are 16 equations in total, 8 of them are redundant in this model. Therefore the number of equations matches the number of unknown variables. M_e can be deduced by solving the 8 equations. The corrected populations are obtained by applying M_e^{-1} to the measured populations $(p'_{gg}, p'_{ge}, p'_{eg}, p'_{ee})^T$. With this calibration technique, the populations for both qubits oscillates around 0.5 and only the rotated qubit displays oscillations during the Rabi experiment.

Alternatively, one can include the information in the readout non-QNDness measurement of Fig. 3.6 and add more parameters in the error matrix to match the number of

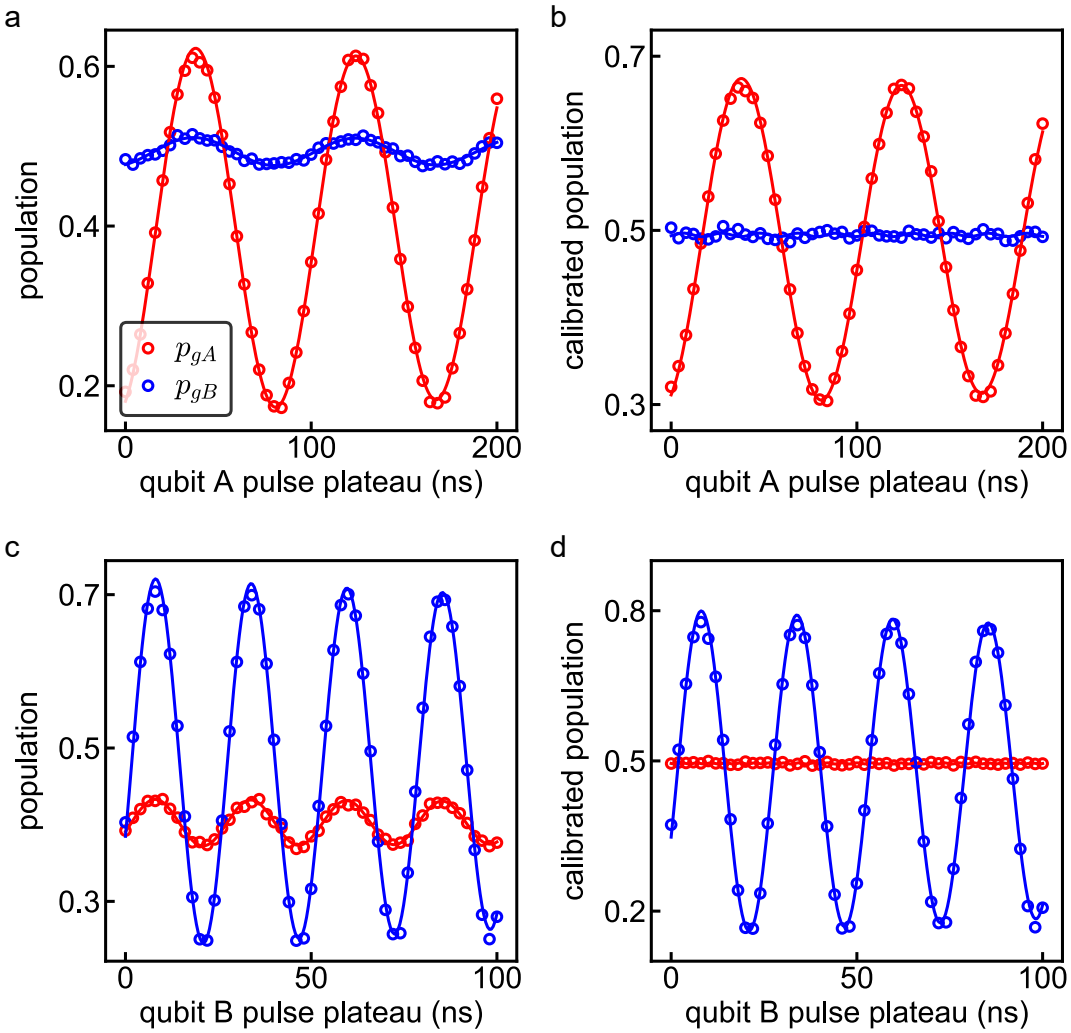

Figure 3.7: Rabi oscillations with and without readout errors correction. Oscillations of qubit A (a, b) and qubit B (c, d). Before correction (left), the Rabi oscillations are not centered around 0.5 because of qubit transitions occuring during the readout. We also correct for readout cross-talk: qubit B readout signal oscillates when qubit A is rotated before correction, and vice-versa.

constraints. For example, we can come up with a 10-parameter matrix

$$M_e = \begin{pmatrix} 1-a_1-b_1-d_1 & b_2 & a_2 & d_2 \\ b_1+e & 1-a_1-b_2-c_1 & c_2 & a_2 \\ a_1-e & c_1+f & 1-a_2-b_1-c_2 & b_2 \\ d_1 & a_1-f & b_1-f & 1-a_2-b_2-d_2 \end{pmatrix}. \quad (3.13)$$

In this matrix, d_1 and d_2 describe the bSWAP-type of readout cross-talk connecting state $|00\rangle$ and $|11\rangle$, in contrast with the SWAP-type parameters c_1 and c_2. The parameter e (f) describes the population that falls into the blob of $|01\rangle$ ($|10\rangle$) when immigrating from blob $|00\rangle$ ($|01\rangle$) to blob $|10\rangle$ ($|11\rangle$). The measurement of Fig. 3.6 gives the fixed point $\vec{P}^*$ of the non-QND effect

$$\vec{P}^* = \begin{pmatrix} p^*_{gg} \\ p^*_{ge} \\ p^*_{eg} \\ p^*_{ee} \end{pmatrix} = M_e \vec{P}^*. \quad (3.14)$$

For this model, 9 constraints in the Rabi measurements are independent. Plus the 3 independent equations in the fixed point definition Eq. 3.14, the 12 constraints can be solved for the 12 unknow variables. Because of the extra information from the non-QNDness measurement in this model, the correction on the population is more robust than the 6-parameter matrix. It needs to be emphasized that these models are purely empirical because the exact dynamics for the non-QNDness in fluxonium-cavity system are not fully understood yet. More theoretical efforts are needed to investigate the accurate physical picture in the presence of cavity photons.

3.2.2 non-QNDness for fluorescence readout

The non-QND effect also exists in the conditional fluorescence measurement, which is understood better than the fluxonium dispersive readout. To test the readout QNDness, we drive the $|0\rangle$-$|3\rangle$ transition for a duration $\tau \gg 1/\Gamma$, pause for a brief period for state $|3\rangle$ to relax, swap the state of interest with state $|0\rangle$, and perform the readout (Fig. 3.8a - top panel). As a result, we acquire the population transients $p_0(t)$, $p_1(t)$, and $p_2(t)$ of states $|0\rangle$, $|1\rangle$, and $|3\rangle$, respectively, during the readout. The fidelity of this population measurement is limited by the swap gate fidelities, which is above 99% for $|0\rangle - |1\rangle$ and above 90% for $|0\rangle - |2\rangle$. The $p_0(t)$-data indicates a gradual leakage of population outside the cycling manifold $\{|0\rangle, |3\rangle\}$ on a characteristic time scale $\tau_{cyc} = 9.6\ \mu$s. Importantly, the leakage involves only states $|1\rangle$ and $|2\rangle$ as the data satisfies $p_0 + p_1 + p_2 = 1$ within the measurement uncertainty (Fig. 3.8a -

bottom panel). The average number of fluorescence cycles $N_{cyc} = \Gamma \times \tau_{cyc} \approx 105$ quantifies the deviation of our readout from ideal QND behavior.

The finite fluorescence lifetime is expected in presence of non-radiative transitions outside the cycling manifold. Additional information about energy relaxation in our circuit was obtained by measuring populations of states $|0\rangle$, $|1\rangle$, and $|2\rangle$ as a function of time following the $|0\rangle$-$|2\rangle$ swap (Fig. 3.8b). Combining the two data sets represented on Fig. 3.8a and b, we constructed a relaxation model based on two additional decay mechanisms, dielectric loss and quasiparticle tunneling across the weak junction. Indeed, such model adequately fits the six experimental curves with only three adjustable parameters: the dielectric loss quality factor $Q_{\text{diel}} = 5 \times 10^5$, previously introduced to explain the $|1\rangle \rightarrow |0\rangle$ decay, the dimensionless quasiparticle density $x_{\text{qp}} = 10^{-6}$, and a fudge-factor of 2.5 in front of the $|3\rangle \rightarrow |2\rangle$ decay rate. The presence of additional decay for this precise transition could be due to a nearly resonant two-level system [66]. From this model we conclude that fluorescence lifetime originates from two error processes. A smaller contribution comes from the direct decay $|3\rangle \rightarrow |1\rangle$ with a characteristic time $36\ \mu s$ due to quasiparticle tunneling. Such process may break the parity selection rule for $\phi_{\text{ext}} \neq 0$, a prediction that has not been tested so far. The dominant error though comes from the decay $|3\rangle \rightarrow |2\rangle$ with a characteristic time of $3.6\ \mu s$ due to dielectric loss in the fluxonium capacitance. Therefore, improving our fabrication procedures will likely increase the fluorescence lifetime and hence the QND-fidelity. Alternatively, with a modified choice of circuit parameters, one can increase the frequency of $|1\rangle$-$|2\rangle$ transition and use it for cycling, in which case the fluorescence lifetime would be limited by the qubit T_1.

3.3 Noise and Quantum Limited Amplifiers

3.3.1 Added Noise

The non-linearity of a Josephson junction makes it inherently an core component to construct amplifiers that are essential for detecting weak microwave signals of qubit systems. Over decades, many different amplifiers are invented with Josephson junctions, including the Josephson Parametric Amplifier (JPA), the Josephson Parametric Converter (JPC), Josephson bifurcation amplifier (JBA), the Josephson Traveling Wave Parametric Amplifier (JTWPA), etc. In this section, the basic principle of JPA will be explained as a simple example among all these amplifiers. After that, we are going to compare it with the JTWPA that we used in our experiments. JPA and JTWPA can be used phase insensitive amplifiers (i.e. phase preserving amplifiers) with equal amplification on both quadratures of the signal in

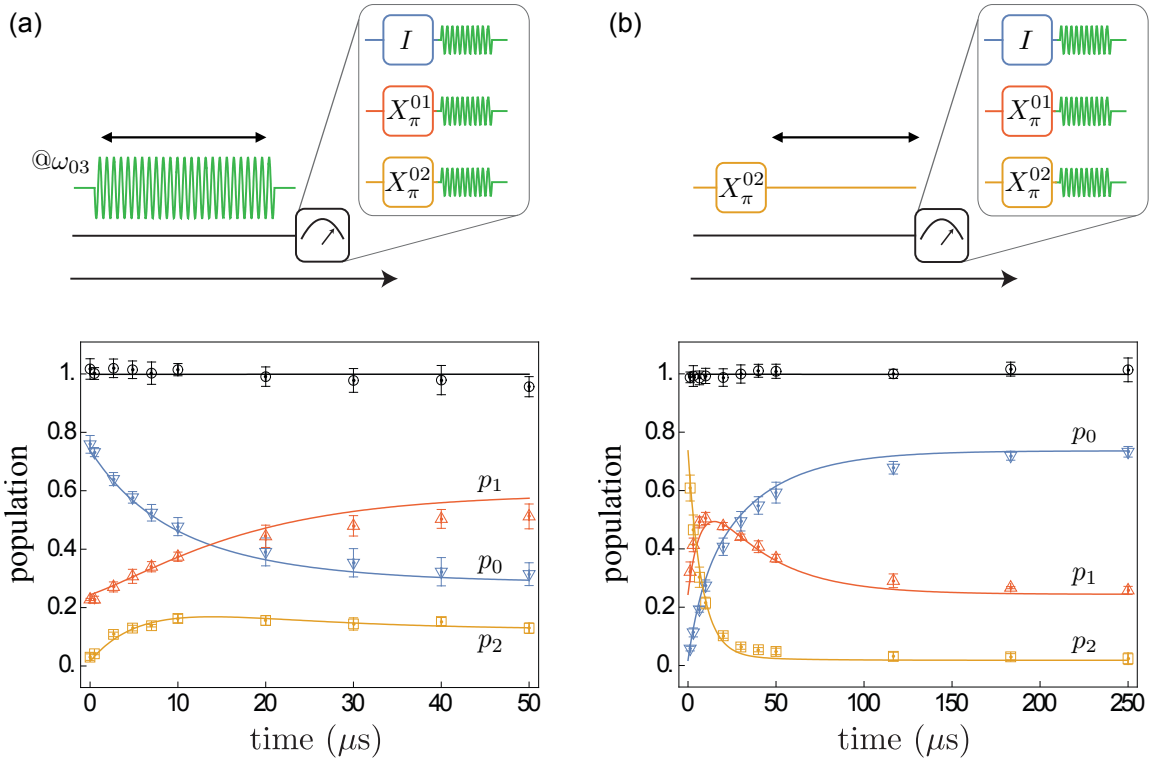

Figure 3.8: Transient dynamics of fluorescence. (a) Time-domain evolution of populations p_0 (down blue triangles), p_1 (up red triangles), and p_2 (yellow squares) induced by cycling of the readout transition. Note that p_0 decays approximately exponentially in time with a characteristic time scale $\tau_{cyc} = 9.6$ μs, after which the population is transfered from state $|0\rangle$ to states $|1\rangle$ and $|2\rangle$. The black circles indicate $p_0 + p_1 + p_2$ and the error bars represent the standard deviation coming from the repetition of the measurements over two days. (b) Free evolution of populations starting predominantly from state $|2\rangle$. The data in both (a) and (b) is adequately explained by an optical pumping model (solid lines) (see text) where the dominant error mechanism is a non-radiative decay due to dielectric loss.

contrast with the phase sensitive amplifier which only amplifies one quadrature.

Before introducing JPA, we need to first understand why we need Josephson-junction-based amplifiers. The general goal of any amplifiers is to fight against noise and extract weak signals but one also need to realize that the noise at the input of the amplifier gets magnified together with the signal. Starting from the photons in the cavity, the noise already exists from Heisenberg uncertainty principle [98]. The electric field of a single-mode signal can be written as

$$E(t) = \frac{1}{2}(ae^{-i\omega t} + a^\dagger e^{i\omega t}). \tag{3.15}$$

Its variance $\langle \Delta E^2 \rangle = \langle |\Delta a|^2 \rangle / 2$, where $\langle |\Delta a|^2 \rangle = \langle |a|^2 \rangle - |\langle a \rangle|^2$ is the symmetric variance of a and $|a|^2 = (aa^\dagger + a^\dagger a)/2$. The uncertainty principle puts an constraint on the variance $\langle |\Delta a|^2 \rangle \geq 1/2$. The lower bound is the half-quantum of the vacuum noise. When it is reached, the noise is quantum limited.

The attenuators and the amplifiers on the measurement line not only modify the noise at the input but also add extra noise [99]. Assuming the noise at the input is N_{in} in terms of the photon number, the noise at the output is $N_{\text{out}} = G(N_{\text{in}} + N_{\text{added}})$. N_{add} is the added noise and G is the gain of the component. $G > 1$ for an amplifier and $G < 1$ for an attenuator. Because the signal also gets modified by the same factor $S_{\text{out}} = GS_{\text{in}}$, the SNR at the output is

$$\text{SNR}_{\text{out}} = \frac{S_{\text{out}}}{N_{\text{out}}} = \frac{\text{SNR}_{\text{in}}}{1 + N_{\text{added}}/N_{\text{in}}}. \tag{3.16}$$

Therefore, any components, including amplifiers, can only degrade the SNR due to the inevitable added noise. This may sound counter-intuitive and does not mean we should not put amplifiers on the measurement line. To understand this paradox, we can first look at the case for the attenuator. The added noise is

$$N_{\text{added}} = \left(\frac{1}{G} - 1\right) N_T \tag{3.17}$$

and N_T is the thermal photon number

$$N_T = \frac{1}{e^{\hbar\omega/k_B T} - 1}. \tag{3.18}$$

T is the physical temperature of the attenuator and give rise to the noise through Planck's blackbody radiation into the line. The prefactor in front of N_T in Eq. 3.17 is crucial to make

the model self-consistent. Without this factor, one can imagine that by connecting a chain of 0 dB attenuators at room temperature, the noise amplitude can be increased to infinity, which is obviously unphysical. Using Eq. 3.17, it can be checked that two consecutive attenuators with the same temperature T and loss factor $L = 1/G$ are equivalent to one attenuator with temperature T and loss factor L^2.

The typical readout frequency in our experiment is 7.5 GHz, corresponding to a temperature of 0.36 K. The thermal photon numbers at different stages of the dilution refrigerator are listed in Table 3.1. The noise is rather small compared to the quantum noise of the photon in the cavity but starts to become significant at the pulse tube plate (3 K). Imagine there is a loss as small as 3 dB, the prefactor $1/G - 1 \approx 1$, indicating an added noise equalling to the thermal noise will be added to the input noise, which is already a significant amount. From Eq. 3.16, it is straightforward that the ratio $N_{\text{added}}/N_{\text{in}}$ determines how much SNR is reduced. Now we can see why amplifiers are necessary. In fact, the strategy is to increase N_{in} and S_{in} simultaneously at the cost of a small portion of SNR, such that the SNR becomes resilient to the N_{added} afterwards because of the small $N_{\text{added}}/N_{\text{in}}$ ratio. Otherwise, the weak qubit signal on the order of 10 photons coming out from the cavity can be easily buried into the thermal noise due to a small loss on the line. Due to the limit of gain on a single amplifier, multiple amplifiers at different stages are required to transmit the signal from the base plate inside the fridge all the way up to the room temperature acquisition setup.

T	14 mK	80 mK	0.78 K	3 K	53 K	300 K
N_T	7e-12	1e-2	1.7	7.8	147	833

Table 3.1: Thermal photon noise at different stages. Photon numbers are calculated from Eq. 3.18 at 7.5 GHz which is the typical readout frequency.

As we mentioned earlier, there is no free lunch in nature. The amplifier itself is always accompanied by an added noise. The Haus-Caves theorem puts a lower bound on the phase insensitive amplifier's added noise that is required by quantum mechanics

$$N_{\text{added}}^{\text{amplifier}} \geq \frac{1}{2}\left(1 - \frac{1}{G}\right). \tag{3.19}$$

The amplifier close to the lower bound is called the quantum limited amplifier. When the gain $G \gg 1$, the amplifier adds at least half of a photon noise to the signal. Generally speaking, the added noise is due to the uncontrolled degrees of freedoms. the added noise can be introduced in the idler mode [100]. One can define an equivalent noise temperature

T_e for an amplifier such that

$$N_{\text{added}}^{\text{amplifier}} = \frac{1}{e^{\hbar\omega/k_B T_e} - 1}. \tag{3.20}$$

In the high temperature limit $k_B T_e \gg \hbar\omega$, or equivalently $N_{\text{added}}^{\text{amplifier}} \gg$, the noise temperature can be approximated as

$$T_e = \frac{N_{\text{added}}^{\text{amplifier}} \hbar\omega}{k_B}. \tag{3.21}$$

Another physical quantity to describe the added noise of an amplifier is the noise figure. It is defined as the reduction of SNR when the input noise is from a resistor at $T_0 = 290$ K,

$$F = \frac{\text{SNR}_{\text{in}}}{\text{SNR}_{\text{out}}} = 1 + \frac{N_{\text{added}}}{N_{\text{in}}} \approx 1 + \frac{T_e}{T_0}. \tag{3.22}$$

In this way, one can immediately know where is optimal to put an amplifier judging by its noise temperature or noise figure.

Quantum efficiency η is a commonly used concept to describe the added noise in the measurement line. For a single amplifier, it is given by

$$\eta = \frac{1}{N_{\text{added}} + 1/2}. \tag{3.23}$$

In some literature, the definition can be slightly different $\tilde{\eta} = \eta/2$. If the amplifier is quantum limited $N_{\text{added}} = 1/2$, $\eta = 1$, indicating this is the best case one can achieve. For the case of an amplification chain with large gain, the total quantum efficiency can be calculated by normalizing the total noise at the output with the total gain

$$\eta_{\text{tot}} = \frac{1}{N_{\text{tot}}/G_{\text{tot}} + 1/2}. \tag{3.24}$$

Just like the property of SNR, adding extra amplifiers will only degrade the total quantum efficiency. A good measurement setup should have the total quantum efficiency close to that of the first stage amplifier, which should be close to 1 [101]–[103].

3.3.2 JPA and JTWPA

JPA is one of the simplest quantum limited amplifier. The circuit model is depicted in Fig. 3.9. The incoming signal consists of a strong pump tone and a weak signal $I_{\text{in}} = I_{\text{pump}} +$

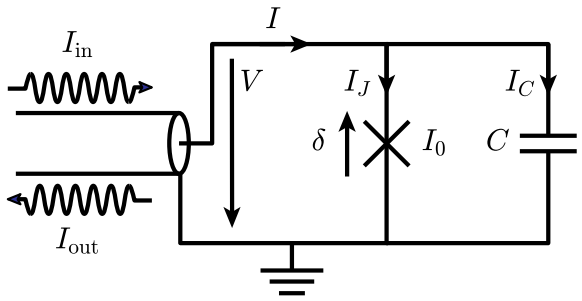

Figure 3.9: Circuit diagram of a JPA galvanically connected to a transmission line. I_{in} and I_{out} are the incoming and outgoing current in the transmission line. The total current at the end of the transmission line is I, which splits into the current going to the Josephson junction (I_J) and the current going to the capacitor (I_C).

I_{signal}. The phase difference across the junction is denoted as δ which can be also separated into two parts corresponding to the pump and the signal $\delta = \delta_{\text{pump}} + \delta_{\text{signal}}$. Because the signal tone is much smaller than the pump tone. We first solve for the system's response to the pump and ignore the signal part. Therefore we assume $I_{\text{in}} = I_{\text{pump}} = I_p \cos(\omega_p t + \varphi)$ and $\delta = \delta_{\text{pump}} = \delta_a \cos \omega_p t$. We are going to introduce the conclusions briefly in this section and leave the derivation in appendix C.1. The relation between the phase oscillation amplitude and the input current amplitude is

$$\left((\omega_0^2 - \omega_p^2)\delta_a - \frac{\omega_0^2}{8}\delta_a^3\right)^2 + (2\gamma\omega_p\delta_a)^2 = \left(\frac{2I_p}{C\phi_0}\right)^2, \tag{3.25}$$

where $\omega_0^2 = I_0/(C\phi_0)$ and $\gamma = 1/(2Z_cC)$. We keep the lowest non-linear term for the Josephson junction.

At small pump power (i.e. small I_p), the circuit behave like a harmonic oscillator and the resonant frequency is ω_0. The Purcell rate is $\Gamma = 2\gamma$. At large pump power, the phase amplitude δ_a's response to the pump at different frequency starts to display non-linearity in Fig. 3.10. When the power is above the critical power, bifurcation starts to occur where two stable states can exist at the same time at one pump tone. In this regime, the system is called Josephson bifurcation amplifier (JBA) [104] which can also have a performance close to the quantum limit.

The system's response to the weak signal can then be solved assuming δ_{pump} is not affected by the small signal. We can define $c_{\text{in(out)}}$ as the field operator for the input (output)

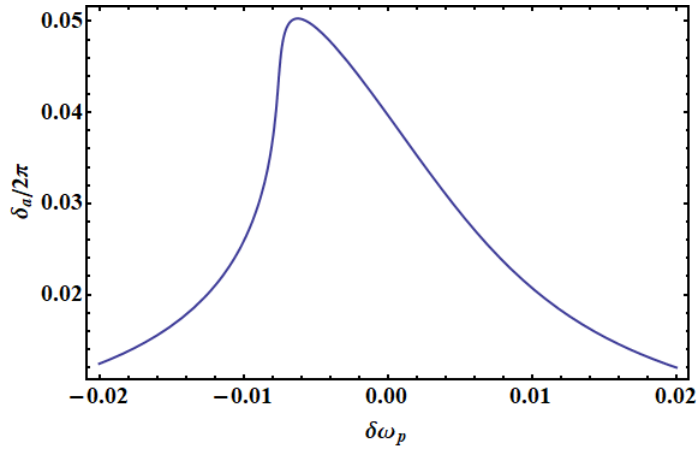

Figure 3.10: Phase amplitude δ_a at different pump frequency. The power is close to the critical power and the curve deviates from the linear Lorentzian response. The external quality factor is 100.

signal and $\omega' = \omega - \omega_p$ is the signal detuning from the pump. Then we have

$$c_{\text{out}}(\omega') = \left(-1 + \frac{2\gamma(-i\omega' - i(\omega_0 - \omega_p) + \gamma - i\omega_0\epsilon/2)}{(-i\omega' + \lambda_0)(-i\omega' + \lambda_1)}\right) c_{\text{in}}(\omega') \tag{3.26}$$

$$+ \frac{\gamma e^{2i\varphi}\omega_0\epsilon/2}{(-i\omega' + \lambda_0)(-i\omega' + \lambda_1)} c_{\text{in}}^\dagger(-\omega'), \tag{3.27}$$

$$= \mathcal{G}(\omega')c_{\text{in}}(\omega') + \mathcal{M}(\omega')c_{\text{in}}^\dagger(-\omega'). \tag{3.28}$$

The parameters $\lambda_{0/1}$ and ϵ are defined as

$$\epsilon = \delta_a^2/4, \tag{3.29}$$

$$\lambda_{0/1} = \gamma \mp \sqrt{\frac{\omega_0^2\epsilon^2}{16} - \left(\omega_0 - \omega_p - \frac{\omega_0\epsilon}{2}\right)^2}. \tag{3.30}$$

For simplicity, let's substitute ω' with ω. The signal gain G_s and image gain G_i can be defined as

$$G_s(\omega) \equiv |\mathcal{G}_s(\omega)|^2, \tag{3.31}$$

$$G_i(\omega) \equiv |\mathcal{M}_s(\omega)|^2. \tag{3.32}$$

The image tone (i.e. the idler tone) and the signal tone are symmetrically distributed on two sides of the pump tone. When the signal only has one mode, the idler mode on the other side of the pump becomes the source of the added noise that will get mixed with the

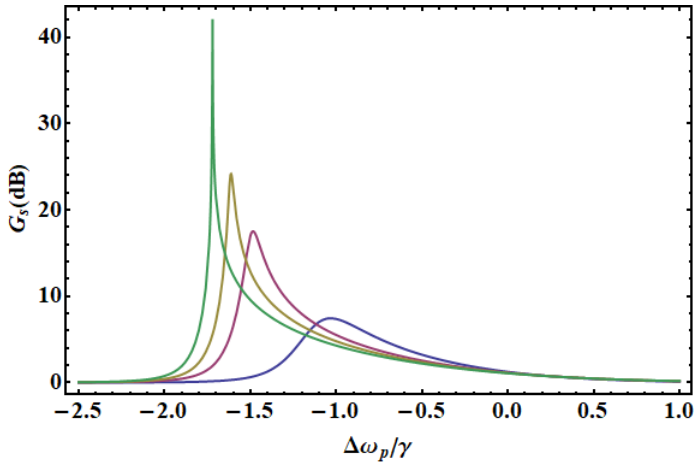

Figure 3.11: Signal gain G_s at different pump frequency and power. The signal frequency is kept the same as the pump frequency in this simulation and $\Delta\omega_p = \omega_{\text{pump}} - \omega_0$. At small power ($P = 0.5P_{\text{critical}}$), the signal gain is small (purple line). When the power is close to the critical power ($P = 0.99P_{\text{critical}}$), the gain peak is high and sharp (green line). The pump frequency at the maximum gain is also further away from the low power resonance frequency ω_0.

signal mode at the output.

As shown in Fig. 3.11, when the pump and signal have the same frequency, the maximum signal gain G_s gets larger with increasing pump power and diverges at critical power P_{critical}. The gain peak shifts to the low frequency side, which is consistent with the bending direction of the curve in Fig. 3.10. On the other hand, we can fix the pump frequency at the maximum gain and change the signal power, as demonstrated in Fig. 3.11. When the signal is at the same frequency as the pump ($\omega = 0$), the gain is maximized. The gain curve is symmetric with respect to the pump frequency. The half-maximum bandwidth B_ω is smaller at higher pump power. One can prove that $B_\omega \propto 1/\sqrt{G_{\text{max}}}$, which is quite common in many amplifiers. At the same time, it is also worth mentioning that, in practice, it is more important to talk about the 'bandwidth' achieving over 20 dB rather than the half-maximum bandwidth B_ω.

The bandwidth B_ω when G_{max} reaches 20 dB is also called dynamic bandwidth. Typically it is on the order of few MHz [59]. From Fig. 3.12, we can see the bandwidth is proportional to γ, which is linked to the external Q of the circuit. Because JPA requires a high-Q system, one can not broaden the bandwidth by simply lower the quality factor. One strategy is to fabricate a SQUID instead of a single junction which adds tunability to the system. By operating at different flux point, one can achieve 20 dB gain over 500 MHz,

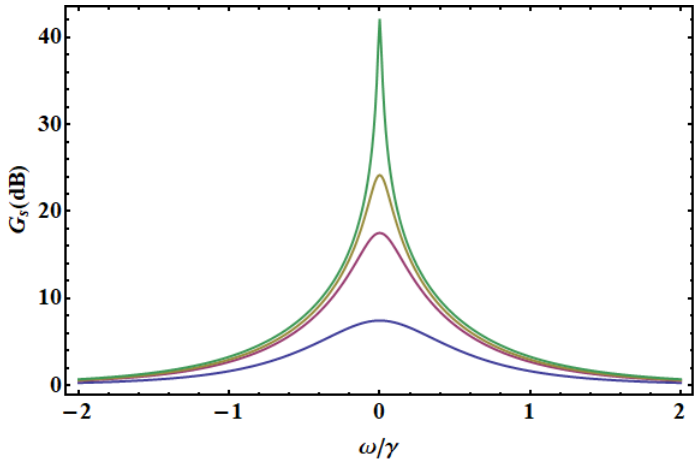

Figure 3.12: Signal gain G_s at different signal frequency and pump power. The pump frequency is set to get the maximum gain. At higher power, the bandwidth is smaller, but the frequency range where the gain is above 20 dB is actually broader.

which is called the static bandwidth.

In recent years, a new type of amplifier called Josephson traveling-wave parametric amplifier was invented. The JTWPA used in our lab is from Lincoln Labs. It takes advantage of a metamaterial transmission line made by Josephson junction chain. It can achieve 20 dB gain over 3 GHz bandwidth by satifying the phase-matching condition. This is accomplished by manipulating the dispersion relation using an array of subwavelength resonators. Apart from the wide bandwidth, JTWPA can also tolerate higher input power than JPA. This is quantified by 1 dB-compression point – the input power when the gain is reduced by 1dB. The typical 1 dB-compression point can be -120 dBm for JPA, while our JTWPA can reach -105 to -95 dBm.

3.4 Initialization Schemes

In fluxonium experiments, fast initialization is instrumental to increase the averaged signal contrast and hence speed up the measurement. It is also going to be indispensable in the future when doing repetitive error corrections on logical qubits during a complicated algorithm. We explored some initialization techniques in our lab and other schemes will also be discussed in this section.

3.4.1 Preselection initialization

If the readout is quite QND, one can preselect the data to achieve an effective initialization in the experiment. At the beginning of each sequence, an additional preselection readout pulse is applied to perform single-shot readout. This means that the acquisition setup will record two set of data in an interleaved way. One corresponds to the measurement result before the sequence and the other is the usual measurement after the sequence.

The first readout pulse is QND, meaning that it does not change the ensamble probability distribution of the mixed state. Therefore directly averaging the post-sequence measurement data will give the same result as if there is no preselection pulse. Instead, one needs to analyze the single-shot histogram of the pre-sequence measurement and select part of the data. For example, as shown in Fig. 3.13, if we want to initialize the qubit to $|10\rangle$ state, we select the sequence indices for which the pre-sequence data fall into the solid circle. Then we pick out the data from the post-sequence measurement that have the same sequence indices. The data after selection look like Fig. 3.13b. The population is concentrated into the $|10\rangle$ blob. There is some residual population visible on $|11\rangle$ state. This is mainly because the non-QNDness of the pre-sequence pulse moves the population to the $|11\rangle$ state.

This initialization method sacrifices the data collection efficiency and is not scalable. As the number of qubit increases, the population of a specific state can decrease exponentially. Because the contrast can only be enhanced after collecting a large amount of data and post-processing, it is not as straightforward as other initialization schemes.

3.4.2 Cavity tone initialization

It is observed that for the devices used in our experiments, the readout can be highly non-QND with a high readout power and long pulse duration. The population tend to be moved to the exicted states, as shown in Fig. 3.14. The mechanism is not fully understood yet, but there is evidence that the high levels are involved during the process. Typically a $10\ \mu$s delay need to be set between the initialization pulse and the following sequence in order to wait for the high level population gets depleted and decays back to the computational space.

We tried this scheme on two different two-qubit devices. We achieved 69 % and 82 % excited state population on one device along with 86 % and 88 % on the other device.

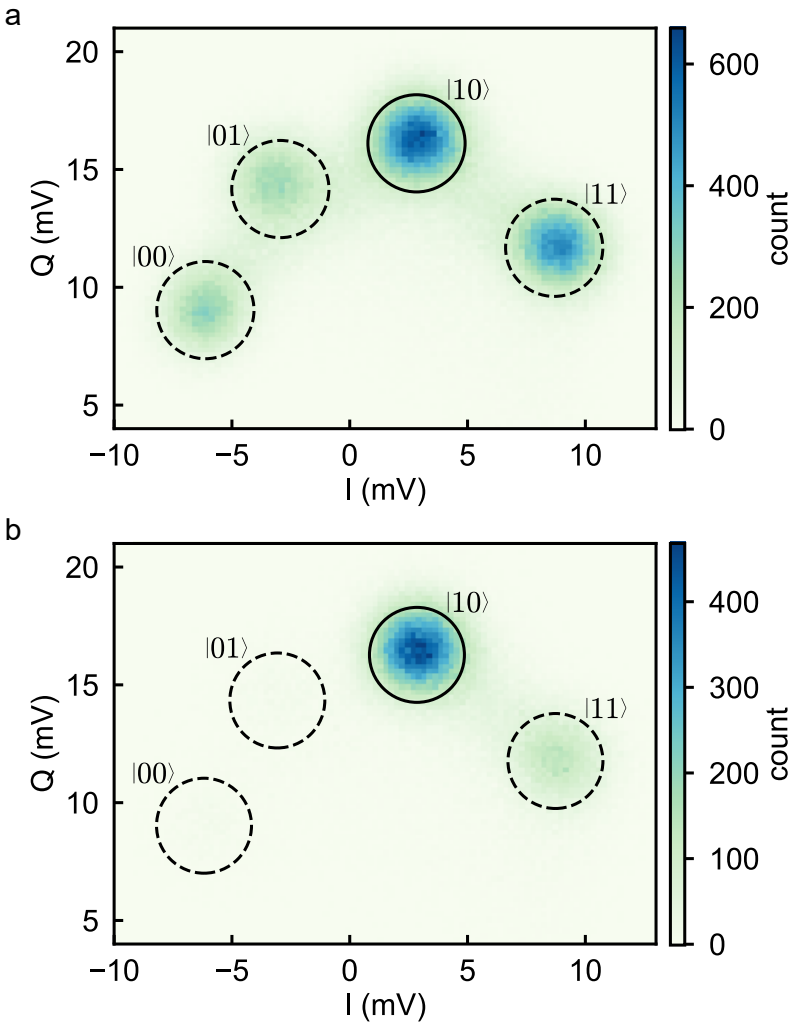

Figure 3.13: Initialization by preselection. (a) Single-shot data from the heralding readout pulse. The populations extracted from the heights of the blobs are $p_{00} = 0.17,\ p_{01} = 0.17,\ p_{10} = 0.37,\ p_{11} = 0.29$. The experiments corresponding to the points within the solid circle are selected in order to initialize the population to $|10\rangle$. (b) Single-shot histograms after preselection. The populations are $p_{00} = 0.02,\ p_{01} = 0.02,\ p_{10} = 0.72,\ p_{11} = 0.25$. There is still a significant population at $|11\rangle$, which is due to the readout non-QNDness.

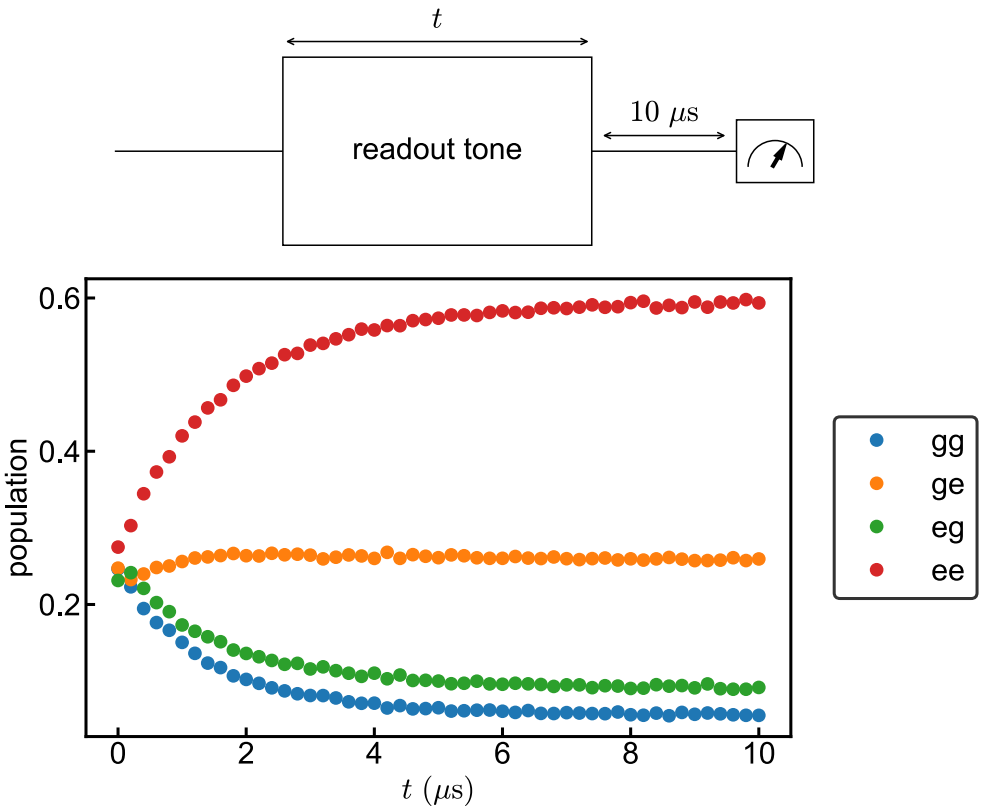

Figure 3.14: Initialization using the cavity pulse Non-QNDness. A strong pump pulse at the readout frequency is applied to pump the qubit population to the excited states. A 10 μs delay is placed after the initialization pulse in order to deplete the population outside the compuational space. The population of the ee state can reach 0.6 after 10 μs of pumping.

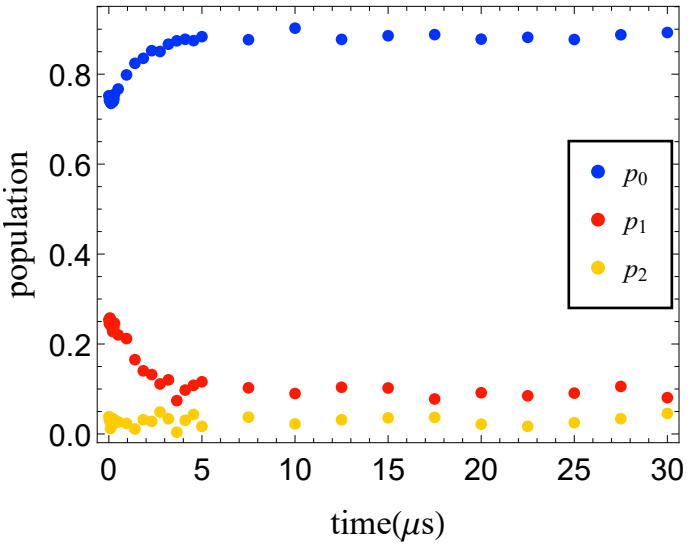

Figure 3.15: Qubit population initialization by pumping $|1\rangle$-$|3\rangle$. Time-domain evolution of populations during $|1\rangle$-$|3\rangle$ pumping. 88% of the population can be prepared to $|0\rangle$ after pumping for 5 μs.

3.4.3 Initialization in the fluorescence experiment

With the ability to drive the even transitions at the flux point in the fluorescence experiment (Sec. 3.1.2), we could prepare the ground state by driving the transition $|1\rangle$-$|3\rangle$ as presented in Fig. 3.15. By design of the readout transition, $|3\rangle$ decays to $|0\rangle$ much faster than to other states. Therefore if thermal population gets pumped to $|3\rangle$, most of it decays to $|0\rangle$. We checked that the qubit can be initialized with $p_0 \approx 0.9$ after 5 μs pumping, limited by the driving strength of the pumping transition $|1\rangle \rightarrow |3\rangle$. In theory, the maximal value of p_0 approaches unity upon increasing T_1 and reducing the error rate of decay from state $|3\rangle$ to state $|1\rangle$.

3.4.4 Other fluxonium initialization schemes

Similar to the fluorescence experiment, the cavity also provides a lossy transition with large radiative decay rate. Here we use $|\alpha n\rangle$ for the joint state with qubit at state α and n photons in the cavity. The transition $|g1\rangle - |g0\rangle$ and $|e1\rangle - |e0\rangle$ decay at a rate of κ that is on the order of tens of MHz and can be utilized to initialize the qubit (Fig. 3.16).

One way to do this is to use the sideband transition $|e0\rangle - |g1\rangle$ [105], [106]. Away from the half flux quanta, one can directly pump this transition just like pumping the $|1\rangle$-$|3\rangle$ transition in the fluorescence experiment. At the half flux quanta, the sideband transition is a

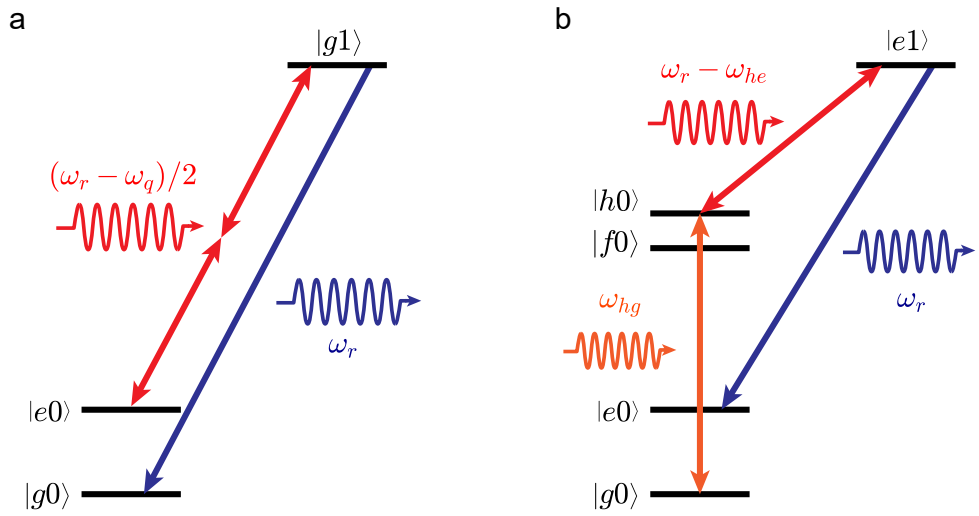

Figure 3.16: Other initialization diagrams. (a) Sideband cooling. The system population is pumped to $|g1\rangle$ using the two-photon transition of the red sideband transition $|e0\rangle - |g1\rangle$ and then decays back to $|g0\rangle$ rapidly. (b) Initialization using the $|h0\rangle$ state. Two microwave drives are applied to the system to move the population from $|g0\rangle$ to $|e1\rangle$ through $|h0\rangle$. The population then decays back to $|e0\rangle$.

forbidden even transition and can not be directly driven. Instead, by applying a strong drive at half of the sideband transition, the population can be pumped up through two-photon process. A initialization fidelity of 99 % has been reported in Ref. [106]. Alternatively, if a fast flux line is available on the chip, one can apply a flux pulse to bias the fluxonium away from the sweet spot temporarily to open the forbidden channel and go back to sweet spot after the initialization pulse [85].

Another approach is to use a intermediate state, for example, the $|h0\rangle$ state [49]. Because $|g0\rangle - |h0\rangle$ and $|h0\rangle - |e1\rangle$ both have large matrix elements, one can drive these two transitions simultaneously to pump the population to $|e1\rangle$ state. A population of 95 % can be initialized to the excited state in this way.

Chapter 4

Microwave Gate Experiments with Fluxonium

Entanglement is a critical resource in quantum information. It makes a quantum computer fundamentally distinct from a classical computer. One might be able to describe superposition of quantum states with classical probabilities. But this type of attempt will fail in the presence of quantum entanglement as it breaks the Bell's inequality. The quantum magics such as quantum teleportation need to be performed at the cost of quantum entanglement, which is also the case for the exponential speedup of the Shor's algorithms. Entanglement is generated with gates on the qubits in a quantum processor and the essential part is two-qubit gates. For superconducting qubits, the gate can be activated with flux [49], [85], [107]–[114] or microwave pulses [115]–[124]. The invention of flux-tunable couplers makes it possible to turn the interaction between qubits on and off on-demand while the microwave toolbox are also being expanded for the fixed frequency qubits. Generally speaking, flux gates have shorter gate times due to its ability to turn on a large interaction. But the qubit coherence time can be degraded away from the sweet spot, especially when the qubit transition crosses two-level defects on the spectrum. On the contrary, the microwave gate are performed with better coherence and does not require a fast flux line, which is simpler in terms of the hardware. However, its gate time is usually longer. The incoherent error of a gate coming from decoherence can be estimated with [125]

$$\epsilon = \frac{t_{\text{gate}}}{3}\left(\frac{1}{T_1} + \frac{1}{T_\phi}\right). \tag{4.1}$$

Therefore the gate time and the coherence both need to be taken into account to get an optimal gate fidelity. Recent experiments have exhibited two-qubit gate fidelity approaching

99.9 % for both types of architecture.

Even though fluxonium is flux-tunable by nature, we focus on microwave-activated gates in this chapter. There are efforts exploiting flux gates on fluxoniums including theoretical proposals and experimental demonstrations [49], [85], [126]–[128]. We believe that microwave gates implemented at flux sweet spot can make the most of the high coherence of fluxonium qubits. We are going to first introduce the tools for characterizing gates including process tomography and randomized benchmarking based techniques. We will discuss our single-qubit gate measurement and then describe different types of two-qubit microwave gates that we explored for fluxoniums. The last section will briefly present our routine for parameter optimization.

4.1 Characterization techniques

We used quantum process tomography (QPT) and various randomized benchmarking based methods to characterize the gates. QPT is a universal technique to identity a quantum operation and can be implemented in most cases. However, it can be limited by state-preparation-and-measurement (SPAM) errors [129]. This concern is addressed in randomized benchmarking techniques by repeating the gates and fitting for the decay constant. There are some other techniques reported in literature but will not be discussed in this section, such as QPT with Pauli transfer matrix representation [130] and the gate set tomography (GST) [131].

4.1.1 Quantum process tomography

Just like quantum state tomography (QST) can depict a full picture of a quantum state, QPT includes all the information of a quantum operation. In our experiments, we perform a process tomography of the gate operation using a standard procedure described in [132], [133]. The quantum process to be characterized is interleaved between one preparation pulse and one tomography pulse chosen in Table 4.1. The process matrix χ characterizes fully the quantum process $\mathcal{E}$. We prepare 16 input states $\{\rho_j\}$ and measure the output states through QST. Using the information from the 16 measurements, we can extract the process matrix χ.

State tomography

For a n qubit system, the Hilbert space dimension is $d = 2^n$. There are $4^n = d^2$ corresponding Pauli matrices $\sigma_{v_1} \otimes \sigma_{v_2} \otimes \cdots \otimes \sigma_{v_n}$, where $v_i = 0, 1, 2, 3$. They are also $d \times d$ matrices and

Preparation pulses	Tomography Pulses
II, $IX_{\pi/2}$, $IY_{\pi/2}$, $IX_{-\pi/2}$, $X_\pi I$, $X_\pi X_\pi$, $X_\pi Y_{\pi/2}$, $X_\pi X_{-\pi/2}$, $Y_{\pi/2}I$, $Y_{\pi/2}X_\pi$, $Y_{\pi/2}Y_{\pi/2}$, $Y_{\pi/2}X_{-\pi/2}$, $X_{-\pi/2}I$, $X_{-\pi/2}X_\pi$, $X_{-\pi/2}Y_{\pi/2}$, $X_{-\pi/2}X_{-\pi/2}$	II, $X_\pi I$, $X_{\pi/2}I$, $X_{-\pi/2}I$, $Y_{\pi/2}I$, $Y_{-\pi/2}I$, IX_π, $X_\pi X_\pi$, $X_{\pi/2}X_\pi$, $X_{-\pi/2}X_\pi$, $Y_{\pi/2}X_\pi$, $Y_{-\pi/2}X_\pi$, $IX_{\pi/2}$, $X_\pi X_{\pi/2}$, $X_{\pi/2}X_{\pi/2}$, $X_{-\pi/2}X_{\pi/2}$, $Y_{\pi/2}Y_{\pi/2}$, $Y_{-\pi/2}Y_{\pi/2}$, $IX_{-\pi/2}$, $X_\pi X_{-\pi/2}$, $X_{\pi/2}X_{-\pi/2}$, $X_{-\pi/2}X_{-\pi/2}$, $Y_{\pi/2}X_{-\pi/2}$, $Y_{-\pi/2}X_{-\pi/2}$, $IY_{\pi/2}$, $X_\pi Y_{\pi/2}$, $X_{\pi/2}Y_{\pi/2}$, $X_{-\pi/2}Y_{\pi/2}$, $Y_{\pi/2}Y_{\pi/2}$, $Y_{-\pi/2}Y_{\pi/2}$, $IY_{-\pi/2}$, $X_\pi Y_{-\pi/2}$, $X_{\pi/2}Y_{-\pi/2}$, $X_{-\pi/2}Y_{-\pi/2}$, $Y_{\pi/2}Y_{-\pi/2}$, $Y_{-\pi/2}Y_{-\pi/2}$

Table 4.1: Preparation and tomography pulses used for two-qubit quantum process tomography. The first letter refers to the rotation axis and the subscript is the rotation angle. I is the identity. We prepare $d^2 = 16$ input states (where $d = 4$ is the dimension of the Hilbert space). An overcomplete set of 36 pulses is used for the state tomography – combined with a maximum likelihood estimation – to reduce the sensitivity of our tomography to pulse imperfections.

are linearly independent of each other. Therefore the Pauli matrices form the basis for any complex $d \times d$ matrices. This naturally applies to any density state ρ and it can be written as a linear superposition of the Pauli matrices

$$\rho = \frac{1}{2^n} \sum m_{v_1,v_2\cdots v_n} (\sigma_{v_1} \otimes \sigma_{v_2} \otimes \cdots \otimes \sigma_{v_n}) \tag{4.2}$$

with coefficients $m_{v_1,v_2\cdots v_n} = \mathrm{tr}(\sigma_{v_1} \otimes \sigma_{v_2} \otimes \cdots \otimes \sigma_{v_n}\rho)$. For example, a single qubit density matrix is

$$\rho = \frac{1}{2}(I + \mathrm{tr}(X\rho)X + \mathrm{tr}(Y\rho)Y + \mathrm{tr}(Z\rho)Z). \tag{4.3}$$

Here we used the fact that ρ is Hermitian with trace one and there are only three independent real parameters, corresponding to the three Bloch vector coordinates. Similarly, a two-qubit density matrix can be described by 15 independent real parameters. One can definitely write it in terms of the summation of 16 Pauli matrices. Alternatively, we parameterize the density matrix with 16 real parameters as $\rho = \mathcal{T}^\dagger\mathcal{T}/\mathrm{Tr}(\mathcal{T}^\dagger\mathcal{T})$, where $\mathcal{T}$ is a lower

triangular matrix given by

$$\mathcal{T} = \begin{pmatrix} t_1 & 0 & 0 & 0 \\ t_5 + it_6 & t_2 & 0 & 0 \\ t_{11} + it_{12} & t_7 + it_8 & t_3 & 0 \\ t_{15} + it_{16} & t_{13} + it_{14} & t_9 + it_{10} & t_4 \end{pmatrix}. \tag{4.4}$$

This Cholesky decomposition ensures that ρ corresponds to a physical quantum state (see Appendix F of Ref. [134]). Even though we introduced an extra redundant degree of freedom for a more concise representation, it turns out that they can still be handled well in numerical optimizations.

To do QST on a two-qubit joint state, the density matrix of is reconstructed by maximizing the likelihood of a list of 36 measurements obtained by applying the tomography pulses given in Table 4.1. The Maximum Likelihood Estimation (MLE) technique [135] searches the space of density matrices to find the one that is the most likely to reproduce the observations. To calculate the expected output signal for an arbitrary density matrix, we first calibrate the measurement operator

$$M = \beta_{II}\sigma_I \otimes \sigma_I + \beta_{IZ}\sigma_I \otimes \sigma_z + \beta_{ZI}\sigma_z \otimes \sigma_I + \beta_{ZZ}\sigma_z \otimes \sigma_z \tag{4.5}$$

where β_{ij} are complex coefficients. β_{ij} are measured by applying the pulses $\{I, X_\pi\}^{\otimes 2} = \{II, IX_\pi, X_\pi I, X_\pi X_\pi\}$ to the initial state before measuring the output signal, taking into account the initial state effective temperature from the single-shot measurement. After calibrating the measurement operator, we can predict the output signal for a state ρ after any of the 36 tomography pulses. The state ρ is then obtained by maximizing the likelihood of the 36 output measurements over the 16 parameters of $\mathcal{T}$. Here we did not do single-shot readout to directly measure the population in each of the 36 measurements and measured the averaged value $\mathrm{tr}(M\rho)$ instead, simply because fore our data acquisition setup, it is faster than demodulating each recorded trace and fitting the single-shot histograms.

Process matrix

The χ matrix representation is defined as follows. For any quantum process $\mathcal{E}$ acting on a density matrix ρ, the final density matrix can be written as a superposition of basis operators $\tilde{E}_n$ acting on ρ

$$\rho_{\text{final}} = \mathcal{E}(\rho) = \sum_{mn} \tilde{E}_m \rho \tilde{E}_n^\dagger \chi_{mn}. \tag{4.6}$$

The operator basis we choose is $\{\sigma_I/\sqrt{2}, \sigma_x/\sqrt{2}, \sigma_y/\sqrt{2}, \sigma_z/\sqrt{2}\}^{\otimes n}$. χ is a $d^2 \times d^2$ complex matrix containing $d^4 - d^2$ independent real parameters required by the density matrix properties. To calculate χ matrix, we first prepare d^2 linearly independent density matrices that automatically form the basis for any density matrix. When we apply $\mathcal{E}$ to one of these density matrix ρ_j, the final state can be written with the basis

$$\mathcal{E}(\rho_j) = \sum_k \lambda_{jk}\rho_k. \tag{4.7}$$

The density matrix basis is prepared by applying the preparation pulses in Table 4.1. In the experiment, the final state $\mathcal{E}(\rho_j)$ is obtained with QST. It is worth mentioning that the density matrices are not orthogonal to each other (and actually they can be mixed states). The coefficients λ_{jk} can not be directly calculated with $\mathrm{tr}(\mathcal{E}(\rho_j)\rho_k)$ like what we do with the Pauli matrix basis. One need to first calculate the Gram matrix

$$G = \begin{pmatrix} \mathrm{tr}(\rho_1\rho_1) & \dots & \mathrm{tr}(\rho_{d^2}\rho_1) \\ \vdots & \ddots & \vdots \\ \mathrm{tr}(\rho_1\rho_{d^2}) & \dots & \mathrm{tr}(\rho_{d^2}\rho_{d^2}) \end{pmatrix}. \tag{4.8}$$

The coefficients can be calculated by

$$\begin{pmatrix} \lambda_{j1} \\ \vdots \\ \lambda_{jd^2} \end{pmatrix} = G^{-1} \begin{pmatrix} \mathrm{tr}(\mathcal{E}(\rho_j)\rho_1) \\ \vdots \\ \mathrm{tr}(\mathcal{E}(\rho_j)\rho_{d^2}) \end{pmatrix}. \tag{4.9}$$

On the other hand, the right hand side of Eq. 4.6 can be written as

$$\tilde{E}_m\rho_j\tilde{E}_n^\dagger = \sum_k \beta_{jk}^{mn}\rho_k, \tag{4.10}$$

which can be calculated theoretically. Combining Eq. 4.7 and Eq. 4.10, we have

$$\sum_{kmn} \chi_{mn}\beta_{jk}^{mn}\rho_k = \sum_k \lambda_{jk}\rho_k. \tag{4.11}$$

Because the expansion on the basis $\{\rho_k\}$ is unique, the coefficients should all equal

$$\sum_{mn} \beta_{jk}^{mn}\chi_{mn} = \lambda_{jk}. \tag{4.12}$$

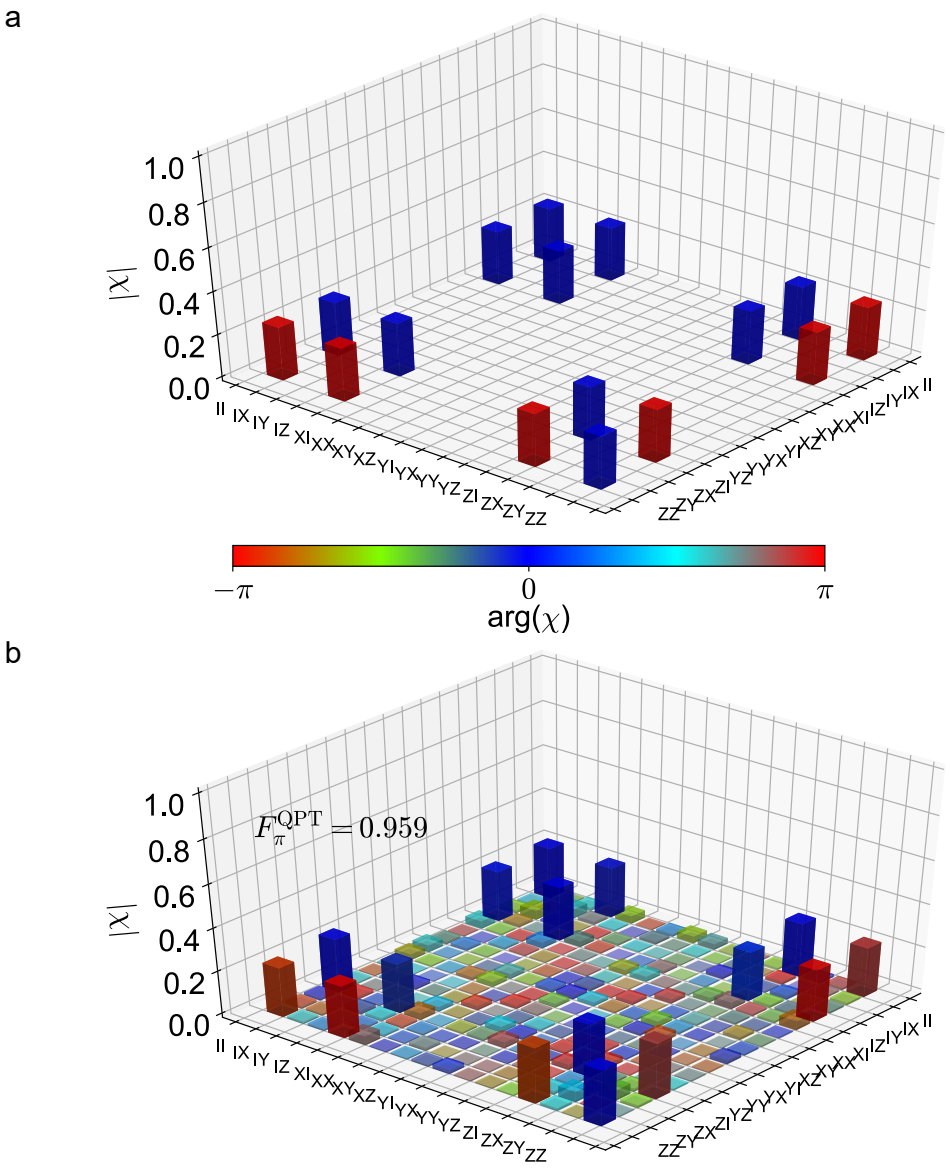

Figure 4.1: χ matrix in quantum process tomography of a CZ gate. (a) The χ matrix of a CZ gate in theory. The height of the histogram indicates the magnitude of the matrix element and the color indicates the phase. The non-zero elements only exist for II, IZ, ZI, ZZ indexes.(b) The measured χ matrix for the CZ gate introduced in Sec. 4.3.1. The fidelity calculated by comparing the χ matrix is 0.959.

Therefore the χ matrix is directly related to the measurement observables through the λ matrix. For convenience, we can reshape the matrix χ and λ to vectors and the tensor β to $d^4 \times d^4$ matrix

$$\beta\vec{\chi} = \vec{\lambda}. \tag{4.13}$$

Then it is straightforward to calculate the vector $\vec{\chi} = \alpha\vec{\lambda}$ with $\alpha = \beta^{-1}$ and reshape $\vec{\chi}$ back to its matrix form. In the case that β^{-1} does not exist, one can always find a generalized inverse α such that $\beta\alpha\beta = \beta$.

The ideal quantum process is described by a unitary operator

$$\mathcal{E}_{\text{ideal}}(\rho) = U\rho U^{\dagger}. \tag{4.14}$$

We can write the unitary operator U in terms of the operator basis $\{\tilde{E}_n\}$

$$U = \sum_n e_n \tilde{E}_n = (\tilde{E}_1, \tilde{E}_2, \cdots, \tilde{E}_{d^2}) \begin{pmatrix} e_1 \\ e_2 \\ \vdots \\ e_{d^2} \end{pmatrix}. \tag{4.15}$$

We can define $\vec{e} = (e_1, e_2, \ldots, e_{d^2})^T$ and the ideal process matrix is $\chi_{\text{ideal}} = \vec{e}\vec{e}^T$ from Eq. 4.6. The gate fidelity of the measured χ matrix [136] compared to χ_{ideal} is $F(\chi, \chi_{\text{ideal}}) = (\text{tr}(\chi^{\dagger}\chi_{\text{ideal}})d + 1)/(d + 1)$. Fig. 4.1 shows the χ matrix histogram of a CZ gate in Sec. 4.3.1 with fidelity 0.959. Additional process matrices χ of CPhase gates for control phases $\phi = \pi/16,\ \pi/8,\ \text{and}\ \pi/4$ are also measured. We found the QPT fidelity saturates around 0.978 due to SPAM errors and it is always lower than the fidelity from the cross-entropy benchmarking experiment.

4.1.2 Randomized benchmarking

Randomized benchmarking (RB) [137]–[140] is a standard technique to quantify the average fidelity of the gate inside the Clifford group [141]. Inspired by this idea, many other similar techniques are invented to focus on different types of fidelity measurements. As will introduced later, interleaved randomized benchmarking (IRB) is used to measure the fidelity of a specific Clifford gate. Purity benchmarking is to measure the average incoherent error of the Clifford group. Cross-entropy benchmarking is used to measure the fidelity of a non-Clifford gate.

There are 24 unique Clifford gates (up to a overall phase factor) in the single-qubit Clifford group. These gates describe any possible rotations between the six axial states (eigenvectors of the Pauli matrices) on the Bloch sphere. Depending on the pulses used in a experiment, the Clifford gate representation can be different as shown in Table 4.2. One can write Clifford gates using only X and Y rotations (including I). Or equivalently, each Clifford gate can be constructed with one X or Y rotations at most with Z rotations. A Clifford gate can have a different number of pulses (i.e. I, X, Y, or Z gates). On average, one Clifford gate has 1.875 pulses In the first representation and 1.833 pulses in the second representation. Two-qubit Clifford group is much larger and has 11520 gates. They fall into four categories: single-qubit based gates, CNOT-like gates, iSWAP-like gates, and SWAP-like gates. Likewise, they can have different representations. For example, one can use CZ gate and single-qubit X and Y rotations to construct the Clifford gates. In this case, it requires on average 1.5 CZ gates and 8.25 single qubit gates to build a two-qubit Clifford gate.

The pulse sequence for a standard RB is depicted as Fig. 4.2a. A series of randomly chosen Clifford gates C_i are applied to the qubit (the random number seed also changes with the sequence length m). From the mathematical properties of a group, we know that multiplying Clifford gates will still end up with a gate in the Clifford group and its inverse also exists in the Clifford group. Therefore we can apply a recovery gate C_r at the end to go back to the initial state. The whole process is equivalent to an identity gate ideally. Due to the gate errors accumulated in the sequence, the final state always deviates from the initial state. We can measure the final state population and average it over many different random Clifford sequence with the same sequence length. The sequence fidelity (sometimes people directly use the qubit population) follows the curve

$$F_{\text{seq}}(m) = Ap^m + B. \tag{4.16}$$

A and B absorb the SPAM errors and the error of the recovery gate. p is the depolarizing parameter that is related to the average error of a Clifford gate $r = (d-1)(1-p)/d$, where $d = 2^n$ is the Hilbert space dimension. The average error for each pulse in the Clifford gate is therefore $r_{\text{pulse}} = r/1.875$ for the left representation in Table 4.2. In the experiment, we fit the exponential decay curve with Eq. 4.16 and use the fitting error to calculate the error bar on the Clifford gate fidelity $F = 1 - r$ (or $1 - r_{\text{pulse}}$ for the fidelity of the pulse). It is obvious that by definition the above formalism can be directly applied to multi-qubit case.

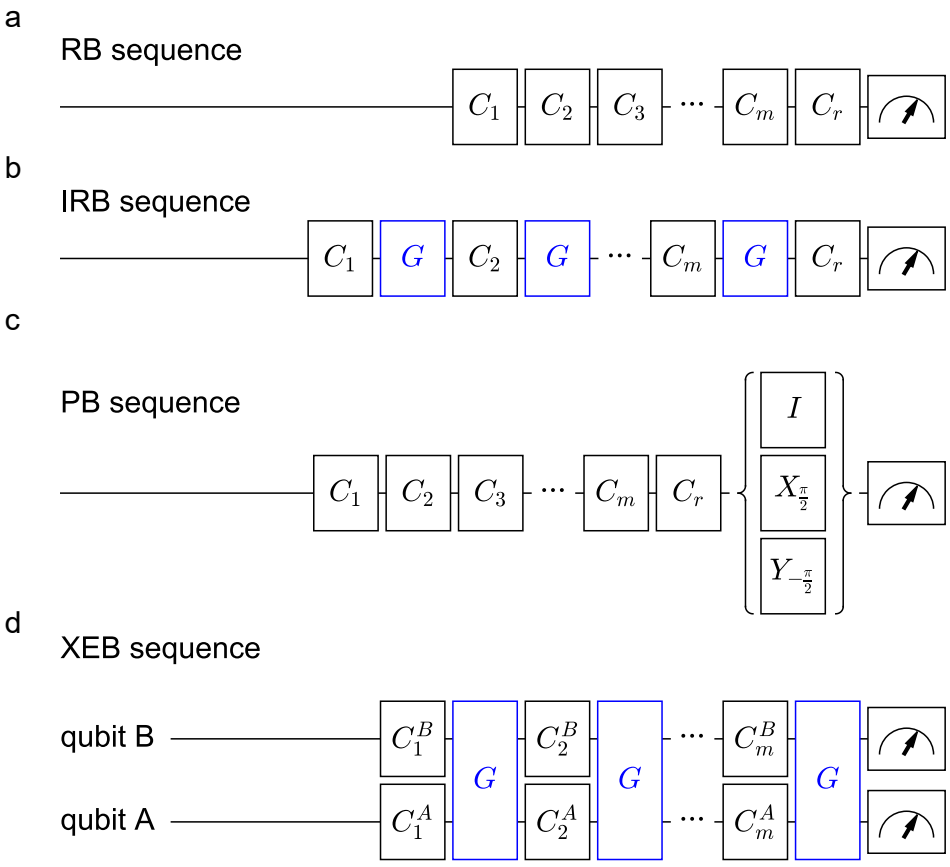

Figure 4.2: Different benchmarking techniques based on random Clifford gates. (a) Standard randomized benchmarking (RB) sequence. A random sequence of Clifford gates $\{C_1, C_2, \cdots, C_m\}$ is applied to the qubit and a recovery gate C_r is applied at the end to convert the qubit back to the initial state. (b) Interleaved randomized benchmarking (IRB) sequence. The test Clifford gate G is inserted after each random Clifford gate in the RB sequence. (c) Single-qubit purity benchmarking (PB) sequence. State tomography pulses are applied at the end of the RB sequence in order to measure the final state purity. (d) Two-qubit cross-entropy benchmarking (XEB) sequence. The sequence consists of m cycles, during which a random single qubit Clifford gate $[C_i^A, C_i^B]$ is applied to both qubits, followed by the test two-qubit gate G. Unlike IRB, the test gate G in XEB can be a non-Clifford gate.

Interleaved randomized benchmarking

If we insert a specific Clifford gate G after each Clifford gate C_i in the RB sequence (see Fig. 4.2b, now C_r needs to undo the sequence including G), we can measure the fidelity of G by comparing the depolarizing parameters from the RB measurement [140]. Let's denote the depolarizing parameter of the IRB measurement by p_G (the one of the RB measurement by p). The gate error of G is given by

$$r_G = \frac{(d-1)(1-p_G/p)}{d}, \tag{4.17}$$

and the gate fidelity is defined as $F_G = 1 - r_G$. One can also insert n repetitions of G into the sequence (G^n is still a Clifford gate). The total incoherent error increases linearly while the unitary error increases in a non-linear way [142]. We use this to demonstrate the CZ gate in Sec. 4.3.2 is limited by decoherence.

Purity benchmarking

To evaluate the average incoherent error of a Clifford gate, one can add tomography pulses at the end of the RB sequence (Fig. 4.2c) to measure the purity of the final states, which is called purity benchmarking (PB) [125], [143]. Gate errors such as misrotations do not change the state purity while decoherence errors do. The purity is defined by $P = \mathrm{tr}(\rho^2)$. It can be normalized so that it ranges from 0 to 1

$$P_{\mathrm{normalized}} = \frac{d}{d-1}\left(P - \frac{1}{d}\right). \tag{4.18}$$

For a single qubit, $P_{\mathrm{normalized}} = \langle\sigma_x\rangle^2 + \langle\sigma_y\rangle^2 + \langle\sigma_z\rangle^2$, which can be directly measured with the three tomography pulses in Fig. 4.2c. One can repeat the same RB sequence with different tomography pulses, calculate the purity, and then average the purity for different random sequences. The purity decays as

$$P_{\mathrm{normalized}}(m) = Au^m + B. \tag{4.19}$$

u is the unitarity. The incoherent error of a Clifford gate on average is

$$r_{\mathrm{incoherent}} = \frac{d-1}{d}(1-\sqrt{u}). \tag{4.20}$$

Cross-entropy benchmarking

Non-Clifford two-qubit gate is a helpful tool to construct a universal gate set for arbitrary unitary operations. Non-Clifford gates can not be evaluated with traditional IRB techniques because it is hard to build a recovery gate for every random sequence. In recent years, cross-entropy benchmarking technique [3], [109], [144], [145] (XEB) was implemented as a universal approach to benchmark non-Clifford gates. Fig. 4.2d shows the pulse sequence for a two-qubit XEB sequence. It is similar to the IRB sequence in the sense that it consists of m cycles. In each cycle, we apply random single-qubit Clifford gates to the two qubits individually, followed by the non-Clifford gate G. At the end of the sequence, instead of applying a recovery gate like what we do in IRB, we directly measure the population distribution of the two qubits $\{p_{00,i}, p_{01,i}, p_{10,i}, p_{11,i}\}$, where $i = 1, 2, \cdots, l$ is the random sequence index. Combining the l distributions into one, we have

$$P_{\text{measured}} = \{p_j\} = \{\frac{p_{00,1}}{l}, \frac{p_{01,1}}{l}, \frac{p_{10,1}}{l}, \frac{p_{11,1}}{l}, \frac{p_{00,2}}{l}, \frac{p_{01,2}}{l}, \frac{p_{10,2}}{l}, \frac{p_{11,2}}{l}, \cdots, \frac{p_{00,l}}{l}, \frac{p_{01,l}}{l}, \frac{p_{10,l}}{l}, \frac{p_{11,l}}{l}\}, \quad (4.21)$$

and $\sum_j^{4l} p_j = 1$. On the other hand, we can calculate the probability distribution $P_{\text{expected}} = \{q_j\}$ in theory with the knowledge of the composition of each random sequence. We can use cross-entropy to quantify the 'distance' between these two distributions

$$S(P_{\text{measured}}, P_{\text{expected}}) = -\sum_j^{4l} p_j \log q_j \quad (4.22)$$

The cross-entropy is minimized when the two distributions are identical. The sequence fidelity can be therefore defined as

$$F_{\text{XEB}} = \frac{S(P_{\text{incoherent}}, P_{\text{expected}}) - S(P_{\text{measured}}, P_{\text{expected}})}{S(P_{\text{incoherent}}, P_{\text{expected}}) - S(P_{\text{expected}}, P_{\text{expected}})}, \quad (4.23)$$

where $P_{\text{incoherent}} = \{1/(4l), 1/(4l), \cdots, 1/(4l)\}$ is the maximally incoherent mixture. When the measured distribution agrees with the expected one, $F_{\text{XEB}} = 1$. When the final states are maximally mixed states, $F_{\text{XEB}} = 0$. By fitting the sequence fidelity versus number of cycles with $F_{\text{XEB}} = Ap^m + B$, the Pauli error per cycle r_{cycle}^P is given by

$$r_{\text{cycle}} = \frac{d-1}{d}(1-p) \quad (4.24)$$

$$r_{\text{cycle}}^P = \frac{d+1}{d} r_{\text{cycle}} \quad (4.25)$$

Then we extract the non-Clifford gate Pauli error r_{G}^P from the equation $(1 - r_{\mathrm{cycle}}^P) = (1 - r_A^P)(1 - r_B^P)(1 - r_{\mathrm{G}}^P)$, where $r_A^P,\ r_B^P$ are the average single-qubit Pauli error measured from the simultaneous RB experiment on the two qubits. The gate fidelity of G is calculated by converting Pauli error back to the gate error r_{G}. Even though XEB is claimed to be able to evade the SPAM errors, a readout error on the order of 10 % coming from non-QNDness still needs to be calibrated out in order to get a reasonable single exponential decaying curve of F_{XEB}.

4.2 Single-qubit Gates

In this section, we are going to show how to perform single-qubit gates, i.e. the $X, Y,$ and Z gates, with microwaves. We will discuss two different scenarios – on-resonance driving and off-resonance driving. In our experiment, we also studied qubit control crosstalk which can be a notable issue for single-qubit gates across a multi-qubit device.

4.2.1 X and Y gates

We can consider a simple spin model in the lab frame

$$H^{\mathrm{lab}} = -\frac{\omega_q}{2}\sigma_z + \frac{\Omega}{2}\cos(\omega_d t + \varphi_d)\sigma_x. \tag{4.26}$$

The second time-dependent term in the Hamiltonian is a classical driving term. For the $0 - 1$ transition of a fluxonium, the drive strength Ω is proportional to the electric field amplitude at the qubit and the fluxonium matrix element $|\langle 0| n |1\rangle|$. In order to obtain an analytical solution, we go into a rotating frame with frequency ω_d and initial phase φ_d for a time-independent Hamiltonian. If we denote the state in the lab frame by $|\psi^{\mathrm{lab}}\rangle$, it becomes $|\psi^{\mathrm{RWA}}\rangle = U^\dagger |\psi^{\mathrm{lab}}\rangle$ in the rotating frame. The transformation operator $U = \exp(-iOt)$, where $O = -\omega_d\sigma_z/2$ is on resonance with the drive. In the rotating frame, the Hamiltonian transforms as

$$H^{\mathrm{RWA}} = U^\dagger H^{\mathrm{lab}} U - iU^\dagger \partial_t U. \tag{4.27}$$

Then we can apply the rotating wave approximation (RWA) to keep the co-rotating term and neglect the counter-rotating term. One can think of the counter-rotating term as a drive with a large detuning $\omega_d + \omega_q \gg \Omega$. As we will demonstrate later, large detuning drive barely changes the qubit population but it can shift the qubit frequency. With RWA,

the Hamiltonian is now time-independent

$$H^{\mathrm{RWA}} = -\frac{\delta}{2}\sigma_z + \frac{\Omega}{2}\cos\varphi_d\sigma_x - \frac{\Omega}{2}\sin\varphi_d\sigma_y. \tag{4.28}$$

$\delta = \omega_q - \omega_d$ is the detuning of the drive. Because there is a degree of freedom on choosing which direction of the x axis on a 2D plane, we can offset the qubit phase by applying a unitary operator $U_\varphi = \exp(i\varphi\sigma_z/2)$ to the system, so that $|\psi^{\mathrm{RWA}}\rangle \rightarrow U_\varphi^\dagger |\psi^{\mathrm{RWA}}\rangle$ and the Hamiltonian becomes

$$H^{\mathrm{RWA}} = -\frac{\delta}{2}\sigma_z + \frac{\Omega}{2}\cos(\varphi_d - \varphi)\sigma_x - \frac{\Omega}{2}\sin(\varphi_d - \varphi)\sigma_y. \tag{4.29}$$

We can choose $\varphi = \varphi_d$ and the drive only involves the σ_x term

$$H^{\mathrm{RWA}} = -\frac{\delta}{2}\sigma_z + \frac{\Omega}{2}\sigma_x. \tag{4.30}$$

When the drive is on resonance, $\delta = 0$. The Bloch sphere does not spin anymore and the qubit evolution is purely an X rotation that is described by

$$U_X = \exp(-i\frac{\theta_X}{2}\sigma_x), \tag{4.31}$$

where $\theta_X = \Omega t$. For example, the gate X_π corresponds to $\theta_X = \pi$ (note that it is not $\theta_X/2 = \pi$), which is a π pulse on the qubit. $X_{2\pi}$ is equivalent to an identity gate in qubit systems because it only brings an overall phase factor to the state. One can realize a Y rotation by changing the phase of the drive to $\varphi_d - \pi/2$ while using the same phase offset $\varphi = \varphi_d$ in Eq. 4.29.

In a typical experiment, the pulses sequences are sent to the device continuously and each sequence contains its own initialization pulse and readout pulse. It is more convenient to treat each sequence as an independent measurement and set the time origin at the beginning of that sequence. However, the microwave generated from the RF source is continuous, meaning that the microwave phase offset ϕ_d may be different for two successive sequences. For example, let's assume the sequence length is T and the phase offset of the first sequence is $\phi_{d,0}$. Hence the phase offset of the second sequence is $\phi_{d,1} = \phi_{d,0} + \omega_d T$. To prevent an X gate in one sequence becomes a Y gate in another sequence, we need to keep in mind that we need to re-define the x axis of the Bloch sphere in each sequence, so that $\varphi = \varphi_d$ is satisfied in Eq. 4.29. This will be important when we come to Sec. 4.3.3.

4.2.2 ac Stark shift and virtual Z gates

The Z rotation can be trickier than the X and Y rotations. We have to keep in mind that we eventually need to work in the rotating frame on resonance with the qubit. We can not just do nothing and wait because the qubit does not spin around the z axis in this frame. The Z gates can be straightforward with the use of a flux pulse which can change the qubit frequency for some time to acquire a Z phase. But this is at the cost of leaving the flux sweet spot which is not the optimal solution. In fact, there are multiple ways to implement Z gates using only microwaves. In practice, the virtual Z gate [146] works the best in our experiment. But before introducing this technique, let's look at the other approaches which are helpful to understand qubit dynamics.

One way to realize a Z rotation is through off-resonance driving. The qubit subjected to Eq. 4.30 rotates on the Bloch sphere around the axis $\vec{n} = (-\delta/2, \Omega/2, 0)$ and the effective Rabi frequency is

$$\Omega_{\text{eff}} = \sqrt{\delta^2 + \Omega^2}, \tag{4.32}$$

meaning that after $t_{2\pi} = 2\pi/\Omega_{\text{eff}}$, the qubit finishes one cycle on the Bloch sphere and returns to its starting point with an overall phase. Therefore the evolution operator in this frame is an identity U_I.

Now we can transform U_I to the on-resonance rotating frame. First, let's define $U_\delta(t) = \exp(i\omega_d t\sigma_z/2)$ is the transformation operator from the lab frame to the off-resonance frame and $U_0(t) = \exp(i\omega_q t\sigma_z/2)$ is from the lab frame to the on-resonance frame. Assuming the evolution begins at t_1 and ends at $t_2 = t_1 + t_{2\pi}$ So the evolution operator in the on-resonance frame is

$$U = U_0^\dagger(t_2)U_\delta(t_2)U_I U_\delta^\dagger(t_1)U_0(t_1) = \exp(-i\frac{\theta_Z}{2}\sigma_z), \tag{4.33}$$

where $\theta_Z = \delta t_{2\pi}$ is picked up due to the different rotating speeds of the two frames.

If we fix the drive strength and increase the detuning such that $\delta \gg \Omega > 0$, the rotation axis of the Rabi oscillation $\vec{n}$ becomes close to the $-z$ axis. We can consider that one cycle acquires a Z phase of -2π (the sign is crucial here). Because the effective Rabi frequency is fast, we can wait for n cycles to accumulate the Z phase $\theta_Z = n\delta t_{2\pi} - 2n\pi$. The average accumulation rate is

$$\bar{\omega_Z} = \frac{\theta_Z}{n t_{2\pi}} = \delta - \sqrt{\delta^2 + \Omega^2}. \tag{4.34}$$

Actually in this large detuning regime, it is not necessary to completely go back to the starting point in the off-resonance frame because it will only lead to a tiny error due to a little bit of X rotation. In this case, the external microwave drive can keep adding Z phase to the qubit as if the qubit frequency is shifted. Indeed, this can be understood with the dressed state approach and the energy difference between the dressed states and the bare states is the ac Stark shift.

We can diagonalize the Hamiltonian Eq. 4.30

$$H_{\text{dressed}} = -\text{sign}(\delta)\frac{\sqrt{\delta^2+\Omega^2}}{2}\sigma_z = -\frac{\delta+\Delta\omega}{2}\sigma_z. \tag{4.35}$$

The ac Stark shift (i.e. the qubit frequency change) is $\Delta\omega = \text{sign}(\delta)\sqrt{\delta^2+\Omega^2}-\delta$. When the drive is red-detuned $\delta = \omega_q - \omega_d > 0$, $\Delta\omega > 0$ indicating the $|0\rangle$ state energy is pushed down and the $|1\rangle$ state energy is pushed up by $|\Delta\omega|/2$, i.e. the transition is 'distended'. When the drive is blue-detuned, the energy levels go to the opposite direction and the transition is 'squeezed'. We denote the dressed eigenstates by $|0'\rangle$ and $|1'\rangle$. One can prove that they are actually located on the rotating axis $\vec{n}$.

When we apply the far-detuned drive $|\delta| \gg \Omega$, we can approximate the original qubit state $|\psi\rangle = \alpha|0\rangle + \beta|1\rangle$ as $|\psi\rangle = \alpha|0'\rangle + \beta|1'\rangle$ in the off-resonance frame, because $|i'\rangle \approx |i\rangle$. That's why we can use the qubit frequency shift to describe the unitary evolution

$$U_Z = \exp(-i(-\frac{\Delta\omega}{2})\sigma_z), \tag{4.36}$$

which is consistent with our previous calculation for the evolution of multiple cycles on the Bloch sphere.

The ac Stark shift picture is straightforward when we are thinking of the accumulated Z rotations with an off-resonant drive. However, it seems it only works at a large detuning, because otherwise we can not have $|i'\rangle \approx |i\rangle$ and the bare states $|i\rangle$ will keep rotating around the axis $\vec{n}$. Fortunately, this issue can be addressed with adiabatic pulses. A process is adiabatic when the Hamiltonian changes slow enough so that the bare eigenstates can follow the evolution of the instantaneous dressed eigenstates. That is, if $H(t)$ changes slowly with time, the eigenstates $|i(0)\rangle$ of $H(0)$ evolve as $|i(t)\rangle$ up to a phase factor, where $|i(t)\rangle$ is the instantaneous eigenstates of $H(t)$. This idea was implemented in flux pulses [107] which tune the repulsion between two coupled states. We can use the same Hamiltonian of

Eq. 4.30 to describe the two levels

$$H(t) = -\frac{\delta(t)}{2}\sigma_z + \frac{\Omega}{2}\sigma_x \tag{4.37}$$

and assume $\delta = \delta(t)$ changes with flux. The population that does not follow the dressed state is

$$P_{\text{lost}} = \exp(-\frac{\pi\Omega^2}{2|\partial_t\delta|}), \tag{4.38}$$

which is called the Landau-Zener tunnel probability [147]. The adiabatic condition is satisfied when $P_{\text{lost}} \ll 1$, indicating that $|\partial_t\delta| \ll \Omega^2$. For microwave pulses, we can fix δ and change the pulse amplitude over time $\Omega = \Omega(t)$. Similarly, we can have the adiabatic condition for microwave pulses is

$$|\partial_t\Omega| \ll \delta^2. \tag{4.39}$$

As long as Eq. 4.39 is satisfied, the initial eigenstates will follow the rotating axis $\vec{n}$ as it slowly travels away from the z axis with increasing pulse amplitude and comes back when the pulse is slowly turned off. In this case, we can safely use ac Stark shift to describe this process even if $|\delta| \sim \Omega$ without worrying about the σ_x error. The adiabatic pulse can be understood in the frequency domain. We can take a Gaussian pulse for example. Assume the pulse has a width of 2σ in time domain, its Fourier transform is also Gaussian with a width of $1/(2\sigma)$. If the pulse changes slowly with time, σ is large and its Fourier spectrum is sharp so that there is less frequency component on the qubit transition that has a detuning δ away from the Gaussian center.

One can immediately point out the disadvantage of an adiabatic pulse which is that it requires a long time to finish such an operation. Again We can take the Gaussian pulse for example to do a rough estimation. Assume the pulse has a width of 2σ and amplitude of Ω_m that is on the same order of magnitude with the detuning $\Omega_m \sim \delta$. Therefore $\partial_t\Omega(t) \sim \Omega_m/\sigma$ and Eq. 4.39 leads to $\sigma \gg \Omega_m/\delta^2 \sim 1/\delta$. If $\delta/(2\pi)$ is on the order of 10 MHz, the width of the pulse needs to be much larger than 100 ns, which is definitely too long for a single qubit gate. To mitigate this problem, we can leverage the pulse-shaping techniques such as the Derivative Removal by Adiabatic Gate (DRAG) [148]–[150]. The basic idea is to add an auxiliary pulse on the other quadrature (i.e. through σ_y) with an amplitude that is proportional to $\partial_t\Omega(t)/\delta$, which reduce the Fourier spectrum near the transition. With this technique, the pulse can be faster while maintaining part of the adiabaticity. In fact, DRAG

was originally proposed to suppress the leakage to the higher levels in transmon systems. This is because the anharmonicity of transmon is on the order of 100 MHz. If a pulse with $\Omega = 50$ MHz with a duration of 10 ns is applied to the $0-1$ transition, the $1-2$ transition will also be off-resonantly driven, which is inevitable. Therefore adiabaticity is required to make sure the population can come back to the computational states.

Another way to realize a Z gate is to use a combination of X and Y gates. As demonstrated in Table 4.2, the Clifford group can be constructed using X and Y rotations. For example,

$$Y_\pi \cdot X_\pi = Z_\pi, \tag{4.40}$$

$$X_{-\pi/2} \cdot Y_{\pi/2} \cdot X_{\pi/2} = Z_{-\pi/2}, \tag{4.41}$$

$$X_{-\pi/2} \cdot Y_{-\pi/2} \cdot X_{\pi/2} = Z_{\pi/2}. \tag{4.42}$$

The errors of these Z gates are the summation of the corresponding X and Y gate errors. The consequence is that the Z gate is always much worse than the X and Y gates.

Finally, we are going to introduce the optimal realization of Z gates for our experiments – the virtual Z gate. When we want to perform a Z gate, intuitively we will rotate the Bloch sphere around the z axis by applying certain pulses. One just need to realize that rotating the Bloch sphere is equivalent to rotating the x and y axes in the opposite direction and the solution is going to be much simpler. Whenever we perform a Z gate, we only need to redefine the directions of the x and y axes conceptually without changing the qubit physically. That is why it is called the virtual Z gate, as it happens instantly on the software level. As we derived in Sec. 4.2.1, the X gate is defined after we choose the direction of the x axis by setting $\varphi = \varphi_d$ in Eq. 4.29. Hence the same microwave pulse can be a Y rotation if we set $\varphi = \varphi_d - \pi/2$, and a Y pulse becomes an X pulse in with the new definition.

For example, let's say we want to apply a sequence as $X_\pi \cdot Z_{\pi/2} \cdot X_\pi \cdot Y_\pi$. The first X_π pulse is applied with the drive phase φ_d (meaning that $\varphi = \varphi_d$). The virtual $Z_{\pi/2}$ gate changes the axis definition and now $\varphi = \varphi_d - \pi/2$, which is memorized by the pulse sequence compiling program. Therefore when we apply the second X_π pulse, we need to change the drive phase to be $\varphi_d + \pi/2$, which is a $Y_{-\pi}$ pulse in the original definition. For the last Y_π pulse, the drive phase should be φ_d, which is a X_π pulse in the original definition. In the end, the sequence will just look like $X_\pi \cdot Y_{-\pi} \cdot X_\pi$ in the original definition. Other arbitrary virtual Z rotation angles can be implemented in the same way. Unlike a physical Z pulse, the virtual Z gate affects the definition of all the X and Y types of gate (including the two-qubit gates with X or Y terms) after it in the sequence, while the Z type of gates are not affected (such as CPhase gates). Thus the program needs to keep track of the virtual rotation angles

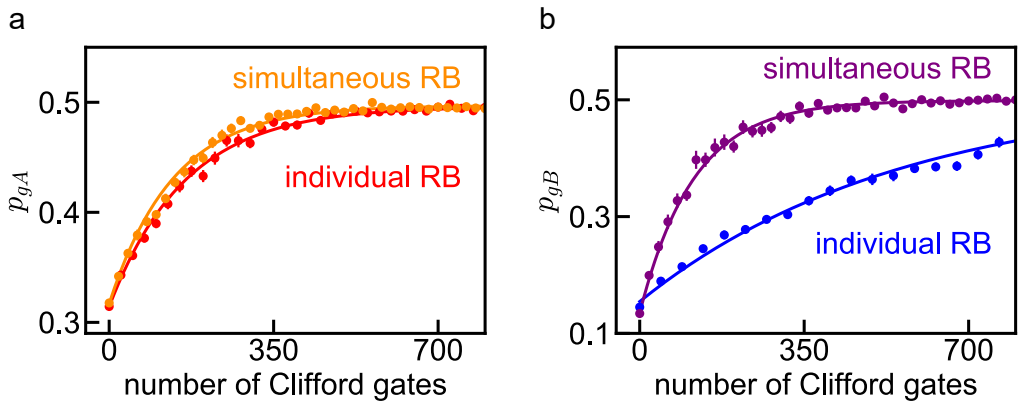

Figure 4.3: Single-qubit gate RB for a two-qubit device. (a) Ground state population of qubit A and (b) population of qubit B as a function of the sequence length. A list of 51 randomly chosen sequence of Clifford gates are applied to the individually or simultaneously to the qubits before applying a recovery gate. The average single qubit fidelity for qubit A (resp. qubit B) for a gate duration of 45 ns (resp. 26 ns) is $(99.69 \pm 0.01)\%$ (resp. $(99.91 \pm 0.003)\%$) in the individual case and $(99.63 \pm 0.01)\%$ (resp. $(99.57 \pm 0.01)\%$) in the simultaneous case. The duration of a simultaneous operation is given by the longest gate time (gate time of qubit A or gate time of qubit B if a zero-duration pulse is applied to A). Taken this into account, the residue error on qubit B comes from cross-talk

throughout the sequence in order to assign the correct phase to the microwave pulses.

Because the virtual Z gate has zero duration, it is almost immune to decoherence just like identity gate, except for the case where qubit A is applied with an X or Y gate and qubit B applied with a virtual Z gate needs to wait for A to finish. The major error for the virtual Z gate comes from the imperfect microwave IQ mixing, which is negligible compared to other gate errors as long as the IQ mixer is working at the correct parameter range. So the virtual Z gate is almost as perfect as the identity gate in our experiment with fidelity close to 1. What's more, the virtual Z gate is highly flexible with arbitrary phases and they are equally simple to implement. It outperforms all the other realizations of Z gates in every aspect and becomes our optimal option. This is the reason that we chose the second representation of single-qubit Clifford group in Table 4.2 when benchmarking the gates. However, this does not mean the ac Stark shift is not an important effect. As we will introduce in the rest of this chapter, it can still play a major role in cross-talk and two-qubit gates.

4.2.3 Cross-talk

The cross-talk between single-qubit gates on different qubits can be classified as quantum cross-talk and classical cross-talk [123], [151]–[153]. Quantum cross-talk refers to the entangling operators between the qubits. It can be the static ZZ interaction or the cross-resonance ZX terms in the presence of the drive. We will come back to them in Sec. 4.3. Classical cross-talk, on the contrary, is manifested as IX or IZ types of terms that do not create entanglement. This usually happens when the control signal on one qubit drive line leaks to other qubit drive lines through the mutual capacitance or inductance. In this case, two remote qubits can be affected by each other's control signal if their control lines are too close somewhere on the device. The classical cross-talk can also happen when the electromagnetic field generated by the drive line on one qubit is not localized enough in space, such that it is sensed by other nearby qubits. The latter case is especially significant in a 3D architecture. This type of leakage is small, but can contribute to an error on the order of 0.001 to the single-qubit gates. One can partly solve this problem by increase the detuning between the qubits, such that the X types of misrotations are converted to the Z type of error described by the ac Stark shift, which can be also suppressed with large detuning. But as the number of qubit increases, this can potentially lead to the problem of frequency. One can also apply corrections to the single-qubit pulses. For example, when applying a X gate on qubit A, we can apply a weak Z rotation simultaneously on qubit B to cancel out the ac Stark shift (this does not work with the virtual Z gate if qubit B is applied with X or Y rotations at the same time). This approach can be tedious with a large number of qubits. A clever way to address the classical cross-talk is to eliminate it on the hardware level through ground plane shielding with airbridges [3], [154], [155].

In our experiment, we characterized cross-talk between two qubits by performing single-qubit RB on each qubit – individually and simultaneously. Z rotations are performed with virtual Z gates. Therefore, our Z rotations and identity gates have a zero duration. In the individual single-qubit RB sequence, one Clifford gate contains on average 0.83 physical pulses. As shown in Fig. 4.3, the average individual single-qubit fidelity is $(99.69 \pm 0.01)\%$ for qubit A with 45 ns-long pulses and $(99.91 \pm 0.003)\%$ for qubit B with 26 ns-long pulses.

In our simultaneous RB sequence, there is a possible idle time for one qubit when the other qubit is rotated on the Bloch sphere. So the simultaneous RB sequence is longer than the individual RB sequences with the same number of Clifford gates. The change of fidelity when operating the qubits simultaneously cannot be directly associated to cross-talks but can be thought of as an upper bound of the cross-talk. With such sequences, the simultaneous single qubit fidelity is $(99.63 \pm 0.01)\%$ for qubit A and $(99.57 \pm 0.01)\%$ for qubit

B. Because qubit A has longer pulses than qubit B, the change of qubit A fidelity should be closer to the cross-talk error, which is still quite small compared to the other errors such as incoherent error.

By assigning the same sequence length to the individual RB and simultaneous RB, one can quantify the cross-talk (or addressability) following the procedure described in [156]. Even though this condition is not satisfied in our measurement, we can still measure the correlations in the errors by examining $\delta p = p_{12} - p_{1|2}p_{2|1}$. The depolarizing parameter $p_{1|2}$ is obtained by fitting qubit A population $p_{10} + p_{11}$ in the simultaneous RB and p_{12} is from fitting $p_{00} + p_{11}$. The correlation is $\delta p = (0.11 \pm 0.05)\%$ from our measurements.

4.3 Two-qubit Gates

As we mentioned at the beginning of this chapter, entanglement is essential for quantum speedup. However, it is not a sufficient condition. According to Gottesman–Knill theorem, a circuit consisting of only Clifford gates can be perfectly simulated within polynomial time on a classical computer. Therefore a truely powerful quantum computer should be able to execute a universal gate set, which can construct any unitary operations. This means eventually we need to be able to perform all kinds of non-Clifford gate with the finite number of gates that we can physically implemented. For example, a standard set of universal gates contains the Hadamard gate, phase gate, CNOT gate, and the $\pi/8$ gates. One would need two or more of these gates to construct a specific two-qubit gate needed in an algorithm, such as a CPhase gate required in the Shor's algorithm. This type of composite gate will have an error worse than its components. Therefore, it will be quite beneficial if we have direct access to different types of two-qubit gate from the hardware level. In this way, we can expand the toolbox of the fundamental gates and create shortcuts in a real algorithm.

In this section, we are going to discuss the realization of several microwave two-qubit gate schemes for capacitively coupled fluxoniums, including non-Clifford gate sets. As we will illustrate, entanglement can be either created with the high energy transitions (off-resonance CPhase gate and the near-resonance CZ gate) or using only computational states (off-resonance CPhase gate, bSWAP gate, and the cross-resonance gate).

4.3.1 Off-resonance CPhase gate

An arbitrary control-phase (CPhase) gate can be realized by inducing ZZ interaction with an external microwave drive. Here we are going to introduce two experiments. In one experiment, we leveraged the high energy transitions. In the other experiment, we only

utilized the computatonal states.

For the first experiment, qubit A (B) has a frequency $f_A = 217.2$ MHz ($f_B = 488.9$ MHz). While the qubit lifetimes are above $100\ \mu$s, the Ramsey coherence times are in the $10-14\ \mu s$ interval, limited by insufficient thermalization of the measurement lines. The relevant part of the measured two-qubit spectrum is shown in Fig. 4.4a. The simulated quantity $\Omega_{kl-k'l'}$ attached to every transition is the Rabi frequency that would be induced by a resonant drive with the same amplitude for all transitions. The computational states $|00\rangle$, $|10\rangle$, $|01\rangle$, and $|11\rangle$ are separated in energy from non-computational states by at least a few GHz, which exceeds the qubit frequencies by almost an order of magnitude. Within the computational subspace, the two-qubit dynamics obeys the Hamiltonian

$$H = f_A \frac{ZI}{2} + f_B \frac{IZ}{2} + \xi_{ZZ} \frac{ZZ}{4}, \tag{4.43}$$

where $\xi_{ZZ} = \xi_{ZZ}^{\text{static}} = -357$ kHz is the ZZ-interaction strength. The quantity ξ_{ZZ}^{static} has a negative sign because the non-computational levels push stronger on level $|11\rangle$ than on the other computational levels.

Tuning the magnitude of ξ_{ZZ} by an externally applied microwave drive can be understood as follows. First, let us note that the capacitive coupling leads to much stronger interaction between the non-computational states, splitting the otherwise degenerate transitions $|10\rangle - |20\rangle$ and $|11\rangle - |21\rangle$ by $\Delta = 8.47$ MHz $\gg |\xi_{ZZ}^{\text{static}}|$, which provides us the resource to dynamically modify ξ_{ZZ}. The same is true for other transition pairs, e.g. $|11\rangle - |12\rangle$, $|01\rangle - |02\rangle$, or $|00\rangle - |03\rangle$, $|10\rangle - |13\rangle$, although the splitting may vary. Consider driving the circuit at the frequency f_d, blue-detuned from the $|10\rangle - |20\rangle$ resonance by an amount $\delta \gg \Delta$ (see Fig. 4.4b). Except for the paired transition $|11\rangle - |21\rangle$, there are no other circuit transitions in the GHz-vicinity (see Fig. 4.4a) due to the large anharmonicity. Therefore, the effect of the drive reduces to the attraction between levels in pairs $\{|10\rangle, |20\rangle\}$ and $\{|11\rangle, |21\rangle\}$, while other transitions are not driven. Specifically, if qubit B is in the ground state, there is a positive ac Stark shift $\delta f^{\text{Stark}}(\Omega, \delta) = (\sqrt{\Omega^2 + \delta^2} - \delta)/2$ on the qubit A frequency, which can be thought of as pulling level $|10\rangle$ towards level $|20\rangle$ by the δ-detuned drive (see Sec. 4.2.2). However, this shift is larger when qubit B is in the excited state, because the detuning $(\delta - \Delta)$ is smaller and the effective drive amplitude Ω is larger. Therefore, the qubit acquires a differential ac Stark shift, which is equivalent to modifying the ZZ-term in Eq. 4.43 as $\xi_{ZZ} = \xi_{ZZ}^{\text{static}} + \xi_{ZZ}^{\text{drive}}$, where $\xi_{ZZ}^{\text{drive}} = \delta f^{\text{Stark}}(\Omega_{11-21}, \delta - \Delta) - \delta f^{\text{Stark}}(\Omega_{10-20}, \delta)$. Because $\xi_{ZZ}^{\text{static}} < 0$ and $\xi_{ZZ}^{\text{drive}} > 0$ for typical fluxonium parameters, the total qubit-qubit interaction ξ_{ZZ} in Eq. 4.43 can be tuned through zero or increased by about an order of magnitude compared to the static value by adjusting the drive frequency and amplitude (see Fig. 4.4c

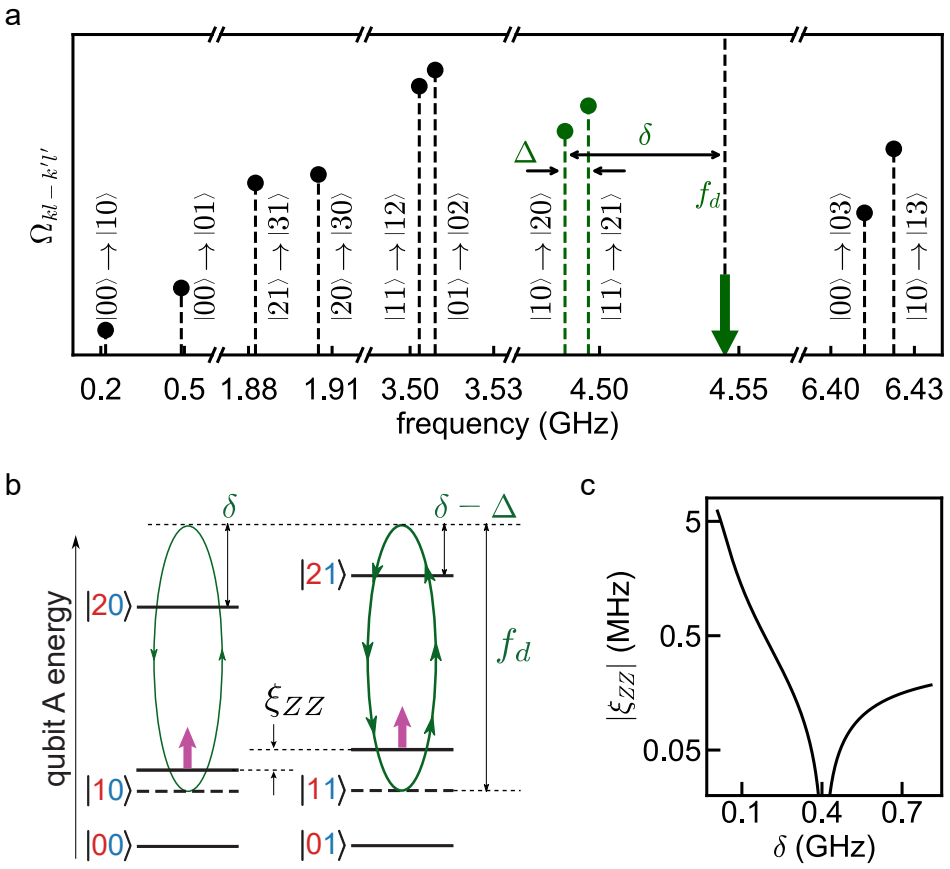

Figure 4.4: Differential ac Stark shift in a two-fluxonium circuit. (a) Spectrum of allowed transitions of the two-fluxonium circuit extracted from spectroscopy data. The simulated quantity $\Omega_{kl-k'l'}$ defines an on-resonance Rabi frequency that a drive field would induce, assuming the field amplitude is frequency-independent. Note that only transitions between states with different parity are allowed. The green arrow indicates the drive frequency f_d used to induce the differential ac Stark shift. (b) Schematic of the energy level diagram for qubit B in the ground state (left) and qubit B in the excited state (right). A drive at frequency f_d pulls the energy level $|11\rangle$ more than the energy level $|10\rangle$, without affecting levels $|00\rangle$ and $|01\rangle$, which is equivalent to a differential ac Stark shift $\xi_{ZZ}^{\text{drive}} > 0$. (c) Calculated total ZZ-interaction rate $\xi_{ZZ} = -|\xi_{ZZ}^{\text{static}}| + \xi_{ZZ}^{\text{drive}}$ for a fixed drive amplitude ($\Omega_{11-21} = 52$ MHz). Note, at an appropriate detuning δ, the total qubit-qubit interaction is switched off, we get $\xi_{ZZ} = 0$.

and Fig. 4.5c).

We verify that the qubit-qubit interaction indeed takes the form of Eq. 4.43 using a tomography protocol depicted in Fig. 4.5a [157]. The pulse sequence shown results in the observation of Ramsey-type fringes oscillating at the frequency ξ_{ZZ}. Fig. 4.5b shows the measured oscillations by sweeping the driving frequency around $f_d \approx 4.5$ GHz and fixing the amplitude such that $\Omega_{11-21} = 52$ MHz. As the drive frequency approaches either the $|10\rangle - |20\rangle$ or $|11\rangle - |21\rangle$ transitions (marked by the black dashed lines at 4.488 GHz and 4.496 GHz, respectively), the ZZ-interaction rate reaches about 6 MHz before the off-resonant ac Stark shift picture breaks down (Fig. 4.5b). Beyond that point, the drive field and the two non-computational transitions undergo a coherent energy exchange, witnessed by the detection of rapidly oscillating ripple features in Fig. 4.5b. The ZZ-interaction can also be controlled by off-resonantly driving the pair of doublets of transitions $|00\rangle - |03\rangle$, $|10\rangle - |13\rangle$, $|01\rangle - |31\rangle$, $|00\rangle - |30\rangle$, near the frequency $f_d' \approx 6.5$ GHz, where we obtained $\xi_{ZZ} > 10$ MHz (Fig. 4.6).

The ZZ-term in Eq. 4.43 can be switched on and off on a time scale of about 10 ns using Gaussian-edge pulses supplemented with the commonly used derivative removal (DRAG) distortion. During the time interval of $\xi_{ZZ}(t) \neq 0$, the states $|10\rangle$ and $|11\rangle$ accumulate different phases ϕ_{10} and ϕ_{11}, which is equivalent to the action of a unitary evolution operator $U = \mathrm{diag}(1, e^{-i\phi_{10}}, 1, e^{-i\phi_{11}})$ in the computational subspace. Using virtual Z rotations, the accumulated phase can be entirely assigned to any state such as $|11\rangle$ to implement a controlled-phase operation $U_{\mathrm{CP}}(\phi) = \mathrm{diag}(1, 1, 1, e^{-i\phi})$ where $\phi = \phi_{11} - \phi_{10}$. In principle, one can modulate both the drive frequency and amplitude during the gate pulse, but for simplicity we fixed the drive frequency and tried two different values, $f_d = 4.545$ GHz (detuned by 49 MHz from transition $|11\rangle - |21\rangle$) and $f_d' = 6.665$ GHz (detuned by 55 MHz from $|00\rangle - |30\rangle$).

At $\phi = \pi$ the CP gate belongs to the Clifford group, i.e. it becomes the controlled-Z gate. Hence, it can be characterized using randomized benchmarking (RB), which evades SPAM limitations. Using procedures similar to those described in Ref. [120], we optimized the gate pulses and obtained a CZ gate fidelity of 0.989 ± 0.001 at $f_d = 4.545$ GHz and 0.991 ± 0.001 at $f_d' = 6.665$ GHz (Fig. 4.7). Next, we characterize the CP gate at $\phi = \pi$ using the cross-entropy benchmarking technique. The XEB procedure applied to the CZ gate at $f_d = 4.545$ GHz yields a gate fidelity of 0.988 ± 0.001 which agrees with the results of randomized benchmarking and hence validates the use of XEB for other values ϕ of the controlled phase.

Finally, we apply the XEB procedure to a family of CP gates with the value of ϕ equally spaced by $\pi/16$. The extracted gate error grows approximately linearly in ϕ with a slope

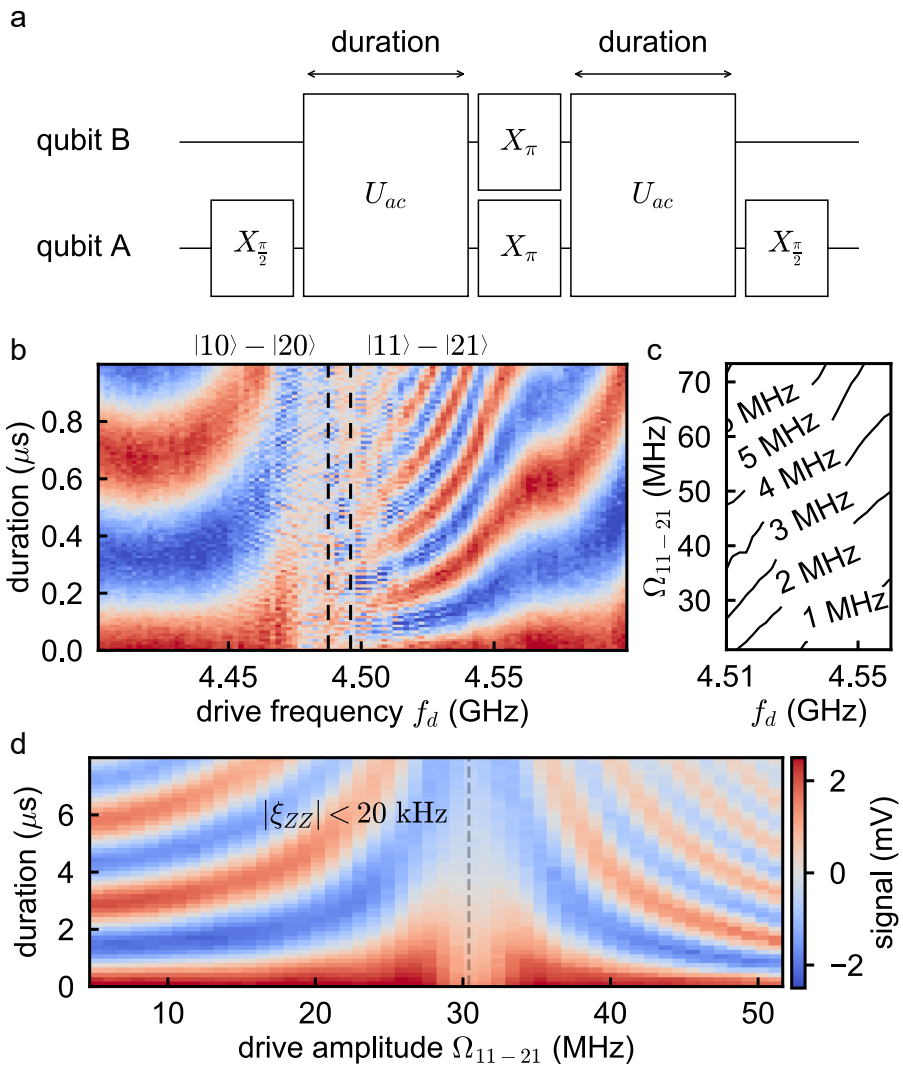

Figure 4.5: Tuning the ZZ-interaction. (a) Pulse sequence used to measure the interaction rate ξ_{ZZ}. The qubits evolve under U_{ac} that corresponds to the ZZ-term in Eq. 4.43. We use a refocusing pulse on each qubit in the middle of the sequence to cancel single-qubit Z rotations. (b) Induced ZZ-interactions (a two-qubit Ramsey-type fringe) as a function of drive frequency around the $|10\rangle - |20\rangle$ and $|11\rangle - |21\rangle$ transitions. The color scale is proportional to $\langle ZI \rangle$, which is related to qubit A population. The oscillation rate expectedly increases on approaching a resonance condition. (c) The induced interaction rate at different drive frequency and drive strength. It can reach about $\xi_{ZZ} = 5$ MHz on-demand. (d) Cancellation of the qubit-qubit interaction. When applying a drive at 4.65 GHz, the ZZ-oscillations slow down and speed back up as the drive amplitude passes though the value $\Omega_{11-21} = 30.4$ MHz. At this point, we can extract that $\xi_{ZZ} < 20$ kHz.

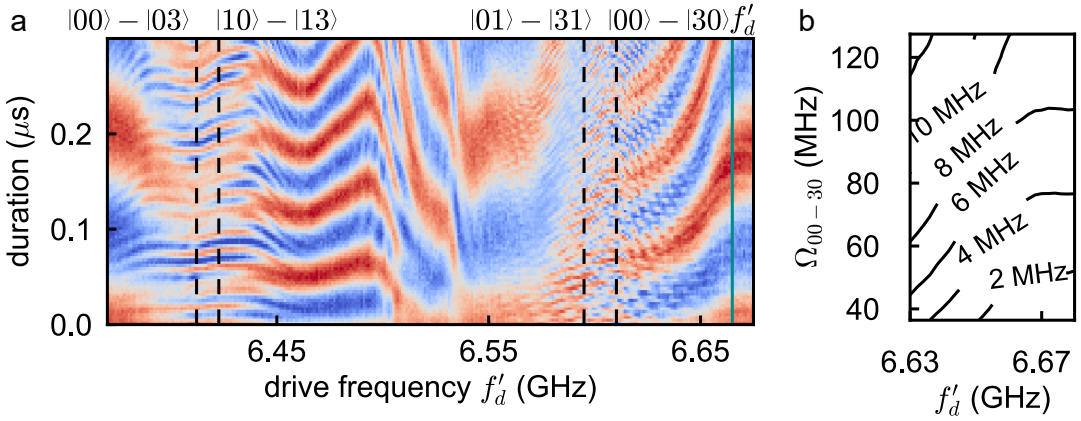

Figure 4.6: ZZ-interactions induced by driving around 6.5 GHz**.** (a) ZZ-oscillations measured with the pulse protocol depicted in Fig. 4.5(a). Within this frequency range, the four transitions $|00\rangle - |03\rangle$, $|10\rangle - |13\rangle$, $|01\rangle - |31\rangle$, and $|00\rangle - |30\rangle$ contribute to the ac Stark shift in the computational subspace. (b) The induced interaction rate at different drive frequency and drive strength. We achieve interaction rates exceeding 10 MHz.

of about 3×10^{-3} per radian (Fig. 4.8(d), circular markers). For $\phi = \pi/16$, the CP gate error reaches 2×10^{-3}, which is close to the experimental resolution limit. In order to understand the origin of the gate error, we performed detailed master-equation simulations of the driven two-fluxonium system with the measured coherence time in Table 4.3 [121]. Our numerical model closely reproduces the data while relying only on experimentally measured parameters (Fig. 4.8(d), square markers). According to the model, the error is entirely due to incoherent processes, while the coherent error is absent down to the 10^{-4} level thanks to the strong anharmonicity of fluxonium's non-computational transitions.

The second experiment is perform on another two-qubit device with $f_A = 498$ MHz and $f_B = 853$ MHz. Compared to the device used in the first experiment, the qubit frequencies are higher and the charge matrix elements are larger leading to a stronger effective coupling between the computational states with the same mutual capacitance between the two fluxonium circuits. This can be supported with the measured static ZZ interaction of 0.7 MHz. Such a strong effective coupling makes it possible to induce substantial ZZ interaction while keeping the population inside the high-coherence computational space.

Similar effects have been explored with transmon systems [122], [123] where the microwave drive needs to be applied to the two qubits simultaneously. This can be understood as an off-resonant effect of the ZX term of the drive (see Sec. 2.4). A ZX term alone can not generate different ac Stark shift because qubit B experiences the same drive strength with a π phase difference depending on the state of qubit A, indicating equal ac Stark shifts

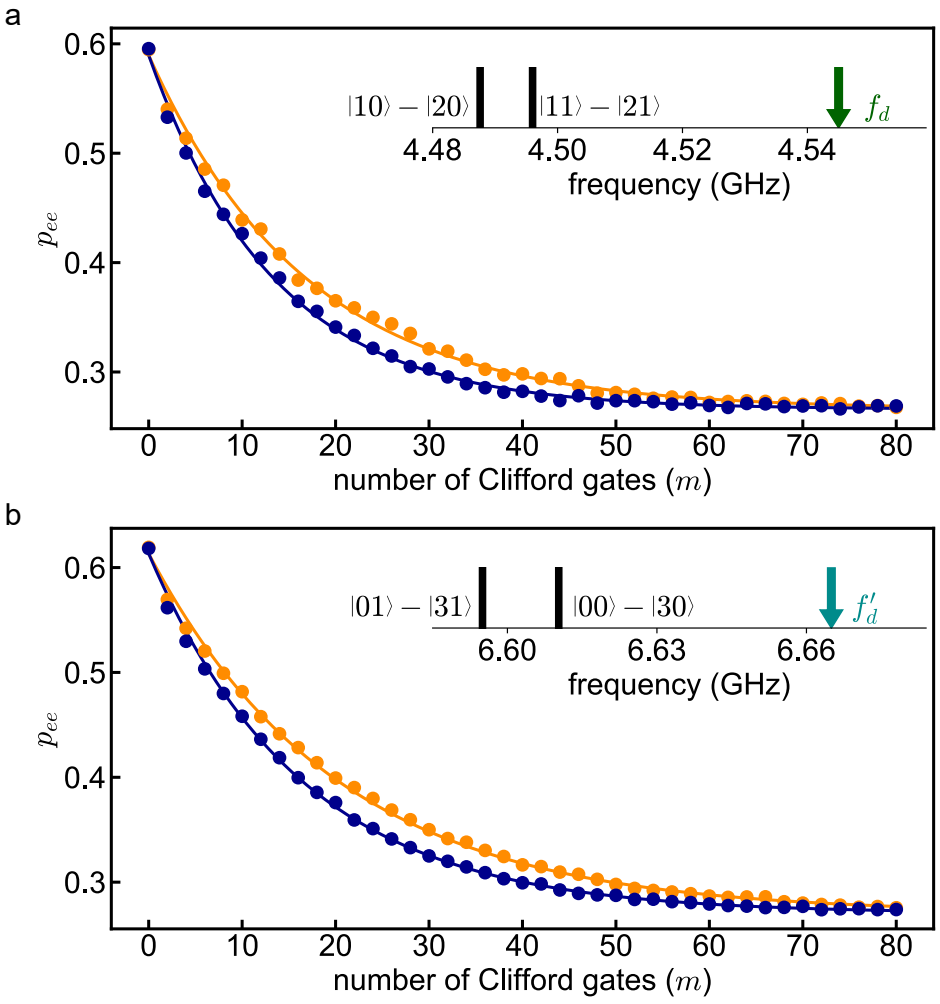

Figure 4.7: Interleaved randomized benchmarking (IRB) for CZ gates. (a) IRB of a 145 ns CZ gate using the $1-2$ manifold. The drive frequency is $f_d = 4.545$ GHz (detuned by 49 MHz from transition $|11\rangle - |21\rangle$) and the drive amplitude is $\Omega_{11-21} = 68$ MHz. The gate fidelity is 0.989 ± 0.001 from IRB, which is consistent with the XEB fidelity on the same gate. (b) IRB of a 115 ns CZ gate using the $0-3$ manifold. The drive frequency is $f'_d = 6.665$ GHz (detuned by 55 MHz from transition $|00\rangle - |30\rangle$) and the drive amplitude is $\Omega_{00-30} = 91$ MHz. The gate fidelity is 0.991 ± 0.001.

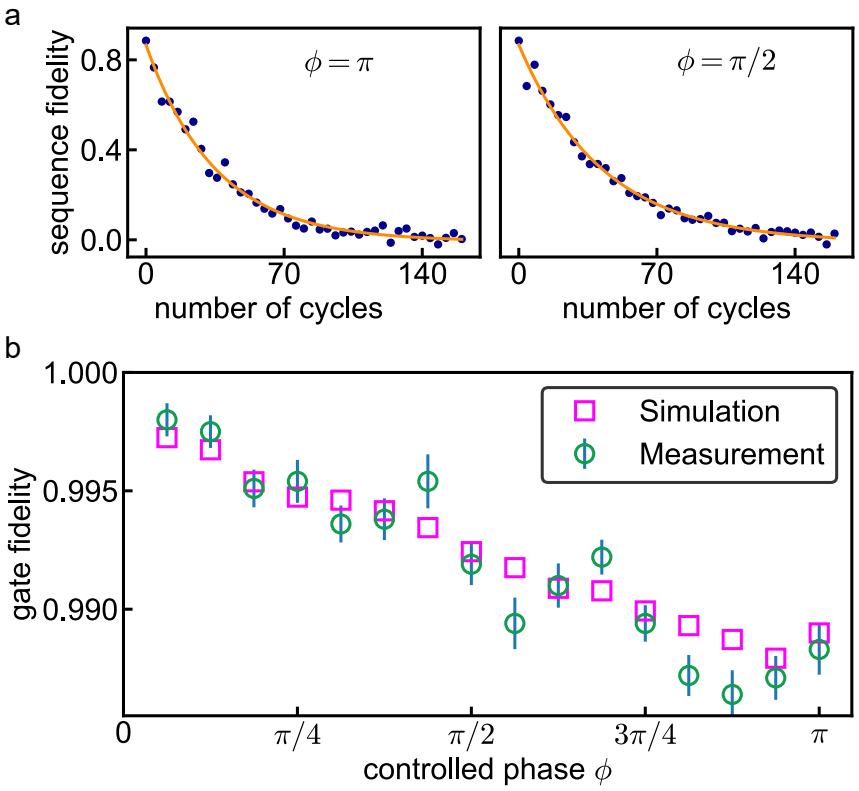

Figure 4.8: Cross-entropy benchmarking for arbitrary CPhase gates. (a) XEB for the phases $\phi = \pi/2$ and π. We extract the Pauli and gate errors from the decay of the XEB sequence fidelity with the number of cycles. The gate fidelity at $\phi = \pi/2$ reaches $(99.2 \pm 0.1)\%$. (b) Fidelity of the controlled-phase gate family. The green circles are obtained by cross-entropy benchmarking and the magenta squares are obtained by master equation simulations using the average T_1 and T_2^E shown in Table 4.3. The gate fidelity averaged over the complete family exceeds 99.2%.

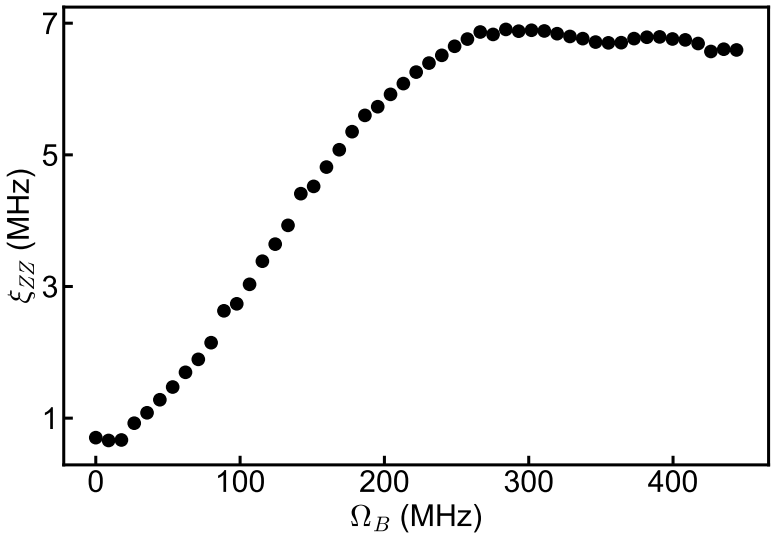

Figure 4.9: Measured ZZ rates when applying the drive near the qubit transitions. The drive frequency is 650 MHz and the drive amplitude Ω_B is the equivalent Rabi rate when driving qubit B on resonance. The data point at 0 pulse amplitude shows the static ZZ interaction of the system is 0.7 MHz. The total ZZ rate gets stronger with larger drive amplitude and then saturates around 7 MHz which is mainly because the rotating wave approximation starts to break down.

in both cases. The symmetry can be broken when an addition IX term is created by applying the drive with the same frequency at qubit B. The non-local input field of the 3D architecture fulfills this requirement by nature, enabling us to induce differential ac Stark shift with only one port.

The ZZ interaction is induced by driving at 650 MHz in Fig. 4.9. We quantify the drive strength with the Rabi frequency of qubit B when applying the same power on resonance. The induced ZZ rate can be as high as 7 MHz, suggesting that a potential fast CZ gate. The ZZ rate saturates at large drive strength. This is mainly because the driving strength starts to be comparable with the qubit frequency and the rotating wave approximation starts to break down. We optimized a CZ gate at $\Omega_B = 133$ MHz. The gate duration is 138 ns and the measured fidelity is $(99.0 \pm 0.1)\%$, which we believe is limited by driving induced decoherence [152], [158] and pulse distortion [106].

4.3.2 Near-resonance CZ gate

A CZ gate can be implemented by Rabi drive $|10\rangle - |20\rangle$ and $|11\rangle - |21\rangle$ at a frequency in between. Let us start by considering the gate transitions $|10\rangle - |20\rangle$ and $|11\rangle - |21\rangle$ as two-level systems. Our gate exploits the geometric-phase accumulations during round trips in these two systems. The accumulated phase can be divided into two parts: the dynamical phase, which is proportional to the evolution time and the energy of the system, and the geometric phase, which depends only on the trajectory followed in the Hilbert space. Applying a microwave tone drives the system with the Hamiltonian

$$H_{\text{drive}} = (\epsilon_A n_A + \epsilon_B n_B)\cos(2\pi f_d t). \tag{4.44}$$

When the drive frequency f_d is nearly resonant with one of the two gate transitions, we observe Rabi oscillations (Fig. 4.10a) with the resonance Rabi frequencies

$$\Omega_{10-20} = |\langle 10|H_{\text{drive}}|20\rangle|, \tag{4.45}$$

$$\Omega_{11-21} = |\langle 11|H_{\text{drive}}|21\rangle|, \tag{4.46}$$

respectively. A strong hybridization of the $|12\rangle$ and $|21\rangle$ states creates an imbalance between the rotation speeds given by the ratio $r = \Omega_{11-21}/\Omega_{10-20} \simeq 1.36$.

In order to eliminate leakage to higher states, one needs to synchronize off-resonance Rabi oscillations determined by the two transitions to ensure that the state vector always comes back to the computational subspace. This is achieved by matching the generalized

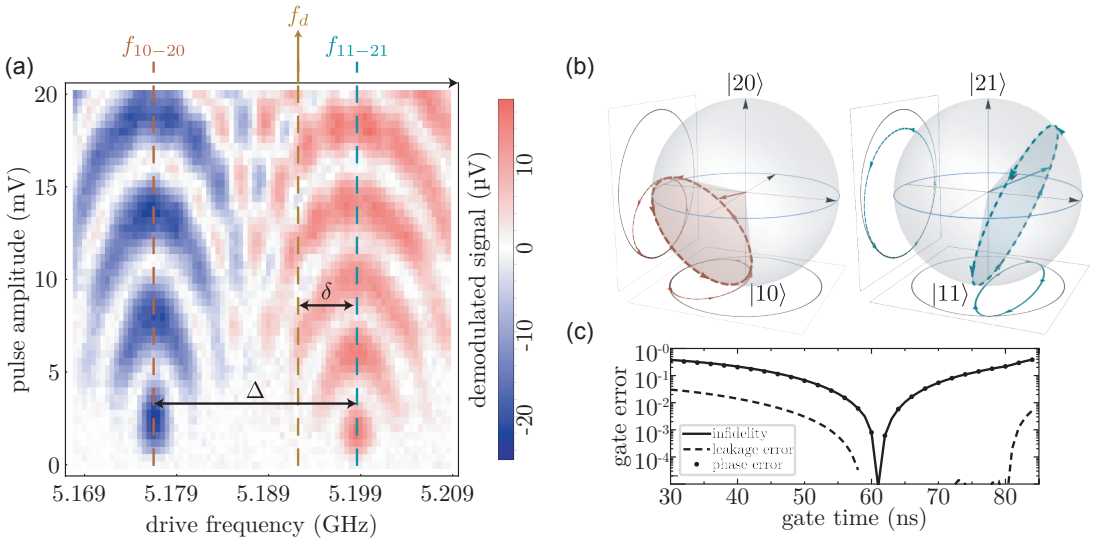

Figure 4.10: Gate principle of the near-resonance CZ gate. (a) Rabi oscillations near the $|10\rangle - |20\rangle$ and $|11\rangle - |21\rangle$ transitions versus driving frequency with a 330 ns-long pulse. The two transitions display different resonance Rabi frequencies characterized by the ratio $r = \Omega_{11-21}/\Omega_{10-20} \simeq 1.36$. The drive frequency f_d indicated in brown given by Eq. 4.48 is used to synchronize the oscillations on the two transitions. (b) Bloch sphere representations of the trajectories in the $\{|10\rangle, |20\rangle\}$ and $\{|11\rangle, |21\rangle\}$ manifolds in the frame rotating at the drive frequency. The quantum state follows a closed path in the Hilbert space leading to a relative phase accumulation given by the difference of the solid angles spanned by the two trajectories. (c) Gate error versus gate duration simulated using the Hamiltonian in the presence of a Gaussian flat-topped pulse and without decoherence. For every gate duration, drive frequency and amplitude are optimized to minimize the coherent leakage error (dashed line). The dots represent the gate error caused by incorrect phase accumulation $\Delta\varphi = \varphi_{11} - \varphi_{10} \neq \pi$. With the optimal pulse duration around ~ 62 ns, the infidelity due to coherent errors is well below 10^{-3}.

Rabi frequencies

$$\Omega = \sqrt{\Omega_{11-21}^2 + \delta^2} = \sqrt{\Omega_{10-20}^2 + (\delta - \Delta)^2}, \tag{4.47}$$

where $\delta = f_{11-21} - f_d$ is the detuning between the $|11\rangle - |21\rangle$ transition and the drive frequency (Fig. 4.10a). A full rotation is then performed in the shortest gate time $t_{\text{gate}} = 1/\Omega$. During the gate operation, the state vector trajectory can be depicted in a Bloch sphere representation (Fig. 4.10b) when the system starts in $|10\rangle$ or $|11\rangle$. These circular trajectories, which are traveled in opposite directions with respect to the centers of the Bloch spheres, define two cones inside the spheres. The cones and directions of travel define the solid angles $\Theta_{10} = 2\pi[1 - (\Delta - \delta)/\Omega]$ and $\Theta_{11} = 2\pi(1 + \delta/\Omega)$, which correspond to a geometric phase accumulation $\varphi_{ij} = -\Theta_{ij}/2$ on state $|ij\rangle$. Our gate thus implements a unitary operation $U = \text{diag}(1, 1, e^{i\varphi_{10}}, e^{i\varphi_{11}})$. Using virtual Z rotations, the phase difference can be assigned to any computational state such as $|11\rangle$ to realize a controlled-phase operation $U = \text{diag}(1, 1, 1, e^{i\Delta\varphi})$ with $\Delta\varphi = \varphi_{11} - \varphi_{10}$. A CZ gate is obtained when $\Delta\varphi = -(\Theta_{11} - \Theta_{10})/2 = -\pi\Delta/\Omega = \pm\pi$. Using this condition in Eq. 4.47 we obtain the optimal drive frequency (brown arrow on Fig. 4.10a)

$$\frac{\delta}{\Delta} = \frac{r^2 - \sqrt{(r^2-1)^2 + r^2}}{r^2 - 1} \simeq 0.29\,. \tag{4.48}$$

For δ given by Eq. 4.48 and $\Omega = \Delta$, a CZ gate with zero leakage is achieved in time exactly $t_{\text{gate}} = 1/\Delta$.

Our understanding of the gate process is validated by simulating the Hamiltonian in the presence of the drive term, given by Eq. 4.44. The full Hamiltonian takes into account the dynamical phase $\phi_{\text{dyn}} = 2\pi\xi_{ZZ}t_{\text{gate}} \simeq 10^{-2} \ll \pi$ which is negligible after one gate operation thanks to the small ZZ-interaction term. Starting with the driving frequency given by Eq. 4.48, we minimize the final populations leakage out of the computational subspace by adjusting the drive amplitude and frequency for every gate duration. Because of the rising and lowering edges of the pulse in the simulation, we find a slightly longer optimal gate duration ~ 62 ns (compared to $1/\Delta = 45.5$ ns) for which coherent errors on the gate fall below $< 10^{-3}$, see Fig. 4.10c. Note, even at the error level of 10^{-4}, the optimal point does not require an excessive fine-tuning of the gate pulse parameters: it corresponds to a fraction of a percent variation in terms of the gate time, gate pulse amplitude, and frequency.

We assess the quality of the optimized CZ gate by iterative interleaved randomized benchmarking [159]. We obtain a reference fidelity $F_{\text{Clifford2}} = (96.0 \pm 0.1)\%$. Interleaving the gate CZ^n, obtained by concatenating n pulses corresponding to a single CZ gate, yields

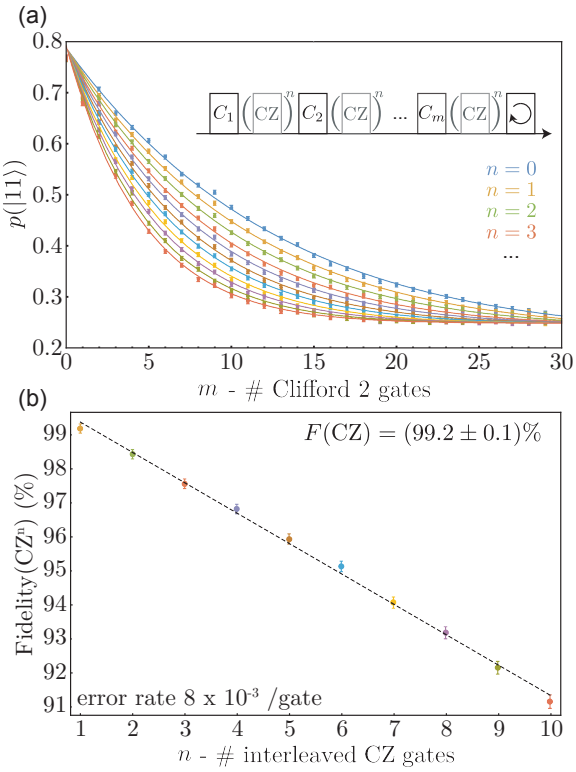

Figure 4.11: IRB of different number of CZ gates. (a) Average probability $p(|11\rangle)$ as a function of sequence length. For each sequence length, we average over 100 random sequences repeated 1500 times. We insert a variable number $n = 0, 1, ..., 10$ (encoded in the color) of CZ gates between the randomly chosen Clifford gates. (b) Fidelity of CZ^n versus n. The gate error grows linearly with n indicating that the errors are incoherent.

the CZ gate fidelity of $F(\mathrm{CZ}) = (99.2 \pm 0.1)\%$ for $n = 1$ (yellow curve in Fig. 4.11a). The error grows linearly with n (we tried $n = 2, 3, ..., 10$) (Fig. 4.11b), which is a solid evidence that the gate error is due to incoherent processes [142].

4.3.3 bSWAP gate

A bSWAP gate can be realized through driving the two-photon transition of the $00 - 11$ transition. We can start from the spin model introduced in Sec. 2.4 and define the total Hamiltonian $H_{\mathrm{tot}} = \tilde{H} + \tilde{F}\cos(\omega_d t + \varphi_3)$ using Eq. 2.37 and Eq. 2.40. To understand the origin of the two-photon effect, we need to first go to a rotating frame with transformation

operator $U_2 = \exp(-iO_2 t)$ and

$$O_2 = \begin{pmatrix} -\omega_d & 0 & 0 & 0 \\ 0 & 0 & 0 & 0 \\ 0 & 0 & 0 & 0 \\ 0 & 0 & 0 & \omega_d \end{pmatrix}, \tag{4.49}$$

which we called the bSWAP gate frame. In this rotating frame, state $|00\rangle$ and $|11\rangle$ become almost degenerate and form a low-energy manifold. We can define $\Delta = -(\tilde{\omega}_B - \tilde{\omega}_A)/2$ and $\delta = \omega_d - (\tilde{\omega}_A + \tilde{\omega}_B)/2$. If we can treat the drive term as a perturbation $\Omega_A, \Omega_B < \Delta$, we can apply Schrieffer-Wolff transformation [160] (see Sec. C.2) to arrive at a Hamiltonian H_{eff} with the effective coupling between $|00\rangle$ and $|11\rangle$ as well as the coupling between $|01\rangle$ and $|10\rangle$

$$\begin{aligned} H_{\text{eff}} = \frac{\alpha_{IZ}}{2} IZ + \frac{\alpha_{ZI}}{2} ZI + \frac{\alpha_{ZZ}}{2} ZZ + \frac{\Omega_{ER}}{4}(XX - YY) \\ + \frac{\Omega_{EI}}{4}(XY + YX) + \frac{\Omega_O}{4}(XX + YY), \end{aligned} \tag{4.50}$$

where $\Omega_{ER} = \Omega_E \cos 2\varphi_3,\ \Omega_{EI} = \Omega_E \sin 2\varphi_3$ and

$$\Omega_E = \frac{\Delta}{2(\Delta^2 - \delta^2)}(\Omega_A^2 \sin 2(\theta_- - \theta_+) + \Omega_B^2 \sin 2(\theta_- + \theta_+)) \tag{4.51}$$

$$\Omega_O = \frac{\delta}{2(\Delta^2 - \delta^2)}(\Omega_A^2 \sin 2(\theta_- - \theta_+) - \Omega_B^2 \sin 2(\theta_- + \theta_+)). \tag{4.52}$$

The IZ, ZI, and ZZ terms are the computational state energies modified by the ac Stark shifts in the rotating frame. Let's ignore these terms for now and focus on the unitary evolution of the last three terms in Eq. 4.50

$$U_{XY} = \begin{pmatrix} \cos\frac{\Omega_E t}{2} & 0 & 0 & -ie^{i(2\varphi_3)} \sin\frac{\Omega_E t}{2} \\ 0 & \cos\frac{\Omega_O t}{2} & -i\sin\frac{\Omega_O t}{2} & 0 \\ 0 & -i\sin\frac{\Omega_O t}{2} & \cos\frac{\Omega_O t}{2} & 0 \\ -ie^{-i(2\varphi_3)} \sin\frac{\Omega_E t}{2} & 0 & 0 & \cos\frac{\Omega_E t}{2} \end{pmatrix}. \tag{4.53}$$

It is clear from Eq. 4.53 that $XX - YY$ and $XY + YX$ terms are the X-like and Y-like Rabi rotations for the $00 - 11$ transition, corresponding to the bSWAP process. Ω_E is the Rabi frequency with a quadratic dependence on the drive amplitude Ω_A, Ω_B and 2φ determines the direction of the rotation axis. The $XX + YY$ term is the X-like Rabi rotation for the $01 - 10$ transition, corresponding to the iSWAP process with Rabi frequency Ω_O, which

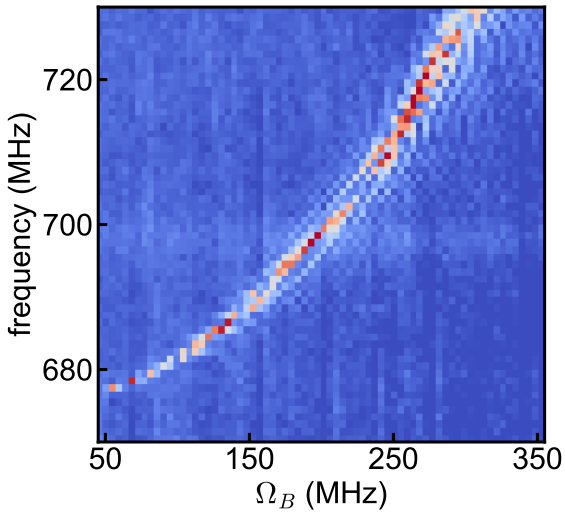

Figure 4.12: Two-tone spectroscopy of the $|00\rangle - |11\rangle$ two-photon transition under different drive strength. The drive amplitude Ω_B is the equivalent Rabi rate when driving qubit B on resonance. At low power, the transition frequency is at 677 MHz. The two-photon transition shifts significantly at higher power due to the unequal ac stark shifts on the two qubits.

should be avoided if we only want a bSWAP gate.

Next, we can include the ac Stark shift terms. Because the ZZ term commutes with all the other terms in Eq. 4.50, we can separate it from the unitary evolution of the other operators $U_H = U_{XYZ}U_{ZZ}$, where U_{XYZ} contains the IZ, ZI, and the X or Y types of terms. For simplicity, we rewrite the single-qubit Z terms as

$$\frac{\alpha_{IZ}}{2}IZ + \frac{\alpha_{ZI}}{2}ZI = \frac{\alpha_+}{4}(IZ + ZI) + \frac{\alpha_-}{4}(IZ - ZI), \tag{4.54}$$

and focus on the off-diagonal terms in U_{XYZ}.

$$U_{XYZ} = \begin{pmatrix} u_{00} & 0 & 0 & -ie^{i(2\varphi_3)}\frac{\Omega_E}{\Omega'_E}\sin\frac{\Omega'_E t}{2} \\ 0 & u_{01} & -i\frac{\Omega_O}{\Omega'_O}\sin\frac{\Omega'_O t}{2} & 0 \\ 0 & -i\frac{\Omega_O}{\Omega'_O}\sin\frac{\Omega'_O t}{2} & u_{10} & 0 \\ -ie^{-i(2\varphi_3)}\frac{\Omega_E}{\Omega'_E}\sin\frac{\Omega'_E t}{2} & 0 & 0 & u_{11} \end{pmatrix}. \tag{4.55}$$

Ω'_E (Ω'_O) are the effective Rabi frequency defined as $\Omega'_E = \sqrt{\alpha_+^2 + \Omega_E^2}$ ($\Omega'_O = \sqrt{\alpha_-^2 + \Omega_O^2}$).

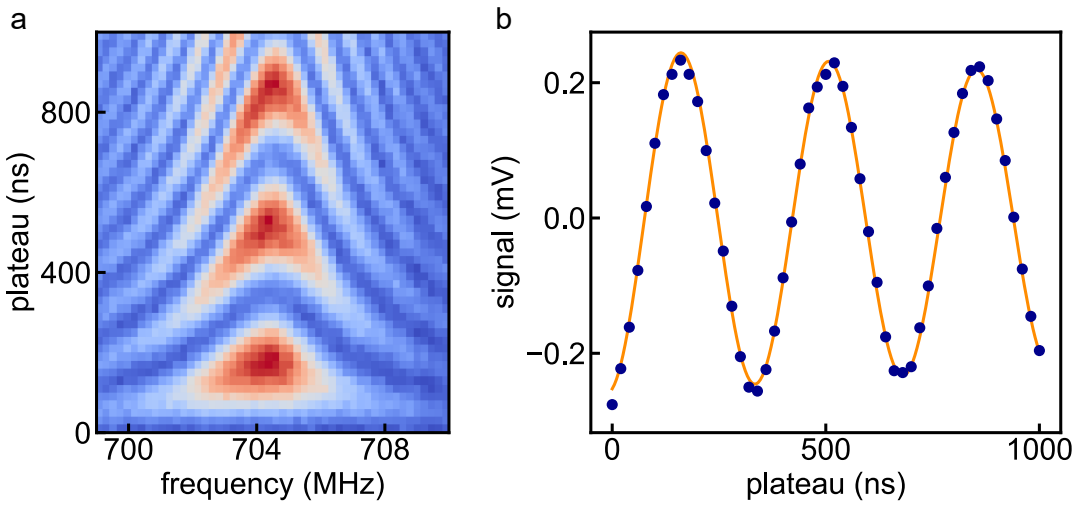

Figure 4.13: Rabi oscillations of the $|00\rangle - |11\rangle$ two-photon transition. (a) chevron pattern of Rabi oscillations at different drive frequency. The drive strength $\Omega_B = 222$ MHz. The pattern is not symmetric with respect to the resonance frequency. (b) Rabi oscillation on resonance. The plateau for a π pulse is 161 ns.

Interestingly, α_+ (α_-) serves as the detuning of the $00-11$ ($10-01$) two-photon transition. This originates from the fact that $IZ+ZI$ does not commute with $XX-YY$ or $XY+YX$ and $IZ-ZI$ does not commute with $XX+YY$. Because α_+ is strongly dependent on ac Stark shifts, the two-photon transition can drift significantly at different drive power, as illustrated in Fig. 4.12. One needs to search for the on-resonance frequency whenever the power is changed to make sure $\alpha_+ = 0$. Because the ac Stark shifts can also depend on the drive frequency, the Rabi chevron pattern is not symmetric in Fig. 4.13 as in a typical Rabi measurement. However, the oscillation contrast is still maximized on resonance. At this frequency, the Rabi oscillation of $10-01$ is small due to the large detuning of α_-.

An vital thing to notice is that, up to now, we are working in the rotating frame of O_2 defined in Eq. 4.49. We still need to transform the unitary operator to the single-qubit gate frame of

$$O_1 = \begin{pmatrix} -\tilde{\omega}_+/2 & 0 & 0 & 0 \\ 0 & -\tilde{\omega}_-/2 & 0 & 0 \\ 0 & 0 & \tilde{\omega}_-/2 & 0 \\ 0 & 0 & 0 & \tilde{\omega}_+/2 \end{pmatrix}, \tag{4.56}$$

and $U_1 = \exp(-iO_1 t)$. For the sake of convenience, we only consider the bSWAP process in

Eq. 4.53 and set $\Omega_E t = \pi$ for a full SWAP between $|00\rangle$ and $|11\rangle$. The unitary operator in the bSWAP gate frame is

$$U_2^{\mathrm{bSWAP}} = \begin{pmatrix} 0 & 0 & 0 & -ie^{i(2\varphi_3)} \\ 0 & 1 & 0 & 0 \\ 0 & 0 & 1 & 0 \\ -ie^{-i(2\varphi_3)} & 0 & 0 & 0 \end{pmatrix}. \tag{4.57}$$

We can assume the bSWAP gate starts at $t = t_1$ and ends at $t = t_2$. Following a similar frame transformation procedure mentioned earlier in Sec. 4.2.2 and illustrated in Fig. 4.14, we have the unitary operator in the single-qubit gate frame

$$U_1^{\mathrm{bSWAP}} = U_1^{\dagger}(t_2)U_2(t_2)U_2^{\mathrm{bSWAP}}U_2^{\dagger}(t_1)U_1(t_1). \tag{4.58}$$

Of course, we need to consider the phase offset of the single-qubit control microwave φ_1 and φ_2, such that $U_1^{\mathrm{bSWAP}} \to U_{\varphi_1}^{\dagger}U_{\varphi_2}^{\dagger}U_1^{\mathrm{bSWAP}}U_{\varphi_2}U_{\varphi_1}$. Therefore in practice, the operator is

$$U_1^{\mathrm{bSWAP}} = \begin{pmatrix} 0 & 0 & 0 & -ie^{i\varphi_E} \\ 0 & e^{-i\Delta(t_1-t_2)} & 0 & 0 \\ 0 & 0 & e^{i\Delta(t_1-t_2)} & 0 \\ -ie^{-i\varphi_E} & 0 & 0 & 0 \end{pmatrix}, \tag{4.59}$$

where $\varphi_E = \delta(t_1+t_2) - \varphi_1 - \varphi_2 + 2\varphi_3$. The diagonal terms in Eq. 4.59 are trivial. They are nothing but fixed single-qubit Z phases. However, the phase on the off-diagonal elements are non-trivial because it depends on the position of the pulse in the sequence through $\delta(t_1+t_2)$! It originates from the fact that a two-qubit system only has two degrees of freedom on choosing the phase offset, therefore a third microwave drive at a different frequency can not maintain a relatively fixed phase over the whole sequence.

To prove that φ_E changes with the pulse position, we performed a Ramsey-type of experiment illustrated in Fig. 4.15. If the unitary operator of the bSWAP pulse takes the form of

$$U^{\mathrm{bSWAP}} = \begin{pmatrix} 0 & 0 & 0 & -ie^{i\varphi_E} \\ 0 & 1 & 0 & 0 \\ 0 & 0 & 1 & 0 \\ -ie^{-i\varphi_E} & 0 & 0 & 0 \end{pmatrix}, \tag{4.60}$$

the observable $\langle ZI \rangle = -\sin\varphi_E = -\sin(2\pi f_\phi t + \phi_0)$. By fitting the Ramsey data in

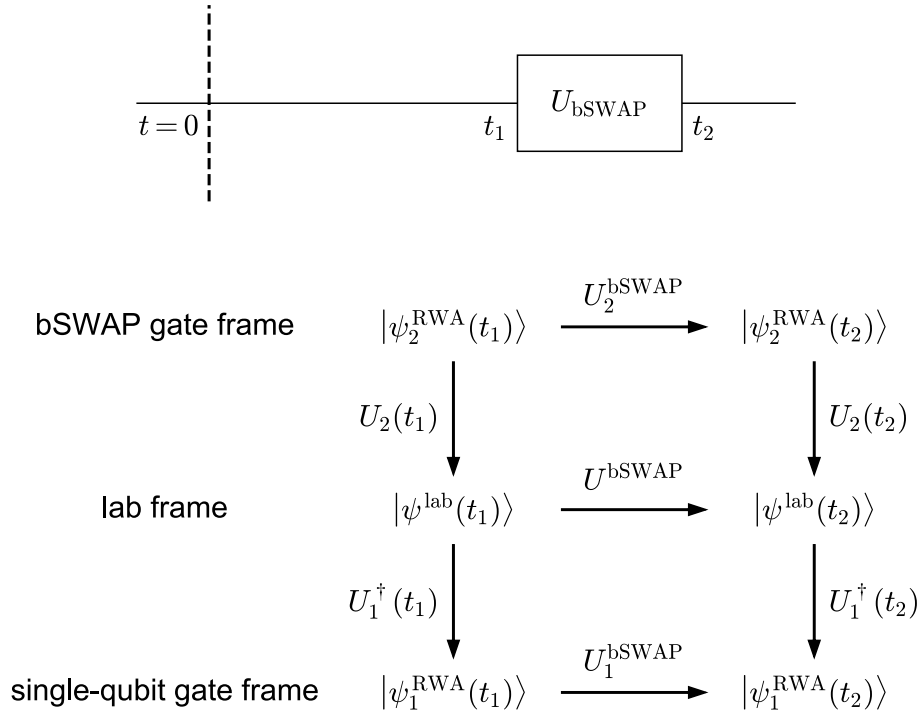

Figure 4.14: Rotating frame transformation for bSWAP gate. $U_1(t)$ is the unitary transformation between the bSWAP gate frame and the lab frame. $U_2(t)$ is the unitary transformation between the single-qubit gate frame and the lab frame. The goal is to obtain the evolution operator in the single-qubit frame U_1^{bSWAP} from the bSWAP gate frame.

Fig. 4.15b, we found $|f_\phi| = 158$ MHz. We can cancel out this effect by assigning a position-dependent phase on the bSWAP pulse such that $\varphi_3 = f_{\text{pulse}}t + \varphi_3^{\text{offset}}$. The Ramsey fringes disappear when $f_{\text{pulse}} = 79$ MHz. These measurements are all consistent with the fact that $|\delta/(2\pi)| = |f_d - (\tilde{f}_A + \tilde{f}_B)/2| = 79$ MHz in our setup.

What's more, because we need to repeat the sequence for many times, φ_E is required to be stable across different consecutive sequences, otherwise the off-diagonal terms will look random over many repetitions and be eventually averaged out. Assume the total duration of a sequence is T. This converts to the condition of $(2\omega_d - \tilde{\omega}_A - \tilde{\omega}_B)T = 2n\pi$, where n is an integer. If three independent RF sources are used for the single-qubit drives and the two-photon drive, they need to be synchronized to the same clock and their relative phase fluctuation should also be small. We monitored the phase difference fluctuations over 30 hours between two RF sources (Rohde&Schwarz SGS100A) in our lab. The relative phase can drift on the order of 0.03, which can be translated into an error of 2e-4 by calculating the fidelity of two unitaries [161]

$$F = \frac{\text{Tr}\left(U^\dagger U\right) + \left|\text{Tr}\left(U_{\text{exp}}^\dagger U\right)\right|^2}{20}. \tag{4.61}$$

Unfortunately, we found a significant ZZ interaction (i.e. α_{ZZ} in Eq. 4.50) is induced as we apply the two-photon drive which is on the same order of the pure bSWAP gate rate. The associated ZZ term can undermine the entangling power of the whole unitary [162]. We noticed that this issue can be addressed by constructing a composite gate as $\sqrt{\text{bSWAP}} - X_\pi I - \sqrt{\text{bSWAP}}$. This composite gate echos out the ZZ interaction and has the same entangling power with a CNOT gate.

4.3.4 Cross-resonance gate

Similar to the transmon system, we can perform cross-resonance (CR) [115] gate on fluxonium qubits as well [106]. The cross-resonance effect can be understood with the ZX terms in Eq. 2.40. when the drive field applied on qubit A is on resonance with qubit B, the qubit B feels a different drive phase based on the state of qubit A. In practice, we worked with fluxoniums in a 3D architecture. The ZX and IX terms can be generated simultaneously. Tuning the relative strength between these two terms can be done by leveraging the two input ports of a 3D cavity. The microwave drive can be applied to the two ports simultaneously (at the same frequency). By adjusting the drive strength and the phase difference of the two ports, one can achieve selective darkening of a transition in the computational

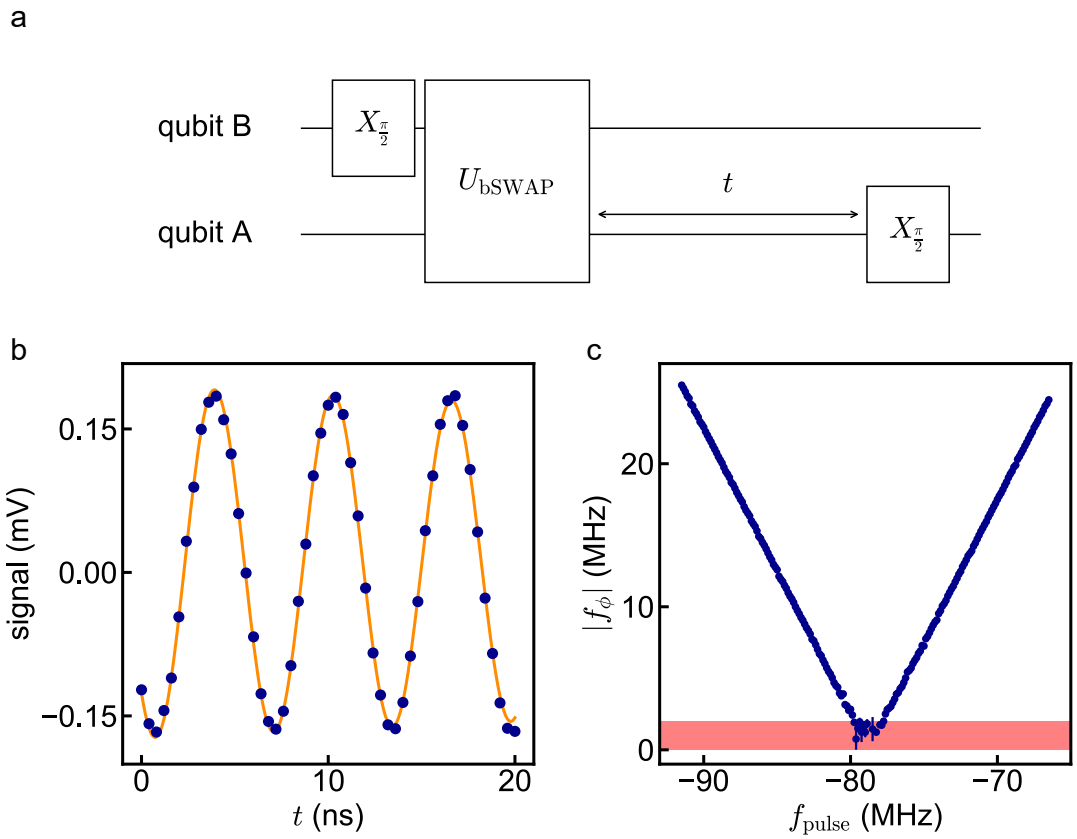

Figure 4.15: bSWAP Ramsey measurements. (a) Pulse sequence to measure the accumulated phase due to different rotating frame. U_{bSWAP} brings an additional phase that depends on the position of the pulse in the sequence. (b) bSWAP Ramsey oscillation. The measured oscillation at $|f_\phi| = 158$ MHz is proportional to $\langle ZI \rangle$, which is related to qubit A population. (c) bSWAP Ramsey oscillation rate $|f_\phi|$ at different pulse phase frequency. The bSWAP pulse phase is changed depending on the position of the pulse center $\phi_{\mathrm{bSWAP}} = 2\pi f_{\mathrm{pulse}} t_{\mathrm{center}}$ to cancel out the additional phase from frame transformation. $|f_\phi|$ vanishes at $f_{\mathrm{pulse}} = 79$ MHz, which is consistent with the frequency difference $|f_\phi|/2 = |f_d - (\tilde{f}_A + \tilde{f}_B)/2|$. The red region indicates the noise floor of $|f_\phi|$ from fitting due to finite sequence length.

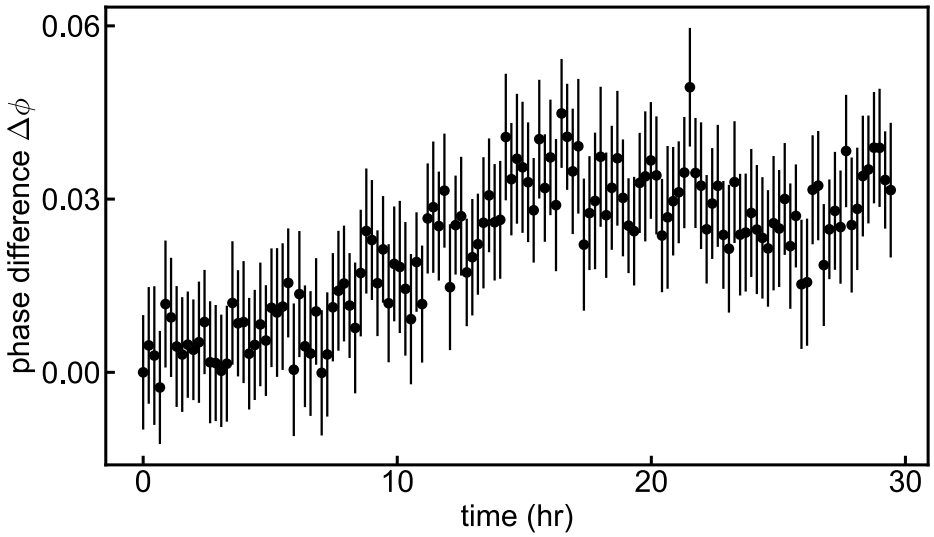

Figure 4.16: Relative fluctuation between two different RF source. A Ramsey experiment is carried out to monitor the phase difference $\Delta\phi$ between two independent Rohde&Schwarz SGS100A RF sources. $\Delta\phi$ can have a drift of 0.03 rad over 30 hours, which can contribute an error of 2e-4 estimated from Eq. 4.61.

space. For example, when $\langle 00| H_{\text{drive}} |01\rangle = 0$ as demonstrated in Fig. 4.17, a CNOT gate can be implemented.

As we discussed in Sec. 4.2.3, the side effect of cross-resonance is the quantum crosstalk as we perform single-qubit gates. This is more severe for the non-local input field of a 3D cavity. One can apply the same trick in the CNOT gate and utilize the two input ports. Likewise, $\langle 00| H_{\text{drive}} |01\rangle = \langle 10| H_{\text{drive}} |11\rangle$ can be achieved by adjusting the drive parameters on the two ports, leading to a full cancellation of a ZX term as we execute the single-qubit gate on B.

4.4 Parameter Optimization

Here is the routine when we optimize the two-qubit gate. We start from optimizing the single-qubit gates. We run Rabi and Ramsey experiments to find the single-qubit pulse duration (amplitude) and frequency. We perform a parameter search optimizing the sequence fidelity of fixed length RB, also known as 'Optimized Randomized Benchmarking for Immediate Tune-up' (ORBIT), with a numerical Nelder-Mead method. This is to fine tune the pulse parameters including the DRAG coefficient.

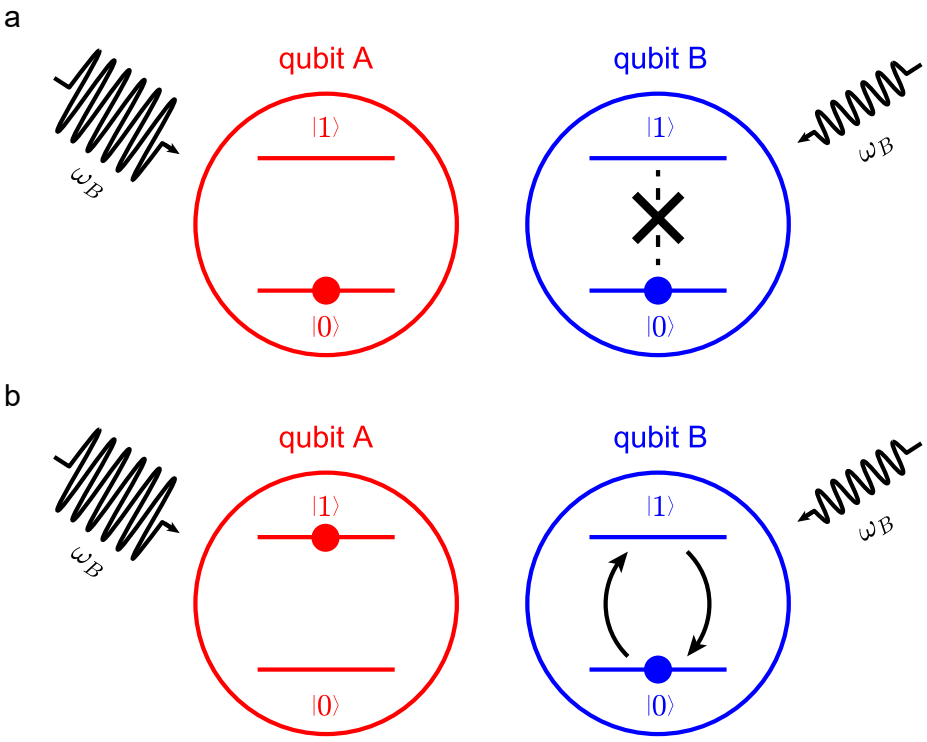

Figure 4.17: Gate principle for a cross-resonance gate. Two microwave drives are applied to the two qubits with different frequency ω_A and ω_B when (a) qubit A is at $|0\rangle$ state and (b) qubit A is at $|1\rangle$ state. The drives have the same frequency but different amplitude and phase. The drive at qubit A generates a ZX term. Combined with the IX term of the drive at qubit B, one can achieve selective darkening of the $|00\rangle - |01\rangle$ transition by adjusting the relative amplitude and phase of the drives. Qubit B can only be driven when qubit A is at $|1\rangle$ state.

Next we perform some basic experiments to determine the parameters of the two-qubit gate. For example, we run Ramsey-type of measurements to measure the ZZ interaction and the single-qubit ac Stark shifts of a CZ gate. Then we confirm the two-qubit unitary with QPT and correct any erroneous Z rotations with virtual Z gates and adjust the controlled phase with pulse duration. In the end, we execute ORBIT on the two-qubit gate to fine tune the duration, DRAG coefficient and the virtual Z rotations. For non-Clifford gates, we used the sequence fidelity of the XEB measurement instead.

X & Y rotations only	with Z rotations
I	I
X_π	X_π
Y_π	X_π
Y_π, X_π	Z_π
$X_{\pi/2}, Y_{\pi/2}$	$Y_{\pi/2}, Z_{\pi/2}$
$X_{\pi/2}, Y_{-\pi/2}$	$Y_{-\pi/2}, Z_{-\pi/2}$
$X_{-\pi/2}, Y_{\pi/2}$	$Y_{\pi/2}, Z_{-\pi/2}$
$X_{-\pi/2}, Y_{-\pi/2}$	$Y_{-\pi/2}, Z_{\pi/2}$
$Y_{\pi/2}, X_{\pi/2}$	$X_{\pi/2}, Z_{-\pi/2}$
$Y_{\pi/2}, X_{-\pi/2}$	$X_{-\pi/2}, Z_{\pi/2}$
$Y_{-\pi/2}, X_{\pi/2}$	$X_{\pi/2}, Z_{\pi/2}$
$Y_{-\pi/2}, X_{-\pi/2}$	$X_{-\pi/2}, Z_{-\pi/2}$
$X_{\pi/2}$	$X_{\pi/2}$
$X_{-\pi/2}$	$X_{-\pi/2}$
$Y_{\pi/2}$	$Y_{\pi/2}$
$Y_{-\pi/2}$	$Y_{-\pi/2}$
$X_{-\pi/2}, Y_{\pi/2}, X_{\pi/2}$	$Z_{-\pi/2}$
$X_{-\pi/2}, Y_{-\pi/2}, X_{\pi/2}$	$Z_{\pi/2}$
$X_\pi, Y_{\pi/2}$	$Z_{\pi/2}, X_{\pi/2}, Z_{\pi/2}$
$X_\pi, Y_{-\pi/2}$	$Z_{\pi/2}, X_{-\pi/2}, Z_{\pi/2}$
$Y_\pi, X_{\pi/2}$	$Z_{-\pi/2}, Y_{\pi/2}, Z_{-\pi/2}$
$Y_\pi, X_{-\pi/2}$	$Z_{-\pi/2}, Y_{-\pi/2}, Z_{-\pi/2}$
$X_{\pi/2}, Y_{\pi/2}, X_{\pi/2}$	$Z_{-\pi/2}, X_\pi, Z_{-\pi}$
$X_{-\pi/2}, Y_{\pi/2}, X_{-\pi/2}$	$Z_{\pi/2}, X_\pi, Z_{-\pi}$

Table 4.2: Single-qubit Clifford gates. The Clifford gates can have different representations based on the pulse used in the experiment.

	T_1 (μs)	T_2^R (μs)	T_2^E (μs)
$\|00\rangle - \|10\rangle$	$158 - 207$	$10 - 12$	$14 - 15$
$\|00\rangle - \|01\rangle$	$116 - 141$	13	$20 - 25$
$\|11\rangle - \|21\rangle$	$4.9 - 6.2$	$2.6 - 2.8$	3.3

Table 4.3: Energy relaxation time T_1, Ramsey coherence time T_2^R, and spin echo coherence time T_2^E. The ranges corresponds to time fluctuations during the experiment.

Chapter 5

Summary

5.1 Fluorescence readout

We showed that a single macroscopic degree of freedom – the superconducting phase-difference – can combine a highly coherent qubit and its QND readout via conditional fluorescence, in full analogy with Dehmelt's electron shelving scheme. This first implementation of conditional readout by fluorescence in superconducting circuits relies on the high anharmonicity of the fluxonium circuit and does not require an additional degree of freedom like other implementations of V and lamda-shaped artificial atoms in circuit-QED [163]–[165]. The present experimental setup can be supplemented with quantum-limited linear amplifiers [166] or recently developed microwave photon counters [167]–[169] for a single-shot operation. Indeed, we measured readout histograms separated by a third of the standard deviation, a quantity that can be increased by a factor 10 by adding a quantum-limited amplifier, leading to measurement distributions overlapping by 1 %. With the current experimental parameters and the fluorescence integration time $\tau_m = 500$ ns, the resulting single-shot measurement would see 5 % of population leaving the ground state during readout. This amount can be reduced below the percent by a moderate increase of the QND-fidelity. Moreover a further increase of the capacitive coupling of the circuit to the waveguide will lead to larger readout coupling rates without affecting the qubit coherence time, which is limited by dielectric loss. Such improvements would make readouts based on conditional fluorescence comparable to state-of-the-art circuit-QED readouts using cavities.

Our approach offers the most direct interface between superconducting qubits and propagating microwave photons while maintaining near state-of-the-art coherence times. These properties make it a useful resource for quantum optics in the microwave range, with applications such as single photon emission and detection and photon routing controlled by

superposition of states [170], [171]. The possibility to route photons in a superposed way is particularly interesting and has not been demonstrated so far, as previous implementations rely on classical controls. From a waveguide QED point of view, the addition of a long-coherence memory transition paves the way to the preparation of highly-entangled state over a quantum network [172] and its use for quantum computation protocols such as teleported gates [173]. Finally our approach is compatible with a 2D implementation and offers high advantages over traditional cQED in terms of scalability, as readout resonators takes the most space due to their mode structure.

5.2 Two-qubit gates

The demonstrated all-microwave control over the ZZ-interaction is technologically attractive for scaling-up superconducting quantum processors. Our scheme has the following advantages. First, it does not require close arrangement of qubit frequencies, in contrast to the case of the cross-resonance (CR) gate [152], [174] for transmons, which would mitigate the spectral crowding issues [152], [175], allows tolerance to fabrication variability, and enables multiplexing of the qubit control. For example, here we used only one input port for the entire experiment. The qubit frequency could be as low as 100 MHz, as in our earlier demonstration of the CZ-gate [120], but it can also be around $200-500$ MHz (the main device here) or even $700-1300$ MHz (the second device here). Second, fluxonium's highly anharmonic spectra allow great flexibility of choosing drive frequencies and to operate the gate in the far-detuned regime, in which higher states are almost unoccupied during the gate operation, reducing leakage error and error due to decoherence of higher states. The required drive power is also comparable to single-qubit rotations [175]. This makes our method highly scalable. Third, our scheme does not require any additional circuitry as in schemes to cancel ZZ coupling using tunable couplers.

Among the previously explored two-qubit gates with a high degree of flexibility, our off-resonance CPhase gate scheme is reminiscent of the resonator-induced phase (RIP) gate [176]–[178] for transmons. The RIP gate populates an auxiliary bus mode with off-resonant photons to induce a differential Stark shift. In comparison, our CP gate requires no auxiliary modes or complex pulse-shaping, has closely-confined driven dynamics, and already enables a higher fidelity in devices with very sub-optimal coherence, all thanks to the strong anharmonicity of fluxoniums.

Dressing qubits with microwave drives to control their interaction opens up a new route to implement on-demand interaction in a qubit register. Similar methods for transmon qubits have been very recently reported by two groups [122], [123]. In both cases, the

ZZ coupling is controlled by driving off-resonantly computational transitions of superconducting circuits. Moreover, Ref. [123] successfully applied this technique to a multiqubit system, demonstrating the scalability of this approach.

Although the benchmarked fidelity of the two-qubit gates is already high in the experiments involving the high energy transition, the current experimental setup contains a number of imperfections, most of which can be eliminated in the next generation experiments. Let us start the discussion by briefly summarising these imperfections.

From the error estimation taking into account the Ramsey coherence times of transitions $|10\rangle - |20\rangle$ and $|11\rangle - |21\rangle$, they contribute to a significant portion both for the off-resonance CPhase gate and the near-resonance CZ gate. Even though the off-resonance CPhase gate can mitigate the decoherence from the higher levels by reducing the drive strength or increasing the detuning, such that the Stark-shifted dressed states have less high level components, this is at the cost of a longer gate time. We believe that the limited coherence time of transitions involving the second excited state is resulted from the relatively short T_1 due to suboptimal fabrication conditions. Importantly, fluxonium's $|1\rangle - |2\rangle$ transition is very similar in term of decoherence mechanisms to a transmon qubit transition [50] and we therefore expect no fundamental obstacles in reaching coherence times around $50 - 100$ μs in the future work.

In the computational subspace, coherence times can potentially exceed 500 μs, given the reported coherece times in Ref. [50]. However, here the qubit coherence time is only several tens of microseconds, even at their flux sweet-spots, which can be explained by the presence of about 5×10^{-3} thermal photons, on average, in the readout resonator. This dephasing source is generic to superconducting circuit experiments and it can be mitigated in the future with improved cryogenic filtering of the measurement lines [179], [180]. Currently the qubit coherence is also susceptible to the first order sensitivity to external flux noise caused by the sweet spot misalignment. The flux difference in the loop of two fluxoniums mainly originates from the magnetic defects in the environment and the magnetic field inhomogeneity of the coil. The sweet spot misalignment should be close to 0.1 % of the flux quanta in order to achieve optimal coherence simultaneously on the two qubits. For the 3D cavity architecture in our experiment, this problem can be solved by tilting the cavity, such that the flux difference coming from the coil can be adjusted to cancel out that from the defects. Another better solution would be to design the two-qubit closer to each other in space. It can be more robust in different magnetic environments. Of course, in the presence of the individual on-chip flux bias line for each qubit, this problem will disappear naturally. With improved qubit coherence, the two-qubit gates only relying on computational states should have much better performance. Our simulation shows that coherent gate errors

in the low 10^{-4}-range are possible for our device parameters and without sophisticated pulse optimization. Because a large drive strength is required for these type of gates, more investigation is needed to confirm whether the coherence could be degraded by the strong drive. Once we achieve such low gate errors, it is nor far from the large scale universal quantum computation.

Turning to our microwave packaging choice, we used a 3D cavity to perform all the gates for the sake of technical simplicity. However, it also generates significant classical cross-talk. The ground-shielding technique in the 2D architecture can enable selective addressing of each qubit and hence improve significantly the single qubit gates fidelity. We believe that scaling of our gate scheme can be done by moving to the 2D-circuit designs, in complete analogy with processors based on capacitively-coupled transmons [6], [181], [182]. Note, our experiment does not benefit from the usually high quality factors of 3D-resonators, and hence it is compatible with a traditional 2D-circuit technology without conceptual modifications.

The single-shot readout in our two-qubit gate experiment with 3D cavities has noticeable non-QND effect, which has not been fully understood yet. Evidence has shown that it is related to the high energy states in the system. Readout error is not less important than the gate error for a logical qubit in QEC. There has been studies [183] carried out to demonstrate that it is possible to perform QND readout with high fidelity on fluxonium qubits. Fully understanding the non-QND mechanism in the fluxonium-cavity system is necessary to achieve a fast and accurate readout operation.

Appendices

Appendix A

Simulation

A.1 Transmission simulation

We use Ansys HFSS to simulate transmission and reflection for a 3D enclosure (cavity, waveguide, etc.) using the driven modal solution. For example, Fig. A.1 shows the design of a waveguide. We set up a vacuum region with perfect conductor boundary condition. We assign wave port excitation conditions at the bottom of the ports, which have a ring shape interface. The S parameters are then simulated by calculating the electromagnetic field inside the box with finite element methods. The simulated S parameters at GHz range are given in Fig. A.2 for the waveguide. In our simulation, we optimize the reflection over various box dimensions and the launcher dimensions to make sure that S_{11} can be below -20 dB over the desired frequency range.

Similar simulation was carried out in a bandpass filter project. We call it a domino bandpass filter because it has many post-shape resonators sitting inside a tunnel (Fig. A.3). These resonators share similar resonant frequencies such that the modes can hybridize to form an energy band to let photons pass through. There are similar launchers at the entrance/exit to couple the travelling photons in the transmission line with the collective modes in the tunnel. The posts are not identical and their dimensions are optimized with a numerical algorithm. The external python script runs the simulation file, acquires the S parameters, and iterates the model dimensions. The optimal design can have GHz range flat pass-band. We machine the filter with the optimized parameters and measure the transmission and reflection with a VNA, as presented in Fig. A.4. The simulation agrees well with the measurements, demonstrating the accuracy of HFSS microwave simulation.

The purpose of this domino bandpass filter is to build a cryogenic broad band Purcell filter made of pure copper for good thermalization. On the other hand, the posts and the

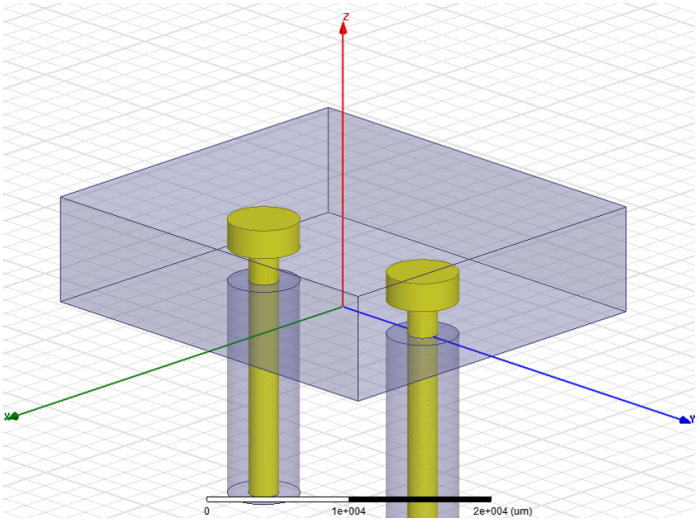

Figure A.1: Waveguide model in HFSS. Wave port excitation conditions are assigned at the bottom of the two ports. The other boundaries and the launchers (the yellow parts) are set to be perfect conductors.

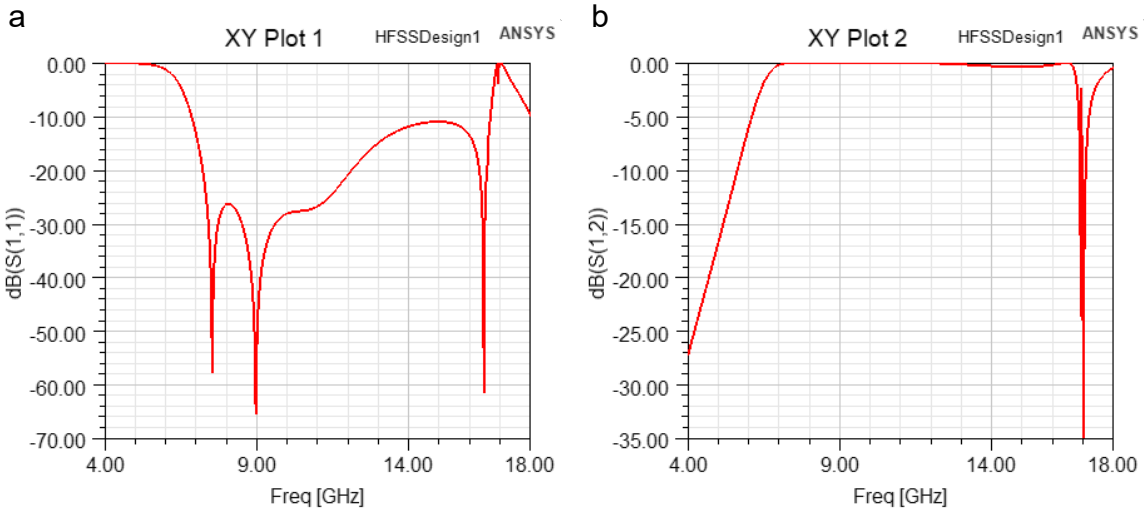

Figure A.2: S parameters simulation of a waveguide. (a) The reflection coefficient $|S_{11}|$. By optimizing the waveguide and the launcher dimensions, it can have a 5 GHz passband where the reflection is below -20 dB. (b) The transmission coefficient $|S_{12}|$. The transmission is flat and approaches 1 within the passband.

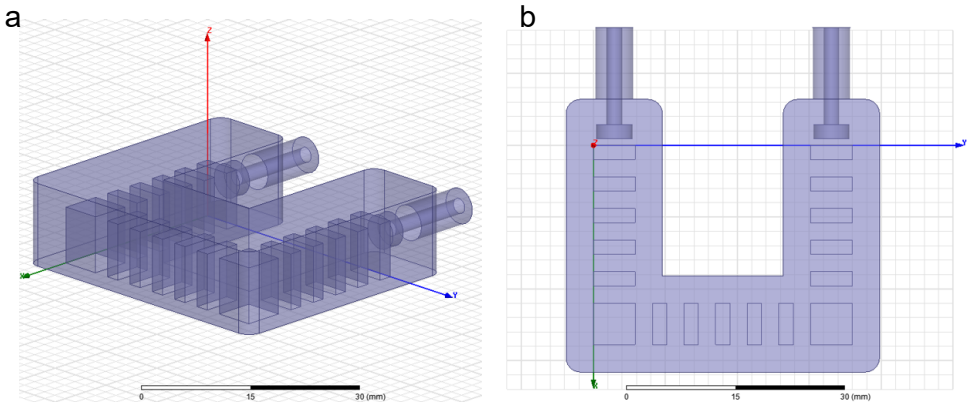

Figure A.3: Domino bandpass filter model in HFSS. (a) Side-view of the filter. Each post is a resonator and coupled to its neighbor. Together they form collective modes and a energy band. Within the band, the photon can travel freely from one post to the next just like dominoes. (b) Top-view of the filter. The launchers are designed to increase the coupling between the post and the transmission line. The dimensions of each post are the parameters to optimize the filter performance. They can be slightly different in order to have a flat passband.

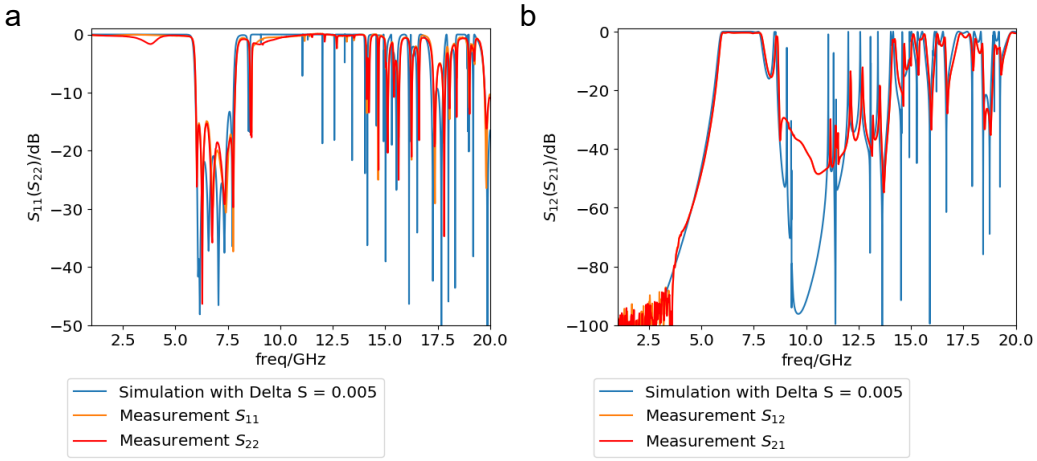

Figure A.4: Domino bandpass filter S parameters. (a) The reflection coefficients. Most resonances can be predicted by the simulation. The parameters are optimized such that the first energy band (around 7 GHz) has a large density of states. Within this passband, the measurements show low reflection coefficients from both ports. (b) Transmission coefficients. The transmission can be flat in GHz range and the simulation agrees well with the measurements.

meandering tunnel are expected to block possible high energy photons in the transmission line that can break the cooper pair and create quasiparticles on the device. However, this component still need more tests and we has not install it in any serious fluxonium experiments yet.

A.2 Coupling simulation

Besides, HFSS can simulate the capacitance and coupling between a lumped element and a resonant mode or the transmission line. For this purpose, we use the eigenmode solution. The qubit is treated as a harmonic oscillator by a lumped inductance connected with a pair of metallic pads (3D objects) as illustrated in Fig. A.5. The lumped inductance is a 2D square sheet assigned with a boundary condition with a specified L. Because the qubit structure is much smaller than the whole box, the mesh needs to be finer around the qubit area for a more accurate solution. The simulation gives the resonant modes in the system, including the 3D modes of the box and the qubit mode. The simulated mode is a complex number with the real part representing the resonant frequency and the imaginary part representing the decay rate. For a perfect conductor boundary condition, the imaginary part is zero. A resistive boundary condition can be assigned to simulate the quality factor of the box mode or the radiative decay rate of the qubit mode. The mode frequencies can be calculated with different lumped inductance L (see Fig. A.6). The mode that changes with L is the qubit mode and can be used to calculate the capacitance of the qubit antenna which gives the E_C in the qubit circuit. The qubit anti-crosses with the box mode that does not change with L. By subtracting the two mode frequencies, one can find the coupling strength between the qubit mode and the box mode.

One can assign a lumped 50 Ω resistance boundary at the ports which is equivalent to a infinitely long transmission line. The imaginary part suggests the radiative decay rate of the qubit. We simulate this in the waveguide experiment and find that it is consistent with the pass-band simulation from the S parameters. In addition, if the waveguide is a reflectional setup (i.e. with only one port open), standing waves are formed inside the box and at certain frequency the electromagnetic field vanishes near the qubit region (indicating a node at the qubit). In this case, the qubit radiation is suppressed (Fig. A.7).

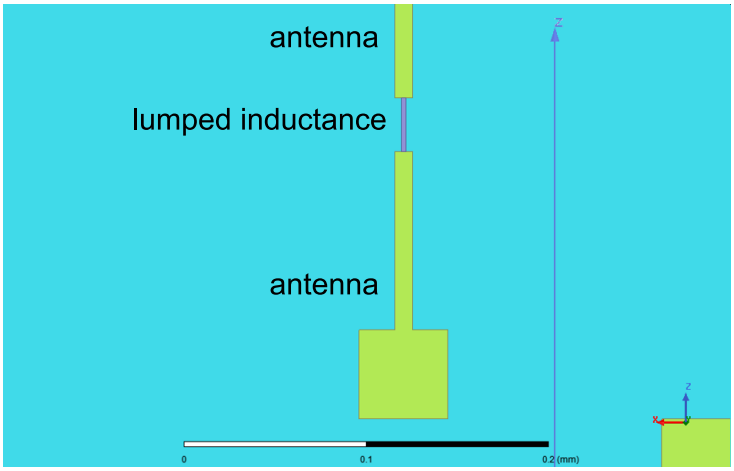

Figure A.5: Lumped inductance in HFSS. A lumped inductance boundary condition is assigned to the surface connecting two metallic antenna in the HFSS model to simulate the qubit. The mesh need to be finer here due to the small dimension compared to the copper box.

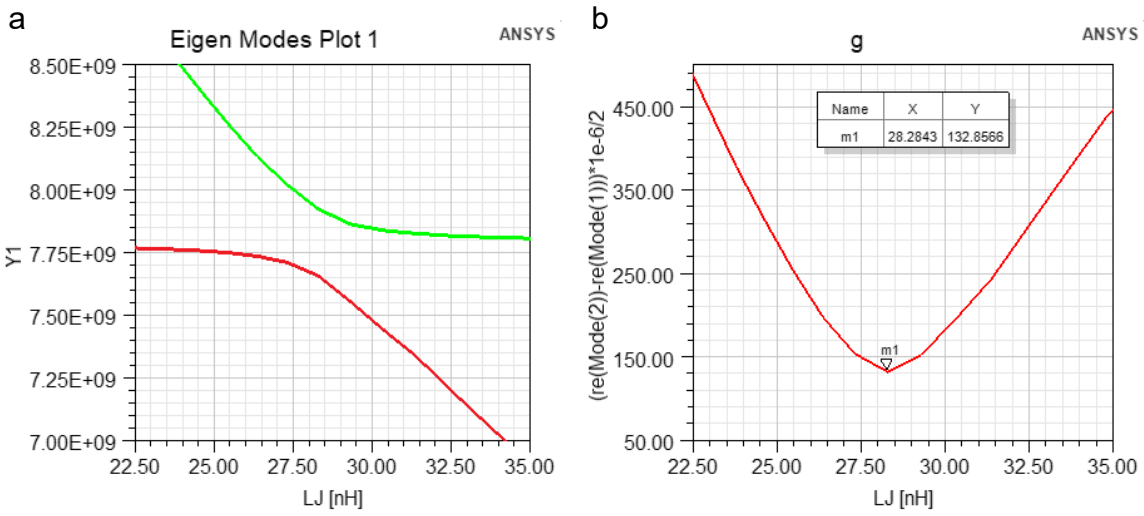

Figure A.6: Simulation of qubit capacitance and coupling strength to the cavity. (a) Simulated mode frequency versus the lumped inductance. A resonant qubit mode is formed with the capacitance from the antenna and the lumped inductance. This mode anti-crosses with the cavity mode which does not change with the lumped inductance. The antenna capacitance can be calculated with the qubit mode frequency away from the anti-crossing. (b) Frequency difference of the simulated two modes. At the anti-crossing point, the frequency difference is at its minimal and can be used to calculate the coupling strength g.

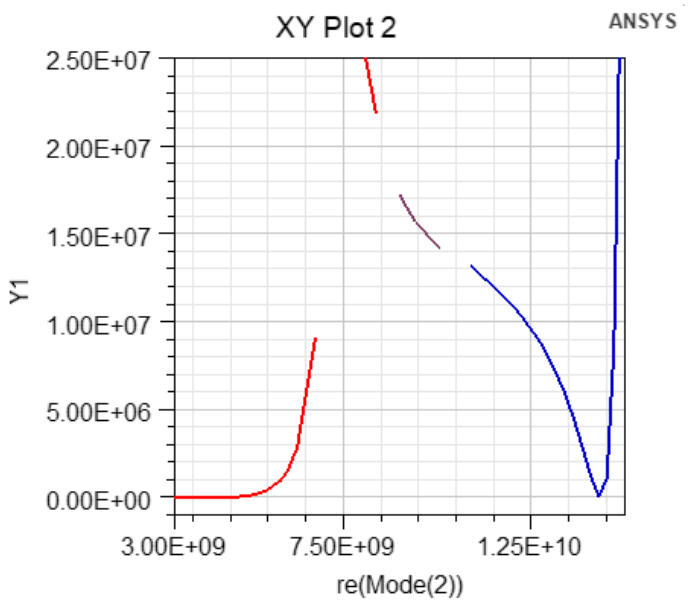

Figure A.7: Simulation of radiative decay rate of a qubit inside a waveguide. The radiative decay rate can be simulated by assigning a 50 Ω lumped resistance boundary condition at the port which is equivalent to a infinitely long transmission line. The simulated modes are complex numbers. The real part is the mode frequency and the imaginary part is the decay rate.

A.3 Fluxonium simulation

We use Qutip python package to simulate fluxonium spectrum and dynamics. We start by constructing the basic quantum operator. The phase and charge operators are expressed as the position and momentum operator in the harmonic oscillator basis. We first diagonalize the single-fluxonium Hamiltonian using a relatively large Hilbert space and use part of the eigenstates with low energy for the coupling Hamiltonian. We use the sesolve method to simulate the unitary evolution for the four computational states in a two-qubit system.

Appendix B

Experiment techniques

B.1 Fabrication

The fabrication process starts from dicing the wafer. We use the high resistivity silicon wafer or sapphire wafer for the device. For silicon samples, we dip in inside the water-ammonium fluoride-hydrofluoric acid solution (Buffer HF Improved from Transene, Inc.) for 2 min to remove the native oxide layer on the surface. The silicon chip treated with this buffer oxide etch (BOE) is expected to have lower dielectric loss tangents. Then we rinse the silicon chip with DI water.

Before spin coating the ebeam resists, we sonicate the chip inside acetone and IPA for 3 min each and blow dry it with nitrogen gas. We apply a layer of MMA EL 13 by spinning at 5000 rpm for 1 min and bake the chip on a hot plate at 180 °C for 1 min. We then apply a layer of 950 PMMA A3 by spinning at 4000 rpm for 1 min and bake it at the same temperature for 30 min.

The fluxoniums are fabricated with the Dolan bridge technique. We do ebeam lithography to write patterns on the resists. For sapphire wafer, this requires an anti-charging layer to remove the accumulated charge during the ebeam writing because sapphire is an insulator. The anti-charging layer is a 11 nm aluminum layer deposited in Plassys. After writing, it is removed by etching the aluminium in potassium hydroxide (KOH) solution. We use Elionix to expose the resist with 100 kV electron beam. Most of the structures are exposed with 1 nA current, except that the long couplers are exposed with 20 nA or 100 nA current.

We develop the mask with a IPA and DI water solution which has 3:1 (IPA:water) volume ratio. The developer is daily kept inside a thermostat at 6 °C. When developing, we create a simple water bath environment for the beaker by adding ice to 200 mL water to keep it

around 6 °C. The chip is dipped inside the developer for 2 min and then visually checked under the microscope.

Then we put the chip into Plassys for deposition and oxidation. The first layer is 20 nm Al deposited at 1 nm/s at an angle of 23.83 °C. Next, oxygen flows into the chamber and the Al layer gets oxidized at 100 mbar for 10 min. After that, oxygen is pumped out. A second layer of Al with 40 nm is deposited at 1 nm/s at an angle of -23.83 °C. Finally we take out the device and start the liftoff process. The chip is submerged in acetone and baked at 60 °C for 3 hr.

Because the optimal ebeam doses change with the machine status or device design. We perform dose tests when necessary. This can be done with different sizes of junctions and doses of the critical region. We also find that the plasma frequency of our junction can drift by a factor of two throughout the year. It is suspected this is related to the change of the ambient humidity. After a device is fabricated, it can age at the atmosphere. The plasma frequency goes down and $0-1$ transition frequency at half flux quanta goes up. It is possible that qubit frequency increase by 10 % in a month. To target the qubit frequency within the desirable range, apart from carefully controlling the fabrication condition to reach consistency, the laser annealing technique attracts more interests recently [184], [185].

B.2 3D cavity

We run HFSS simulation introduced in Appendix A to determine the dimension of the 3D cavity. The cavity is manufactured with CNC machining using copper 101. The cavity is polished with sand paper and Dremel tool. We also tried electropolishing but did not see significant improvement on qubit coherence yet. We typically use non-magnetic connectors at the input and output ports if available. A thin copper wire is soldered with the pin of the connector. It reaches inside the box to couple to the cavity mode. By adjusting the length of the wire, we can approximately have the wanted external quality factor by fitting the reflection with Eq. 3.1. Because we use indium wire to seal the connectors, the measured external quality factor can change with or without the indium seal due to 1 mm level of change on the length of the wire inside the box. Therefore, it is better to seal the connectors first and adjusting the length of the wire by cutting it if it is too long. The input port and output port are on different parts of the cavity. When we measure the external quality factor of one port on one part, we use the other part from a spare cavity without ports to prevent the cavity mode from being modified by a long pin. After preparing the ports, we mount the chip in the cavity by sandwiching small pieces of indium wire for better thermal contact and also securing the chip in place. Finally the cavity is sealed with indium

and clamped with a vice to make sure the indium has a tight contact with other surfaces.

B.3 Cryogenic setup

The wiring diagram for the two-qubit experiment is presented in Fig. B.1. The experiment was carried out in Bluefors LD 250 cryogen-free dilution refrigerator (DR). As explained in Sec. 3.3, we need multi-stage amplification on the readout line and multiple cryogenic circulators are installed to prevent the noise propagating in the reverse direction. Ideally, the attenuators on the driving line should be all placed at the base plate for minimum added noise. But due to the cooling power of each plate, the attenuators are also distributed on multiple stages. We can simulate the thermal photon numbers of the setup depicted in Fig. B.1 with the formalism introduced in Sec. 3.3. The dashed curves with different color in Fig. B.2a show the attenuated thermal photons coming from the attenuators at different temperature. Even though the thermal photons from room temperature and 3 K plate are attenuated heavily, they are still the dominant contributors of the noise. At 7.5 GHz, which is the typical cavity frequency, the total photon number is 1.7e-3, corresponding to an effective temperature of 56 mK. However, this is only the ideal case because the real temperature of the attenuators should be higher than that of the fridge plates. Additional attenuation at base temperature is required for lower thermal photon number and hence higher qubit coherence. At the same time, one also need to make sure the attenuators are well thermalized and driving power will not heat up the fridge.

We use homemade Eccosorb filters (see Fig. B.3) on the driving line to absorb high energy photons that can leads to quasiparticle loss on the qubit. Eccosorb CR 110 has low loss at GHz range and starts heavy attenuation above 100 GHz [186]. The 4.8 mm diameter through-hole of the copper body is designed to match the 50 Ω impedance based on the relative permittivity of Eccosorb CR 110 [187]. The connectors are sealed with indium. We pot Eccosorb in the through-hole and bake it at around 100 °C for lower viscosity and shorter cure time.

We wind long superconducting (SC) wires T48B-SW-M using a drill around a brass cylinder body to make the coil. The wire diameter is 0.102 mm and the total room temperature resistance is 7.85 kΩ. The incoming wire and the outgoing wire are anchored onto the coil body with stycast 2850 and are twisted together where they leave the coil to cancel out stray magnetic field. We use manganin wire as the guiding wire because manganin wire is thicker and more visible while the SC wire is very fragile. The wires are thermalized onto the posts (screws) at the 100 mK and 4K plates using GE varnish. Above the 4 K plate, the wires are soldered to a connector which connects to normal wires. On our setup, we notice

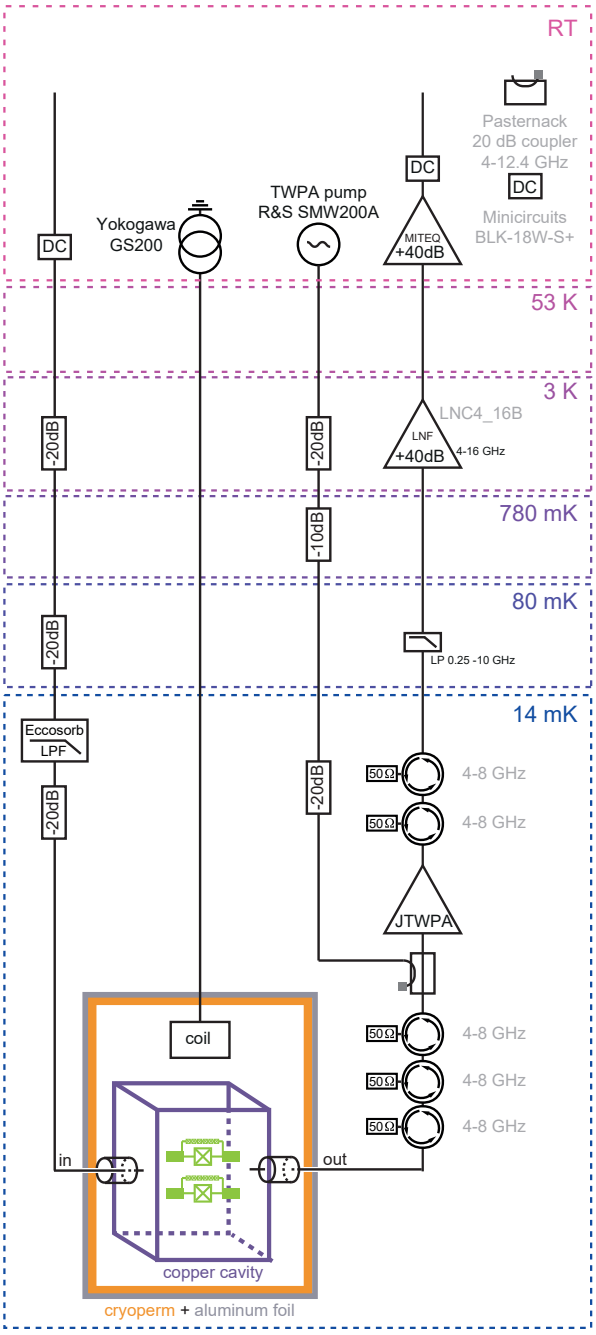

Figure B.1: Low temperature wiring diagram of the two qubit experiment. The thermal photons are attenuated by multi-stage attenuators. The readout signal is amplified by multi-stage amplifiers. The circulators are necessary to keep out the amplifier back amplification and the thermal noise.

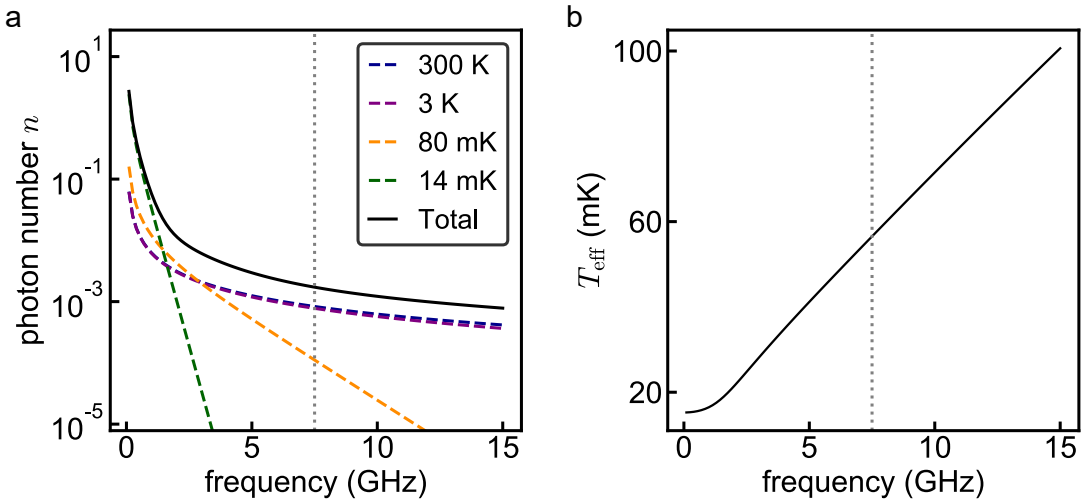

Figure B.2: Thermal photon number simulation. (a) Thermal photon numbers from different stages. Each stage attenuates the thermal photons from the upper stages and also radiates the photons at its own temperature. The thermal photon number (black line) seen by the cavity is a summation of all the stages. The dotted vertical line indicates the cavity frequency at 7.5 GHz and the photon number at this frequency is 1.7e-3. (b) Effective temperature calculated from the total thermal photon numbers. Even though the effective temperature is higher at the high frequency, the actual photon number is lower. The effective temperature at 7.5 GHz is 56 mK.

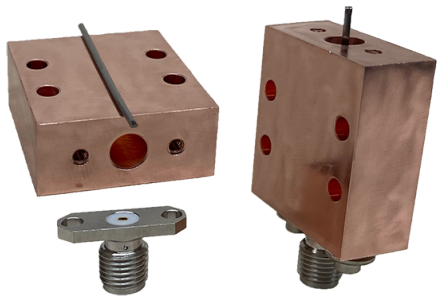

Figure B.3: Homemade Eccosorb filter. The homemade Eccosorb filter is assembled with a copper body, two stainless steel SMA connectors on each side and a stainless steel center pin. After mounting one connector and the center pin, Eccosorb CR110 is potted around the pin. When fully cured, the other connector can be installed. There are four free-fit 4-40 screw holes on the copper body for being mounted onto the cold fingers and thermalized.

the fridge temperature will have noticeable increase when the coil current is above 30 mA.

B.4 Room temperature setup

We used two different room temperature heterodyne setups as described in Fig. B.4. In Fig. B.4a, we use a single-sideband-mixer (SSB) to mix down the RF source frequency f_{LO} to $f_r = f_{\mathrm{LO}} - f_{\mathrm{mod}}$ before the signal goes into the fridge. On the other hand, the same RF source acts as the local oscillator and mixes with the readout signal coming from the fridge at the IQ mixer. Both I and Q channels are demodulated and their combination can cancel out the noise at $f_r = f_{\mathrm{LO}} + f_{\mathrm{mod}}$. To prove this, we can assume the signal coming out of the RF source is $S_{\mathrm{LO}} = A_{\mathrm{LO}} \cos(2\pi f_{\mathrm{LO}} t + \varphi_1)$, where φ_1 is an arbitrary phase offset. The readout signal coming out of the fridge is $S_{\mathrm{out}} = A_{\mathrm{out}} \cos(2\pi f_r t + \varphi_1 + \Delta\varphi)$, where $\Delta\varphi$ is dependent on the measurement line and the device. Then let's consider the noise components at frequency $f_{\mathrm{LO}} \pm f_{\mathrm{mod}}$, as they will go into the demodulated signal. So we write the total signal as

$$\begin{aligned} S_{\mathrm{out}} = A_{\mathrm{out}} \cos(2\pi f_r t + \varphi_1 + \Delta\varphi) + N_- \cos(2\pi (f_{\mathrm{LO}} - f_{\mathrm{mod}})t + \varphi_-) \\ + N_+ \cos(2\pi (f_{\mathrm{LO}} + f_{\mathrm{mod}})t + \varphi_+). \end{aligned} \tag{B.1}$$

After the IQ mixer, the I and Q channels can be written, without loss of generality, as

$$\begin{aligned} S_{\mathrm{I}} = B_{\mathrm{out}} \cos(2\pi f_{\mathrm{mod}} t - \Delta\varphi) + M_- \cos(2\pi f_{\mathrm{mod}} t + \varphi_1 - \varphi_-) \\ + M_+ \cos(-2\pi f_{\mathrm{mod}} t + \varphi_1 - \varphi_+), \end{aligned} \tag{B.2}$$

$$\begin{aligned} S_{\mathrm{Q}} = B_{\mathrm{out}} \sin(2\pi f_{\mathrm{mod}} t - \Delta\varphi) + M_- \sin(2\pi f_{\mathrm{mod}} t + \varphi_1 - \varphi_-) \\ + M_+ \sin(-2\pi f_{\mathrm{mod}} t + \varphi_1 - \varphi_+). \end{aligned} \tag{B.3}$$

We can demodulated the signal after digitizing the data and use phasor to represent the terms on the IQ plane.

$$s_{\mathrm{I}} = b_{\mathrm{out}} e^{-i\Delta\varphi} + m_- e^{i(\varphi_1 - \varphi_-)} + m_+ e^{-i(\varphi_1 - \varphi_+)}, \tag{B.4}$$

$$s_{\mathrm{Q}} = i b_{\mathrm{out}} e^{-i\Delta\varphi} + i m_- e^{i(\varphi_1 - \varphi_-)} - i m_+ e^{-i(\varphi_1 - \varphi_+)}. \tag{B.5}$$

Therefore we can keep $s = s_I - i s_Q = 2 b_{\mathrm{out}} e^{-i\Delta\varphi} + 2 m_- e^{i(\varphi_1 - \varphi_-)}$ to cancel out the noise component at $f_{\mathrm{LO}} \pm f_{\mathrm{mod}}$.

The other setup in Fig. B.4b, however, have two separate RF sources, one as the LO and the other as the readout tone. The readout RF source itself is connected to an AWG and is

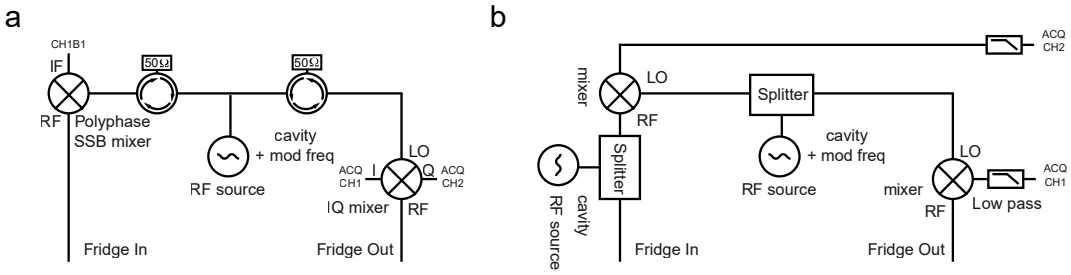

Figure B.4: Room temperature readout signal demodulation schemes. (a) The first scheme. The output signal from the RF source is cavity frequency plus the modulation frequency. It gets splitted with the SMA T-adapter. One way goes to the single-sideband (SSB) mixer and gets down-converted to the cavity frequency. The other way goes to the LO port of the IQ mixer and is used to mix down the signal from the fridge. (b) The second scheme. The left RF source is at cavity frequency. It gets splitted with a power splitter (Minicircuits ZFRSC-183-s+). One way directly goes to the fridge. The other way gets mixed with the LO as the phase reference channel.

IQ (and pulse) modulated. The two channels of the acquisition card are assigned as a signal channel and a reference channel to cancel out the relative phase fluctuation between the two RF sources. Compared to the setup above, this setup has more phase stability on the final demodulated value because the relative phase fluctuation on the AWG can be cancelled as well. This setup requires more RF sources but because we use the built-in IQ modulation on the readout RF, the output power can be much larger than the first setup.

Because we need to combine multiple microwave tones with large power in the fluxonium experiment, we used different microwave components to combine the signals. Minicircuits ZFRSC-183-S+ is a two-port power combiner and the total loss is about 7 dB. ZN4PD1-63HP-S+ is a four-port combiner with a similar loss. The SMA T adapter can be also used as a two-port power combiner with lower loss but the isolation is worse than the minicircuits one. The directional coupler is used as a combiner when one port can tolerate high attenuation (20 dB). In this way, the other port can send the signal almost without loss.

Appendix C

Derivations

C.1 Signal Gain for JPA

In this section, we are going to derive the signal gain for a JPA presented in Sec. 3.3.2 in a classical way. A quantum mechanical description can be found in Ref. [59]. The first step is to find the equation of motion (EOM) for the phase difference δ in Fig. 3.9. The total current is the sum of the current in the two branches $I = I_C + I_J$. Using the Josephson equations, we have

$$I_C = \frac{d(CV)}{dt} = C\phi_0 \frac{d^2\delta}{dt^2}, \tag{C.1}$$

$$I_J = I_0 \sin\delta. \tag{C.2}$$

On the other hand, for the propagating waves in a transmission line, the voltage and the current satisfy the following relation

$$I = I_{\text{in}} - I_{\text{out}}, \tag{C.3}$$

$$V = V_{\text{in}} + V_{\text{out}} = (I_{\text{in}} + I_{\text{out}})Z_c. \tag{C.4}$$

Combining Eq. C.3 and Eq. C.4,

$$I = 2I_{\text{in}} - V/Z_c = 2I_{\text{in}} - \frac{\phi_0}{Z_c}\frac{d\delta}{dt}. \tag{C.5}$$

Substituting Eq. C.1 and Eq. C.2 in to Eq. C.5, we have the EOM of the phase δ

$$C\phi_0\frac{d^2\delta(t)}{dt^2}+\frac{\phi_0}{Z_c}\frac{d\delta(t)}{dt}+I_0\sin\delta=2I_{\rm in}(t). \tag{C.6}$$

Let's keep the lowest non-linear term $\sin\delta\approx\delta-\delta^3/6$ and define $\omega_0^2=I_0/(C\phi_0)$, $\gamma=1/(2Z_cC)$. The EOM can be simplified as

$$\frac{d^2\delta(t)}{dt^2}+2\gamma\frac{d\delta(t)}{dt}+\omega_0^2(\delta(t)-\frac{\delta^3(t)}{6})=\frac{2I_{\rm in}(t)}{C\phi_0} \tag{C.7}$$

The incoming field can be separated into two parts – a large pump and a weak signal. $I_{\rm in}=I_{\rm pump}+I_{\rm signal}$. We can first neglect the signal and solve for the phase amplitude in the presence of the pump. Assuming $I_{\rm in}=I_{\rm pump}=I_p\cos(\omega_pt+\varphi)$ and $\delta=\delta_{\rm pump}=\delta_a\cos\omega_pt$, Eq. C.7 will lead to Eq. 3.25 in the main text

$$\left((\omega_0^2-\omega_p^2)\delta_a-\frac{\omega_0^2}{8}\delta_a^3\right)^2+(2\gamma\omega_p\delta_a)^2=\left(\frac{2I_p}{C\phi_0}\right)^2. \tag{C.8}$$

Here we neglect the fast rotating term and simplify δ^3 as

$$\delta^3=\delta_a^3\cos^3\omega_pt=\frac{\delta_a^3}{4}(3\cos\omega_pt+\cos3\omega_pt)\approx\frac{\delta_a^3}{4}3\cos\omega_pt \tag{C.9}$$

Next we can deal with the weak signal part assuming it does not affect the pump. We can write

$$I_{\rm in}=I_p\cos(\omega_pt+\varphi)+I_{\rm signal}, \tag{C.10}$$

$$\delta=\delta_a\cos\omega_pt+\delta_{\rm signal}. \tag{C.11}$$

Similarly from Eq. C.7, the EOM for the signal tone is

$$\frac{d^2\delta_{\rm signal}(t)}{dt^2}+2\gamma\frac{d\delta_{\rm signal}(t)}{dt}+\omega_1^2(t)\delta_{\rm signal}(t)=\frac{2}{C\phi_0}I_{\rm signal}(t). \tag{C.12}$$

$\omega_1(t)$ is defined as

$$\omega_1^2(t)=\omega_0^2\left(1-\frac{\delta_a^2}{4}+\frac{\delta_a^2}{4}\cos(2\omega_pt-2\varphi)\right) \tag{C.13}$$

The coefficient of the differential equation Eq. C.12 is time dependent. We can solve it in the frequency domain, or equivalently, by introducing the field operators.

$$I_{\text{signal}}(t) = \sqrt{\frac{\hbar}{2Z_c}} \int_0^\infty \frac{d\omega}{2\pi} \sqrt{\omega} a_{\text{in}}(\omega) e^{-i\omega t} + \text{h.c.}, \tag{C.14}$$

$$\delta_{\text{signal}}(t) = \int_0^\infty \frac{d\omega}{2\pi} \delta_s(\omega) e^{-i\omega t} + \text{h.c.}. \tag{C.15}$$

In this way, Eq. C.12 becomes

$$(\omega_0^2(1-\epsilon) - \omega^2 - i2\gamma\omega)\delta_s(\omega) - \frac{\omega_0^2\epsilon}{2} e^{2i\varphi} \delta_s^\dagger(2\omega_p - \omega) = \frac{4\gamma\sqrt{Z_c}}{\phi_0} \sqrt{\frac{\hbar\omega}{2}} a_{\text{in}}(\omega), \tag{C.16}$$

where $\epsilon = \delta_a^2/4$. We can define $\omega' = \omega - \omega_p$ as the detuning between the signal mode and the pump tone. The operator of the internal field in the JPA circuit is

$$c(\omega') = \sqrt{\frac{2E_J}{\hbar\omega_0}} \delta_s(\omega_p + \omega'). \tag{C.17}$$

The field operators of the input and output signal are $c_{\text{in(out)}}(\omega') = a_{\text{in(out)}}(\omega_p + \omega')$. With the new field operators, Eq. C.16 yields

$$(\omega_0 - \omega_p - \omega' - \frac{\omega_0\epsilon}{2} - i\gamma)c(\omega') - \frac{\omega_0\epsilon}{4} e^{2i\varphi} c^\dagger(-\omega') = \sqrt{2\gamma} c_{\text{in}}(\omega'). \tag{C.18}$$

From the input-output theory (or the boundary condition Eq. C.4 equivalently), we have $c_{\text{out}}(\omega') + c_{\text{in}}(\omega') = -i\sqrt{2\gamma}c(\omega')$. Then we can get rid of the internal field operator $c(\omega')$ and express c_{out} in terms of c_{in}

$$c_{\text{out}}(\omega') = \left(-1 + \frac{2\gamma(-i\omega' - i(\omega_0 - \omega_p) + \gamma - i\omega_0\epsilon/2)}{(-i\omega' + \lambda_0)(-i\omega' + \lambda_1)}\right) c_{\text{in}}(\omega') \tag{C.19}$$

$$+ \frac{\gamma e^{2i\varphi}\omega_0\epsilon/2}{(-i\omega' + \lambda_0)(-i\omega' + \lambda_1)} c_{\text{in}}^\dagger(-\omega'), \tag{C.20}$$

$$= \mathcal{G}(\omega') c_{\text{in}}(\omega') + \mathcal{M}(\omega') c_{\text{in}}^\dagger(-\omega'), \tag{C.21}$$

which is Eq. C.19 in the main text. The parameter $\lambda_{0/1}$ is

$$\lambda_{0/1} = \gamma \mp \sqrt{\frac{\omega_0^2\epsilon^2}{16} - \left(\omega_0 - \omega_p - \frac{\omega_0\epsilon}{2}\right)^2}. \tag{C.22}$$

C.2 Schrieffer-Wolf Transformation

Imagine a Hamiltonian with a low-energy manifold and a high-energy manifold. If there is an inter-manifold coupling, we can apply Schrieffer-Wolf transformation to find an effective intra-manifold coupling. To clarify this point, we take the $00-11$ two-photon transition introduced in Sec. 4.3.3 for an example. We denote the unperturbed Hamiltonian by H_0

$$H_0 = \begin{pmatrix} \epsilon_{00} & 0 & 0 & 0 \\ 0 & \epsilon_{01} & 0 & 0 \\ 0 & 0 & \epsilon_{10} & 0 \\ 0 & 0 & 0 & \epsilon_{11} \end{pmatrix}. \tag{C.23}$$

Inside the bSWAP gate frame (see Eq. 4.49), $|00\rangle$ and $|11\rangle$ become almost degenerate ($|\delta| << |\Delta|$)

$$H_0 = \begin{pmatrix} \delta & 0 & 0 & 0 \\ 0 & \Delta & 0 & 0 \\ 0 & 0 & -\Delta & 0 \\ 0 & 0 & 0 & -\delta \end{pmatrix}. \tag{C.24}$$

We can rearrange the order of the basis

$$H_0 = \begin{pmatrix} \delta & 0 & 0 & 0 \\ 0 & -\delta & 0 & 0 \\ 0 & 0 & \Delta & 0 \\ 0 & 0 & 0 & -\Delta \end{pmatrix}, \tag{C.25}$$

such that the upper left block is the low-energy manifold and the lower right block is the high-energy manifold. Therefore, we can write the total Hamiltonian in the form of

$$H = H_0 + V = \begin{pmatrix} H_{0l} & 0 \\ 0 & H_{0h} \end{pmatrix} + \begin{pmatrix} 0 & V_{lh} \\ V_{hl} & V_{hh} \end{pmatrix}, \tag{C.26}$$

where V is the driving term. Because $V = V^\dagger$, we can know $V_{hl} = V_{lh}^\dagger$. The drive near the two-photon transition frequency ($\sim (\tilde{\omega}_A + \tilde{\omega}_B)/2$) provides a coupling term connecting the two manifolds. It can not exchange population between them because of large detuning. However, this coupling effectively links $|00\rangle$ and $|11\rangle$ in the low-energy manifold. The dynamics can be solved by treating the driving term as a perturbation and block-diagonalizing

H. We can assume

$$H_{\text{eff}} = \exp(iS)(H_0 + V)\exp(-iS) = \begin{pmatrix} H_l^{\text{eff}} & 0 \\ 0 & H_h^{\text{eff}} \end{pmatrix}, \tag{C.27}$$

and $S = S^{(1)} + S^{(2)} + O(V^3)$. Similarly, $H_{\text{eff}} = H_0 + H_{\text{eff}}^{(1)} + H_{\text{eff}}^{(2)} + O(V^3)$. Neglecting the high order terms,

$$H_{\text{eff}} = [1 + iS^{(1)} + iS^{(2)} - \frac{1}{2}\left(S^{(1)}\right)^2](H_0 + V)[1 - iS^{(1)} - iS^{(2)} - \frac{1}{2}\left(S^{(1)}\right)^2] + \cdots . \tag{C.28}$$

Therefore

$$H_{\text{eff}}^{(1)} = i[S^{(1)}, H_0] + V \tag{C.29}$$

$$H_{\text{eff}}^{(2)} = i[S^{(2)}, H_0] - \frac{1}{2}\left(S^{(1)}\right)^2 H_0 - \frac{1}{2}H_0\left(S^{(1)}\right)^2 + S^{(1)}H_0S^{(1)} + i[S^{(1)}, V]. \tag{C.30}$$

We assume $S^{(1)}$ takes the form of

$$S^{(1)} = \begin{pmatrix} 0 & S_{lh}^{(1)} \\ S_{hl}^{(1)} & 0 \end{pmatrix}. \tag{C.31}$$

The first order term of the effective Hamiltonian is

$$H_{\text{eff}}^{(1)} = \begin{pmatrix} 0 & i(S_{lh}^{(1)}H_{0h} - H_{0l}S_{lh}^{(1)}) + V_{lh} \\ i(S_{hl}^{(1)}H_{0l} - H_{0h}S_{hl}^{(1)}) + V_{hl} & V_{hh} \end{pmatrix}. \tag{C.32}$$

Block-diagonalization requires

$$i\left(S_{lh}^{(1)}H_{0h} - H_{0l}S_{lh}^{(1)}\right) + V_{lh} = 0, \tag{C.33}$$

$$i\left(S_{hl}^{(1)}H_{0l} - H_{0h}S_{hl}^{(1)}\right) + V_{hl} = 0. \tag{C.34}$$

These conditions can be used to determine $S_{lh}^{(1)}$ and $S_{hl}^{(1)}$. In our example, $S_{lh}^{(1)}$ and $S_{hl}^{(1)}$ are 2×2 matrices. Assume $|p\rangle$ and $|q\rangle$ are the low and high energy eigenstates of H_0 in Eq. C.25 with energy E_p and E_q. The matrix elements of $S_{lh}^{(1)}$ can be calculated with

$$\langle p|\, S_{lh}^{(1)}\, |q\rangle = -i\frac{\langle p|\, V_{lh}\, |q\rangle}{E_p - E_q}, \tag{C.35}$$

and $S^{(1)}_{hl} = \left(S^{(1)}_{lh}\right)^\dagger$. After obtaining $S^{(1)}$, we can check the second order term $H^{(2)}_{\text{eff}}$. Here we list all the terms in Eq. C.30 explicitly.

$$i[S^{(2)}, H_0] = \begin{pmatrix} 0 & i\left(S^{(2)}_{lh} H_{0h} - H_{0l} S^{(2)}_{lh}\right) \\ i\left(S^{(2)}_{hl} H_{0l} - H_{0h} S^{(2)}_{hl}\right) & 0 \end{pmatrix}, \tag{C.36}$$

$$-\frac{1}{2}\left(S^{(1)}\right)^2 H_0 - \frac{1}{2} H_0 \left(S^{(1)}\right)^2 = -\frac{1}{2}\begin{pmatrix} S^{(1)}_{lh} S^{(1)}_{hl} H_{0l} + H_{0l} S^{(1)}_{lh} S^{(1)}_{hl} & 0 \\ 0 & S^{(1)}_{hl} S^{(1)}_{lh} H_{0h} + H_{0h} S^{(1)}_{hl} S^{(1)}_{lh} \end{pmatrix}, \tag{C.37}$$

$$S^{(1)} H_0 S^{(1)} = \frac{1}{2}\begin{pmatrix} S^{(1)}_{lh} H_{0h} S^{(1)}_{hl} & 0 \\ 0 & S^{(1)}_{hl} H_{0l} S^{(1)}_{lh} \end{pmatrix}, \tag{C.38}$$

$$i[S^{(1)}, V] = \begin{pmatrix} i\left(S^{(1)}_{lh} V_{hl} - V_{lh} S^{(1)}_{hl}\right) & i S^{(1)}_{lh} V_{hh} \\ -i V_{hh} S^{(1)}_{hl} & i\left(S^{(1)}_{hl} V_{lh} - V_{hl} S^{(1)}_{lh}\right) \end{pmatrix}. \tag{C.39}$$

Similarly, block-diagonalization requires

$$i\left(S^{(2)}_{lh} H_{0h} - H_{0l} S^{(2)}_{lh}\right) + i S^{(1)}_{lh} V_{hh} = 0, \tag{C.40}$$

$$i\left(S^{(2)}_{hl} H_{0l} - H_{0h} S^{(2)}_{hl}\right) - i V_{hh} S^{(1)}_{hl} = 0. \tag{C.41}$$

$S^{(2)}$ can be determined from the above equations. Fortunately we don't need to solve them in our case because the diagonal terms does not depend on $S^{(2)}$. Additionally, $V_{hh} = 0$ in our example. This makes the problem simpler and we have

$$H^{(2)}_{\text{eff}} = -\frac{1}{2}\left(S^{(1)}\right)^2 H_0 - \frac{1}{2} H_0 \left(S^{(1)}\right)^2 + S^{(1)} H_0 S^{(1)} + i[S^{(1)}, V]. \tag{C.42}$$

The last step is to change the basis order back and we can arrive at Eq. 4.50 in Sec. 4.3.3.

Bibliography

[1] J. Preskill, "Quantum computing 40 years later," pp. 1–49, Jun. 2021.

[2] P. Benioff, "The computer as a physical system: A microscopic quantum mechanical Hamiltonian model of computers as represented by Turing machines," *Journal of Statistical Physics*, vol. 22, no. 5, pp. 563–591, 1980, ISSN: 00224715. DOI: 10.1007/BF01011339.

[3] F. Arute, K. Arya, R. Babbush, *et al.*, "Quantum supremacy using a programmable superconducting processor," *Nature*, vol. 574, no. 7779, pp. 505–510, 2019, ISSN: 14764687. DOI: 10.1038/s41586-019-1666-5.

[4] Z. Chen, K. J. Satzinger, J. Atalaya, *et al.*, "Exponential suppression of bit or phase errors with cyclic error correction," *Nature*, vol. 595, no. 7867, pp. 383–387, Jul. 2021, ISSN: 0028-0836. DOI: 10.1038/s41586-021-03588-y.

[5] R. Barends, A. Shabani, L. Lamata, *et al.*, "Digitized adiabatic quantum computing with a superconducting circuit," *Nature*, vol. 534, no. 7606, pp. 222–226, 2016, ISSN: 14764687. DOI: 10.1038/nature17658.

[6] A. Kandala, A. Mezzacapo, K. Temme, M. Takita, M. Brink, J. M. Chow, and J. M. Gambetta, "Hardware-efficient variational quantum eigensolver for small molecules and quantum magnets," *Nature*, vol. 549, no. 7671, pp. 242–246, 2017, ISSN: 14764687. DOI: 10.1038/nature23879.

[7] I. Aleiner, F. Arute, K. Arya, *et al.*, "Accurately computing electronic properties of materials using eigenenergies," *arXiv*, 2020.

[8] C. D. Bruzewicz, J. Chiaverini, R. McConnell, and J. M. Sage, "Trapped-ion quantum computing: Progress and challenges," *Applied Physics Reviews*, vol. 6, no. 2, 2019, ISSN: 19319401. DOI: 10.1063/1.5088164.

[9] Z. Leghtas, G. Kirchmair, B. Vlastakis, R. J. Schoelkopf, M. H. Devoret, and M. Mirrahimi, "Hardware-efficient autonomous quantum memory protection," *Physical Review Letters*, vol. 111, no. 12, pp. 1–5, 2013, ISSN: 00319007. DOI: 10.1103/PhysRevLett.111.120501.

[10] N. Ofek, A. Petrenko, R. Heeres, *et al.*, "Extending the lifetime of a quantum bit with error correction in superconducting circuits," *Nature*, vol. 536, no. 7617, pp. 441–445, 2016, ISSN: 14764687. DOI: 10.1038/nature18949.

[11] A. Grimm, N. E. Frattini, S. Puri, S. O. Mundhada, S. Touzard, M. Mirrahimi, S. M. Girvin, S. Shankar, and M. H. Devoret, "Stabilization and operation of a Kerr-cat qubit," *Nature*, vol. 584, no. 7820, pp. 205–209, 2020, ISSN: 14764687. DOI: 10.1038/s41586-020-2587-z.

[12] W. B. Gao, X. C. Yao, J. M. Cai, H. Lu, P. Xu, T. Yang, C. Y. Lu, Y. A. Chen, Z. B. Chen, and J. W. Pan, "Experimental measurement-based quantum computing beyond the cluster-state model," *Nature Photonics*, vol. 5, no. 2, pp. 117–123, 2011, ISSN: 17494885. DOI: 10.1038/nphoton.2010.283.

[13] A. Wallraff, D. I. Schuster, A. Blais, L. Frunzio, R. S. Huang, J. Majer, S. Kumar, S. M. Girvin, and R. J. Schoelkopf, "Strong coupling of a single photon to a superconducting qubit using circuit quantum electrodynamics," *Nature*, vol. 431, no. 7005, pp. 162–167, 2004, ISSN: 00280836. DOI: 10.1038/nature02851.

[14] A. Blais, R. S. Huang, A. Wallraff, S. M. Girvin, and R. J. Schoelkopf, "Cavity quantum electrodynamics for superconducting electrical circuits: An architecture for quantum computation," *Physical Review A - Atomic, Molecular, and Optical Physics*, vol. 69, no. 6, pp. 1–14, 2004, ISSN: 10502947. DOI: 10.1103/PhysRevA.69.062320.

[15] D. I. Schuster, "Circuit Quantum Electrodynamics," Ph.D. dissertation, 2007.

[16] V. Bouchiat, D. Vion, P. Joyez, D. Esteve, and M. H. Devoret, "Quantum Coherence with a Single Cooper Pair," *Physica Scripta*, vol. T76, no. 1, p. 165, 1998, ISSN: 0031-8949. DOI: 10.1238/Physica.Topical.076a00165.

[17] Y. Nakamura, Y. A. Pashkin, and J. S. Tsai, "Coherent control of macroscopic quantum states in a single-Cooper-pair box," *Nature*, vol. 398, no. 6730, pp. 786–788, Apr. 1999, ISSN: 0028-0836. DOI: 10.1038/19718.

[18] M. H. Devoret, *Quantum fluctuations in electrical circuits*, S. Reynaud, E. Giacobino, and J. Zinn-Justin, Eds. Elsevier Science, 1997, pp. 351–386.

[19] S. E. Nigg, H. Paik, B. Vlastakis, G. Kirchmair, S. Shankar, L. Frunzio, M. H. Devoret, R. J. Schoelkopf, and S. M. Girvin, "Black-Box Superconducting Circuit Quantization," *Physical Review Letters*, vol. 108, no. 24, p. 240 502, Jun. 2012, ISSN: 0031-9007. DOI: 10.1103/PhysRevLett.108.240502.

[20] U. Vool and M. Devoret, "Introduction to quantum electromagnetic circuits," *International Journal of Circuit Theory and Applications*, vol. 45, no. 7, pp. 897–934, 2017, ISSN: 1097007X. DOI: 10.1002/cta.2359.

[21] I. Chiorescu, Y. Nakamura, C. J. Harmans, and J. E. Mooij, "Coherent quantum dynamics of a superconducting flux qubit," *Science*, vol. 299, no. 5614, pp. 1869–1871, 2003, ISSN: 00368075. DOI: 10.1126/science.1081045.

[22] J. M. Martinis, M. H. Devoret, and J. Clarke, "Energy-level quantization in the zero-voltage state of a current-biased Josephson junction," *Physical Review Letters*, vol. 55, no. 15, pp. 1543–1546, 1985, ISSN: 00319007. DOI: 10.1103/PhysRevLett.55.1543.

[23] J. Koch, T. M. Yu, J. Gambetta, A. A. Houck, D. I. Schuster, J. Majer, A. Blais, M. H. Devoret, S. M. Girvin, and R. J. Schoelkopf, "Charge-insensitive qubit design derived from the Cooper pair box," *Physical Review A*, vol. 76, no. 4, p. 042 319, Oct. 2007, ISSN: 1050-2947. DOI: 10.1103/PhysRevA.76.042319.

[24] V. E. Manucharyan, J. Koch, L. I. Glazman, and M. H. Devoret, "Fluxonium: Single cooper-pair circuit free of charge offsets," *Science*, vol. 326, no. 5949, pp. 113–116, Oct. 2009, ISSN: 00368075. DOI: 10.1126/science.1175552.

[25] F. Yan, S. Gustavsson, A. Kamal, *et al.*, "The flux qubit revisited to enhance coherence and reproducibility," *Nature Communications*, vol. 7, pp. 1–9, 2016, ISSN: 20411723. DOI: 10.1038/ncomms12964.

[26] A. Gyenis, P. S. Mundada, A. Di Paolo, T. M. Hazard, X. You, D. I. Schuster, J. Koch, A. Blais, and A. A. Houck, "Experimental Realization of a Protected Superconducting Circuit Derived from the $0 - \pi$ Qubit," *PRX Quantum*, vol. 2, no. 1, p. 010 339, Mar. 2021, ISSN: 2691-3399. DOI: 10.1103/PRXQuantum.2.010339.

[27] I. V. Pechenezhskiy, R. A. Mencia, L. B. Nguyen, Y.-H. Lin, and V. E. Manucharyan, "The superconducting quasicharge qubit," *Nature*, vol. 585, no. 7825, pp. 368–371, Sep. 2020, ISSN: 0028-0836. DOI: 10.1038/s41586-020-2687-9.

[28] B. D. Josephson, "Possible new effects in superconductive tunnelling," *Physics Letters*, vol. 1, no. 7, pp. 251–253, 1962, ISSN: 00319163. DOI: 10.1016/0031-9163(62)91369-0.

[29] J. Gao, "The Physics of Superconducting Microwave Resonators," Ph.D. dissertation, 2008.

[30] S. Morohashi, K. Gotoh, and N. Yokoyama, "Fabrication of a tantalum-based josephson junction for an X-ray detector," *Japanese Journal of Applied Physics, Part 1: Regular Papers and Short Notes and Review Papers*, vol. 39, no. 6 A, pp. 3371–3377, 2000, ISSN: 00214922. DOI: 10.1143/jjap.39.3371.

[31] M. R. Vissers, J. S. Kline, J. Gao, D. S. Wisbey, and D. P. Pappas, "Reduced microwave loss in trenched superconducting coplanar waveguides," *Applied Physics Letters*, vol. 100, no. 8, 2012, ISSN: 00036951. DOI: 10.1063/1.3683552.

[32] J. B. Chang, M. R. Vissers, A. D. Córcoles, *et al.*, "Improved superconducting qubit coherence using titanium nitride," *Applied Physics Letters*, vol. 103, no. 1, pp. 3–6, 2013, ISSN: 00036951. DOI: 10.1063/1.4813269.

[33] A. Bruno, G. De Lange, S. Asaad, K. L. Van Der Enden, N. K. Langford, and L. Dicarlo, "Reducing intrinsic loss in superconducting resonators by surface treatment and deep etching of silicon substrates," *Applied Physics Letters*, vol. 106, no. 18, pp. 4–8, 2015, ISSN: 00036951. DOI: 10.1063/1.4919761.

[34] A. Shearrow, G. Koolstra, S. J. Whiteley, N. Earnest, P. S. Barry, F. J. Heremans, D. D. Awschalom, E. Shirokoff, and D. I. Schuster, "Atomic layer deposition of titanium nitride for quantum circuits," *Applied Physics Letters*, vol. 113, no. 21, 2018, ISSN: 00036951. DOI: 10.1063/1.5053461.

[35] N. Pankratova, H. Lee, R. Kuzmin, K. Wickramasinghe, W. Mayer, J. Yuan, M. G. Vavilov, J. Shabani, and V. E. Manucharyan, "Multiterminal Josephson Effect," *Physical Review X*, vol. 10, no. 3, p. 31 051, 2020, ISSN: 21603308. DOI: 10.1103/physrevx.10.031051.

[36] A. P. M. Place, L. V. H. Rodgers, P. Mundada, *et al.*, "New material platform for superconducting transmon qubits with coherence times exceeding 0.3 milliseconds," *Nature Communications*, vol. 12, no. 1, p. 1779, Dec. 2021, ISSN: 2041-1723. DOI: 10.1038/s41467-021-22030-5.

[37] D. M. Tennant, L. A. Martinez, K. M. Beck, S. R. O'Kelley, C. D. Wilen, R. McDermott, J. L. DuBois, and Y. J. Rosen, "Low frequency correlated charge noise measurements across multiple energy transitions in a tantalum transmon," *arXiv*, pp. 1–8, Jun. 2021.

[38] C. Wang, X. Li, H. Xu, *et al.*, "Towards practical quantum computers: transmon qubit with a lifetime approaching 0.5 milliseconds," *npj Quantum Information*, vol. 8, no. 1, 2022, ISSN: 20566387. DOI: 10.1038/s41534-021-00510-2.

[39] Y. Aharonov and D. Bohm, "Significance of Electromagnetic Potentials in the Quantum Theory," *Physical Review*, vol. 115, no. 3, pp. 485–491, Aug. 1959, ISSN: 0031-899X. DOI: 10.1103/PhysRev.115.485.

[40] V. E. Manucharyan, "Superinductance," Ph.D. dissertation, 2012.

[41] A. Kou, W. C. Smith, U. Vool, I. M. Pop, K. M. Sliwa, M. Hatridge, L. Frunzio, and M. H. Devoret, "Simultaneous Monitoring of Fluxonium Qubits in a Waveguide," *Physical Review Applied*, vol. 9, no. 6, p. 64 022, 2018, ISSN: 23317019. DOI: 10.1103/PhysRevApplied.9.064022.

[42] M. Reagor, "Superconducting Cavities for Circuit Quantum Electrodynamics," Ph.D. dissertation, 2015, p. 220.

[43] R. P. Budoyo, "Effects of Optical Illumination on Superconducting Quantum Devices," Ph.D. dissertation, 2015.

[44] R. Kuzmin, R. Mencia, N. Grabon, N. Mehta, Y. H. Lin, and V. E. Manucharyan, "Quantum electrodynamics of a superconductor–insulator phase transition," *Nature*

Physics, vol. 15, no. 9, pp. 930–934, 2019, ISSN: 17452481. DOI: 10.1038/s41567-019-0553-1.

[45] R. Kuzmin, N. Mehta, N. Grabon, R. Mencia, and V. E. Manucharyan, "Superstrong coupling in circuit quantum electrodynamics," *npj Quantum Information*, vol. 5, no. 1, p. 20, Dec. 2019, ISSN: 2056-6387. DOI: 10.1038/s41534-019-0134-2.

[46] L. Grünhaupt, M. Spiecker, D. Gusenkova, *et al.*, "Granular aluminium as a superconducting material for high-impedance quantum circuits," *Nature Materials*, vol. 18, no. 8, pp. 816–819, 2019, ISSN: 14764660. DOI: 10.1038/s41563-019-0350-3.

[47] M. Peruzzo, F. Hassani, G. Szep, A. Trioni, E. Redchenko, M. Žemlička, and J. M. Fink, "Geometric Superinductance Qubits: Controlling Phase Delocalization across a Single Josephson Junction," *PRX Quantum*, vol. 2, no. 4, p. 1, 2021, ISSN: 26913399. DOI: 10.1103/PRXQuantum.2.040341.

[48] A. Somoroff, "Quantum Computing with Fluxonium: Digital and Analog Directions," Ph.D. dissertation, 2022.

[49] H. Zhang, S. Chakram, T. Roy, N. Earnest, Y. Lu, Z. Huang, D. K. Weiss, J. Koch, and D. I. Schuster, "Universal Fast-Flux Control of a Coherent, Low-Frequency Qubit," *Physical Review X*, vol. 11, no. 1, p. 011 010, Jan. 2021, ISSN: 2160-3308. DOI: 10.1103/PhysRevX.11.011010.

[50] L. B. Nguyen, Y.-H. Lin, A. Somoroff, R. Mencia, N. Grabon, and V. E. Manucharyan, "High-Coherence Fluxonium Qubit," *Physical Review X*, vol. 9, no. 4, p. 041 041, Nov. 2019, ISSN: 2160-3308. DOI: 10.1103/PhysRevX.9.041041.

[51] A. Somoroff, Q. Ficheux, R. A. Mencia, H. Xiong, R. V. Kuzmin, and V. E. Manucharyan, "Millisecond coherence in a superconducting qubit," *arXiv*, vol. 1, Mar. 2021.

[52] S. M. Girvin, *Circuit QED: superconducting qubits coupled to microwave photons*, 2014.

[53] D. I. Schuster, A. A. Houck, J. A. Schreier, *et al.*, "Resolving photon number states in a superconducting circuit," *Nature*, vol. 445, no. 7127, pp. 515–518, Feb. 2007, ISSN: 0028-0836. DOI: 10.1038/nature05461.

[54] L. B. Nguyen, "Toward the Fluxonium Quantum Processor," Ph.D. dissertation, 2020.

[55] N. A. Masluk, "Reducing the losses of the fluxonium artificial atom," Ph.D. dissertation, 2012, p. 186.

[56] K. N. Nesterov, I. V. Pechenezhskiy, C. Wang, V. E. Manucharyan, and M. G. Vavilov, "Microwave-activated controlled- Z gate for fixed-frequency fluxonium qubits," *Physical Review A*, vol. 98, no. 3, p. 30 301, 2018, ISSN: 24699934. DOI: 10.1103/PhysRevA.98.030301.

[57] K. N. Nesterov, C. Wang, V. E. Manucharyan, and M. G. Vavilov, "Controlled-NOT gates for fluxonium qubits via selective darkening of transitions," *arXiv*, pp. 1–12, Feb. 2022.

[58] H.-P. Breuer and F. Petruccione, *The Theory of Open Quantum Systems*, 1. Oxford University Press, Jan. 2007, vol. 4, pp. 1–23, ISBN: 9780199213900. DOI: 10.1093/acprof:oso/9780199213900.001.0001.

[59] Q. Ficheus, "Quantum Trajectories with Incompatible Decoherence Channels," Ph.D. dissertation, 2016.

[60] I. M. Pop, K. Geerlings, G. Catelani, R. J. Schoelkopf, L. I. Glazman, and M. H. Devoret, "Coherent suppression of electromagnetic dissipation due to superconducting quasiparticles," *Nature*, vol. 508, no. 7496, pp. 369–372, 2014, ISSN: 14764687. DOI: 10.1038/nature13017.

[61] J. Bylander, S. Gustavsson, F. Yan, F. Yoshihara, K. Harrabi, G. Fitch, D. G. Cory, Y. Nakamura, J. S. Tsai, and W. D. Oliver, "Noise spectroscopy through dynamical decoupling with a superconducting flux qubit," *Nature Physics*, vol. 7, no. 7, pp. 565–570, 2011, ISSN: 17452481. DOI: 10.1038/nphys1994.

[62] P. J. O'Malley, J. Kelly, R. Barends, *et al.*, "Qubit Metrology of Ultralow Phase Noise Using Randomized Benchmarking," *Physical Review Applied*, vol. 3, no. 4, pp. 1–11, 2015, ISSN: 23317019. DOI: 10.1103/PhysRevApplied.3.044009.

[63] Y. V. Nazarov, Ed., *Quantum Noise in Mesoscopic Physics*. Dordrecht: Springer Netherlands, 2003, ISBN: 978-1-4020-1240-2. DOI: 10.1007/978-94-010-0089-5.

[64] A. A. Clerk, M. H. Devoret, S. M. Girvin, F. Marquardt, and R. J. Schoelkopf, "Introduction to quantum noise, measurement, and amplification," *Reviews of Modern Physics*, vol. 82, no. 2, pp. 1155–1208, Apr. 2010, ISSN: 0034-6861. DOI: 10.1103/RevModPhys.82.1155.

[65] C. Wang, C. Axline, Y. Y. Gao, T. Brecht, Y. Chu, L. Frunzio, M. H. Devoret, and R. J. Schoelkopf, "Surface participation and dielectric loss in superconducting qubits," *Applied Physics Letters*, vol. 107, no. 16, 2015, ISSN: 00036951. DOI: 10.1063/1.4934486.

[66] P. V. Klimov, J. Kelly, Z. Chen, *et al.*, "Fluctuations of Energy-Relaxation Times in Superconducting Qubits," *Physical Review Letters*, vol. 121, no. 9, p. 90 502, 2018, ISSN: 10797114. DOI: 10.1103/PhysRevLett.121.090502.

[67] E. M. Purcell, "Spontaneous Emission Probabilities at Radio Frequencies," in *Physical Review*, vol. 69, 1995, pp. 681–681. DOI: 10.1007/978-1-4615-1963-8{_}40.

[68] A. A. Houck, J. A. Schreier, B. R. Johnson, *et al.*, "Controlling the spontaneous emission of a superconducting transmon qubit," *Physical Review Letters*, vol. 101, no. 8, pp. 1–4, 2008, ISSN: 00319007. DOI: 10.1103/PhysRevLett.101.080502.

[69] P. Kumar, S. Sendelbach, M. A. Beck, J. W. Freeland, Z. Wang, H. Wang, C. C. Yu, R. Q. Wu, D. P. Pappas, and R. McDermott, "Origin and Reduction of 1 /f Magnetic Flux Noise in Superconducting Devices," *Physical Review Applied*, vol. 6, no. 4, pp. 1–5, 2016, ISSN: 23317019. DOI: 10.1103/PhysRevApplied.6.041001.

[70] C. M. Quintana, Y. Chen, D. Sank, *et al.*, "Observation of Classical-Quantum Crossover of 1 /f Flux Noise and Its Paramagnetic Temperature Dependence," *Physical Review Letters*, vol. 118, no. 5, pp. 1–6, 2017, ISSN: 10797114. DOI: 10.1103/PhysRevLett.118.057702.

[71] G. Catelani, R. J. Schoelkopf, M. H. Devoret, and L. I. Glazman, "Relaxation and frequency shifts induced by quasiparticles in superconducting qubits," *Physical Review B - Condensed Matter and Materials Physics*, vol. 84, no. 6, pp. 1–25, 2011, ISSN: 10980121. DOI: 10.1103/PhysRevB.84.064517.

[72] G. Catelani, J. Koch, L. Frunzio, R. J. Schoelkopf, M. H. Devoret, and L. I. Glazman, "Quasiparticle relaxation of superconducting qubits in the presence of flux," *Physical Review Letters*, vol. 106, no. 7, pp. 4–7, 2011, ISSN: 00319007. DOI: 10.1103/PhysRevLett.106.077002.

[73] L. Glazman and G. Catelani, "Bogoliubov quasiparticles in superconducting qubits," *SciPost Physics Lecture Notes*, pp. 1–42, 2021, ISSN: 2590-1990. DOI: 10.21468/scipostphyslectnotes.31.

[74] S. Gustavsson, F. Yan, G. Catelani, *et al.*, "Suppressing relaxation in superconducting qubits by quasiparticle pumping," *Science*, vol. 354, no. 6319, pp. 1573–1577, 2016, ISSN: 10959203. DOI: 10.1126/science.aah5844.

[75] C. Wang, Y. Y. Gao, I. M. Pop, *et al.*, "Measurement and control of quasiparticle dynamics in a superconducting qubit," *Nature Communications*, vol. 5, pp. 1–7, 2014, ISSN: 20411723. DOI: 10.1038/ncomms6836.

[76] A. P. Vepsäläinen, A. H. Karamlou, J. L. Orrell, *et al.*, "Impact of ionizing radiation on superconducting qubit coherence," *Nature*, vol. 584, no. 7822, pp. 551–556, 2020, ISSN: 14764687. DOI: 10.1038/s41586-020-2619-8.

[77] U. Vool, I. M. Pop, K. Sliwa, *et al.*, "Non-poissonian quantum jumps of a fluxonium qubit due to quasiparticle excitations," *Physical Review Letters*, vol. 113, no. 24, pp. 2–6, 2014, ISSN: 10797114. DOI: 10.1103/PhysRevLett.113.247001.

[78] D. Ristè, C. C. Bultink, M. J. Tiggelman, R. N. Schouten, K. W. Lehnert, and L. Dicarlo, "Millisecond charge-parity fluctuations and induced decoherence in a superconducting transmon qubit," *Nature Communications*, vol. 4, no. May, pp. 1–6, 2013, ISSN: 20411723. DOI: 10.1038/ncomms2936.

[79] R. Barends, J. Wenner, M. Lenander, *et al.*, "Minimizing quasiparticle generation from stray infrared light in superconducting quantum circuits," *Applied Physics Letters*, vol. 99, no. 11, p. 113 507, Sep. 2011, ISSN: 0003-6951. DOI: 10.1063/1.3638063.

[80] K. Serniak, S. Diamond, M. Hays, V. Fatemi, S. Shankar, L. Frunzio, R. J. Schoelkopf, and M. H. Devoret, "Direct Dispersive Monitoring of Charge Parity in Offset-Charge-Sensitive Transmons," *Physical Review Applied*, vol. 12, no. 1, p. 1, 2019, ISSN: 23317019. DOI: 10.1103/PhysRevApplied.12.014052.

[81] S. Diamond, V. Fatemi, M. Hays, *et al.*, "Distinguishing parity-switching mechanisms in a superconducting qubit," 2022.

[82] R. P. Riwar, A. Hosseinkhani, L. D. Burkhart, Y. Y. Gao, R. J. Schoelkopf, L. I. Glazman, and G. Catelani, "Normal-metal quasiparticle traps for superconducting qubits," *Physical Review B*, vol. 94, no. 10, pp. 1–10, 2016, ISSN: 24699969. DOI: 10.1103/PhysRevB.94.104516.

[83] R. P. Riwar and G. Catelani, "Efficient quasiparticle traps with low dissipation through gap engineering," *Physical Review B*, vol. 100, no. 14, pp. 1–14, 2019, ISSN: 24699969. DOI: 10.1103/PhysRevB.100.144514.

[84] K. Li, S. K. Dutta, Z. Steffen, D. Poppert, S. Keshvari, J. Bowser, B. S. Palmer, C. J. Lobb, and F. C. Wellstood, "Long-lived transmons with different electrode layouts," *MRS Advances*, vol. 7, no. 13-14, pp. 273–277, May 2022, ISSN: 2059-8521. DOI: 10.1557/s43580-022-00265-8.

[85] F. Bao, H. Deng, D. Ding, *et al.*, "Fluxonium: an alternative qubit platform for high-fidelity operations," *arXiv*, 2021.

[86] N. Cottet, H. Xiong, L. B. Nguyen, Y.-H. Lin, and V. E. Manucharyan, "Electron shelving of a superconducting artificial atom," *Nature Communications*, vol. 12, no. 1, p. 6383, Dec. 2021, ISSN: 2041-1723. DOI: 10.1038/s41467-021-26686-x.

[87] P. Magnard, S. Storz, P. Kurpiers, *et al.*, "Microwave Quantum Link between Superconducting Circuits Housed in Spatially Separated Cryogenic Systems," *Physical Review Letters*, vol. 125, no. 26, p. 260 502, 2020, ISSN: 10797114. DOI: 10.1103/PhysRevLett.125.260502.

[88] N. Cottet, "Energy and Information in Fluorescence with Superconducting Circuits," Ph.D. dissertation, 2019.

[89] A. G. Fowler, M. Mariantoni, J. M. Martinis, and A. N. Cleland, "Surface codes: Towards practical large-scale quantum computation," *Physical Review A - Atomic, Molecular, and Optical Physics*, vol. 86, no. 3, 2012, ISSN: 10502947. DOI: 10.1103/PhysRevA.86.032324.

[90] S. Krinner, N. Lacroix, A. Remm, *et al.*, "Realizing Repeated Quantum Error Correction in a Distance-Three Surface Code," *arXiv*, pp. 1–28, Dec. 2021.

[91] Y. Zhao, Y. Ye, H.-L. Huang, *et al.*, "Realization of an Error-Correcting Surface Code with Superconducting Qubits," *arXiv*, Dec. 2021.

[92] B. Yurke, "Squeezed-state generation using a Josephson parametric amplifier," *Journal of the Optical Society of America B*, vol. 4, no. 10, p. 1551, Oct. 1987, ISSN: 0740-3224. DOI: 10.1364/JOSAB.4.001551.

[93] R. Movshovich, B. Yurke, P. G. Kaminsky, A. D. Smith, A. H. Silver, R. W. Simon, and M. V. Schneider, "Observation of zero-point noise squeezing via a Josephson-parametric amplifier," *Physical Review Letters*, vol. 65, no. 12, pp. 1419–1422, Sep. 1990, ISSN: 0031-9007. DOI: 10.1103/PhysRevLett.65.1419.

[94] M. A. Castellanos-Beltran, K. D. Irwin, G. C. Hilton, L. R. Vale, and K. W. Lehnert, "Amplification and squeezing of quantum noise with a tunable Josephson metamaterial," *Nature Physics*, vol. 4, no. 12, pp. 928–931, 2008, ISSN: 17452481. DOI: 10.1038/nphys1090.

[95] D. H. Slichter, R. Vijay, S. J. Weber, S. Boutin, M. Boissonneault, J. M. Gambetta, A. Blais, and I. Siddiqi, "Measurement-induced qubit state mixing in circuit QED from Up-converted dephasing noise," *Physical Review Letters*, vol. 109, no. 15, pp. 1–5, 2012, ISSN: 00319007. DOI: 10.1103/PhysRevLett.109.153601.

[96] M. Boissonneault, J. M. Gambetta, and A. Blais, "Dispersive regime of circuit QED: Photon-dependent qubit dephasing and relaxation rates," *Physical Review A - Atomic, Molecular, and Optical Physics*, vol. 79, no. 1, 2009, ISSN: 10502947. DOI: 10.1103/PhysRevA.79.013819.

[97] D. Sank, Z. Chen, M. Khezri, *et al.*, "Measurement-Induced State Transitions in a Superconducting Qubit: Beyond the Rotating Wave Approximation," *Physical Review Letters*, vol. 117, no. 19, pp. 1–6, 2016, ISSN: 10797114. DOI: 10.1103/PhysRevLett.117.190503.

[98] C. M. Caves, J. Combes, Z. Jiang, and S. Pandey, "Quantum limits on phase-preserving linear amplifiers," *Physical Review A - Atomic, Molecular, and Optical Physics*, vol. 86, no. 6, pp. 1–37, 2012, ISSN: 10502947. DOI: 10.1103/PhysRevA.86.063802.

[99] David M. Pozar, *Microwave engineering*, ISBN: 9780470631553.

[100] M. a. Castellanos-Beltran, "Development of a Josephson Parametric Amplifier for the Preparation and Detection of Nonclassical States of Microwave Fields by," Ph.D. dissertation, 2010, p. 300.

[101] C. Macklin, K. O'Brien, D. Hover, M. E. Schwartz, V. Bolkhovsky, X. Zhang, W. D. Oliver, and I. Siddiqi, "A near-quantum-limited Josephson traveling-wave parametric amplifier," *Science*, vol. 350, no. 6258, pp. 307–310, Oct. 2015, ISSN: 0036-8075. DOI: 10.1126/science.aaa8525.

[102] S. Hacohen-Gourgy, L. S. Martin, E. Flurin, V. V. Ramasesh, K. B. Whaley, and I. Siddiqi, "Quantum dynamics of simultaneously measured non-commuting observables," *Nature*, 2016, ISSN: 14764687. DOI: 10.1038/nature19762.

[103] S. Touzard, A. Kou, N. E. Frattini, V. V. Sivak, S. Puri, A. Grimm, L. Frunzio, S. Shankar, and M. H. Devoret, "Gated Conditional Displacement Readout of Superconducting Qubits," *Physical Review Letters*, vol. 122, no. 8, p. 80 502, 2019, ISSN: 10797114. DOI: 10.1103/PhysRevLett.122.080502.

[104] I. Siddiqi, R. Vijay, F. Pierre, C. M. Wilson, M. Metcalfe, C. Rigetti, L. Frunzio, and M. H. Devoret, "RF-driven Josephson bifurcation amplifier for quantum measurement," *Physical Review Letters*, vol. 93, no. 20, pp. 1–4, 2004, ISSN: 00319007. DOI: 10.1103/PhysRevLett.93.207002.

[105] V. E. Manucharyan, J. Koch, M. Brink, L. I. Glazman, and M. H. Devoret, "Coherent oscillations between classically separable quantum states of a superconducting loop," Oct. 2009.

[106] E. Dogan, D. Rosenstock, L. L. Guevel, H. Xiong, R. A. Mencia, A. Somoroff, K. N. Nesterov, M. G. Vavilov, V. E. Manucharyan, and C. Wang, "Demonstration of the Two-Fluxonium Cross-Resonance Gate," vol. 49, no. 6, 2022.

[107] L. Dicarlo, J. M. Chow, J. M. Gambetta, *et al.*, "Demonstration of two-qubit algorithms with a superconducting quantum processor," *Nature*, vol. 460, no. 7252, pp. 240–244, 2009, ISSN: 00280836. DOI: 10.1038/nature08121.

[108] S. Li, A. D. Castellano, S. Wang, *et al.*, "Realisation of high-fidelity nonadiabatic CZ gates with superconducting qubits," *npj Quantum Information*, vol. 5, no. 1, pp. 1–7, 2019, ISSN: 20566387. DOI: 10.1038/s41534-019-0202-7.

[109] R. Barends, C. M. Quintana, A. G. Petukhov, *et al.*, "Diabatic Gates for Frequency-Tunable Superconducting Qubits," *Physical Review Letters*, vol. 123, no. 21, 2019, ISSN: 10797114. DOI: 10.1103/PhysRevLett.123.210501.

[110] M. C. Collodo, J. Herrmann, N. Lacroix, C. K. Andersen, A. Remm, S. Lazar, J.-c. Besse, T. Walter, A. Wallraff, and C. Eichler, "Implementation of Conditional-Phase Gates based on tunable ZZ-Interactions," *arXiv*, May 2020. DOI: 10.1103/PhysRevLett.125.240502.

[111] Y. Sung, L. Ding, J. Braumüller, *et al.*, "Realization of high-fidelity CZ and ZZ-free iSWAP gates with a tunable coupler," *arXiv*, pp. 1–27, Nov. 2020. DOI: 10.1103/PhysRevX.11.021058.

[112] V. Negîrneac, H. Ali, N. Muthusubramanian, *et al.*, "High-fidelity controlled-Z gate with maximal intermediate leakage operating at the speed limit in a superconducting quantum processor," *arXiv*, pp. 1–13, Aug. 2020. DOI: 10.1103/PhysRevLett.126.220502.

[113] X. Li, T. Cai, H. Yan, *et al.*, "Tunable Coupler for Realizing a Controlled-Phase Gate with Dynamically Decoupled Regime in a Superconducting Circuit," *Physical Review Applied*, vol. 14, no. 2, pp. 1–14, 2020, ISSN: 23317019. DOI: 10.1103/PhysRevApplied.14.024070.

[114] Y. Xu, J. Chu, J. Yuan, *et al.*, "High-Fidelity, High-Scalability Two-Qubit Gate Scheme for Superconducting Qubits," *Physical Review Letters*, vol. 125, no. 24, Jun. 2020, ISSN: 10797114. DOI: 10.1103/PhysRevLett.125.240503.

[115] J. M. Chow, A. D. Córcoles, J. M. Gambetta, *et al.*, "Simple all-microwave entangling gate for fixed-frequency superconducting qubits," *Physical Review Letters*, vol. 107, no. 8, pp. 1–5, 2011, ISSN: 00319007. DOI: 10.1103/PhysRevLett.107.080502.

[116] J. M. Chow, J. M. Gambetta, A. W. Cross, S. T. Merkel, C. Rigetti, and M. Steffen, "Microwave-activated conditional-phase gate for superconducting qubits," *New Journal of Physics*, vol. 15, 2013, ISSN: 13672630. DOI: 10.1088/1367-2630/15/11/115012.

[117] A. Noguchi, A. Osada, S. Masuda, S. Kono, K. Heya, S. P. Wolski, H. Takahashi, T. Sugiyama, D. Lachance-Quirion, and Y. Nakamura, "Fast parametric two-qubit gates with suppressed residual interaction using a parity-violated superconducting qubit," *arXiv*, May 2020. DOI: 10.1103/PhysRevA.102.062408.

[118] D. M. Abrams, N. Didier, B. R. Johnson, M. P. d. Silva, and C. A. Ryan, "Implementation of XY entangling gates with a single calibrated pulse," *Nature Electronics*, vol. 3, no. 12, pp. 744–750, Dec. 2020, ISSN: 2520-1131. DOI: 10.1038/s41928-020-00498-1.

[119] S. Krinner, P. Kurpiers, B. Royer, P. Magnard, I. Tsitsilin, J.-C. Besse, A. Remm, A. Blais, and A. Wallraff, "Demonstration of an All-Microwave Controlled-Phase Gate between Far-Detuned Qubits," *Physical Review Applied*, vol. 14, no. 4, pp. 1–10, 2020, ISSN: 23317019. DOI: 10.1103/physrevapplied.14.044039.

[120] Q. Ficheux, L. B. Nguyen, A. Somoroff, H. Xiong, K. N. Nesterov, M. G. Vavilov, and V. E. Manucharyan, "Fast Logic with Slow Qubits: Microwave-Activated Controlled-Z Gate on Low-Frequency Fluxoniums," *Physical Review X*, vol. 11, no. 2, p. 021 026, May 2021, ISSN: 2160-3308. DOI: 10.1103/PhysRevX.11.021026.

[121] H. Xiong, Q. Ficheux, A. Somoroff, L. B. Nguyen, E. Dogan, D. Rosenstock, C. Wang, K. N. Nesterov, M. G. Vavilov, and V. E. Manucharyan, "Arbitrary controlled-phase gate on fluxonium qubits using differential ac Stark shifts," *Physical Review Research*, vol. 4, no. 2, p. 023 040, Apr. 2022, ISSN: 2643-1564. DOI: 10.1103/PhysRevResearch.4.023040.

[122] B. K. Mitchell, R. K. Naik, A. Morvan, A. Hashim, J. M. Kreikebaum, B. Marinelli, W. Lavrijsen, K. Nowrouzi, D. I. Santiago, and I. Siddiqi, "Hardware-Efficient Microwave-Activated Tunable Coupling Between Superconducting Qubits," *arXiv*, no. 1, May 2021. DOI: 10.1103/PhysRevLett.127.200502.

[123] K. X. Wei, E. Magesan, I. Lauer, *et al.*, "Quantum crosstalk cancellation for fast entangling gates and improved multi-qubit performance," *arXiv*, Jun. 2021.

[124] A. Kandala, K. X. Wei, S. Srinivasan, E. Magesan, S. Carnevale, G. A. Keefe, D. Klaus, O. Dial, and D. C. McKay, "Demonstration of a High-Fidelity cnot Gate for Fixed-Frequency Transmons with Engineered ZZ Suppression," *Physical Review Letters*, vol. 127, no. 13, p. 130 501, Sep. 2021, ISSN: 0031-9007. DOI: 10.1103/PhysRevLett.127.130501.

[125] Z. Chen, "Metrology of Quantum Control and Measurement in Superconducting Qubits A," Ph.D. dissertation, 2018, pp. 227–249.

[126] I. N. Moskalenko, I. S. Besedin, I. A. Simakov, and A. V. Ustinov, "Tunable coupling scheme for implementing two-qubit gates on fluxonium qubits," *Applied Physics Letters*, vol. 119, no. 19, p. 194 001, Nov. 2021, ISSN: 0003-6951. DOI: 10.1063/5.0064800.

[127] Y. Chen, K. N. Nesterov, V. E. Manucharyan, and M. G. Vavilov, "Fast Flux Entangling Gate for Fluxonium Circuits," *arXiv*, pp. 1–10, Oct. 2021.

[128] I. N. Moskalenko, I. A. Simakov, N. N. Abramov, A. A. Grigorev, D. O. Moskalev, A. A. Pishchimova, N. S. Smirnov, E. V. Zikiy, I. A. Rodionov, and I. S. Besedin, "High fidelity two-qubit gates on fluxoniums using a tunable coupler," pp. 1–18, Mar. 2022.

[129] D. A. Lidar and T. A. Brun, Eds., *Quantum Error Correction*. Cambridge: Cambridge University Press, 2013, ISBN: 9781139034807. DOI: 10.1017/CBO9781139034807.

[130] J. M. Chow, J. M. Gambetta, A. D. Córcoles, *et al.*, "Universal quantum gate set approaching fault-tolerant thresholds with superconducting qubits," *Physical Review Letters*, vol. 109, no. 6, pp. 1–5, 2012, ISSN: 00319007. DOI: 10.1103/PhysRevLett.109.060501.

[131] E. Nielsen, J. K. Gamble, K. Rudinger, T. Scholten, K. Young, and R. Blume-Kohout, "Gate Set Tomography," *Quantum*, vol. 5, 2021, ISSN: 2521327X. DOI: 10.22331/Q-2021-10-05-557.

[132] M. A. Nielsen and I. Chuang, *Quantum Computation and Quantum Information*. Cambridge University Press, 2010, ISBN: 9781107002173.

[133] A. D. Córcoles, J. M. Gambetta, J. M. Chow, J. A. Smolin, M. Ware, J. Strand, B. L. Plourde, and M. Steffen, "Process verification of two-qubit quantum gates by randomized benchmarking," *Physical Review A - Atomic, Molecular, and Optical Physics*, vol. 87, no. 3, pp. 1–4, 2013, ISSN: 10502947. DOI: 10.1103/PhysRevA.87.030301.

[134] T. Roy, S. Kundu, M. Chand, S. Hazra, N. Nehra, R. Cosmic, A. Ranadive, M. P. Patankar, K. Damle, and R. Vijay, "Implementation of Pairwise Longitudinal Coupling in a Three-Qubit Superconducting Circuit," *Physical Review Applied*, vol. 7, no. 5, pp. 1–15, 2017, ISSN: 23317019. DOI: 10.1103/PhysRevApplied.7.054025.

[135] Z. Hradil, "Quantum-state estimation," *Physical Review A - Atomic, Molecular, and Optical Physics*, vol. 55, no. 3, R1561–R1564, 1997, ISSN: 10941622. DOI: 10.1103/PhysRevA.55.R1561.

[136] J. M. Chow, J. M. Gambetta, L. Tornberg, J. Koch, L. S. Bishop, A. A. Houck, B. R. Johnson, L. Frunzio, S. M. Girvin, and R. J. Schoelkopf, "Randomized benchmarking and process tomography for gate errors in a solid-state qubit," *Physical Review Letters*, vol. 102, no. 9, pp. 1–4, 2009, ISSN: 00319007. DOI: 10.1103/PhysRevLett.102.090502.

[137] J. Emerson, M. Silva, O. Moussa, C. Ryan, M. Laforest, J. Baugh, D. G. Cory, and R. Laflamme, "Symmetrized characterization of noisy quantum processes," *Science*, vol. 317, no. 5846, pp. 1893–1896, 2007, ISSN: 00368075. DOI: 10.1126/science.1145699.

[138] E. Knill, D. Leibfried, R. Reichle, J. Britton, R. B. Blakestad, J. D. Jost, C. Langer, R. Ozeri, S. Seidelin, and D. J. Wineland, "Randomized benchmarking of quantum gates," *Physical Review A - Atomic, Molecular, and Optical Physics*, vol. 77, no. 1, pp. 1–7, 2008, ISSN: 10502947. DOI: 10.1103/PhysRevA.77.012307.

[139] E. Magesan, J. M. Gambetta, and J. Emerson, "Scalable and robust randomized benchmarking of quantum processes," *Physical Review Letters*, vol. 106, no. 18, pp. 8–11, 2011, ISSN: 00319007. DOI: 10.1103/PhysRevLett.106.180504.

[140] E. Magesan, J. M. Gambetta, B. R. Johnson, *et al.*, "Efficient measurement of quantum gate error by interleaved randomized benchmarking," *Physical Review Letters*,

vol. 109, no. 8, pp. 1–5, 2012, ISSN: 00319007. DOI: 10.1103/PhysRevLett.109.080505.

[141] D. Gottesman, "Theory of fault-tolerant quantum computation," *Physical Review A - Atomic, Molecular, and Optical Physics*, vol. 57, no. 1, pp. 127–137, 1998, ISSN: 10941622. DOI: 10.1103/PhysRevA.57.127.

[142] S. Sheldon, L. S. Bishop, E. Magesan, S. Filipp, J. M. Chow, and J. M. Gambetta, "Characterizing errors on qubit operations via iterative randomized benchmarking," *Physical Review A*, vol. 93, no. 1, pp. 1–5, 2016, ISSN: 24699934. DOI: 10.1103/PhysRevA.93.012301.

[143] J. Wallman, C. Granade, R. Harper, and S. T. Flammia, "Estimating the coherence of noise," *New Journal of Physics*, vol. 17, no. 11, p. 113 020, Nov. 2015, ISSN: 1367-2630. DOI: 10.1088/1367-2630/17/11/113020.

[144] C. Neill, P. Roushan, K. Kechedzhi, *et al.*, "A blueprint for demonstrating quantum supremacy with superconducting qubits," *Science*, vol. 360, no. 6385, pp. 195–199, 2018, ISSN: 10959203. DOI: 10.1126/science.aao4309.

[145] B. Foxen, C. Neill, A. Dunsworth, *et al.*, "Demonstrating a Continuous Set of Two-Qubit Gates for Near-Term Quantum Algorithms," *Physical Review Letters*, vol. 125, no. 12, pp. 1–20, 2020, ISSN: 10797114. DOI: 10.1103/PhysRevLett.125.120504.

[146] D. C. McKay, C. J. Wood, S. Sheldon, J. M. Chow, and J. M. Gambetta, "Efficient Z gates for quantum computing," *Physical Review A*, vol. 96, no. 2, p. 022 330, Aug. 2017, ISSN: 2469-9926. DOI: 10.1103/PhysRevA.96.022330.

[147] D. A. Stech, *Quantum and Atom Optics*. 2007.

[148] F. Motzoi, J. M. Gambetta, P. Rebentrost, and F. K. Wilhelm, "Simple Pulses for Elimination of Leakage in Weakly Nonlinear Qubits," *Physical Review Letters*, vol. 103, no. 11, pp. 1–4, 2009, ISSN: 00319007. DOI: 10.1103/PhysRevLett.103.110501.

[149] J. M. Gambetta, F. Motzoi, S. T. Merkel, and F. K. Wilhelm, "Analytic control methods for high-fidelity unitary operations in a weakly nonlinear oscillator," *Physical Review A - Atomic, Molecular, and Optical Physics*, vol. 83, no. 1, pp. 1–13, 2011, ISSN: 10502947. DOI: 10.1103/PhysRevA.83.012308.

[150] L. S. Theis, F. Motzoi, S. Machnes, and F. K. Wilhelm, "Counteracting systems of diabaticities using DRAG controls: The status after 10 years(a)," *Epl*, vol. 123, no. 6, pp. 1–7, 2018, ISSN: 12864854. DOI: 10.1209/0295-5075/123/60001.

[151] F. Motzoi and F. K. Wilhelm, "Improving frequency selection of driven pulses using derivative-based transition suppression," *Physical Review A - Atomic, Molecular, and Optical Physics*, vol. 88, no. 6, pp. 1–15, 2013, ISSN: 10502947. DOI: 10.1103/PhysRevA.88.062318.

[152] S. Sheldon, E. Magesan, J. M. Chow, and J. M. Gambetta, "Procedure for systematically tuning up cross-talk in the cross-resonance gate," *Physical Review A*, vol. 93, no. 6, pp. 1–5, 2016, ISSN: 24699934. DOI: 10.1103/PhysRevA.93.060302.

[153] P. Mundada, G. Zhang, T. Hazard, and A. Houck, "Suppression of Qubit Crosstalk in a Tunable Coupling Superconducting Circuit," *Physical Review Applied*, vol. 12, no. 5, p. 1, 2019, ISSN: 23317019. DOI: 10.1103/PhysRevApplied.12.054023.

[154] A. Dunsworth, R. Barends, Y. Chen, *et al.*, "A method for building low loss multi-layer wiring for superconducting microwave devices," *Applied Physics Letters*, vol. 112, no. 6, pp. 1–5, 2018, ISSN: 00036951. DOI: 10.1063/1.5014033.

[155] Y. Wu, W.-S. Bao, S. Cao, *et al.*, "Strong quantum computational advantage using a superconducting quantum processor," *arXiv*, Jun. 2021. DOI: 10.1103/PhysRevLett.127.180501.

[156] J. M. Gambetta, A. D. Córcoles, S. T. Merkel, *et al.*, "Characterization of addressability by simultaneous randomized benchmarking," *Physical Review Letters*, vol. 109, no. 24, 2012, ISSN: 00319007. DOI: 10.1103/PhysRevLett.109.240504.

[157] J. M. Chow, J. M. Gambetta, E. Magesan, *et al.*, "Implementing a strand of a scalable fault-tolerant quantum computing fabric," *Nature Communications*, vol. 5, pp. 1–9, 2014, ISSN: 20411723. DOI: 10.1038/ncomms5015.

[158] Z. Huang, P. S. Mundada, A. Gyenis, D. I. Schuster, A. A. Houck, and J. Koch, "Engineering Dynamical Sweet Spots to Protect Qubits from 1/f Noise," *Physical Review Applied*, vol. 15, no. 3, p. 034 065, Mar. 2021, ISSN: 2331-7019. DOI: 10.1103/PhysRevApplied.15.034065.

[159] E. Magesan, J. M. Gambetta, and J. Emerson, "Characterizing quantum gates via randomized benchmarking," *Physical Review A - Atomic, Molecular, and Optical Physics*, vol. 85, no. 4, pp. 1–16, 2012, ISSN: 10502947. DOI: 10.1103/PhysRevA.85.042311.

[160] S. Bravyi, D. P. DiVincenzo, and D. Loss, "Schrieffer–Wolff transformation for quantum many-body systems," *Annals of Physics*, vol. 326, no. 10, pp. 2793–2826, Oct. 2011, ISSN: 00034916. DOI: 10.1016/j.aop.2011.06.004.

[161] L. H. Pedersen, N. M. Møller, and K. Mølmer, "Fidelity of quantum operations," *Physics Letters A*, vol. 367, no. 1-2, pp. 47–51, Jul. 2007, ISSN: 03759601. DOI: 10.1016/j.physleta.2007.02.069.

[162] K. N. Nesterov, Q. Ficheux, V. E. Manucharyan, and M. G. Vavilov, "Proposal for entangling gates on fluxonium qubits via a two-photon transition," *arXiv*, pp. 1–13, Nov. 2020. DOI: 10.1103/PRXQuantum.2.020345.

[163] É. Dumur, B. Küng, A. K. Feofanov, T. Weissl, N. Roch, C. Naud, W. Guichard, and O. Buisson, "V-shaped superconducting artificial atom based on two inductively

coupled transmons," *Physical Review B*, vol. 92, no. 2, p. 020 515, Jul. 2015, ISSN: 1098-0121. DOI: 10.1103/PhysRevB.92.020515.

[164] M. Naghiloo, M. Abbasi, Y. N. Joglekar, and K. W. Murch, "Quantum state tomography across the exceptional point in a single dissipative qubit," *Nature Physics*, vol. 15, no. 12, pp. 1232–1236, 2019, ISSN: 17452481. DOI: 10.1038/s41567-019-0652-z.

[165] Z. K. Minev, S. O. Mundhada, S. Shankar, P. Reinhold, R. Gutiérrez-Jáuregui, R. J. Schoelkopf, M. Mirrahimi, H. J. Carmichael, and M. H. Devoret, "To catch and reverse a quantum jump mid-flight," *Nature*, vol. 570, no. 7760, pp. 200–204, 2019, ISSN: 14764687. DOI: 10.1038/s41586-019-1287-z.

[166] N. Bergeal, F. Schackert, M. Metcalfe, R. Vijay, V. E. Manucharyan, L. Frunzio, D. E. Prober, R. J. Schoelkopf, S. M. Girvin, and M. H. Devoret, "Phase-preserving amplification near the quantum limit with a Josephson ring modulator," *Nature*, vol. 465, no. 7294, pp. 64–68, 2010, ISSN: 00280836. DOI: 10.1038/nature09035.

[167] A. Opremcak, I. V. Pechenezhskiy, C. Howington, *et al.*, "Measurement of a superconducting qubit with a microwave photon counter," *Science*, vol. 361, no. 6408, pp. 1239–1242, 2018, ISSN: 10959203. DOI: 10.1126/science.aat4625.

[168] S. Kono, K. Koshino, Y. Tabuchi, A. Noguchi, and Y. Nakamura, "Quantum nondemolition detection of an itinerant microwave photon," *Nature Physics*, vol. 14, no. 6, pp. 546–549, 2018, ISSN: 17452481. DOI: 10.1038/s41567-018-0066-3.

[169] J. C. Besse, S. Gasparinetti, M. C. Collodo, T. Walter, P. Kurpiers, M. Pechal, C. Eichler, and A. Wallraff, "Single-Shot Quantum Nondemolition Detection of Individual Itinerant Microwave Photons," *Physical Review X*, vol. 8, no. 2, p. 21 003, 2018, ISSN: 21603308. DOI: 10.1103/PhysRevX.8.021003.

[170] I. C. Hoi, C. M. Wilson, G. Johansson, T. Palomaki, B. Peropadre, and P. Delsing, "Demonstration of a single-photon router in the microwave regime," *Physical Review Letters*, vol. 107, no. 7, pp. 1–5, 2011, ISSN: 00319007. DOI: 10.1103/PhysRevLett.107.073601.

[171] I. Shomroni, S. Rosenblum, Y. Lovsky, O. Bechler, G. Guendelman, and B. Dayan, "All-optical routing of single photons by a one-atom switch controlled by a single photon," *Science*, vol. 345, no. 6199, pp. 903–906, Aug. 2014, ISSN: 10959203. DOI: 10.1126/science.1254699.

[172] B. Kannan, M. J. Ruckriegel, D. L. Campbell, *et al.*, "Waveguide quantum electrodynamics with superconducting artificial giant atoms," *Nature*, vol. 583, no. 7818, pp. 775–779, 2020, ISSN: 14764687. DOI: 10.1038/s41586-020-2529-9.

[173] K. S. Chou, J. Z. Blumoff, C. S. Wang, P. C. Reinhold, C. J. Axline, Y. Y. Gao, L. Frunzio, M. H. Devoret, L. Jiang, and R. J. Schoelkopf, "Deterministic teleportation of a quantum gate between two logical qubits," *Nature*, vol. 561, no. 7723, pp. 368–373, 2018, ISSN: 14764687. DOI: 10.1038/s41586-018-0470-y.

[174] V. Tripathi, M. Khezri, and A. N. Korotkov, "Operation and intrinsic error budget of a two-qubit cross-resonance gate," *Physical Review A*, vol. 100, no. 1, pp. 1–21, 2019, ISSN: 24699934. DOI: 10.1103/PhysRevA.100.012301.

[175] S. Krinner, S. Lazar, A. Remm, C. Andersen, N. Lacroix, G. Norris, C. Hellings, M. Gabureac, C. Eichler, and A. Wallraff, "Benchmarking Coherent Errors in Controlled-Phase Gates due to Spectator Qubits," *Physical Review Applied*, vol. 14, no. 2, p. 024 042, Aug. 2020, ISSN: 2331-7019. DOI: 10.1103/PhysRevApplied.14.024042.

[176] A. W. Cross and J. M. Gambetta, "Optimized pulse shapes for a resonator-induced phase gate," *Physical Review A - Atomic, Molecular, and Optical Physics*, vol. 91, no. 3, pp. 1–12, 2015, ISSN: 10941622. DOI: 10.1103/PhysRevA.91.032325.

[177] H. Paik, A. Mezzacapo, M. Sandberg, *et al.*, "Experimental Demonstration of a Resonator-Induced Phase Gate in a Multiqubit Circuit-QED System," *Physical Review Letters*, vol. 117, no. 25, pp. 1–5, 2016, ISSN: 10797114. DOI: 10.1103/PhysRevLett.117.250502.

[178] S. Puri and A. Blais, "High-Fidelity Resonator-Induced Phase Gate with Single-Mode Squeezing," *Physical Review Letters*, vol. 116, no. 18, pp. 1–5, 2016, ISSN: 10797114. DOI: 10.1103/PhysRevLett.116.180501.

[179] Z. Wang, S. Shankar, Z. K. Minev, P. Campagne-Ibarcq, A. Narla, and M. H. Devoret, "Cavity Attenuators for Superconducting Qubits," *Physical Review Applied*, vol. 11, no. 1, p. 1, 2019, ISSN: 23317019. DOI: 10.1103/PhysRevApplied.11.014031.

[180] F. Yan, D. Campbell, P. Krantz, *et al.*, "Distinguishing Coherent and Thermal Photon Noise in a Circuit Quantum Electrodynamical System," *Physical Review Letters*, vol. 120, no. 26, p. 260 504, 2018, ISSN: 10797114. DOI: 10.1103/PhysRevLett.120.260504.

[181] J. Kelly, R. Barends, A. G. Fowler, *et al.*, "State preservation by repetitive error detection in a superconducting quantum circuit," *Nature*, vol. 519, no. 7541, pp. 66–69, 2015, ISSN: 14764687. DOI: 10.1038/nature14270.

[182] J. S. Otterbach, R. Manenti, N. Alidoust, *et al.*, "Unsupervised Machine Learning on a Hybrid Quantum Computer," 2017.

[183] D. Gusenkova, M. Spiecker, R. Gebauer, *et al.*, "Quantum non-demolition dispersive readout of a superconducting artificial atom using large photon numbers," *arXiv*, pp. 1–14, Sep. 2020. DOI: 10.1103/PhysRevApplied.15.064030.

[184] J. B. Hertzberg, E. J. Zhang, S. Rosenblatt, *et al.*, "Laser-annealing Josephson junctions for yielding scaled-up superconducting quantum processors," *npj Quantum Information*, vol. 7, no. 1, 2021, ISSN: 20566387. DOI: 10.1038/s41534-021-00464-5.

[185] E. J. Zhang, S. Srinivasan, N. Sundaresan, *et al.*, "High-performance superconducting quantum processors via laser annealing of transmon qubits," *Science Advances*, vol. 8, no. 19, pp. 1–8, May 2022, ISSN: 2375-2548. DOI: 10.1126/sciadv.abi6690.

[186] H. Hemmati, J. C. Mather, and W. L. Eichhorn, "Submillimeter and millimeter wave characterization of absorbing materials," *Applied Optics*, vol. 24, no. 24, p. 4489, 1985, ISSN: 0003-6935. DOI: 10.1364/ao.24.004489.

[187] L. Valenziano, O. A. Peverini, M. Zannoni, R. Tascone, G. Addamo, G. Virone, M. Lumia, S. Mariotti, and A. De Rosa, "New RF data on ECCOSORB CR/MF absorber," *Millimeter, Submillimeter, and Far-Infrared Detectors and Instrumentation for Astronomy VII*, vol. 9153, no. November 2016, p. 91532X, 2014, ISSN: 1996756X. DOI: 10.1117/12.2056315.